Experimental Rock Physics and Applied Geophysical Models for Long-Term Monitoring of Carbon Dioxide Injected Reservoirs

by

Alan James Mur

Bachelor of Science in Geology and English Writing, University of Pittsburgh, 2008

Submitted to the Graduate Faculty of the

Kenneth P. Dietrich School of Arts and Sciences in partial fulfillment

of the requirements for the degree of

Doctor of Philosophy

University of Pittsburgh

2014

UNIVERSITY OF PITTSBURGH

DIETRICH SCHOOL OF ARTS AND SCIENCES

Geology & Planetary Science

This dissertation was presented

by

Alan James Mur

It was defended on

November 27, 2013

and approved by

Mark Abbott, Department Chair and Professor, Geology and Planetary Science

Thomas Anderson, Professor Emeritus, Geology and Planetary Science

Daniel Bain, Assistant Professor, Geology and Planetary Science

Yee Soong, Scientist and Team Leader, National Energy Technology Laboratory

Dissertation Advisor: William Harbert, Professor, Geology and Planetary Science

Experimental Rock Physics and Applied Geophysical Models for Long-Term Monitoring of Carbon Dioxide Injected Reservoirs

Alan James Mur, PhD

University of Pittsburgh, 2014

Experimental Rock Physics and Applied Geophysical Models for Long-Term Monitoring of Carbon Dioxide Injected Reservoirs

Alan James Mur, PhD

University of Pittsburgh, 2014

New methods of frequency and stress dependent petrophysical modeling are developed to link and predict laboratory, well log, and seismic scale pore fluid and pressure effects. These effects include pressure induced pore expansion, dissolution and material loss, and fluid effects on bulk properties. Petrophysical models that incorporate wave propagation at ultrasonic, well log, and seismic frequencies are produced with effective pressure and fluid dependent elements in reservoir limestone and sandstone for the purpose of reservoir monitoring.

The petrophysical model introduces stress sensitivity elements into bulk and shear moduli to account for non-linear elastic behavior at the low effective pressure regimes. Stress effects are modeled by defining stiff and compliant pore classes with assigned stress sensitivities based on geometric properties. The c_{33} elastic constant is then modified to include frequency dependent attenuation in the P wave velocity model. The characteristic frequencies are defined by not only the passing wave frequency but also key properties including permeability, fluid viscosity, and bulk modulus. The model input parameters are derived from core measurements and multi-scale observations including core velocity measurements, scanning electron microscopy, and computed micro tomography.

Limestone dissolution is observed in laboratory experiments performed with reactor vessels at in situ conditions using CO_2-H_2O mixes. The petrophysical models are updated to reflect the observed dissolution results. Further, the before and after μCT analysis of the samples reveal

internal porosity gains, accompanied by decreases in pore surface area to volume ratios, which are seen to be limiters in chemical reaction rates.

Finally, CO_2 quantification techniques in reservoir pore space are explored. Modeled and observed properties are implemented to interpret repeat reflection seismic surveys in which changes in pore pressure and pore-filling fluid density occur. The Sandstone and limestone reservoir fluid substitution models are compared with seismic anomalies to delineate pressure effects from fluid property effects. Impedance models at the sandstone reservoir reveal a 25% maximum acoustic impedance decrease with a fluid substitution filling the reservoir with 75% CO_2. This significant impedance difference leads to increased reflectivity, which is confirmed with actual 4-D reflection seismic surveying.

TABLE OF CONTENTS

LIST OF TABLES

LIST OF FIGURES

PREFACE

The Ph.D. journey at the University of Pittsburgh has been long and winding. As an undergraduate I was given to opportunity to work with Dr. Bill Harbert at the Honors College Yellowstone Field Camp for two exciting years. I remember a conversation while hopping on snow drifts that gave me the impression that geophysicists spend all of their time outdoors! My assumption was slightly off. Fortunately, the time spent inside academically and conversationally exploring the seemingly endless store of knowledge inside of Bill's head has more than balanced any discrepancies.

My committee members Yee Soong, Tom Anderson, Dan Bain, and Mark Abbott have aided my understanding of chemistry, climatology, water, and tectonics immensely over the past years. At NETL I would like to thank for their support: Dustin Crandall, Dustin Mcintyre, Bob Warzinski, Yongkoo Seol, Brian Strazisar, and Barbara Kutchko; Igor Haljasmaa for being a great experimentalist/sage and Jim Fazio for keeping me safe from high pressures and temperatures.

I recognize Chris Purcell for all disagreements that we had as geologist versus physicist. These were the most important personal discoveries to date. His Victorian hobbyist style has taught us all to value our time.

I thank my family and all of my parental guides for attempting to listen to what I had to say about rock physics, Stephen Kennedy, Serge Shapiro, Dolly Chavez, Shannon Granahan, the coolest office mates: Erich Zorn, Matt Finkenbinder, Aubrey Hillman, and David Pompeani; my oldest friends Leland Frye and Rob Sneed; and Cindy Lisica for the finish line push.

I must also thank these institutions for making my research financially possible: NETL-DOE and the URS/RDS contracts that supported this research (URS 4000.2.651.072.001.361/

4000.4.641.061.001.532 for multi-scale synthesis and petrophysical modeling of experimental and field data and RDS 606.08.05.201/606.08.05.202 for Effects of pore-filling fluids on seismic wave properties, rock physics and seismic imaging of subsurface CO_2). The Honors College for helping me explore the West, The University of Pittsburgh and finally Schlumberger, SMT, and Ikon for the incredible geophysical software support.

1.0 INTRODUCTION

I present a model that predicts elastic property changes in sandstone and limestone due to long term CO_2 exposure and injection. To better understand how a rock behaves under stress and filled with varying fluid mixtures, multiple data sets at the micro (10^{-6} m, micro computed tomography), meso (10^{-1} to 10^{1} m, core experiments and well logs) and reflection seismic scales (10^{3} m, seismic reflection survey) are integrated to develop fluid tracking methods in rock matrices useful in long-term subsurface CO_2 seismic monitoring. The National Energy Technology Laboratory (NETL) of the United States Department of Energy has investigated the capture of CO_2 at power plants, storage potential of depleted reservoirs and long term monitoring of the buried gas (NETL 2012). Much technical and functional knowledge has already been gained through industrial development of enhanced oil recovery (EOR) techniques (SPE 1999). For economic and accountability assurances, injected subsurface CO_2 must be quantified and monitored at a low cost. To quantify the volume of CO_2 in reservoir pore space through the use of seismic surveying techniques, thorough understanding of the rock elastic properties is required. Seismic response is altered as reservoir structure, pressure, and permeability vary. Representative carbonate and sandstone reservoir materials were measured and models were produced for CO_2 injection scenarios for the dual goal of long-term CO_2 storage and enhanced oil recovery monitoring.

This study was conducted in collaboration with the Bureau of Economic Geology (BEG) in Austin, Texas. The field site is the Pennsylvanian-Permian carbonate reservoir on a unitized oil field. The site has had ongoing CO_2 injection since 1972 for EOR purposes. Reservoir rock material, log data from a number of wells, and multiple seismic surveys both before and after CO_2 injections were provided for the study of the limestone unit. The core material was imaged using scanning electron microscope and computed tomography techniques.

Data from another CO_2 EOR site were also used for reservoir seismic response modeling. Previous mineralogical analysis on a near-injection observation well (Lu et al. 2012), a full suite of log data at the injector well, two 3-D seismic reflection surveys, and two vertical seismic profile surveys were used in this project.

1.1 MULTI-SCALE ANALYSIS

4-D models of reservoirs are more accurate if the rock characteristics are assessed and characterized across a wide spectrum of scales. In order to assess rocks properties from micrometer to kilometer scale, the following tools and techniques were employed from small to large scale: micro computed tomography, scanning electron microscopy, meso-scale computed tomography, ultrasonic rock velocity measurement, sonic rock velocity measurement, vertical seismic surveying, and 3-D seismic surveying. The relationship of instrument resolution to reservoir coverage is shown (Figure 1). 3-D surface seismic covers the largest fraction of a reservoir and provides the framework for models which must be informed by the described higher

resolution instruments. It is our intention to use the observations across scales to produce 4-D models of reservoirs that can account for effective pressure and fluid density changes.

Land-based, 3-D seismic reflection surveys have resolution limitations due to wavelength. Smaller scale observations are meant to overcome scaling heterogeneities by populating and characterizing the space between interpreted horizons. For instance, p-wave rock velocities in the earth range from Vp = 200 to 4000 m/s in unconsolidated materials, Vp = 2000 to 6500 m/s in sedimentary rocks, and up to Vp = 8500 m/s in ultramafic rocks (Kearey et al. 2002). Due to high-frequency attenuation, the usable land reflection survey frequency spectrum normally ranges from 2 to 120 Hz (Sheriff et al. 1995) with a modern high end up to 150 Hz. The wavelength of a 100 Hz wave in a 3000 m/s rock is 30 meters, so according to Rayleigh's criterion, resolution in this bandwidth is limited to, at best, a half wave length (15 meters for 100 Hz wave).

The first enhancement of vertical resolution compared with reflection seismic methods is vertical seismic profile surveying (VSP). This method has the advantage of shortened travel time due to the placement of geophones downhole. As attenuation is partially dependent on the distance traveled by the seismic wave, less high end frequencies are lost in a VSP survey. The VSP surveys we analyzed were performed with vibrator sweeps up to 250 Hz. Assuming the same Vp = 3000 m/s rock, the 250 Hz wavelength becomes 12 meters (half wave of 6 meters). Cross well surveys reach source frequencies up to 2000 Hz with wavelength resolution to less than 3 meters, but are two dimensional by nature. Consequently, even with high-frequency reservoir sized surveys, the unique structures, bedding, and pore space is unresolvable. Objects smaller than seismic reflection resolution size requirements have an effect on the bulk rock properties over the viewing interval, but inversions for these properties are non-unique.

Wireline well logging allows for the sampling of rock properties at decimeter (10^{-1} m) scale. Logs are correlated with seismic through down sampling to ensure proper seismic time-depth conversion and wavelet information. Once a reasonable level of seismic to well calibration has been reached, rock properties are interpolated throughout the reservoir using interpreted seismic reflection horizons or surface model boundaries as constraints.

The rock properties distributed to the reservoir are found by characterizing the rocks at finer scale with XRD, SEM, CT, and μCT imaging. Porous reservoir rock is composed of a mixture of minerals with distinct properties. The arrangement of mineral material can have a major effect on the behavior of sound waves through the rock (e.g. anisotropic compressibility of phyllosilicates due to mineral lattice characteristics). At the micron scale, X-ray crystallography is used to identify mineral signatures for bulk mineral moduli. At the crystal scale, compressibility is defined along lattice orientation. Mineral mixing models (Hill 1952, Hashin et al. 1961, Thomsen 1972) produce bulk mineral moduli, often under the assumption of isotropy.

For the limestone imaged, the microscopic resolution achievable on the fine grained cement called for a technique to characterize the empty-space as opposed to grain contact and grain orientation characterization techniques (Thomsen 1995, Brajanovski et al. 2005). Anisotropy caused by material arrangement is modeled as aligned cracks and pores.

Scanning electron microscopy and X-ray micro-tomography are used to identify the structures that define the dynamic physical behaviors of the rock. These properties are then used as inputs for the well log mineral model which can then better predict elastic properties. The better constrained well log values allow for the tuning and confirmation of seismic trained forward and inverse models (Section 5.1). These models produce reservoir properties such as mineralogy, porosity, permeability, and all elastic properties.

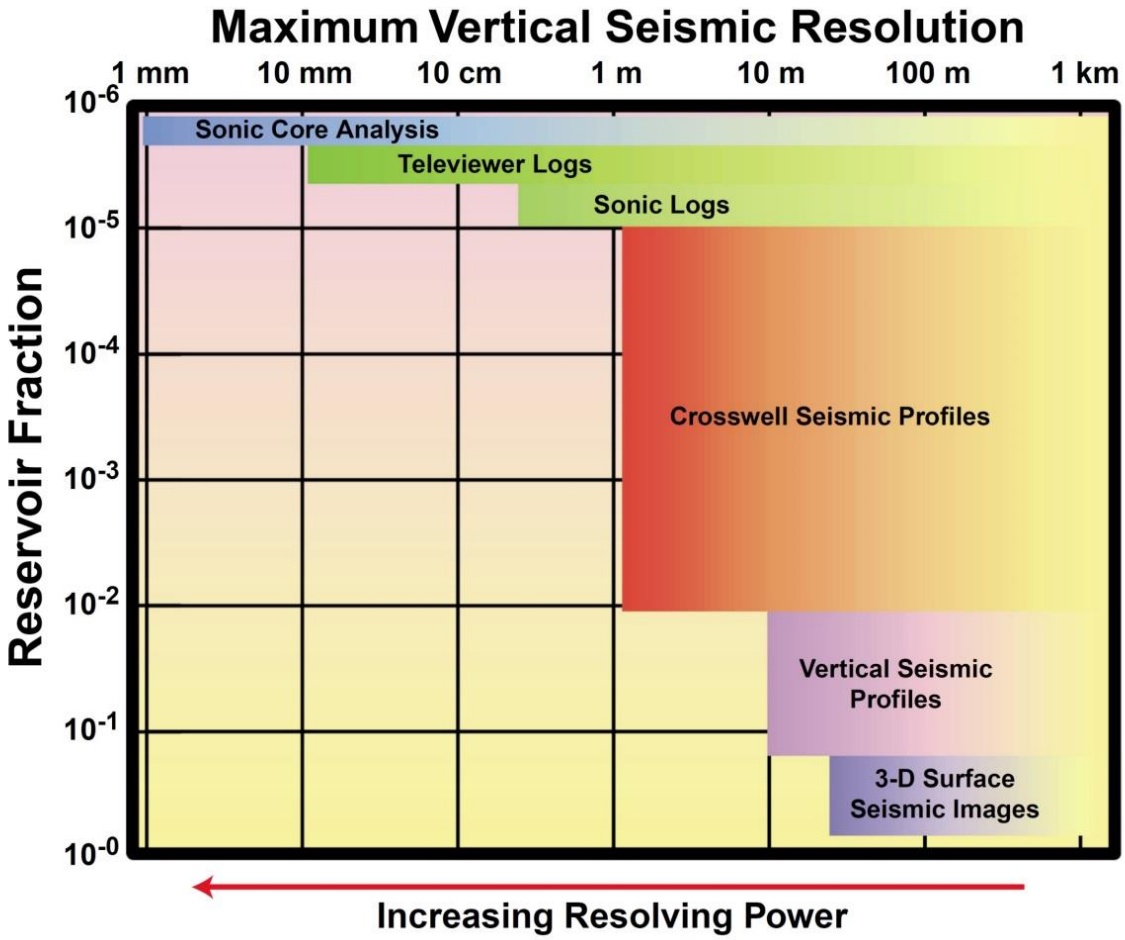

Figure 1. Resolving power and volume coverage of various seismic tools (Harris et al. 2001). High resolution instruments cover only a small fraction of a reservoir whereas low resolution instruments cover a high fraction of the reservoir. The key to integration of all scales with good inversion and interpolation techniques.

1.2 GEOLOGIC SETTING

The geologic, depositional and production histories of the sandstone and reef carbonate fields have been extensively studied and reviewed as hydrocarbons have been produced from them since 1943 and 1948, respectively (Larkin 2006, Lu et al. 2012).

1.2.1 Carbonate Reef Reservoir

The key reservoir units in the carbonate reef are the Cisco and Canyon Reef Pennsylvanian age Limestone units (Figure 4). The carbonate units, which lie at an average depth of 1900-2200 meters in the northern part of the Midland Basin (see Figure 2), comprise the Horseshoe Atoll. The location of interest is found on the east side of this atoll (Langston et al. 1988).

1.2.1.1 Depositional History

For the model of material deposition in the Horseshoe Atoll, a standard schematic model for an isolated carbonate platform as described by (Emery et al. 1996) is used. Figure 5 and Figure 6 give the sequence stratigraphy interpretation along with the interpreted reflection seismic cross sections of the reef. The interpretation follows a sinusoidal relative sea level curve: transgressive, maximum flooding, highstand, lowstand, and finally the platform is drowned and buried in shale.

The Wolfcamp formation, composed of 400-600 meters of marine shales that overlie the reservoir unit (Vest 1970, Larkin 2006, O'Dowd 2008), includes the Dean siltstone. The units have been interpreted as part of a high-stand sea level rise flooding surface and after the reef mounds were buried, subsidence occurred to the west, causing tilting of the reef complex to the west. Maturing hydrocarbons eventually migrated to the eastern edge of the reef. Figure 3 shows the present structure and end result of this burial process. Figure 4 shows the stratigraphy of the Carboniferous-Permian section.

At this location, more than 1600 wells were in production by 1951, three years after the discovery of the Canyon Reef formation. By 1951, 4.5% of the original oil in place (OOIP) had been produced, and reservoir pressure had dropped by 50%. Using solution gas drive as an

enhanced oil recovery method, it was estimated that only 19% of the oil was recoverable. In 1953, the regional well operators joined forces and water injection techniques were developed and implemented. Eventually, the use of CO_2 in flooding was determined to be the most economical decision and began in 1971 (Langston et al. 1988). Table 1 gives a collection of industry collected porosity and permeability values in this locality.

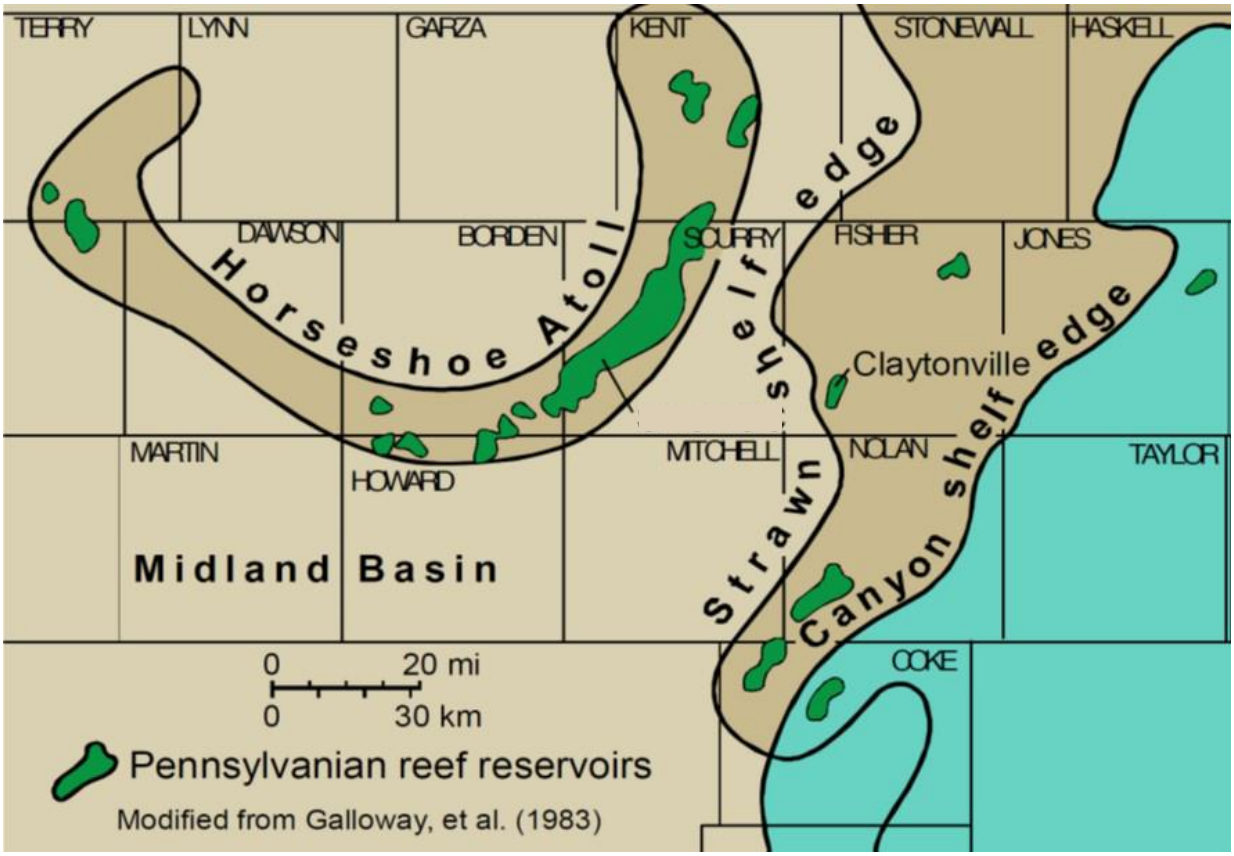

Figure 2. Coverage map of Horseshoe Atoll (Galloway 1983, Hilterman 1983, O'Dowd 2008).

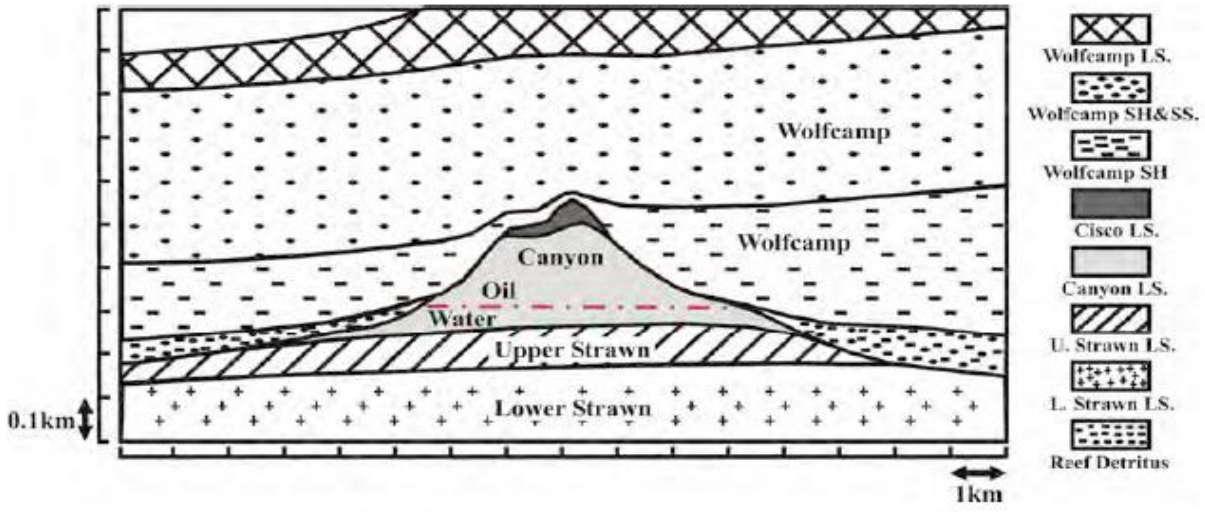

Figure 3. General cross sections showing reef structure (Vest 1970). Initial oil water line is marked in red.

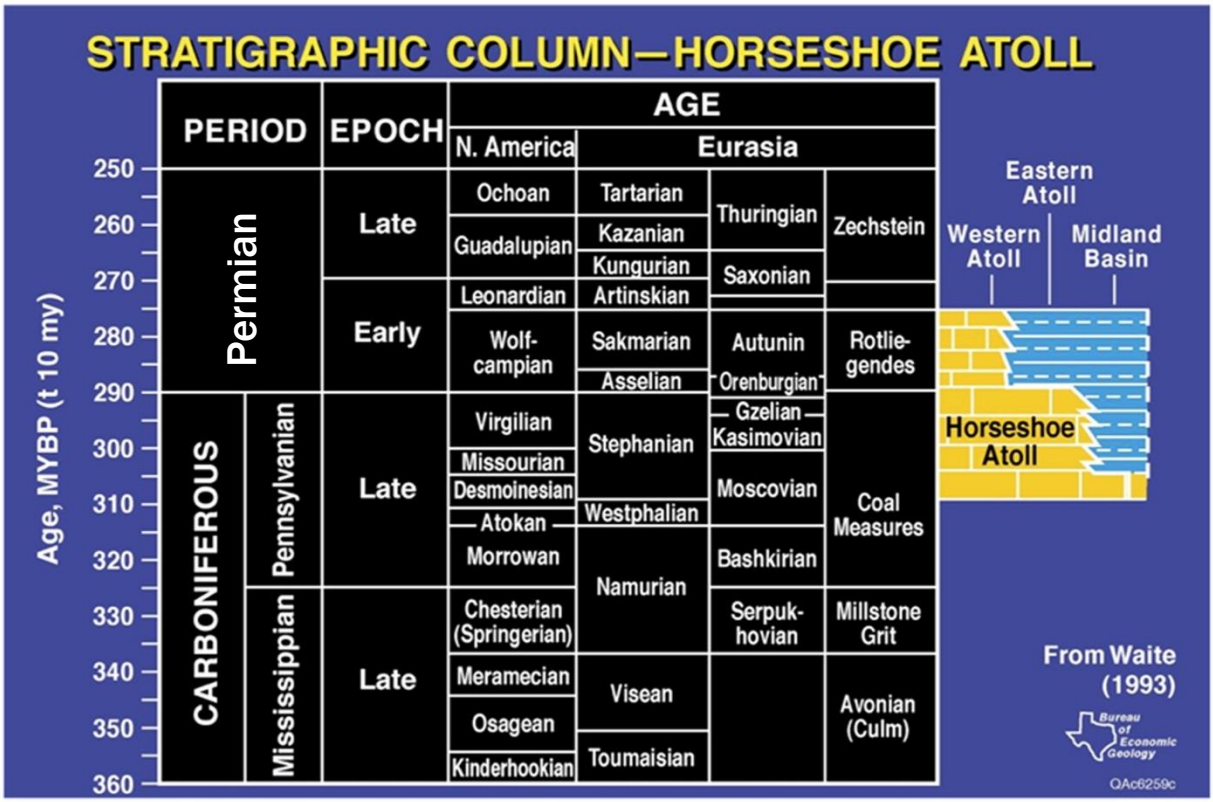

Figure 4. Stratigraphic column of Horseshoe Atoll (Waite 1993). The studied reservoir is part of the Eastern Atoll.

Table 1. Carbonate reef facies, porosity, and permeability modified from (Han 2008).

Porosity (%), facies (when available)	Permeability (mD) (when available)	Source
18.53, 6.39	2.2 - 2.8	This study
(0~20)	N/A	Bergenback et al. (1953)
6 (0~30)	4.5 (0~85): matrix 2500: cracks/fractures	Myers et al. (1956)
6	(0-85)	Burnside (1959)
10.3	30.6	Vest (1970)
3.93 (over gross thickness)	19.4	Kane (1979)
9.41	3.03	Langston et al. (1988)
9.8 (0~22.5)	19 (0.1~1760)	Raines (2005)
7.6	19.4	Brnak et al. (2006)
15~20: Sponge mound facies	N/A	Schatzinger (1988)
<15: Phylloid mound facies	N/A	Schatzinger (1988), Reid et al. (1991)
20~30: Oolitic grainstone facies	N/A	Schatzinger (1988)
poor, up to 5: Pertida mud facies	N/A	
poor, up to 10: Breccia facies	N/A	
25~30: Oolitic grainstone facies	>100	Reid et al. (1991)
20~25: Bioclastic grainstone facies	10~50	
15~20: Algal wackestone facies	<10	

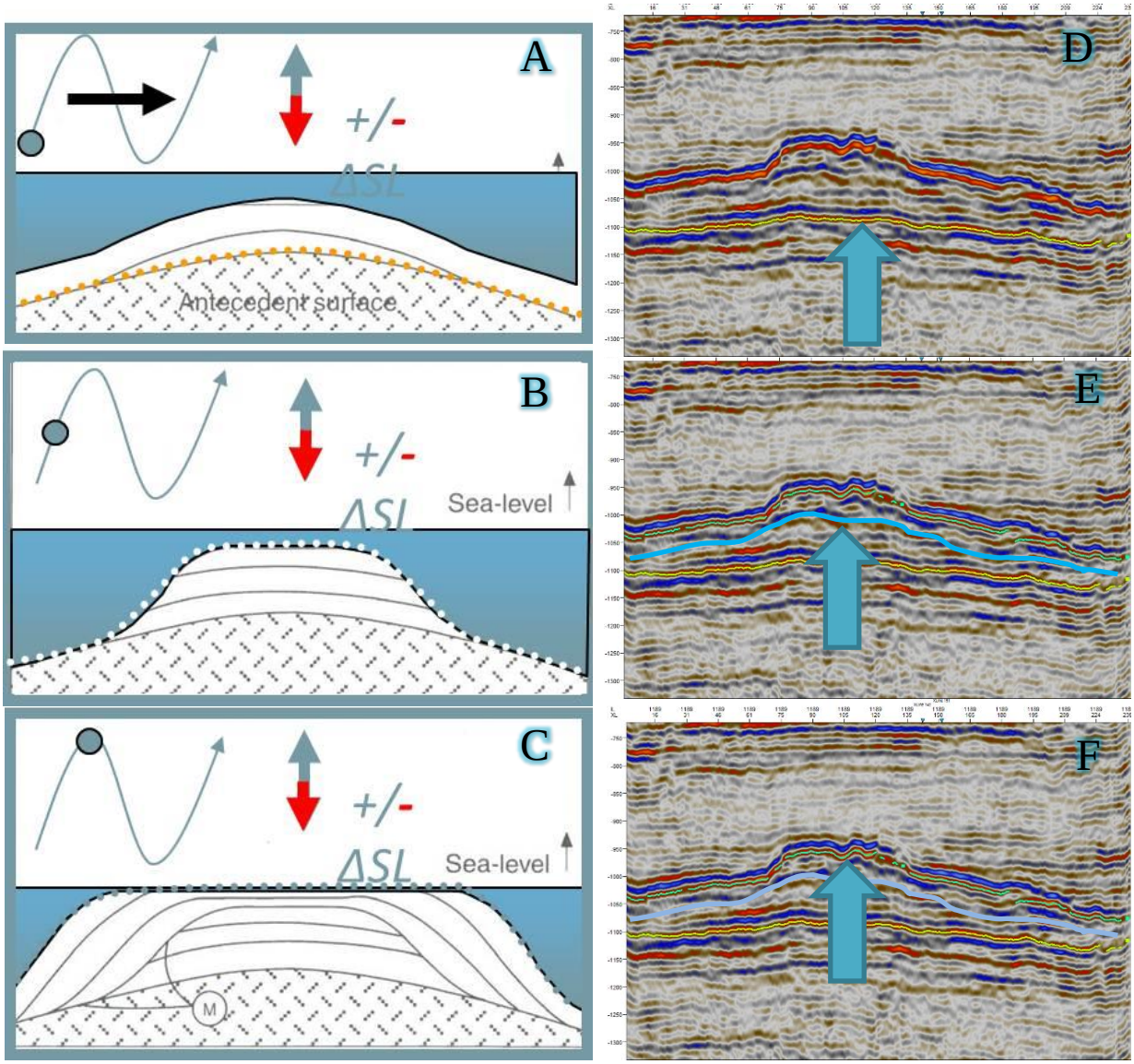

Figure 5. Stratigraphy (A, B, C) and reflection seismic interpretation (D, E, F) of the carbonate reef platform described. In D, E, and F the blue and red shading on the seismic sections indicate the reflected wave amplitude: red (+), blue (-). The blue arrow on the seismic sections indicates the depositional surface corresponding to the stratigrapic cartoon.

(A,D): Transgressive systems tract. Biogenic carbonate builds, deposits on low energy stand.

(B,E): Maximum flooding surface. Sedimentation increases with sea level rise.

(C,F): Highstand systems tract. Reef deposition angles outward, slumping. (Emery et al. 1996)

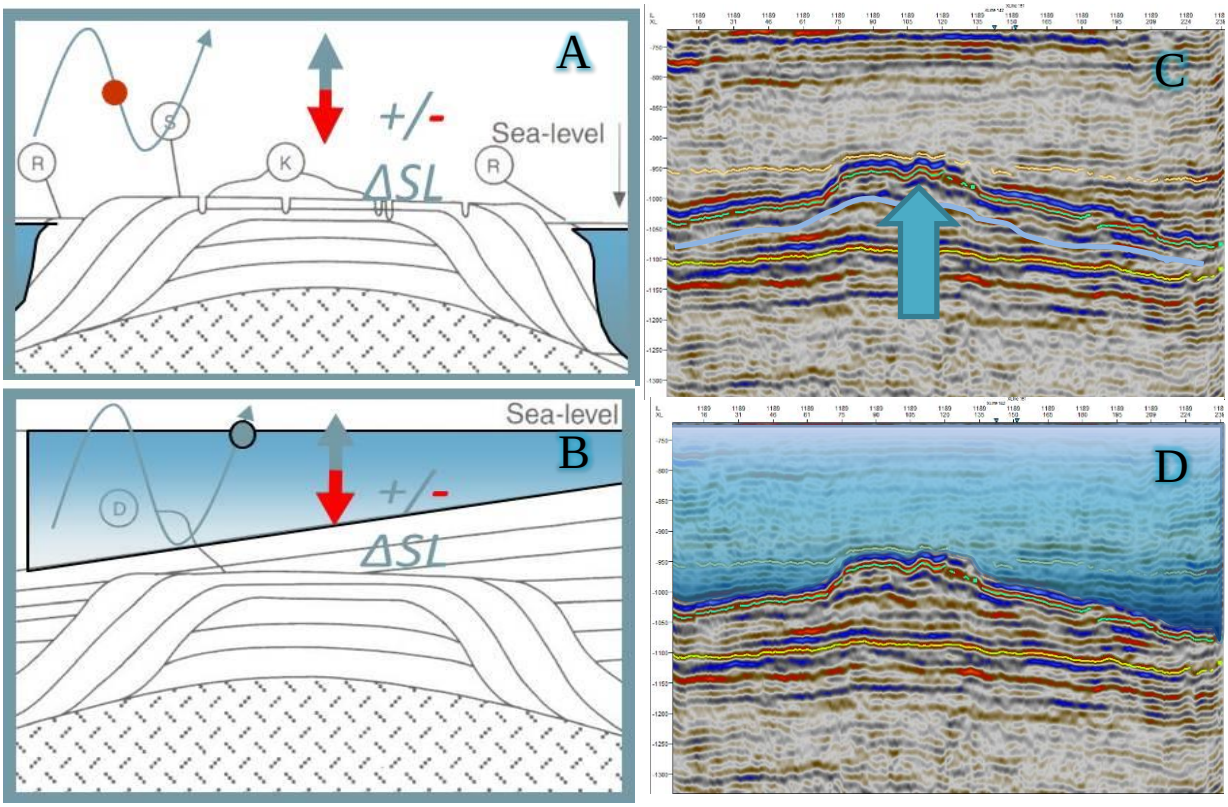

Figure 6. Stratigraphy (A, B) and reflection seismic interpretation (C, D) of carbonate reef platform Part 2. In C, D the blue arrow on the seismic sections indicates the depositional surface corresponding to the stratigrapic cartoon.

(A, C): Lowstand systems tract. Sea level fall, erosion, shedding of material down slope.

(B, D): Platform drowning. Reef completely buried with relative sea level rise (subsidence as well) (Emery et al. 1996).

1.2.1.2 Core Material and Data

Two cores (diameter approximately three inches) were provided by the Bureau of Economic Geology (Austin) and Kinder Morgan from the carbonate reef well reservoir units. All experiments were performed on a subset from these cores representative of high and low porosity formation materials. The high porosity (HP) material comes from a depth of 6500 ft. (1981 m), has a desiccator-dry bulk density of 2.20 g/cm^3 and helium porosimeter-measured porosity of 18.53%. The low porosity (LP) material comes from a depth of 6180 ft. (1884 m), has a desiccator-dry bulk density of 2.55 g/cm^3 and porosity of 6.39%. For velocity measurements, 2 inch (5.08 cm) diameter samples were cut from the HP and LP material(Purcell 2012). Ultrasonic velocity measurement and setup was done at NETL and is further explained in 2.2.

1.2.2 Cranfield Sandstone Reservoir

Along the southern rim of the Mississippi Salt Basin, in southwest Mississippi, lies the lower Tuscaloosa trend. Sand reservoirs within the trend have been produced since their discovery in the 1940s. A system of traps has been recognized in the five producing reservoirs including: up dipping stratigraphic traps with lateral pinch-outs, sealing faults, and an anticline (Womack 1950, Hersch 1987, Zhang et al. 2012). Figure 7 shows the injection site location on a geologic cross-section across the Gulf of Mexico as well as the stratigraphy from the Cretaceous to the Pleistocene at that location. The upper Cretaceous, Tuscaloosa formations are the zones of interest. They consist of shaley sand units (subsea depths of 3000-4200 meters) divided by slightly sandy shales. Zhang et al. states that average porosity for the gas and oil zone is ~20% (Zhang et al. 2012), permeability ranges from 0 to 8690 mD (average 280 mD) and water saturation is at least 47%.

The reservoir unit of interest is the “D-E Sandstone,” which contains chlorite cement and has an average permeability of 100mD (Hovorka et al. 2011).

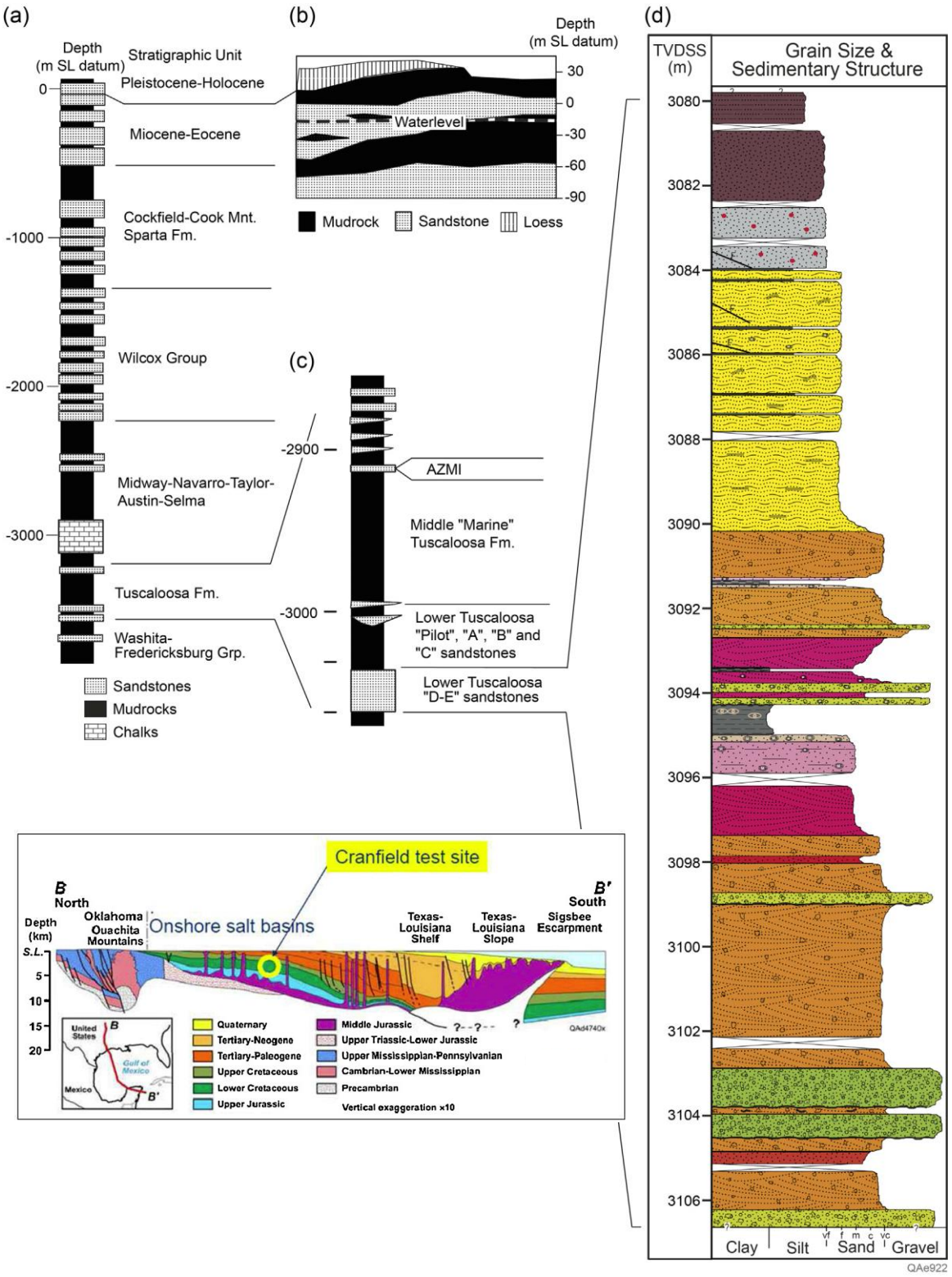

Figure 7. Stratigraphy of the Cranfield formation, Cretaceous interval highlighted, and geologic cross section (Galloway et al. 1999, Hovorka et al. 2013).

2.0 ROCK PHYSICS MODELING

Rock physics is understood as the application of Hooke's law to rock while considering physical properties such as mineralogy, porosity, fractures, fluids, permeability, and stress state. Hooke's law is generalized in tensor form to provide three physical dimensions of elasticity to fully describe volumetric stress. Elements of this tensor based construction can be described with Lamé's parameters which represent bulk modulus, young's modulus, shear modulus, Poisson's ratio, p-wave modulus, and Lame's first parameter (λ). Relevant elastic parameters, a number of which standardized by (Mavko et al. 1998), are used to understand and describe seismic data, fluid substitution, rock mechanics, infrastructure, drilling methods, and production.

Hooke's law is used to relate stress and strain in elastic materials. In the traditional one-dimensional representation of a spring, the force, F, applied to the spring is proportional to the displacement, x, by a constant, *k:*

$$\boldsymbol{F = -kx} \qquad \textbf{(1)}$$

$$\boldsymbol{k = \frac{\Delta F}{\Delta x}} \qquad \textbf{(2)}$$

Strain, *x,* will be generally represented with epsilon, *ε*, stress, *F,* will be represented with sigma, *σ,* and stiffness, *k,* will be represented with *c* so that:

$$\boldsymbol{\sigma = -c\varepsilon} \qquad \textbf{(3)}$$

subscripts are used to describe the position of the variable in an appropriate property matrix. Figure 8 shows a generalization of the stress tensor. Strain can be similarly described. This general form can be simplified to describe to rock in three dimensional space. Many of the vectors pictured

will be equal and opposite as the goal is not to describe a rock being thrown, but a wave moving through a usually static sample.

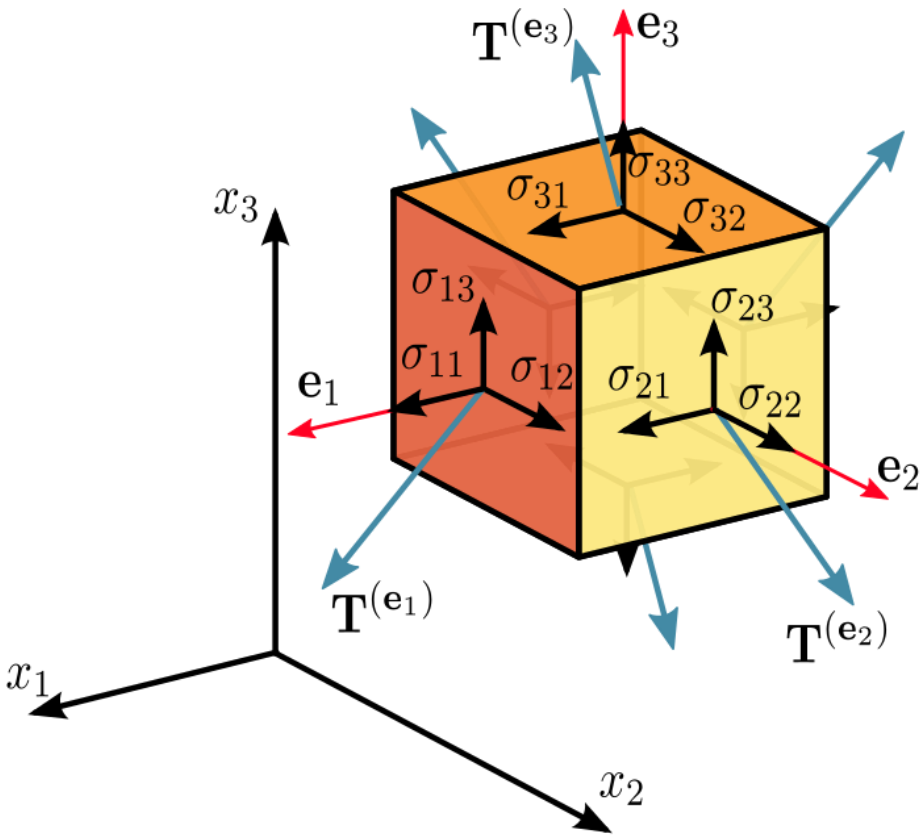

Figure 8. Cartesian system and guide to tensor notation. Stress and strain is distributed to three components on a given face. In this example (Sanpaz 2009), stress directions are arbitrarily numbered with subscripts 1,2,3. Subscripts in further calculations may use subscript i, j, k notation, denoting non-rotation from x, y, z orientation.

A clear and mathematically unified compilation of classic equations and derivations from a number of scientific and linguistic backgrounds e.g. (Zoeppritz 1919, Biot 1955, Birch 1961, Timoshenko et al. 2011) is presented in The Rock Physics Handbook (Mavko et al. 1998). The following equations describe the relationship of various moduli that can be used to describe an isotropically elastic material.

(Note that λ and μ are the only rock parameters needed to describe the stress given that strain is described):

$$\boldsymbol{\sigma_{ij} = \lambda \delta_{ij} \varepsilon_{\alpha\alpha} + 2\mu \varepsilon_{ij}} \quad \textbf{(4)}$$

and

$$\boldsymbol{\varepsilon_{ij} = \frac{1}{E}((1+\nu)\sigma_{ij} - \nu \delta_{ij} \sigma_{\alpha\alpha})} \quad \textbf{(5)}$$

In which

ε_{ij} **= elements of the strain tensor**

σ_{ij} **=elements of the stress tensor**

$\varepsilon_{\alpha\alpha}$ **= volumetric strain (sum over repeated index)**

$\sigma_{\alpha\alpha}$**=mean stress times 3 (sum over repeated index)**

δ_{ij} **= 0 if** $i \neq j$**, 1 if** $i = j$

and K, μ, E and ν are defined below.

Bulk modulus, K, is defined as the ratio of hydrostatic stress, σ_0, to volumetric strain:

$$\boldsymbol{K = \frac{\sigma_0}{\varepsilon_{\alpha\alpha}}, \sigma_0 = \frac{1}{3}\sigma_{\alpha\alpha} = K\varepsilon_{\alpha\alpha},} \quad \textbf{(6)}$$

Shear modulus, μ, is defined as the ratio of shear stress to shear strain:

$$\boldsymbol{\mu = \frac{\sigma_{ij}}{2\varepsilon_{ij}}, \sigma_{ij} = 2\mu\varepsilon_{ij}, i \neq j} \quad \textbf{(7)}$$

Young's modulus, E, is defined as the ratio of extensional stress to extensional strain in a uniaxial stress state:

$$\boldsymbol{E = \frac{\varepsilon_{zz}}{\sigma_{zz}}, \quad \sigma_{xx} = \sigma_{yy} = \sigma_{xy} = \sigma_{xz} = \sigma_{yz} = 0} \quad \textbf{(8)}$$

Poisson's ratio, ν, is defined as minus the ratio of lateral strain to axial strain in a uniaxial stress state:

$$\boldsymbol{\nu = -\frac{\varepsilon_{xx}}{\varepsilon_{aa}}, \sigma_{xx} = \sigma_{yy} = \sigma_{xy} = \sigma_{xz} = \sigma_{yz} = 0} \quad \textbf{(9)}$$

P-wave modulus, M, is defined as the ratio of axial stress to axial strain in a uniaxial strain state:

$$M = \rho V_P^2 \qquad (10)$$

$$\sigma_{zz} = M\varepsilon_{zz}, \quad \sigma_{xx} = \sigma_{yy} = \sigma_{xy} = \sigma_{xz} = \sigma_{yz} = 0 \qquad (11)$$

Table 2 describes the various algebraic relationships between common elastic constants.

Table 2. Relationships of elastic constants in isotropic materials (Birch 1961, Mavko et al. 1998).

K =	E =	λ =	ν =	M =	μ =
$\lambda + \frac{2\mu}{3}$	$\mu\frac{3\lambda + 2\mu}{\lambda + \mu}$		$\frac{\lambda}{2(\lambda + \mu)}$	$2(\lambda + \mu)$	
	$9K\frac{K - \lambda}{3K - \lambda}$		$\frac{\lambda}{2K - \lambda}$	$3K - 2\lambda$	$\frac{3(K - \lambda)}{2}$
	$9K\frac{K\mu}{3K + \mu}$	$K - \frac{2\mu}{3}$	$\frac{3K - 2\mu}{2(3K + \mu)}$	$K + \frac{4\mu}{3}$	
$\frac{E\mu}{3(3\mu - E)}$		$\mu\frac{E - 2\mu}{(3\mu - E)}$	$\frac{E}{2\mu} - 1$	$\mu\frac{4\mu - E}{3\mu - E}$	
		$3K\frac{3K - E}{9K - E}$	$\frac{3K - E}{6K}$	$3K\frac{3K + E}{9K - E}$	$\frac{3KE}{9K - E}$
$\lambda\frac{1 + \nu}{3\nu}$	$\lambda\frac{(1 + \nu)(1 - 2\nu)}{\nu}$			$\lambda\frac{1 - \nu}{\nu}$	$\lambda\frac{1 - 2\nu}{2\nu}$
$\lambda\frac{2(1 + \nu)}{3(1 - 2\nu)}$	$2\mu(1 + \nu)$	$\mu\frac{2\nu}{1 - 2\nu}$		$\mu\frac{2 - 2\nu}{1 - 2\nu}$	
	$3K(1 - 2\nu)$	$3K\frac{\nu}{1 + \nu}$		$3K\frac{1 - \nu}{1 + \nu}$	$3K\frac{1 - 2\nu}{2 + 2\nu}$
$\frac{E}{3(1 - 2\nu)}$		$\frac{E\nu}{(1 + \nu)(1 - 2\nu)}$		$\frac{E(1 - \nu)}{(1 + \nu)(1 - 2\nu)}$	$\frac{E}{(2 + 2\nu)}$

2.1 ROCK FRAMEWORK

To unify research data that may have scaling or instrument simplicity issues, an approach describing the elasticity of materials at varying levels of symmetry is necessary. It is common in seismic imaging to assume that rock moduli are isotropic. This is effective for producing reflection seismic volumes for the purpose of geological interpretation on conventional reservoirs. However, as computing power advances, the complexities of rock (e.g. mineral alignment, fracture orientation, pore orientation, fluid saturation, quality factor, and permeability) can be accounted for over large volumes, allowing for accurate prediction of pore pressure, pore-filling fluids, and in situ stress.

Before equations of motion are applied to the medium, the pore space is described as it causes dynamic effects on the elasticity tensor. Terms such as "soft, compliant, stiff, available, open, and closed" are used to describe porosity in rocks. These terms reflect the pressure regimes in which rock behavior can drastically change, yet still be considered linearly elastic. In order to implement these terms, the stiffness tensor must be developed and defined for various degrees of symmetry. This process, again, begins with Hooke's law which states that σ_{ij} is linearly proportional to the strain ε_{ij} as shown in:

$$\boldsymbol{\sigma_{ij} = c_{ijkl}\varepsilon_{kl}} \qquad \textbf{(12)}$$

the elastic stiffness tensor, c_{ijkl}, is of fourth-rank and has a total of eighty-one components. As not all components are independent and symmetrical, stress-strain values implies that:

$$\boldsymbol{c_{ijkl} = c_{jikl} = c_{ijlk} = c_{jilk}} \qquad \textbf{(13)}$$

Which reduces the number of independent constants to thirty-six. A unique strain energy potential requires that:

$$c_{ijkl} = c_{klij} \tag{14}$$

Which reduces the number of independent constants to twenty-one. Isotropic, linear elastic materials have maximum symmetry and are completely characterized by two independent constants (μ and λ). Using Bond transformation matrices the stiffness elements can be displayed by a 6 x 6 matrix (Mavko et al. 1998). For a linear elastic, isotropic material, the stiffness elements are:

$$\begin{bmatrix} c_{11} & c_{12} & c_{12} & 0 & 0 & 0 \\ c_{12} & c_{11} & c_{12} & 0 & 0 & 0 \\ c_{12} & c_{12} & c_{11} & 0 & 0 & 0 \\ 0 & 0 & 0 & c_{44} & 0 & 0 \\ 0 & 0 & 0 & 0 & c_{44} & 0 \\ 0 & 0 & 0 & 0 & 0 & c_{44} \end{bmatrix}, \quad c_{12} = c_{11} - 2c_{44} \tag{15}$$

These elements are related to Lamé's parameters μ and λ by

$$c_{11} = \lambda + 2\mu, \quad c_{12} = \lambda, \quad c_{44} = \mu \tag{16}$$

(Mavko et al. 1998)

The lowest symmetry material, that with triclinic symmetry (orthorhombic), requires twenty-one constants (nine independent) to be described, but this generalization can be accomplished within this 6 x 6 framework:

$$\begin{bmatrix} c_{11} & c_{12} & c_{13} & 0 & 0 & 0 \\ c_{12} & c_{22} & c_{23} & 0 & 0 & 0 \\ c_{13} & c_{23} & c_{33} & 0 & 0 & 0 \\ 0 & 0 & 0 & c_{44} & 0 & 0 \\ 0 & 0 & 0 & 0 & c_{55} & 0 \\ 0 & 0 & 0 & 0 & 0 & c_{66} \end{bmatrix} \tag{17}$$

In this work, porosity is described using geometric shape models to determine stiffness. Mineral grain contact models are also used (Madonna et al. 2012), but for very fine-grained cement, this is an unfeasible approach.

To relate elastic moduli to wave velocity, density is introduced. With density, bulk, extensional and shear moduli, compressional (V_p) and shear (V_s) wave velocity can be determined. Further, the product of density and particle velocity, impedance, is a crucial parameter in understanding reflection and transmission of waves at bulk material interfaces.

2.2 LABORATORY ROCK PROPERTY MEASUREMENTS

Ultrasonic velocity measurements were performed on multiple rock cores using a New England Research (NER) Autolab 1500. This system supports most standard rock mechanics test regimens, such as hydrostatic compression, unconfined compression, confined compression, creep, and uniaxial strain. Each of these tests may be performed at pore pressures and temperatures representative of reservoir conditions (NER 2006). In the discussed experiments, maximum effective pressures did not exceed 60 MPa.

A schematic diagram of the NER Autolab 1500 pressure vessel is shown in Figure 9. In the Autolab 1500, the pressure vessel is divided into two chambers separated with a moveable piston. The specimen resides in the lower pressure chamber, which replicates the overburden pressure. The higher pressure in the upper chamber moves the piston in contact with the sample assembly. When the pressure in the upper chamber is greater than that in the lower chamber, a differential force is applied to the specimen.

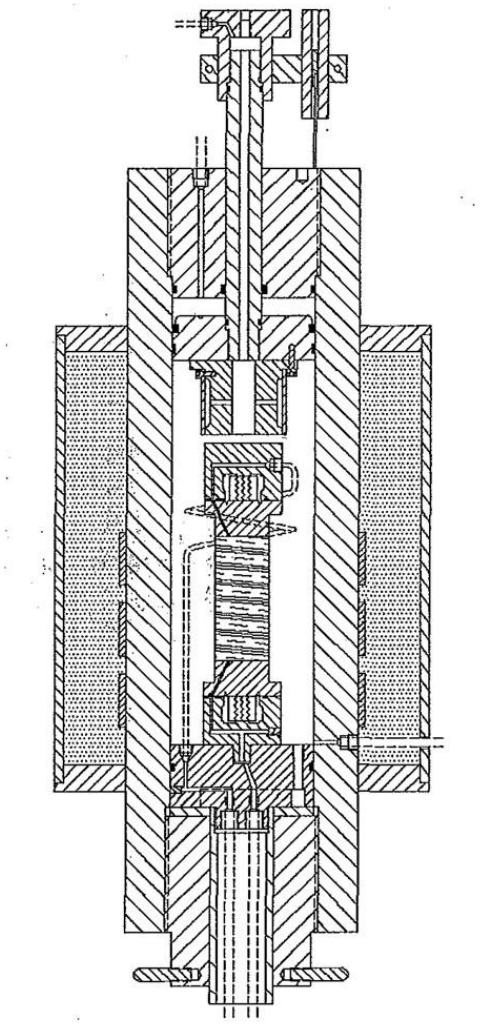

Figure 9. Schematic diagram of Autolab 1500 pressure vessel (NER 2006).

The differential force, F, exerted on the sample is given by:

$$\boldsymbol{F = P_a A_a - P_c A_c - f_s} \qquad \textbf{(18)}$$

where P_a is the pressure in the higher pressure side, A_a is the effective area of the piston on the higher pressure side, P_c is the confining pressure, A_c is the area of the piston on the lower pressure side, and f_s is the seal friction. Since the seal friction is not accurately known and changes with confining pressure, the differential force on the specimen is measured with an internal load cell mounted on either the low pressure side of the piston or the base pedestal (NER 2006).

Cores were cut parallel to bedding (see Figure 10), dried in a desiccator jar, weighed and measured with calipers. Porosity was measured using a helium porosimeter. To regulate confining pressure in the core chamber, rubber sleeves were cut and fit around each sample. The excess length of rubber sleeve was then tightly tied with wire around the transducer-receiver core ends (Figure 13).

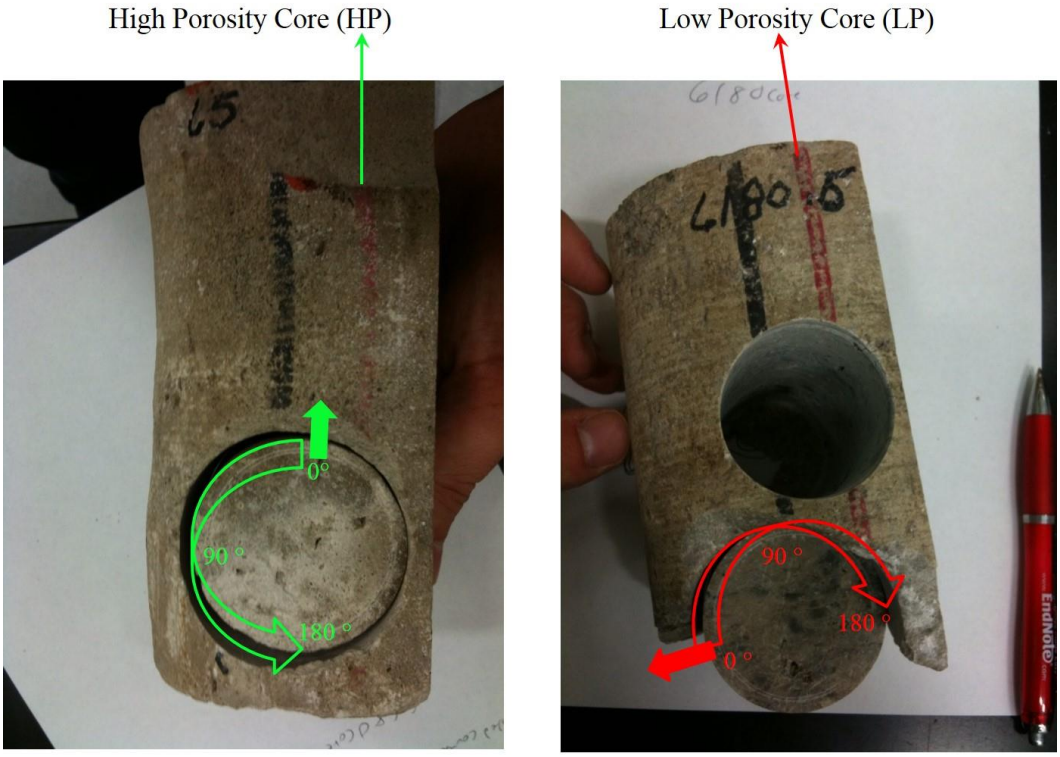

Figure 10. Core subsampling parallel to bedding: black and red lines orient original vertical axis, subsample rotation arc shown for S-wave velocity anisotropy measurements.

Once in the AutoLab, the sample ends are connected to a plumbing line that produces pore pressure and flow with gasses or fluids. With this setup, ultrasonic P and S-wave velocities are measured with a transducer-receiver system or stress dependent permeabilities are measured with a retrofitted Auto-Perm 500 device while adjusting effective pressure within the system. First

arrivals of P and S-waves are identified, picked, and combined with rock dimensions and used to determine the relevant ultrasonic elastic wave velocity (Appendix A).

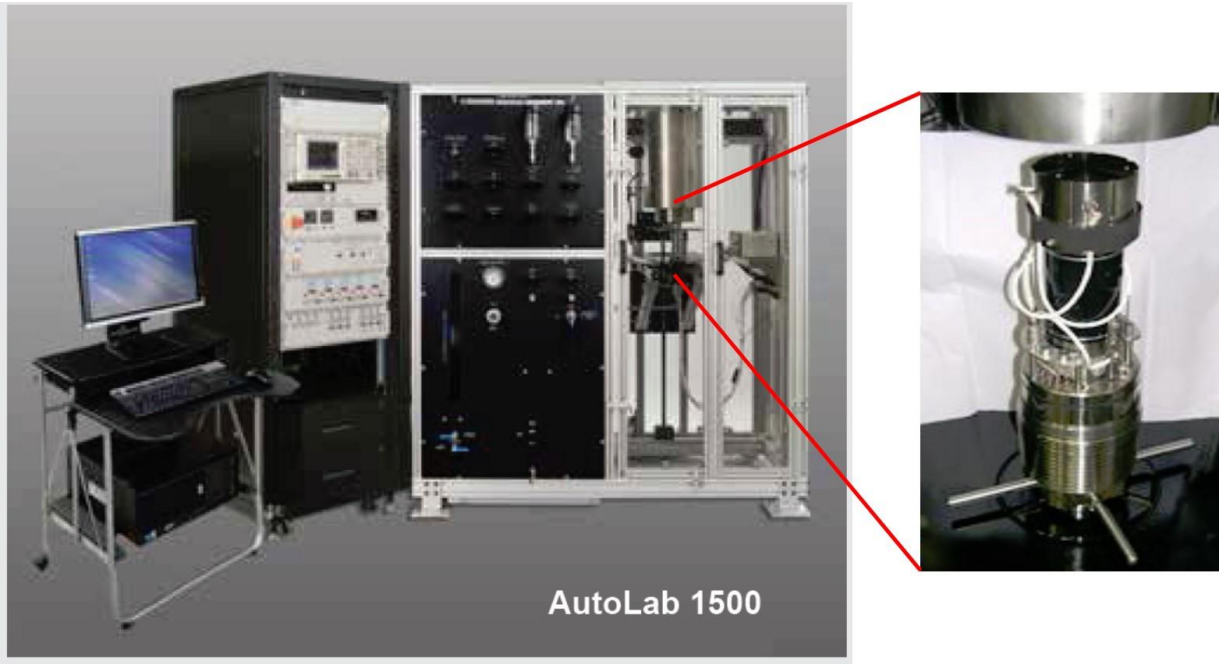

Figure 11. NER Autolab 1500 and sonic velocity core holder assembly (NER 2013).

Figure 12. The measured core is normal to bedding. The line at the top indicates the upwell direction. The curve describes the rotation of the core along which velocities were measured.

Figure 13. Transducer and receiver core ends.

2.2.1 Stress Dependence of Rock Velocity

In the case of fluid injection, the increase in pore pressure (decrease in effective pressure: Equation 27) moves rock toward the non-linear elastic, pore opening state. This state must be modeled to understand pore pressure effects caused by fluid injection into reservoir pore space. It is observed with laboratory measurements that sonic velocity in rock increases dramatically over the effective pressure (P_{eff} = difference between confining and pore pressure) range 0.1 to 15 MPa. This

increase can be attributed to the closure of "cracks" or "compliant porosity." Using equations developed by (Zimmerman et al. 1986, Eberhart-Phillips et al. 1989, Freund 1992, Jones 1995, Prasad et al. 1997, Khaksar et al. 1999, Carcione et al. 2001, Kirstetter et al. 2001, Kaselow et al. 2004), observed values (e.g. porosity, pore shape, mineralogy) may be introduced into the velocity model. The simplified equation

$$V(P_{eff}) = A + BP - Ce^{-P_{eff}D} \quad (19)$$

with A, B, C, and D as experimental fitting parameters and P as effective pressure, describes a pressure dependent velocity (or bulk modulus, K) that has a linear aspect, A+BP, as well as a pressure dependent exponential (Ce^{-PeffD}) that decreases with increasing pressure. The exponential figure contains compliant porosity information in the D term, which is later defined in terms of stress sensitivity of compliant porosity. As effective pressure (P_{eff}) increases, the rock velocity behaves linearly after compliant porosity has been closed. Figure 14 shows a model of high aspect porosity. In this case, cracks attached to a stiff pore close under confining pressure. Figure 15 further shows a network of complaint and stiff pores. Some pores will be completely closed with increased confining pressure while others may be partially closed. A few key guidelines to identifying compliant porosity are that:

1. Pores with high aspect ratio (long axis/short axis) close more easily under pressure than stiff or ideally spherical pores.
2. Small cracks on the edges of large pores, although not separate pores, are closeable

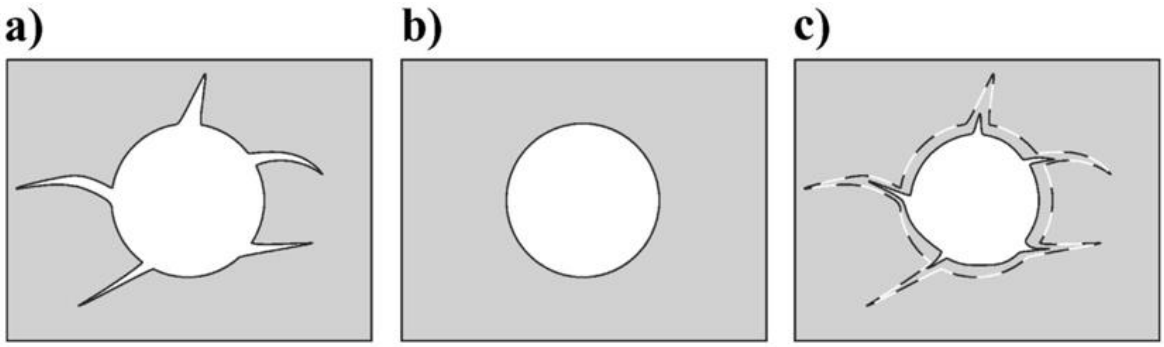

Figure 14. Idealized sketch of pore space. (a) In the unloaded state, the pore space consists of stiff pores and compliant pores, in contrast to (b) the reference state, where the pore space consists only of stiff pores. (c) In the loaded case, both stiff and compliant pores are deformed by an applied load. (Shapiro 2005).

The rock model will consider the sensitivity of a pore to increased confining pressure. This is achieved through geometric descriptions of pore shapes. A spherical pore represents the minimum stress sensitivity whereas elongated cracks, described by measured aspect ratios, are used to define the compliant porosity stress sensitivity.

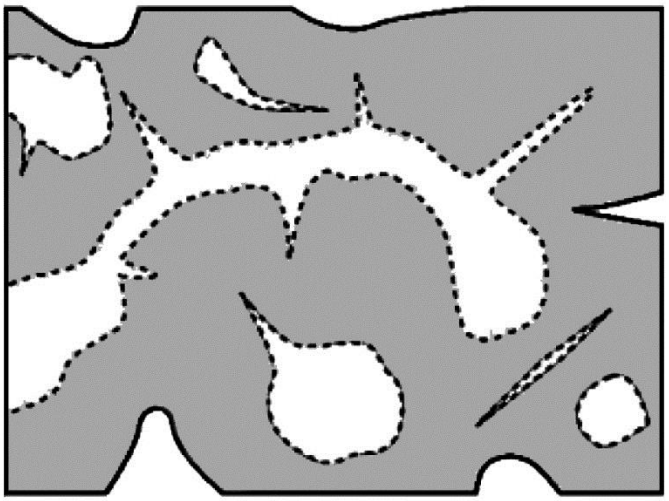

Figure 15. Sketch of complex pore structure consisting of crack-like compliant voids (high aspect ratio) and stiff more or less isometric pores. (Kaselow et al. 2004). Cracks leading off of circular pores *and* general high aspect ratio pores are considered to be compliant porosity.

Velocity is expected to vary with effective pressure variation. Porosity (ϕ), through stress sensitivity affects compressibility, K, as well as bulk density, ρ (K and ρ define p-wave velocity: Equation 37). Velocity versus effective pressure curve produced by lab measurements shown in Figure 16 behaves as Equation 19 predicts: linear elasticity shown by a subtle slope highlighted with a green arrow (between P_{eff} = 5 and 50 MPa increases linearly) and compliant porosity stress sensitivity following an exponential to a negative power (subtracts exponential as confining pressure approaches 0) highlighted with red.

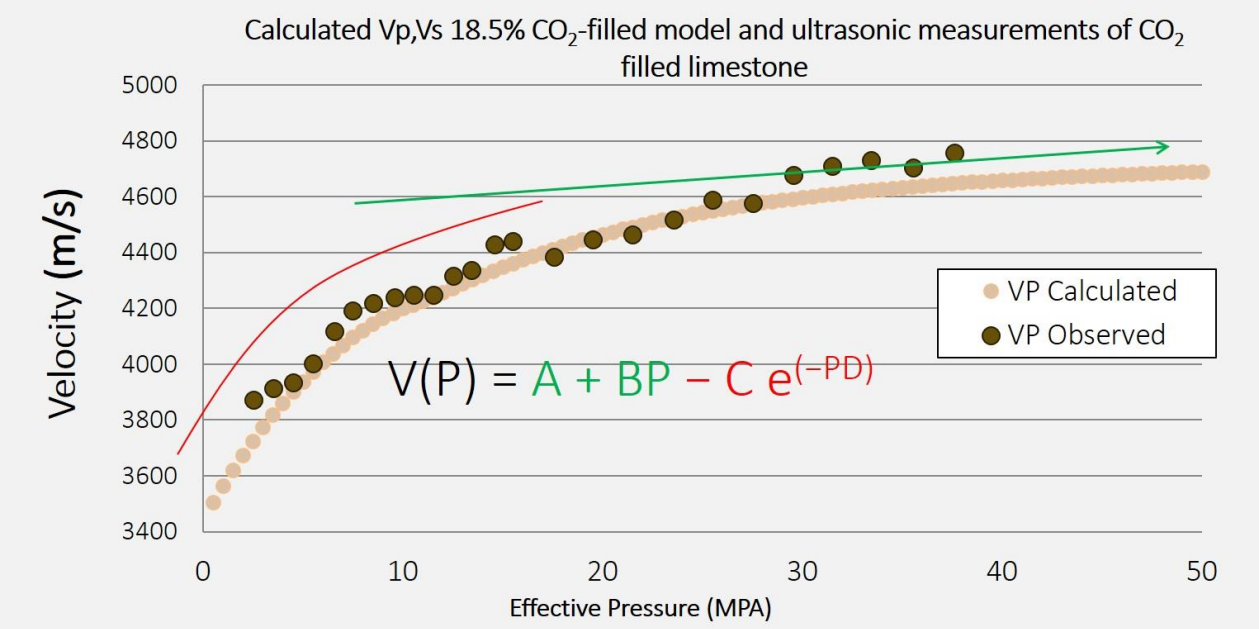

Figure 16. Observed (dark points) and modeled (light points) sonic velocity variations with effective pressure. An exponential increase is seen in sonic velocity over the low effective pressure range. Injection of CO_2 decreases effective pressure and velocity decrease becomes non-linear.

With mathematically defined rock matrix properties, velocity sensitivity with fluid substitutions can be better constrained. This petrophysical model considers an isotropic, porous rock with estimations of stress sensitivities:

$$\boldsymbol{\theta_s \approx 1 + \frac{3K_0}{4\mu_0}} \quad \textbf{(20)}$$

$$\boldsymbol{\theta_C \approx \frac{K_{gr}(3K_0+4\mu_0)}{\pi\gamma\mu_{gr}(3K_0+\mu_0)}} \quad \textbf{(21)}$$

$$\boldsymbol{\theta_{S\mu} \approx 1 + \frac{6K_0+2\mu_0}{9K_0+8\mu_0}} \quad \textbf{(22)}$$

$$\boldsymbol{\theta_{C\mu} \approx \frac{1}{5}\left[1 + \frac{4(3K_0+4\mu_0)(9K_{gr}+4\mu_0)}{3\pi\gamma(3K_0+\mu_0)(3K_0+2\mu_0)}\right]} \quad \textbf{(23)}$$

where γ = pore aspect ratio and the isotropic Voigt-Reuss-Hill averaging technique:

$$\boldsymbol{Voigt\ Average = K_V = \sum_1^n K_1 f_1 + K_2 f_2 + \cdots K_n f_n} \quad \textbf{(24)}$$

$$\boldsymbol{Reuss\ Average = K_R = \sum_1^n \frac{1}{\frac{K_1}{f_1}+\frac{K_2}{f_2}+\cdots\frac{K_n}{f_n}}} \quad \textbf{(25)}$$

$$\boldsymbol{Voigt - Reuss - Hill\ Average = K_0 = \frac{K_R+K_V}{2}} \quad \textbf{(26)}$$

in which K_n (or μ_n) denotes the given mineral modulus and f_n is the volume fraction of the given mineral, is used to define mineral bulk modulus, K_0, and mineral shear modulus, μ_0 (Shapiro 2003). θ_{xx} are unit-less quantities that define the sensitivity of the pore space with respect to pressure.

The pore space is divided into stiff and compliant porosity by:

$$\boldsymbol{\phi = \phi_c + [\phi_{s0} + \phi_s]} \quad \textbf{(27)}$$

$$\boldsymbol{P_{eff} = P_{Confining} - P_{Pore}} \quad \textbf{(28)}$$

where ϕ = bulk interconnected porosity, ϕ_c = compliant porosity, ϕ_{s0} = stiff porosity at an effective pressure (P_{eff})= 0 and ϕ_s is the stiff porosity that is changed at varying effective pressures (if P_{eff} > 0, effective pressure is positive ϕ_s is negative,; if P_{eff} < 0, ϕ_s is positive, and if no load is applied ϕ_s = 0.)

To represent the change in stiff porosity, a simple sphere shape pore model is used to define the dry rock frame K_{dryS}:

$$\boldsymbol{\frac{1}{K_{dryS}} = \frac{1}{K_0} + \frac{\phi}{K_{\varphi sphere}}} \quad \textbf{(29)}$$

$$\boldsymbol{\frac{1}{\mu_{dryS}} = \frac{1}{\mu_0} + \frac{\phi_{s0}}{\mu_{\varphi sphere}}} \quad \textbf{(30)}$$

$$\boldsymbol{K_{\phi sphere} = K_0 \frac{2(1-2\nu_{min})}{3(1-\nu_{min})}} \quad \textbf{(31)}$$

$$\boldsymbol{\mu_{\phi sphere} = \mu_0 \frac{2(7-5\nu_{min})}{15(1-\nu_{min})}} \quad \textbf{(32)}$$

Where K_0 and μ_0 are the mineral bulk and shear moduli and ν_{min} is the Voigt-Reuss-Hill average determined Poisson's ratio of the mineral matrix. $K_{\phi sphere}$ and $\mu_{\phi sphere}$ define the stiff pore incompressibility, in this case of calcite, assuming stiff porosity consists of spherical pores (Mavko

et al. 1998). Using these parameters, pressure dependent, dry rock bulk and shear moduli are defined as:

$$K_{dry}(P_{eff}) = K_{dryS}\left[1 + \theta_s\left(\frac{1}{K_{dryS}} - \frac{1}{K_0}\right)P_{eff} - \phi_{c0}\theta_c e^{(-\theta_c P_{eff}/K_{dryS})}\right] \quad \textbf{(33)}$$

$$\mu_{dry}(P_{eff}) = \mu_{dryS}\left[1 + \theta_{s\mu}\left(\frac{1}{K_{dryS}} - \frac{1}{K_0}\right)P_{eff} - \phi_{c0}\theta_c e^{(-\theta_c P_{eff}/K_{dryS})}\right] \quad \textbf{(34)}$$

(Shapiro 2003)

that may be used in various fluid substitution models. In this case:

$$K_{sat} = K_{dry} + \frac{(1-\frac{K_{dry}}{K_0})2}{\frac{\phi}{K_{fluid}} + \frac{1-\phi}{K_0} - \frac{K_0}{K_0^2}} \quad \textbf{(35)}$$

(Gassmann 1951, McKenna et al. 2003)

along with a bulk density summation where ρ_{fluid} is the density at a given pressure and $\rho_{mineral}$ is the mineral density (assumed constant),

$$\rho_{bulk}(P_{eff}) = (1-\phi)\rho_{mineral} + \phi\rho_{fluid}(P_{eff}) \quad \textbf{(36)}$$

to calculate pressure dependent P and S-wave velocities:

$$V_P(P_{eff}) = \sqrt{\frac{(K_{sat}+(4/3)\mu_{sat})}{\rho_{bulk}}} \quad \textbf{(37)}$$

$$V_S(P_{eff}) = \sqrt{\frac{\mu_{sat}}{\rho_{bulk}}} \quad \textbf{(38)}$$

Using pressure dependent Lamé parameters, modeled results can be compared with experimental results. Cross plots of density independent Young's modulus, Shear modulus, Poisson's ratio, and Bulk modulus,

$$E = 3K(1-2v) \quad \textbf{(39)}$$

$$\mu = \frac{3K(1-2v)}{2(1+v)} \quad \textbf{(40)}$$

$$v = \frac{E}{2G} - 1 \quad \textbf{(41)}$$

$$K = \frac{E}{3(1-2\nu)} \quad \textbf{(42)}$$

can be used to further emphasize and understand stress dependence of the material.

2.2.2 Frequency Dependence of Rock Velocity and Wave Attenuation

Rock properties are contributors to the model elasticity tensor and depending on the application and need for accuracy, this system may be manipulated to represent an isotropic elastic material or a material with directionally dependent variations in elasticity. To describe the rock properties that cause velocity dispersion and attenuation effects, energy absorbing systems are considered. As a wave passes through a material, particularly porous rock, the non-solid internal pore-filling materials can cause irregularities due to fluid flow. The application of "squirt flow" in saturated and patchy-saturated rocks to Biot's equations has been extensively explored by (Stanford University) Dvorkin, Mavko, Nur, and (Curtin University of Technology) Gurevich. Sources of attenuation, often described in isotropic and anisotropic frameworks, include energy dispersion at interfaces, wave travel time in pores, and internal material friction.

It has been observed that fluid filled rocks contain a frequency dependent attenuation component (Johnston et al. 1979, Toksöz et al. 1979). This frequency dependent attenuation has been interpreted as an effect of high wave frequency pore fluid "freezing," in which the fluid, temporary pressurized by the wave front, has no time to flow through a pore throat (Pride et al. 2004). Whereas at seismic frequencies, fluids are induced to flow through permeable networks as sound waves pass through the material (Dvorkin et al. 1995). A challenge with measuring rock velocities in the laboratory is that the sound wave frequency is generally a much higher frequency than seismic frequencies (an 8 Hz wavelength is longer than the entire length of a laboratory core

sample). Therefore, laboratory sonic frequency is in the megahertz range and "translation" to the seismic spectrum is necessary for both velocity and attenuation. To measure the transmission frequency spectrum of the laboratory transducer-receiver setup, experiments were performed on low attenuation aluminum cores. The aluminum is assumed to be essentially attenuation-less. It can seen from comparison of aluminum frequency-amplitude spectra to carbonate amplitude-frequency spectra that at least an order of magnitude of amplitude attenuation occurs in the carbonate samples (Figure 18).

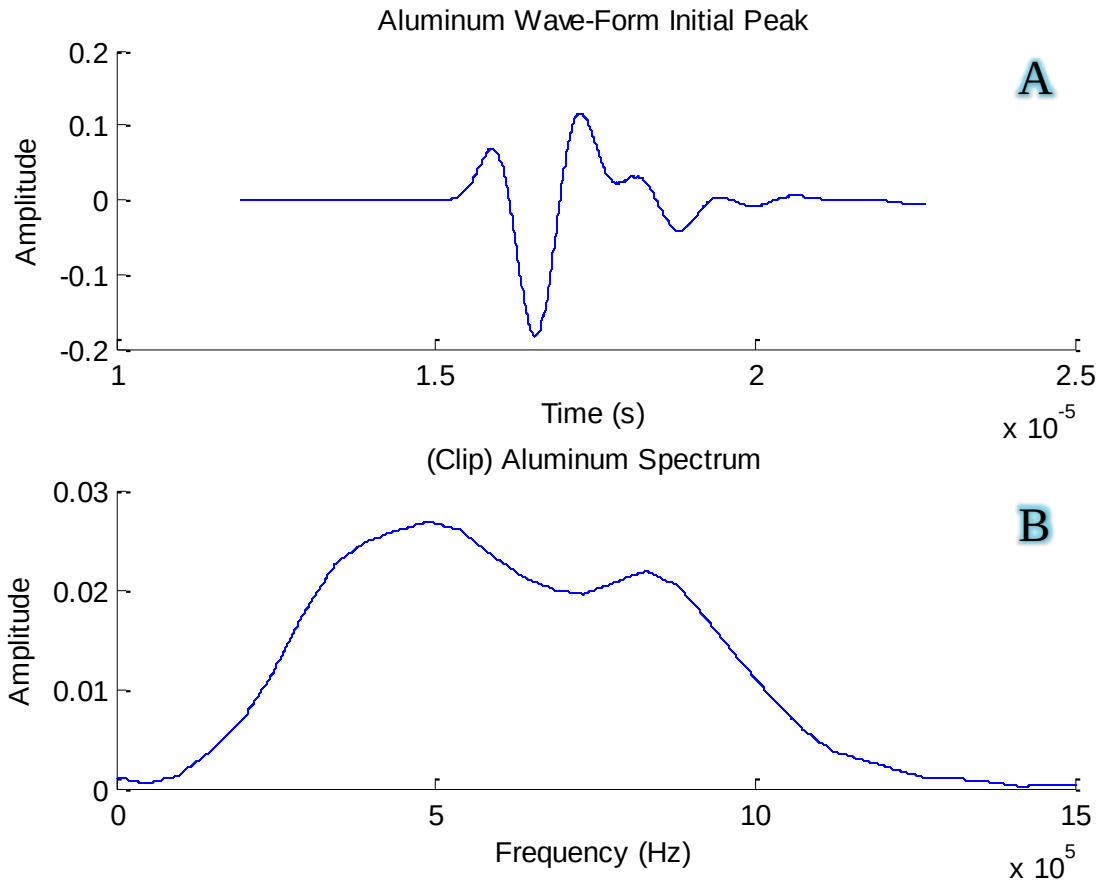

Figure 17. Aluminum wave-form (A) and frequency spectrum (B) measured in Autolab-1500 (Delaney 2013).

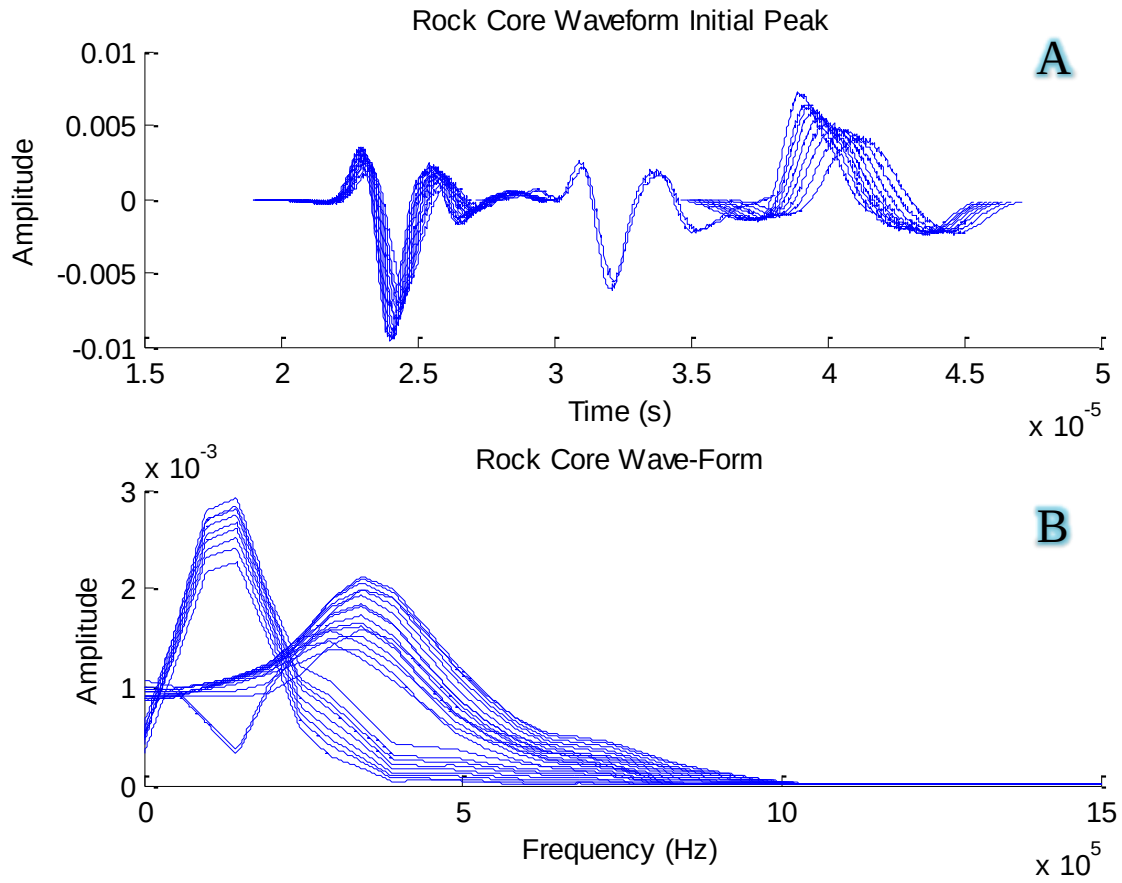

Figure 18. 18% porosity carbonate saturated with deionized water: first arrival and amplitude spectrum measured in Autolab-1500 (Delaney 2013). Comparison of the frequency peaks are shifted and amplitudes are attenuated in the limestone sample.

Empirical methods determine attenuation by analyzing the slope of a straight fit line through an interval of the frequency spectrum (Delaney 2013). To join the empirical observations with rock physics properties, the petrophysical models of Miroslav Brajanovski, Boris Gurevich, and Michael Schoenberg (Brajanovski et al. 2005, Brajanovski et al. 2006) are used as a foundation in our analysis. These models consider a frequency related velocity dispersion similar to Winkler (1985), but with a more general rock property based approach. In this thesis, I produced a Matlab script (Section 1.01(a)(i)A.1.1) that combines the effective pressure dependent rock moduli (see

2.2) with the frequency-dependent model of (Brajanovski et al. 2005). The final V_p and V_s wave velocity petrophysical model assigns a stress sensitivity to the stiff and compliant porosity moduli, produces pressure dependent bulk and shear moduli, and modifies the moduli to account for frequency dependent factors (e.g. permeability and fluid flow effects).

The frequency attenuation model uses the stiffness tensor for a transversely isotropic elastic solid, which has five independent constants:

$$\begin{bmatrix} c_{11} & c_{12} & c_{13} & 0 & 0 & 0 \\ c_{12} & c_{11} & c_{13} & 0 & 0 & 0 \\ c_{13} & c_{13} & c_{33} & 0 & 0 & 0 \\ 0 & 0 & 0 & c_{44} & 0 & 0 \\ 0 & 0 & 0 & 0 & c_{44} & 0 \\ 0 & 0 & 0 & 0 & 0 & c_{66} \end{bmatrix}, \quad c_{66} = \frac{1}{2}(c_{11} - c_{12}) \tag{43}$$

(Mavko et al. 2003)

Angular dependent velocity is determined from these stiffness parameters:

$$c_{11} = \rho V_p^2(90°) \tag{44}$$

$$c_{12} = c_{11} - 2\rho V_{SH}^2(90°) \tag{45}$$

$$c_{33} = \rho V_p^2(0°) \tag{46}$$

$$c_{44} = \rho V_{SH}^2(0°) \tag{47}$$

where V_p is P-wave velocity, V_s is S-wave velocity, and ρ is density.

Brajanovski 2005 gives the matrix in Lamé parameters:

$$c^{dry} = \begin{pmatrix} \frac{(1-2\langle\gamma\rangle)^2}{\langle 1/L\rangle} + 4\langle\mu\rangle - 4\langle\gamma\mu\rangle & \frac{(1-2\langle\gamma\rangle)^2}{\langle 1/L\rangle} + 2\langle\mu\rangle - 4\langle\gamma\mu\rangle & \frac{1-2\langle\gamma\rangle}{\langle 1/L\rangle} & 0 & 0 & 0 \\ \frac{(1-2\langle\gamma\rangle)^2}{\langle 1/L\rangle} + 2\langle\mu\rangle - 4\langle\gamma\mu\rangle & \frac{(1-2\langle\gamma\rangle)^2}{\langle 1/L\rangle} + 4\langle\mu\rangle - 4\langle\gamma\mu\rangle & \frac{1-2\langle\gamma\rangle}{\langle 1/L\rangle} & 0 & 0 & 0 \\ \frac{1-2\langle\gamma\rangle}{\langle 1/L\rangle} & \frac{1-2\langle\gamma\rangle}{\langle 1/L\rangle} & \frac{1-2\langle\gamma\rangle}{\langle 1/L\rangle} & 0 & 0 & 0 \\ 0 & 0 & 0 & \frac{1}{\langle 1/\mu\rangle} & 0 & 0 \\ 0 & 0 & 0 & 0 & \frac{1}{\langle 1/\mu\rangle} & 0 \\ 0 & 0 & 0 & 0 & 0 & \langle\mu\rangle \end{pmatrix} \quad \textbf{(48)}$$

(Brajanovski et al. 2005)

and incorporates attenuation into the incident compressibility:

$$\frac{1}{c_{33}^{sat}} = \frac{1}{C_b} + \frac{\Delta_N (R_b - 1)^2}{L_b\left[1 - \Delta_N + \Delta_N \sqrt{i\Omega}\cot\left(\frac{C_b}{M_b}\sqrt{i\Omega}\right)\right]} \quad \textbf{(49)}$$

$$V_{p3} = \sqrt{\frac{c_{33}^{sat}}{\rho_b}} \quad \textbf{(50)}$$

$$V_p = \left[Re\left(V_{p3}^{-1}\right)\right]^{-1} \quad \textbf{(51)}$$

$$Q^{-1} = 2V_p Im(V_{p3}^{-1}) \quad \textbf{(52)}$$

(Brajanovski et al. 2006)

where V_p is the real part of the p-wave velocity and Q is the attenuation. Δ_N is the fracture weakness (value ranging between 0 and 1) taken from linear-slip deformation theory (Schoenberg et al. 1988). This term is potentially related to the compliancy term built into the pressure based model. L_b, C_b, M_b, and R_b are dry p-wave modulus, fluid saturated p-wave modulus, pore space modulus, and the "material parameter," respectively. This attenuation model is effected by the interaction of wave half-period and permeability of the rock; as low frequency waves move through rock, pore pressure equilibrates if permeability allows. At high frequencies, pore pressure

cannot equilibrate across pore networks and the rock behaves according to dry frame values. Frequency is introduced in Equation 49 with:

$$\boldsymbol{\Omega = \omega \left(\frac{HM_b}{2C_b D_b} \right)^2} \quad \textbf{(53)}$$

in which Ω is the normalized frequency; ω defines the wave frequency and must be compared to material parameters to ensure the flow induced by the wave is Poiseuille flow (non-turbulent) and that the frequency is below the system resonant frequency: Biot's characteristic frequency and the quotient of p-wave velocity and fracture spacing, H and importantly diffusivity D_b:

$$\boldsymbol{D_b = \frac{\kappa_b M_b L_b}{\eta C_b}} \quad \textbf{(54)}$$

with permeability κ_b, fluid bulk modulus M_b, p-wave modulus L_b and fluid viscosity η (Brajanovski et al. 2006). With this system of equations, rock velocity, attenuation, and effective pressure relations are produced and the model can be adjusted for varying bedding thicknesses and permeability. Ultrasonic velocity is greater in the higher frequencies as can be seen in Figure 19 The predicted attenuation of the model is shown in Figure 20. Note that the attenuation model relies on constant crack orientation and can currently only account for one porosity alignment value. Therefore, this approach may under-predict attenuation.

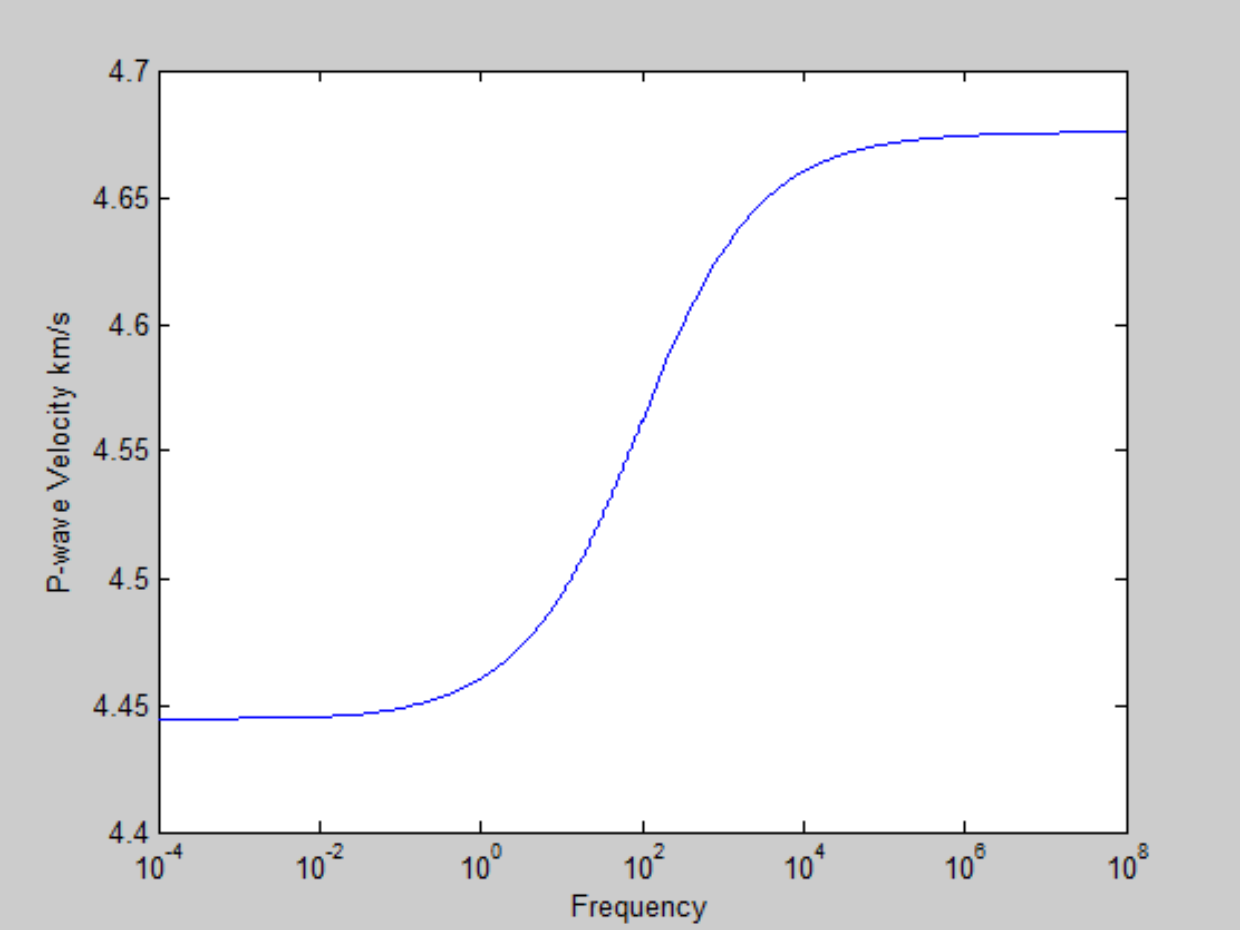

Figure 19. Frequency versus velocity of 18% porosity Permian basin limestone with water as pore filling fluid. With the input parameters for crack spacing and diffusivity, a difference of greater than 200 m/s exists between the ultrasonic measurements and predicted seismic p-wave velocities.

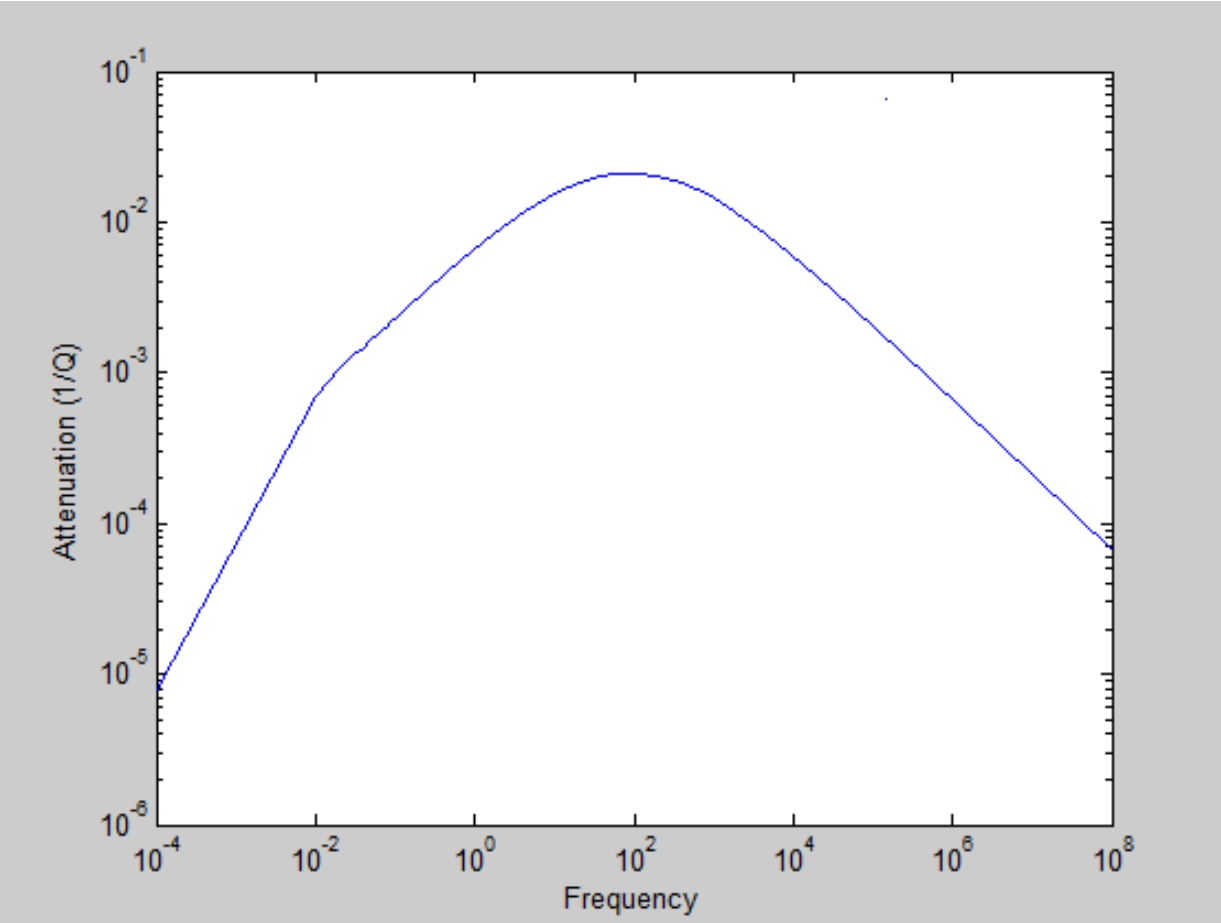

Figure 20. Frequency versus Attenuation of 18% porosity Permian basin limestone with water as the pore filling fluid. An attenuation peak can be seen near the 100 Hz frequency range.

Figure 21 shows the full model with pressure dependent moduli (see section 2.2) at ultrasonic frequencies used in laboratory measurements along with the results of P and S-wave velocity measurements of the 18% porosity limestone. The model (blue line) agrees with observed velocity measurements (colored points). The implication of this result is that once the rock model is properly tuned to ultrasonic or well log results, frequency can be adjusted to produce effective-pressure dependent seismic velocitiy and attenuation values. By processing raw seismic traces with advanced attenuation and velocity models, reflection amplitudes will be more accurate and better focused for purposes of AVO (Amplitude Variation with Offset) analysis.

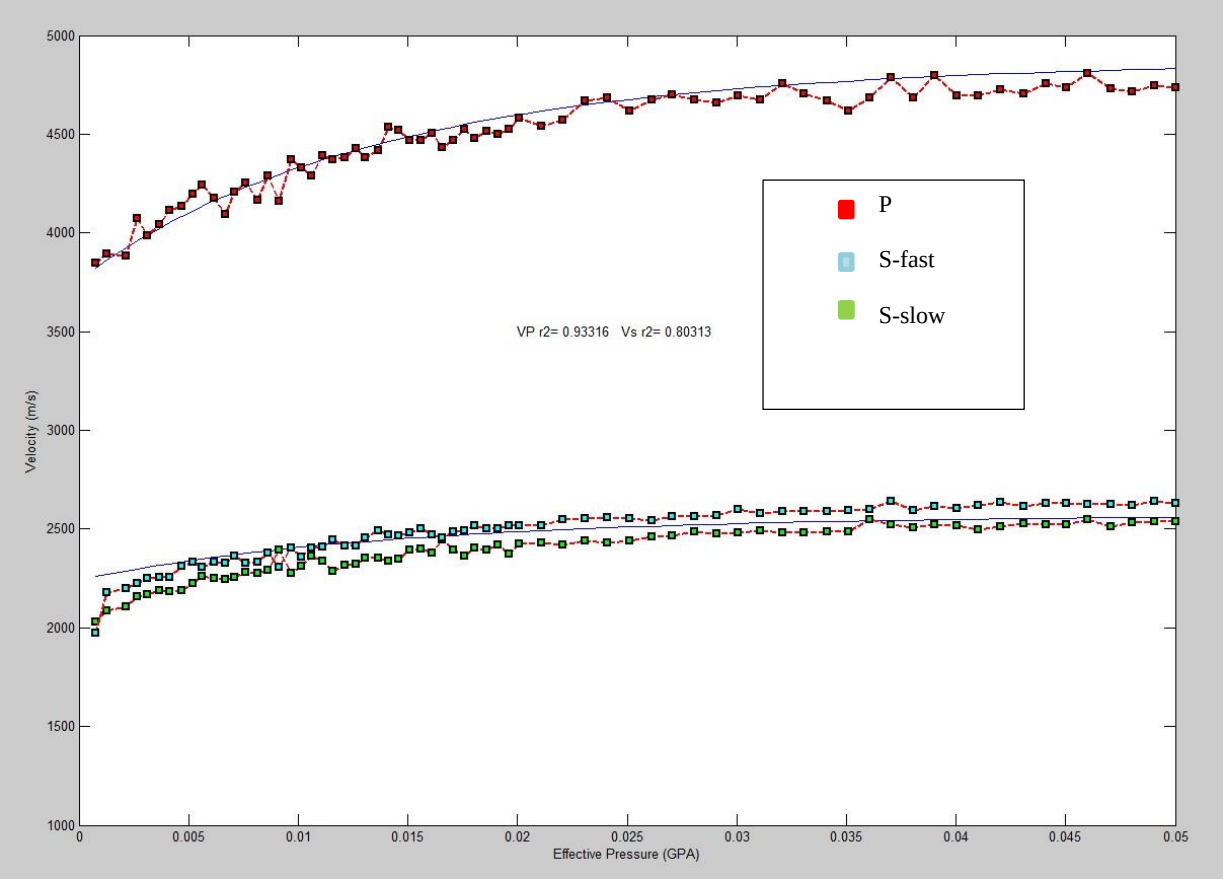

Figure 21. Velocity versus Effective pressure, experimental and modeled results (ultrasonic frequencies). r^2 of p-wave velocity prediction =0.93, r^2 of S-wave velocity prediction (fast and slow averaged) =0.80.

2.3 SONIC VELOCITY MEASUREMENTS AND EFFECTS OF DISSOLUTION

The limestone samples have been tested many times under different effective pressures and with varying pore filling fluids. The initial porosity of the high porosity core was 18.53%. After extensive measurements were performed (Purcell 2012), liquid hydrocarbons from the pressure

chamber leaked into the core assembly and inundated the pore space. After thorough cleaning of the core, the available porosity was decreased to $\phi = 14\%$.

Exposure experimentation consisted of a water saturated limestone sample in a reactor vessel filled to 2000 psi with CO_2 (Full reactor setup is described in 4.0 The sample was not subjected to any elevated pore pressure, so it is assumed that effective pressure was very low. After CO_2 was dissolved into the pore fluids for extended periods of time, the sample was removed and dried in a desiccator; 2% porosity was regained. The comparison of measured velocities, shown in Figure 23, reveal an increase in velocity, post-exposure at low effective pressures. Note that in all cases, in the higher effective pressure region the velocities tend to converge. In the lower effective region, higher velocities, post CO_2, exposure are observed. The modification of model fitting parameters suggests that dissolution causes a decrease in compliant and increase in stiff porosity or an increase in compliant porosity stress sensitivity. Figure 22 shows how porosity perturbations affect the model. Using this the model behavior as a guide to interpretation, it appears that complient porosity has decreased. Figure 24 and Figure 25 show before and after CO_2 experimental velocity results with the velocity model fit to the measured velocity curves. The increase of pore pressure from fluid injection into a reservoir causes a corresponding decrease of effective pressure (Equation 27). The velocity behavior of an injected reservoir unit is therefore left-moving on the velocity-effective pressure plots presented in this thesis.

With input parameters derived from digital analysis and mineralogy derived by backscattered electron microscopy, the aspect ratio and compliant porosity inputs were modified to match observed velocity data (see Table 3). Aspect ratio, γ_c, is used in Equations 21 and 23 to define stress sensitivities of pore space. Porosity, ϕ, is divided into stiff and compliant in Equation 27. These porosities are implemented into stress dependent bulk and shear moduli formulation in

Equations 33 and 34, from which velocities are calculated. These parameter are used to calibrate the digital methods of stiff and compliant porosity segmentation by providing a porosity volume change. The compliant and stiff porosity volume changes caused by dissolution are accounted for with rock velocity model matching. The determined volume changes can be searched for in the 4D digital rock. The observations made with SEM and CT imaging and chemical reactions are further described in 3.2.2.1 and 4.4.

Table 3. Stiff Porosity, Compliant Porosity, and Aspect Ratio of Modeled Samples.

Sample	ϕ_s	ϕ_{c0}	γ_c
Pre-Co_2	0.184625	$3.75x10^{-3}$	$6 X 10^{-4}$
Post-CO_2	0.18500	$3.50x10^{-3}$	$7.5 X 10^{-4}$
Percent Change	+0.2%	-6%	+25%

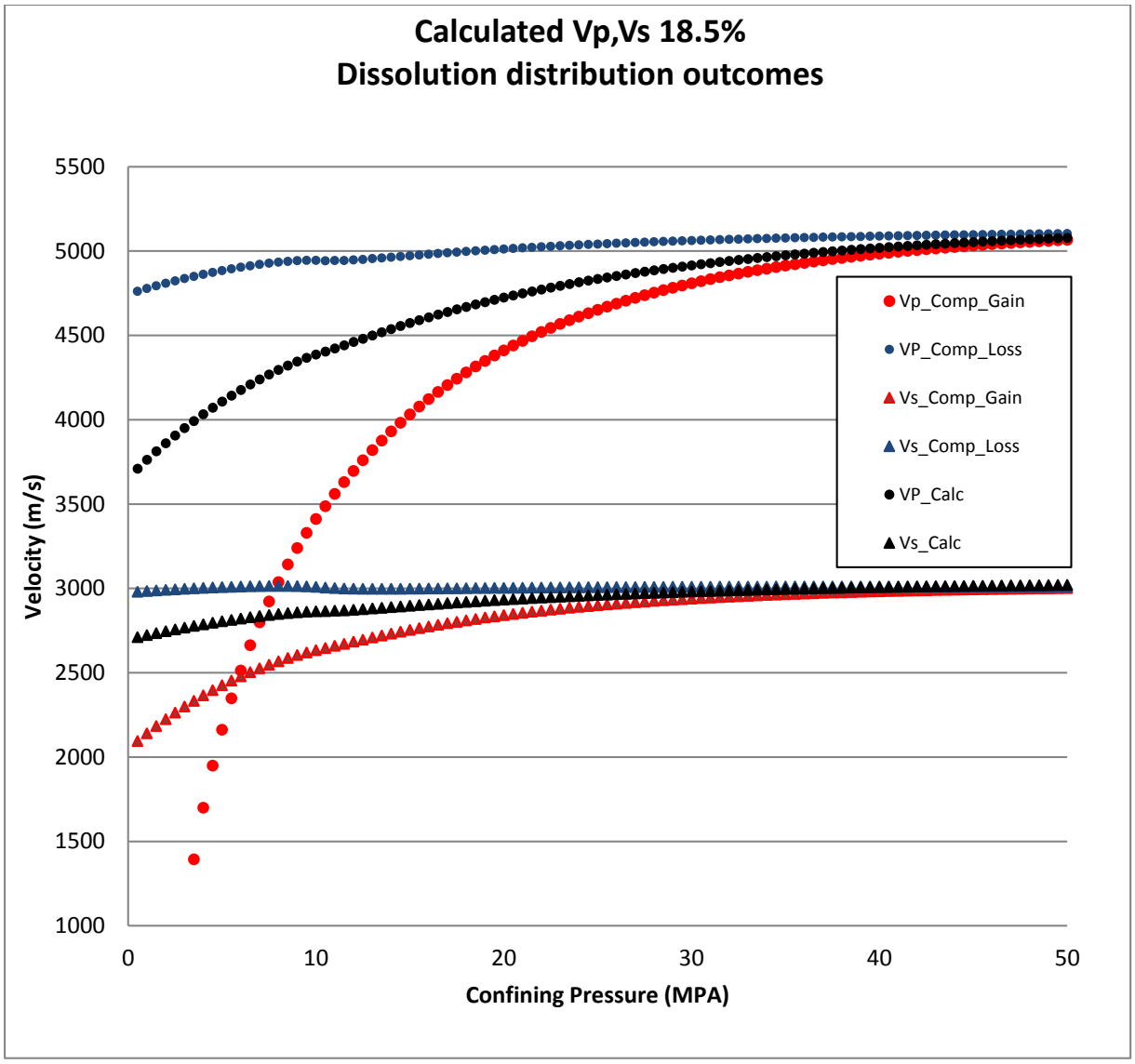

Figure 22. Velocity model with compliant porosity distributions. The black symbols are the original p and s models (circle and triangles, respectively). The blue symbols show the model adjusted for a loss of compliant porosity. The red symbols show a gain of compliant porosity.

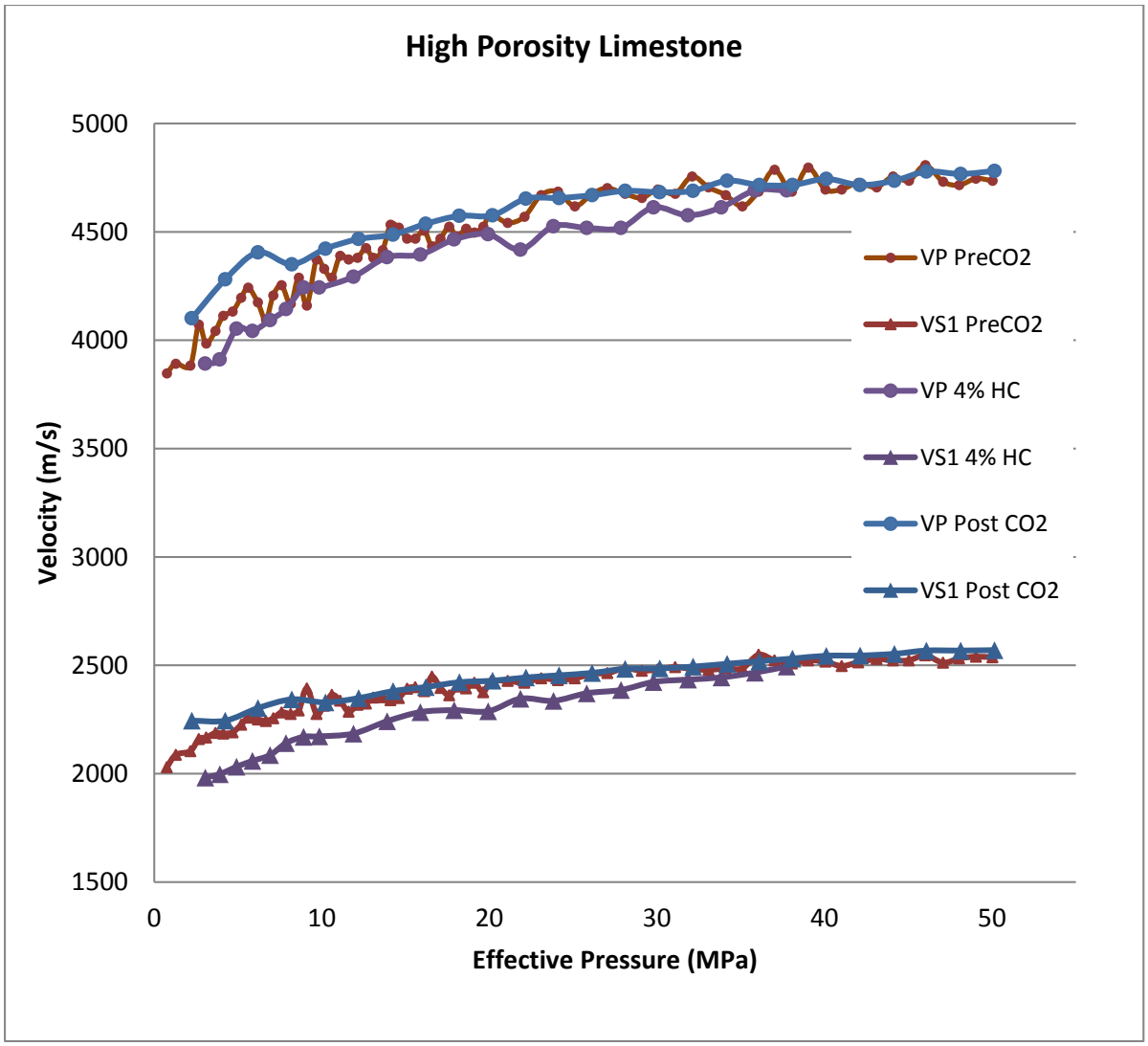

Figure 23. P and fast S-wave velocities before exposure (red), with hydrocarbon inundation (purple), and post-exposure (blue). The lower effective pressure regime is subject to both pressure and fluid effects. However, at P_{eff} above 40 MPa, velocities converge as compliant porosity is fully closed and linear elastic rock matrix properties dominate pressure response.

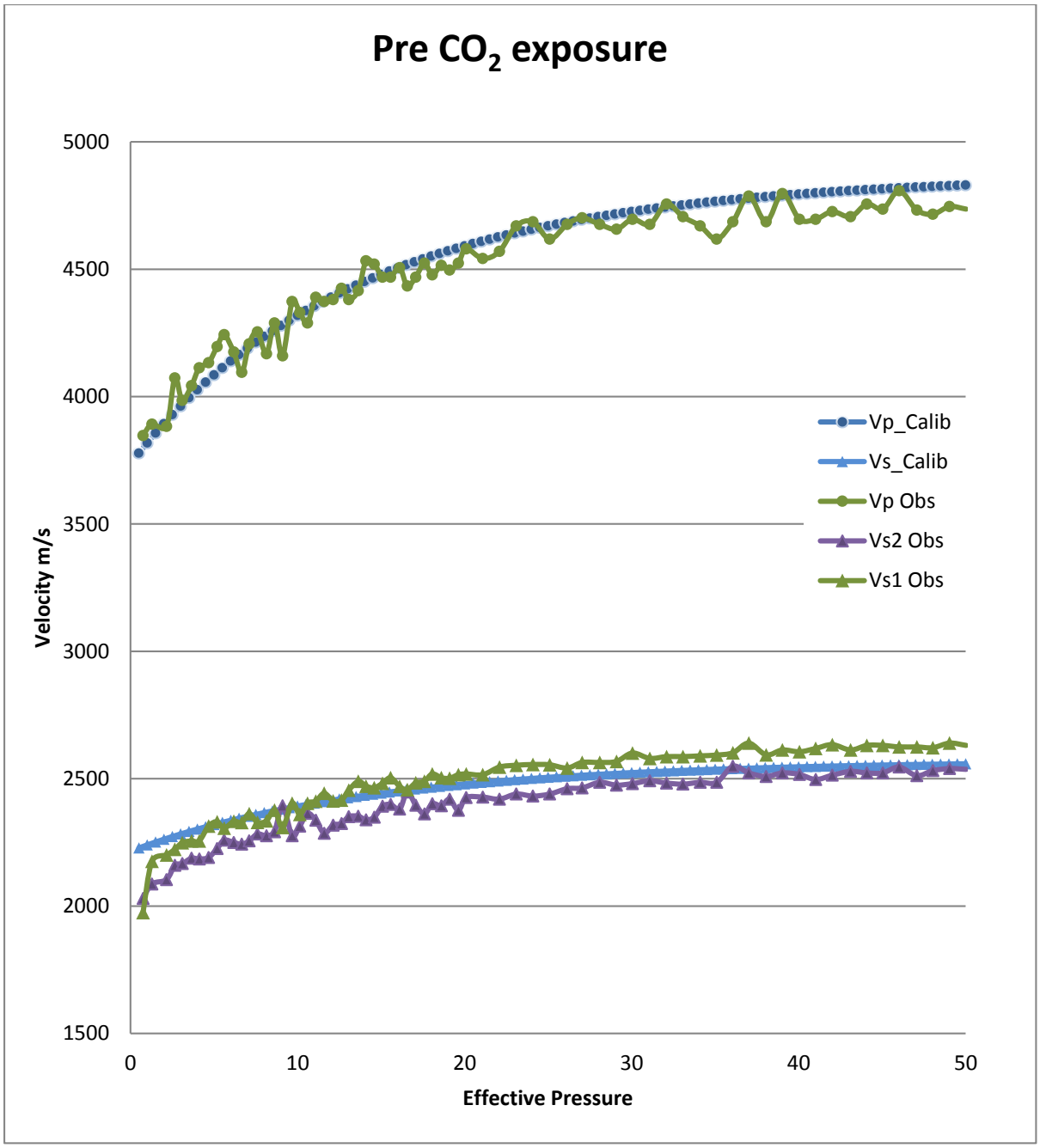

Figure 24. Measured (green, purple) and modeled (blue) velocities of 18.5% porosity limestone with air as pore filling fluid, Pre CO_2 exposure. Fitting parameters from Table 3.

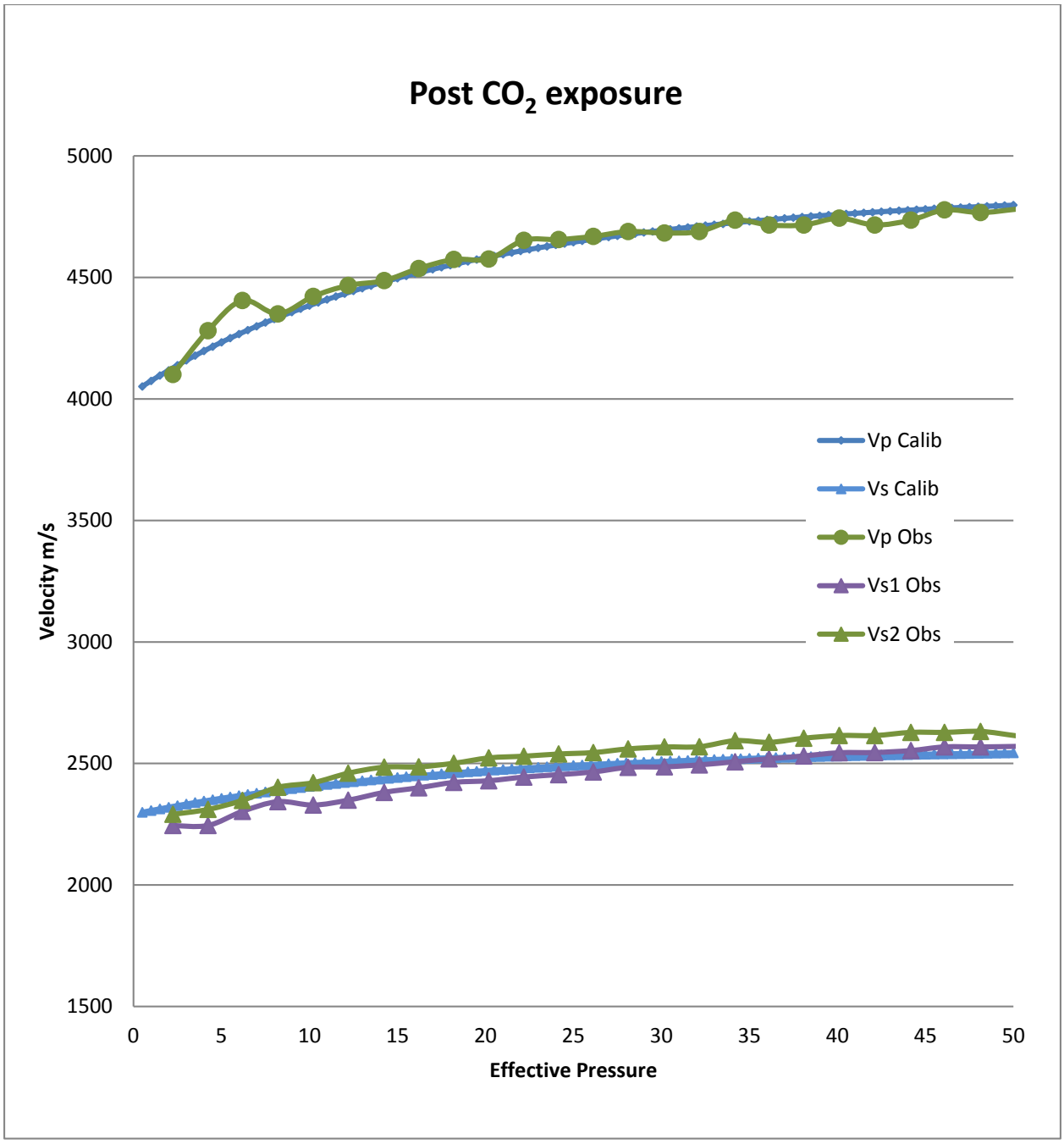

Figure 25. Measured (green, purple) and modeled (blue) velocities of 18.5% porosity limestone with air as pore filling fluid, Post CO_2 exposure. Fitting parameters from Table 3.

2.4 SUMMARY

The formulation of a bulk elastic rock property model based on observable physical properties has been a success. In order to observe and quantify compliant porosity with imaging, the aspect ratio, compliant porosity, and stiff porosity values found in velocity modeling are used to classify the pore space in digital rocks. The modeling process has given insights for needed resolution and scale settings for successful digital rock imaging techniques. The noteworthy 6% loss of compliant porosity is a small fraction of the bulk sample (about 1/3 X 10^{-3}% of total sample volume). Observation of this porosity approaches current μCT digital resolution limits. The 25% increase in compliant porosity aspect ratio can be attributed to the connection of long flat cracks and the small (0.2%) gain in stiff porosity could be a product of the new crack face configuration under effective pressure.

This model is useful for reservoir modeling as well. Stress sensitivity observations and reservoir pore pressure can be taken into account when substituting or predicting pore filling fluids; fluid compressibility moduli vary but shear moduli are normally zero (with the exception of heavy oils and tars). The effects due to pressure can therefore precisely predict P and S-wave behavior and the fluid effects can be determined by the excess P-wave changes.

3.0 DIGITAL IMAGING AND POROSITY ANALYSIS

This study consisted of three scales of characterization: large area 2-D micron scale, small volume 3-D micron scale and large volume 3-D decimeter scale. The first SEM mosaic shows the texture and dimensionality of pores and the need to account for both micro and macro porosity. After the preliminary analysis of the samples, the services of Steven Kennedy at RJLee Group were required for further 2-D analysis. This study revealed high resolution chemical composition as well as more accurate 2-D pore characteristics. At centimeter-size x,y dimensions, these two SEM analysis produced large 2-D pore datasets with more than 20,000 pore descriptions in each set. The micro CT sets have the most data at the highest magnification level. They most accurately display pore volumetrics and orientations, but do not contain the elemental information that can be provided by the High-Z analysis. Medical CT scans show zones of relatively greater and lesser porosity over larger rock volumes.

3.1 SCANNING ELECTRON MICROSCOPY ANALYSIS

For the preliminary SEM/XRD analysis, samples were polished with increasing grit (100-600) grinding paper, dried in a desiccator, and coated with graphite. They were then analyzed in secondary electron mode on the NETL-Pittsburgh SEM machine.

At RJLee Group, a Keyence digital microscope was used for optical and an Aspex Personal SEM 75 for scanning electron microscopy. The Aspex Personal SEM 75 was used to produce two,

4 megabyte SEM images measuring 2048 x 2048 pixels. Full01.tif was taken at 380x and the scale is 0.12850 micrometers per pixel. Full02.tif was taken at 27x and the scale is 1.80845 micrometers per pixel. The montage rock.tif is a 440 unit rectangular grid (20 images horizontal by 22 images vertical) of 512 x 512 pixel images acquired at 200x. The scale is 0.86816 μm per pixel. The overall size of the analyzed SEM montage was 0.35 x 0.39 in (8.89 x 9.78 mm).

These SEM images were used to develop parameters of a 3D rock analysis (Appendix A) consisting of three mutually perpendicular planar samples cut from an original orientation-known rock column (Figure 26). The samples were epoxy impregnated to allow for quantitative pore analysis. The mutually perpendicular, epoxy impregnated, polished samples (two 40mm x 45mm samples and one 80mm x 40mm sample) were produced from a core column and analyzed. The analysis produced an optical montage, a backscattered electron SEM (BSEM) montage, a CCSEM (computer-controlled scanning electron microscope) point count analysis and a CCSEM High-Z (small point average atomic number) analysis.

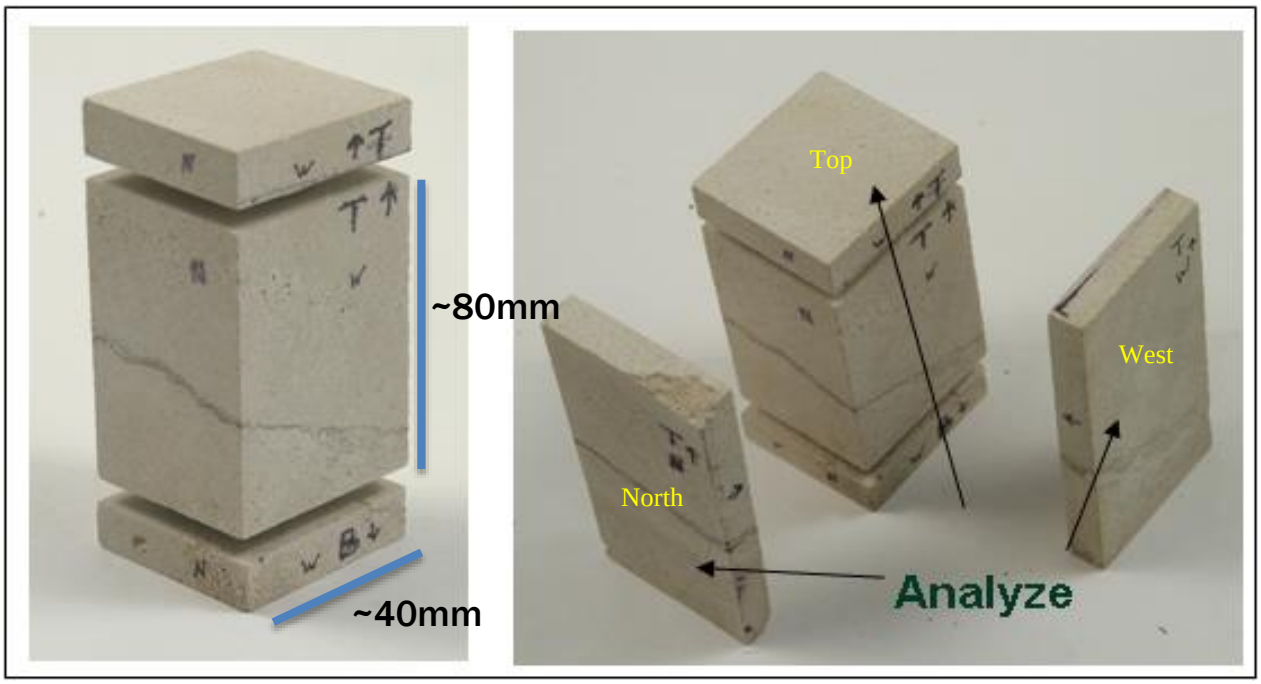

Figure 26. Photographs of the trimmed sample used by RJLee Group. The right image shows the North, Top and West.

3.1.1 Preliminary Scanning and Porosity Discrepancies

Optical microscopy performed at the NETL lab shows the reef carbonate limestone samples to be fossil-rich carbonates with stylolites and abundant ammonoid bioclasts composed of >80% calcite, variable amounts of dolomite, quartz, apatite, and clay minerals. The primary minerals observed through XRD were calcium carbonate (~99%) and dolomite (~1%), along with a small amount of impurities. The pore structure is best described as vuggy, meaning cavernous empty spaces created by secondary dissolution of macrofossils, dolomitization, and removal of organic material

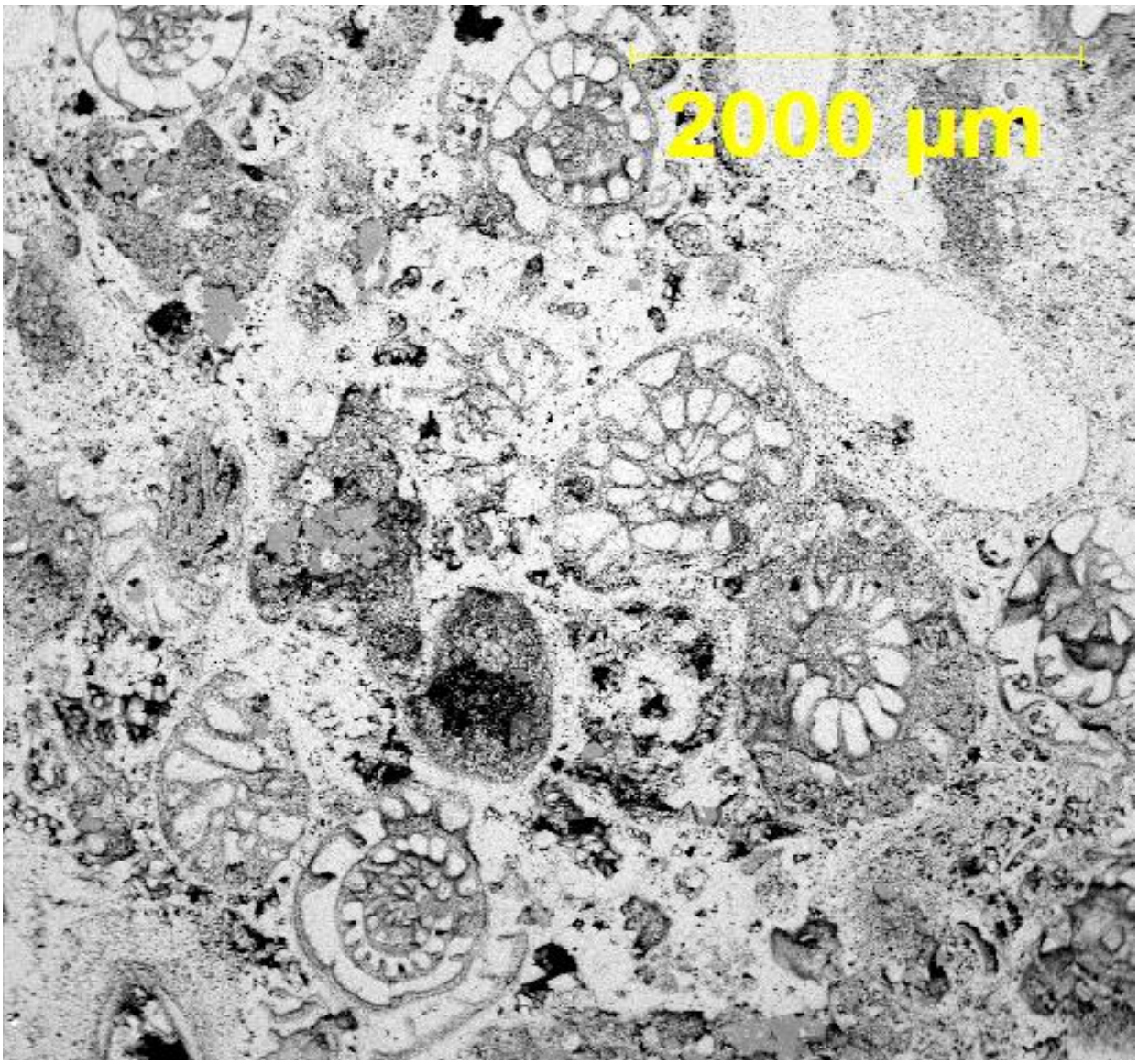

Figure 27. Low magnification SEM image of carbonate sample, showing the presence of macro-fossils, vugs, and secondary dolomitization.

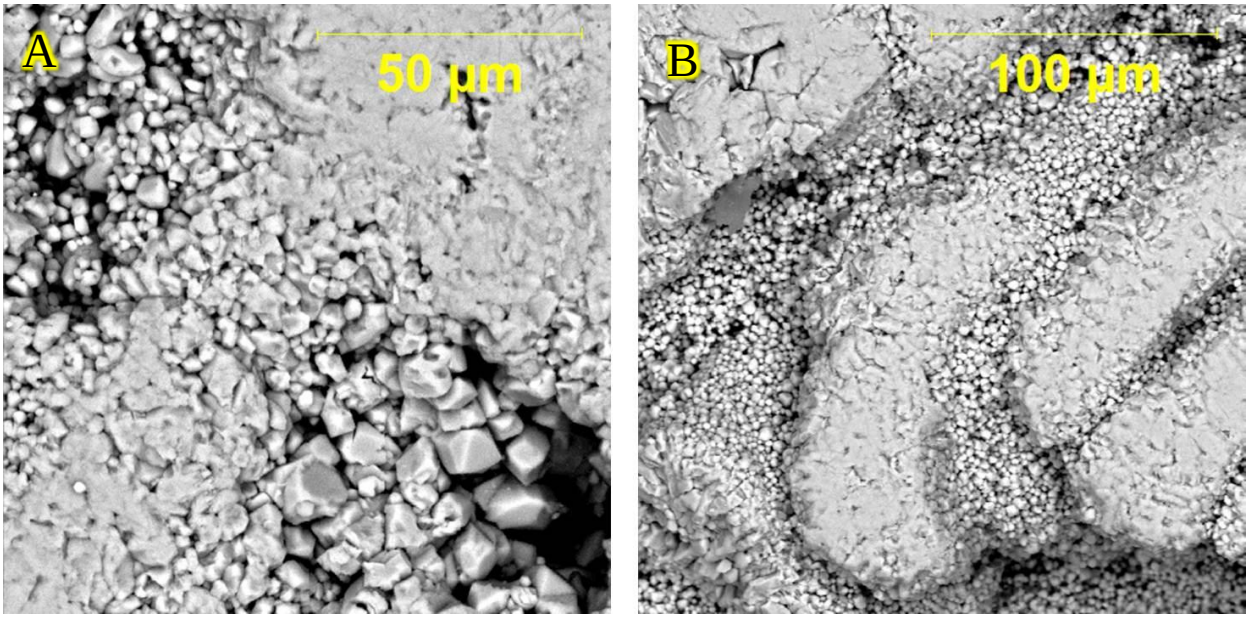

Figure 28. Higher magnification SEM image of carbonate. In this image A) higher magnification, B) lower magnification, the macro fossil structure is differentiable from matrix and dolomitization is visible in vugs.

Figure 28 shows the primary elements in the sample. In characterizing the pore structure, large vuggy pores (likely from dolomitization) as well as a mixture of small (< 20 micron) irregularly shaped calcite grains are observed. Figure 27 shows the fossiliferous texture on the macro scale, while Figure 28 shows a partially dissolved fossil, supporting the notion that a multi-scale approach to pore structure must be used.

For the original RJLee Group montage (3.1.1), an analysis tool was designed to classify the grayscale intensity (0-255) into three classes: Dark, cave-like structures fell between 0-75 and were classified as macro porosity. Continuous matrix fell in the 75-116 range. Bright, energy-scattering textural features from 116-255 and were defined as micro porosity. The class layer was simplified with a spatial analyst boundary clean operation. Then, polygons were drawn around the groups of similarly classed pixels, creating a polygon map of macro/micro pores and matrix. Since the macro pore class includes many small vugs and comparatively fewer large vugs, the

macro pore perimeter data were divided into the low varying small vugs, and larger vugs. A pore perimeter length of greater than 11.25 microns was chosen as the dividing line between small and large vugs because there is limited variation in pore perimeter at low pixel count values.

This geographic information systems (GIS) analysis tool effectively became a matrix-pore boundary texture analysis method. It revealed that in the 18% porosity sample, there exists macro-porosity (6%) as well as high percentages of micro-porosity (57.5%). The micro porosity is a mix of mineral and pore space in the polished SEM images. Pore space and matrix values are balanced with helium porosimeter measurements by sub-dividing "microporosity" into matrix and available porosity. Micro-porosity has a higher surface area to volume ratio than that of the macro pores. To produce chemical models that require surface area values for rate of reaction modeling (Lasaga et al. 1981, Khinast et al. 1996) as well as sonic velocity values related to micro versus macro pore percentages (Baechle et al. 2008), further scans that emphasize porosity in a true 2D space were required.

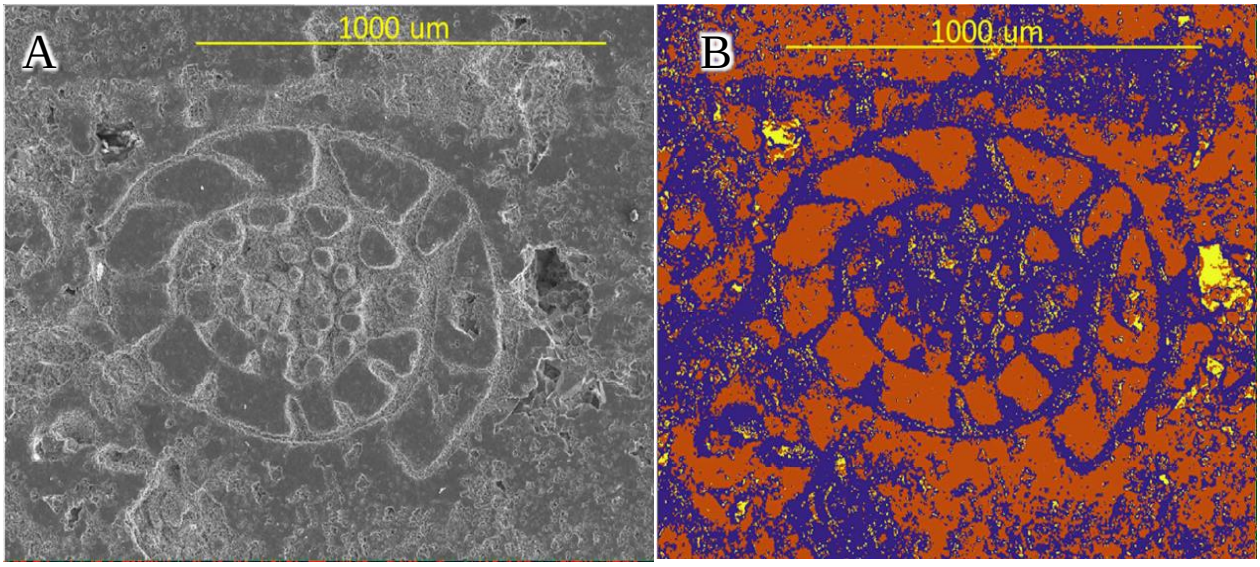

Figure 29. Original SEM image (A) and rock classification (B) of matrix (orange), macroporosity (yellow), microporosity (purple).

3.1.2 Pore Topology Quantification and Analysis (PTQA) Tool

A method to calculate pore count, orientation, and physical dimensions in SEM images was developed. ArcGIS and Fiji (a build of the ImageJ image processing software) were used on an SEM montage composed of 10240 horizontal pixels and 11264 vertical pixels (0.868 micron/pixel). This ArcGIS tool (Figure 30) segments the gray-scale image into three classes, isolates the pore class, simplifies the edges of the pore bodies, turns the pixel class into polygons, subsets pores greater than a particular area, and exports the subset as a binary image to be analyzed by ImageJ. The ImageJ analysis produces, among many other attributes, angle values for the long axis of an ellipsoid that encircles each individual pore (Figure 31). These angle values are then imported, mapped and associated with the pore polygons in ArcMap.

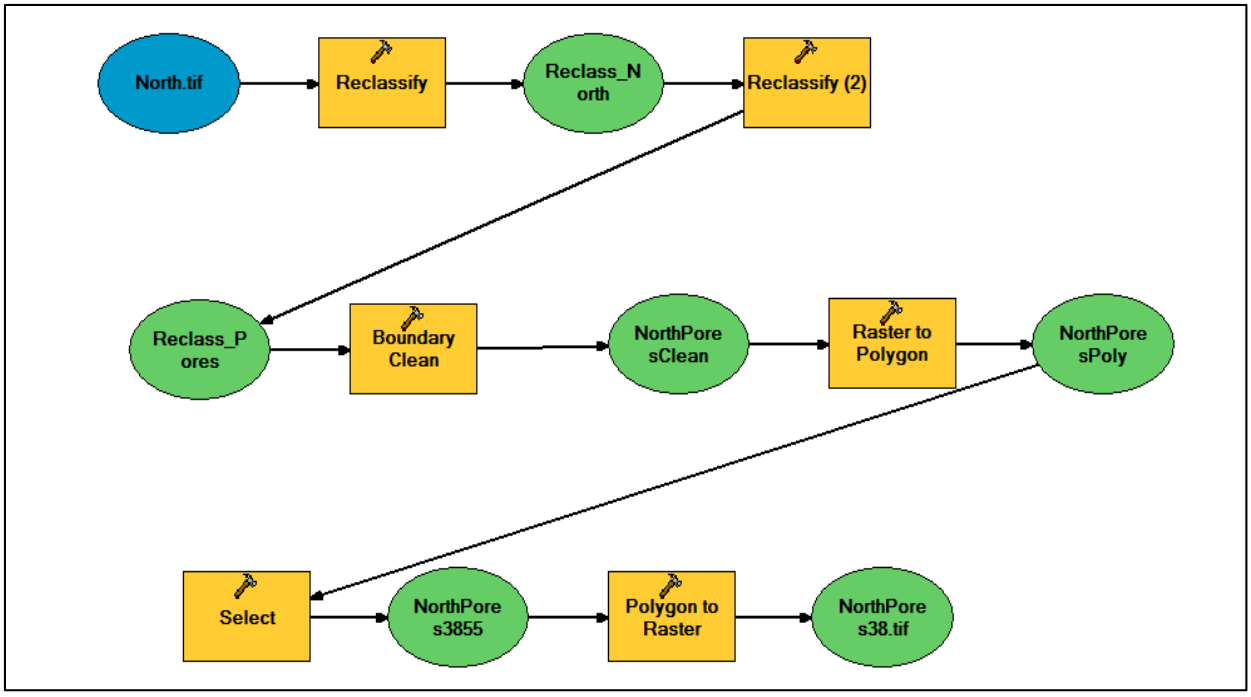

Figure 30. Model for pore analysis categorizes by brightness, nulls out everything but pore classes, smoothes edges of pores, creates polygons of pore perimeters (defines area), selects pores of a given size, and exports the pores which are then encircled with ellipsoids whose characteristics are analyzed.

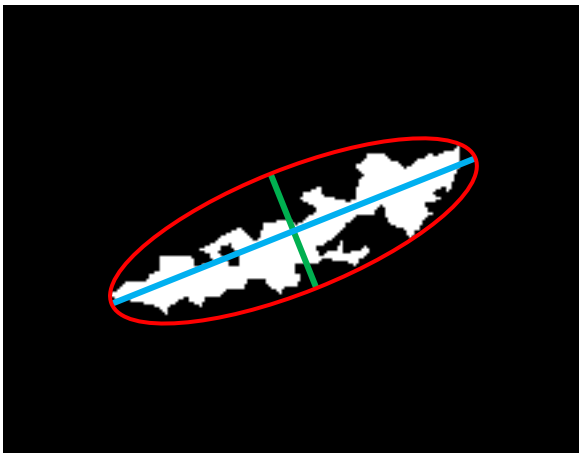

Figure 31. Pore orientation and aspect ratio analysis approach is shown above. A selected pore is depicted with white pixels and matrix with black pixels. The best fit ellipse to the pore shape is shown in red, ellipse major axis is shown in blue, and the ellipse minor axis is shown in green. These and axis orientation angle (to the image x-axis) from each pore are recorded to a geodatabase.

3.1.2.1 Refinement of Method

After the image analysis techniques and methods were developed with the initial sample mosaic, additional samples were taken from the low porosity core. These samples were cut perpendicularly to check for 3D pore orientation characteristics. Sample preparation methodology is refined in accordance with Stutzman et al. (Stutzman 1999) findings on epoxy impregnation. Hardened epoxy improves contrast between pore space and matrix, strengthens the microstructure, and improves its ability to withstand mechanical preparation without fracturing, plucking out mineral grains, or filling voids with debris (Stutzman 1999). The mutually perpendicular, epoxy impregnated, polished samples (2 40mm x 45mm samples and 1 80mm x 40mm sample, prepared by the RJLee Group) were produced from a core column and analyzed.

3.1.2.2 Results of the Analysis

The SEM imaging analysis produced an optical montage, a backscattered electron SEM (BSEM) montage, a CCSEM (computer controlled scanning electron microscope) point count analysis and a CCSEM High-Z analysis. Table 4 shows the results of the backscattered electron imaging analysis. Earlier visual and XRD mineralogical analysis confirmed the presence of calcite and dolomite. High-Z analysis characterizes particles that are larger than 0.2 μm and are brighter than the matrix in the BSEM image (where brightness is proportional to average atomic number). The analysis revealed the presence of trace amounts of phosphorus, sulfur, titanium, vanadium, chromium, iron, nickel, copper, strontium, zircon, and barium. The full chemical report is included in Appendix A.

Table 4. Point count analysis of low porosity limestone.

% Classes	Top	West	North
Calcite	84.12	78.65	68.91
Calcite+Qtz	5.27	9.9	20.05
Dolomite	4.48	4.36	5.3
Quartz	0.19	0.57	0.69
Apatite	0.1	0.03	0.11
AlSi	0.02	0.04	ND
Misc.	0.64	1.66	1.33
Pore	5.18	4.79	3.59
N. Counts	4193	10000	5620

3.1.2.3 Segmentation of the SEM images

The classification system developed for epoxy impregnated SEM images was slightly different than the original method. Once impregnated, samples no longer exhibit the depth or dimensionality that non-impregnated polished samples displayed. In this binary scheme, micro (inferred through texture in non-epoxy-impregnated sample) and macro porosity (pore diameter greater than pixel diameter) are combined.

There are two peaks in the grayscale (0-255, 0=black and 255=white) pixel distribution: one at about 35 and one at about 100. The pixels are segmented into three classes: 0 - 55, 56 - 100, and 101 - 255. This classification accounts for porosity in the 0-55 grayscale unit class and mineralogy two matrix classes that define calcite and dolomite grains. The darkest pixel (pore) class is selected and a binary subset raster is created. This raster data is then converted to polygons in ArcGIS. Note that for pore sizes less than a certain pixel count, the ellipsoids that the image processing software inscribe create non-unique axis orientation angles, 90°, 180°, and 45° due to the simplicity of shapes made from few squares. Therefore, in calculating the pore orientations, pores with a square area of less than 60 μm^2 were omitted from the analysis. The pore size classes and are represented with colors and pore polygon orientations are visualized with cross hatches overlying pores (Figure 32).

The pore polygon set is then converted back into a raster .tiff file and loaded into Fiji. The .tiff is thresholded and area, size, axis length, orientation, circularity, and solidity of individual pores determined using a particle analysis tool. Individual pore and average pore statistics were determined using this tool. Figure 33 shows the overall statistics of pore orientation and distribution of area of the "West" slice. The most pore space occupies pores with area values between 10000 and 100000 μm^2. The pores were subset into three classes (<1000, 1000-10000, and >10000 μm^2). Rose plots show that the distribution of pore area on top of the angular distribution (Figure 37). Statistics calculated are shown in Figure 51 and Figure 56. The ratio of perimeter-to-area vs area gives a sense of pore wall complexity which is an important factor in understanding where reaction of rock material with a solution will most likely occur. Solidity describes how much of the encircled ellipse that the pore fills, and aspect ratio is the long axis

divided by the short axis. The pore map in Figure 32 shows pore distribution tendencies on the macro scale.

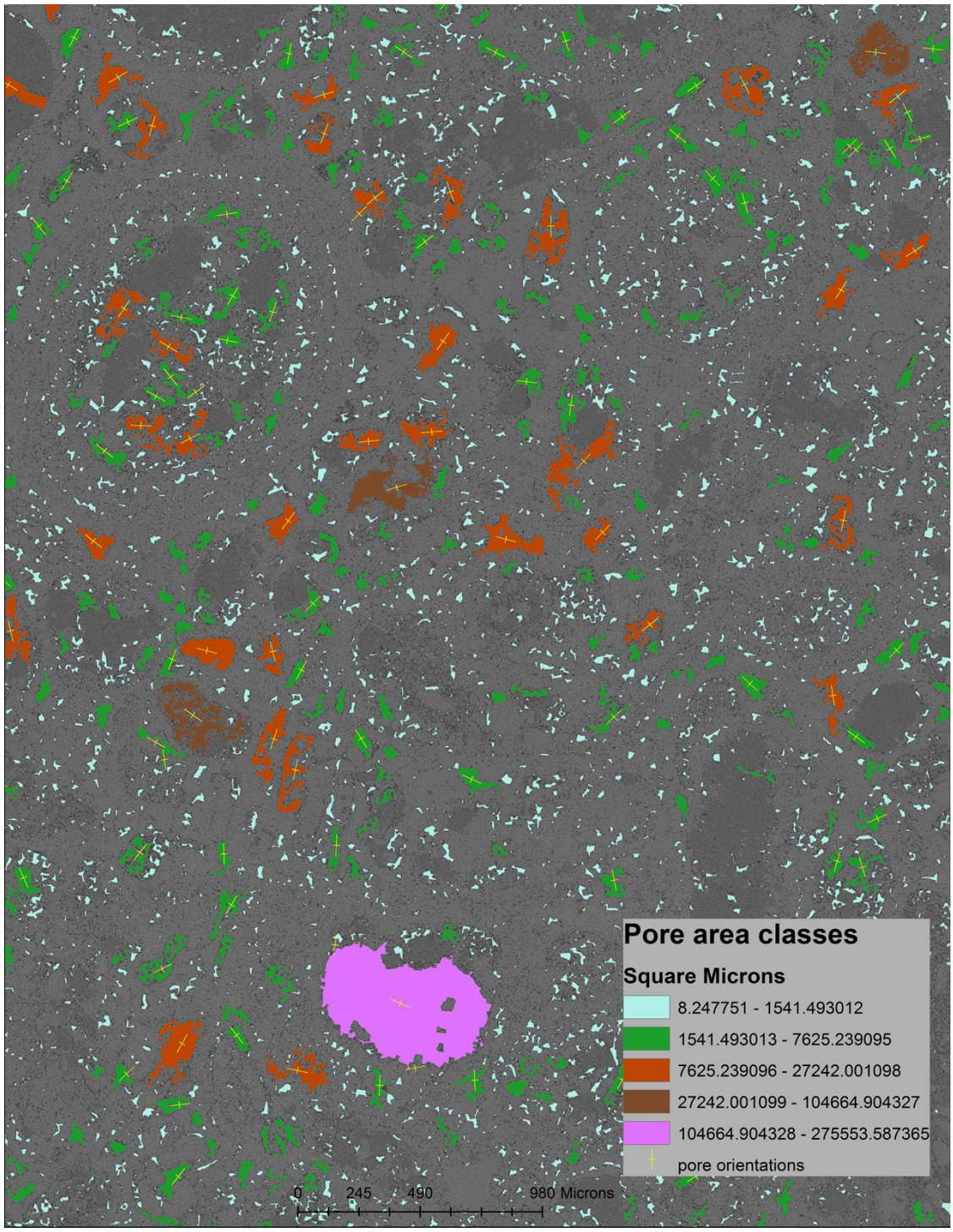

Figure 32. "Top" plane SEM images from three plane analysis (Figure 26). Pore classes by area with orientation overlay.

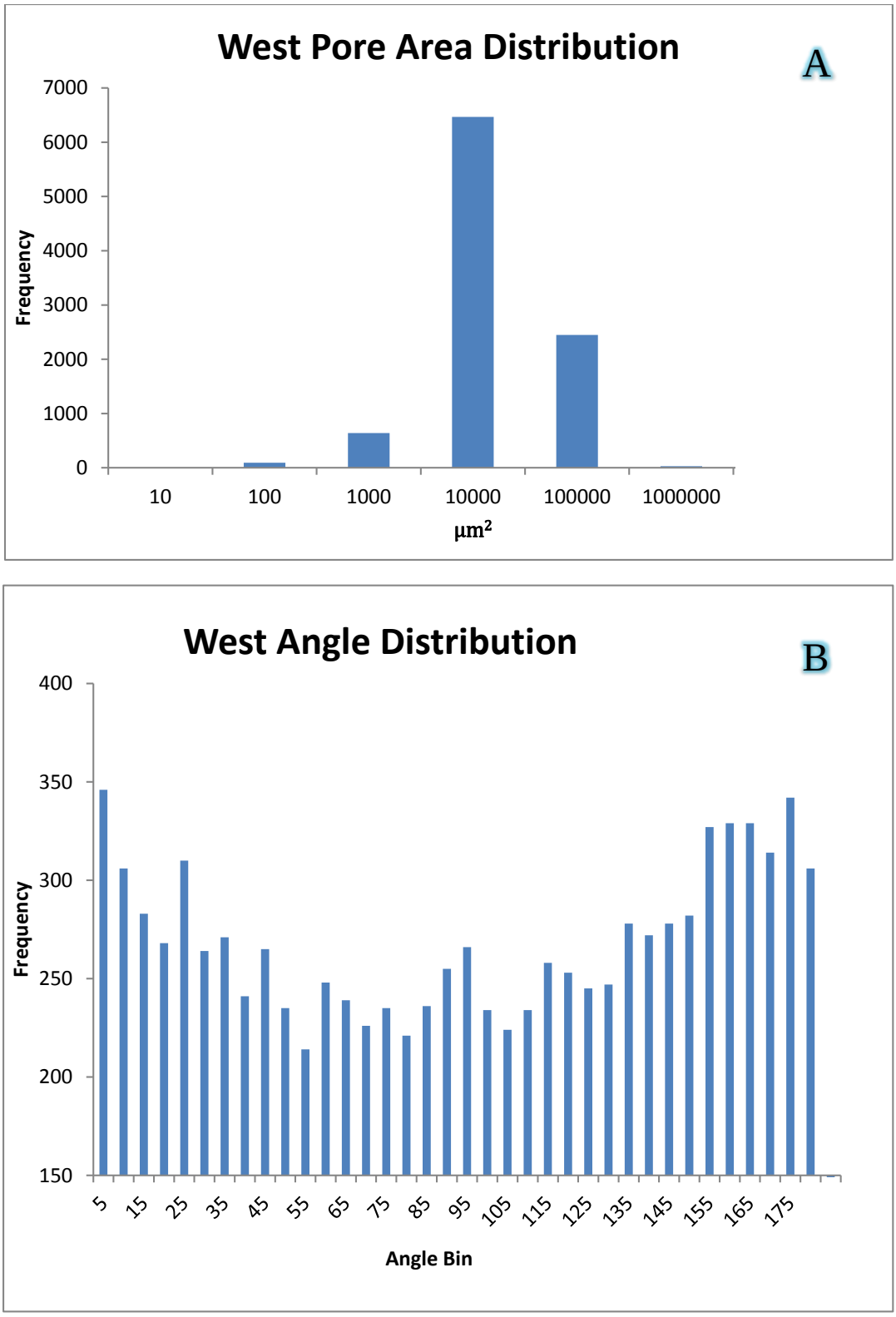

Figure 33. "West" plane data from three plane analysis (Figure 26): pore area size (A) and angle distribution (B).

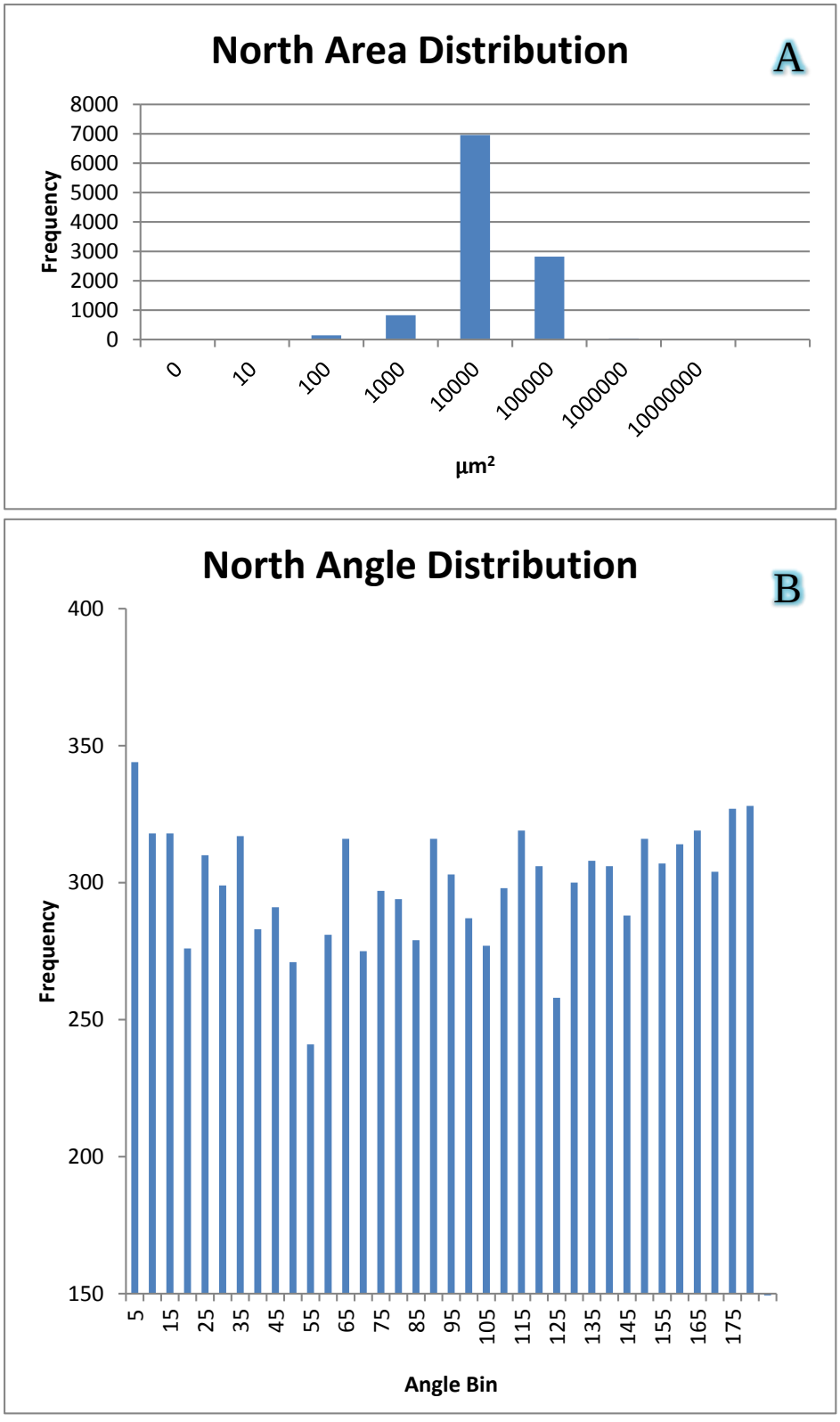

Figure 34. Pore information for "North" from three plane analysis (Figure 26): area (A) and angle distribution (B).

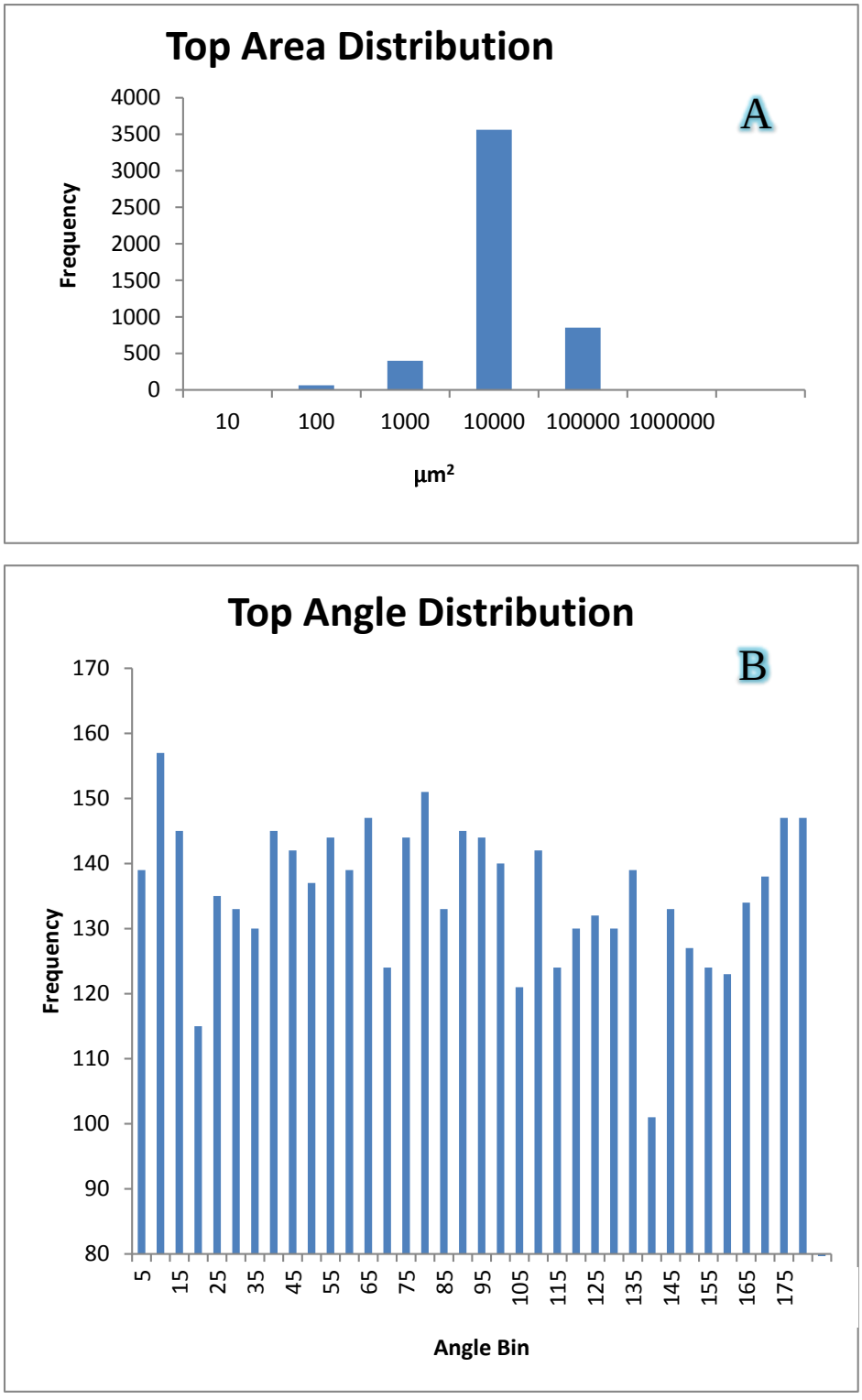

Figure 35. Pore information for "Top" from three plane analysis (Figure 26): area (A) and angle distribution (B).

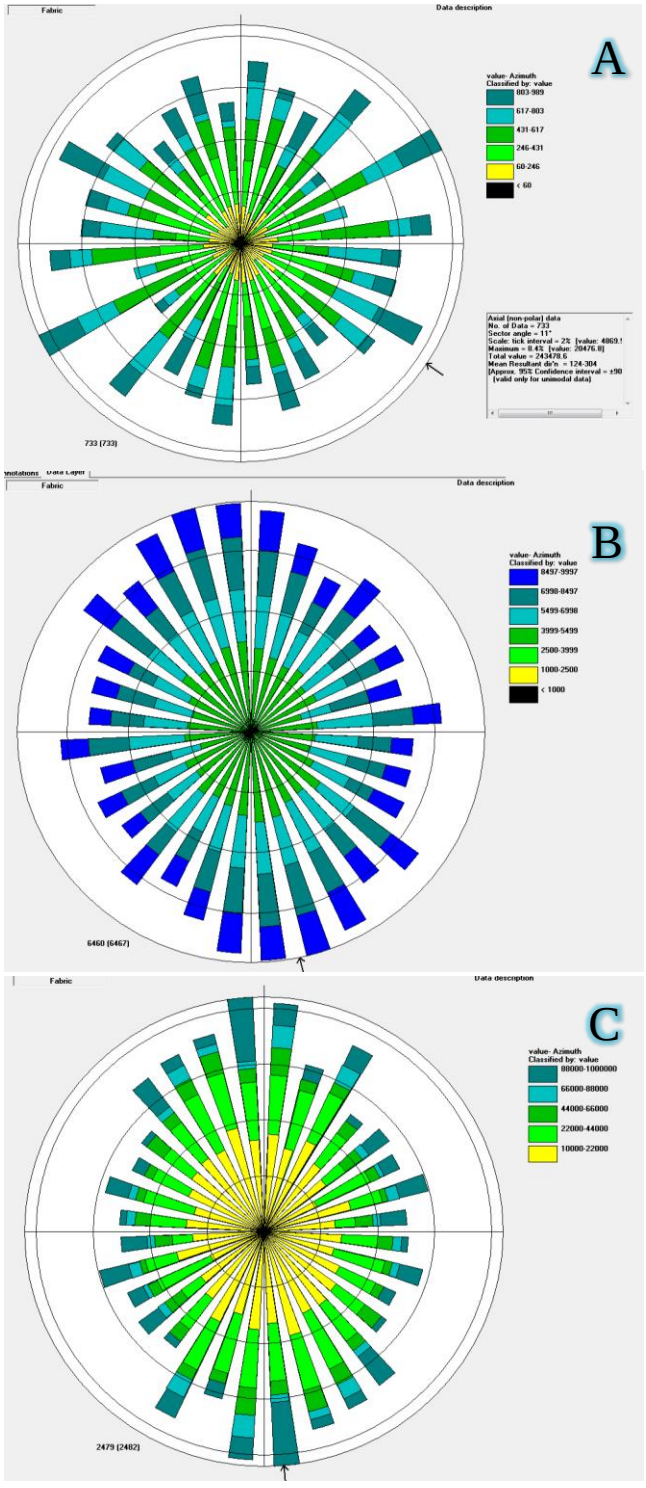

Figure 36. (A) West pore orientations < 1000 μm^2, (B) West pore orientations, area range 1000-10000 μm^2. (C) West pore orientations > 10000 μm^2.

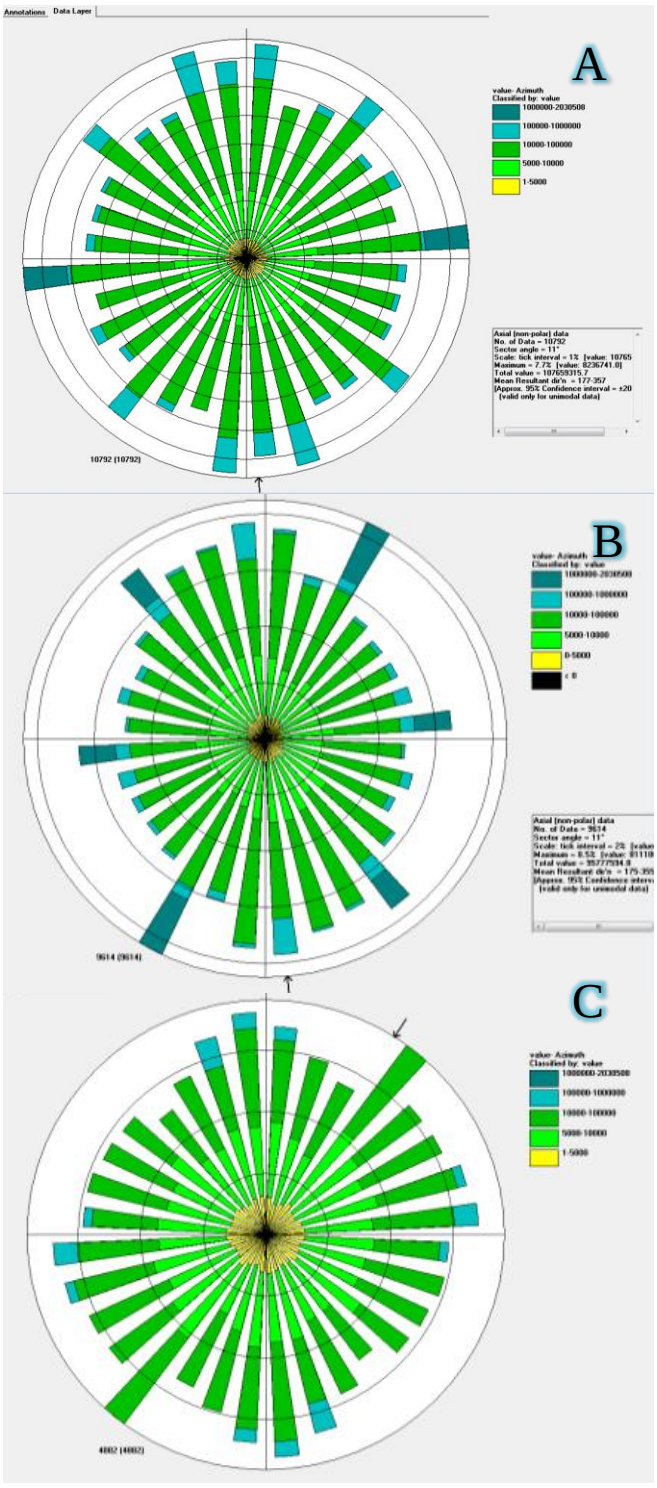

Figure 37. Rose diagrams of total pore size distributions and orientations for all orthogonal sides (North (A), West (B), Top (C) datasets).

3.1.2.4 Vector Representation of Pore Statistics

To construct the 3-D vector representation of the pores at various sizes, components from the image analysis data of the three-perpendicular plane data were used. On each face, the average direction of the short axis was used as the direction of maximum weakness. I calculated the distribution of compressional weakness to the x, y, and z directions with the following equations:

$$\boldsymbol{Top}: \boldsymbol{y_T = \cos\Theta_T}, \boldsymbol{x_T = \sin\Theta_T} \quad \textbf{(55)}$$

$$\boldsymbol{North}: \boldsymbol{y_N = \cos\Theta_N}, \boldsymbol{z_N = \sin\Theta_N} \quad \textbf{(56)}$$

$$\boldsymbol{West}: \boldsymbol{x_W = \sin\Theta_W}, \boldsymbol{z_W = \cos\Theta_W} \quad \textbf{(57)}$$

I then added the all components of x, y, and z and normalized each pore group to the largest component. Table 5 shows three pore ranges and the average pore size. This allows a simple visualization of each pore class maximum compliancy direction from (0, 0, 0) origin. Figure 38 shows how the orientation of the vector is applied to a pore of a given size. The average aspect ratio (found by dividing the best-fit ellipse long axis by the best-fit ellipse short axis of each pore) for all pores was 2.10. With this methodology, rocks with more pore orientation anisotropy can be characterized and quickly modeled using Thomsen's anisotropy parameters (Thomsen 1986). These parameters (ε, γ) are approximately the relationships between fast and slow (V_p) P and (V_s) S-wave velocities (subscript numeral indicates rotational angle of core sample):

$$\varepsilon \approx \frac{V_{P90} - V_{P0}}{V_{P0}}$$

$$\gamma \approx \frac{V_{S\|90} - V_{S0}}{V_{S0}}$$

Table 5. Unit vectors average axis lengths in microns for three pore size classes and total average.

	Average Long Axis µm	Average Short Axis µm	x_{unit}	y_{unit}	z_{unit}
Pores < 1000 um^2	28.16	13.41	0.990652	0.892918117	1
1000um^2<Pores<10000um^2	119.44	56.87	1	0.957266597	0.978281112
Pores>10000um^2	219.95	104.74	1	0.947971424	0.971934549
Average of All Pores	135.1	64.33	1	0.950796576	0.977695118

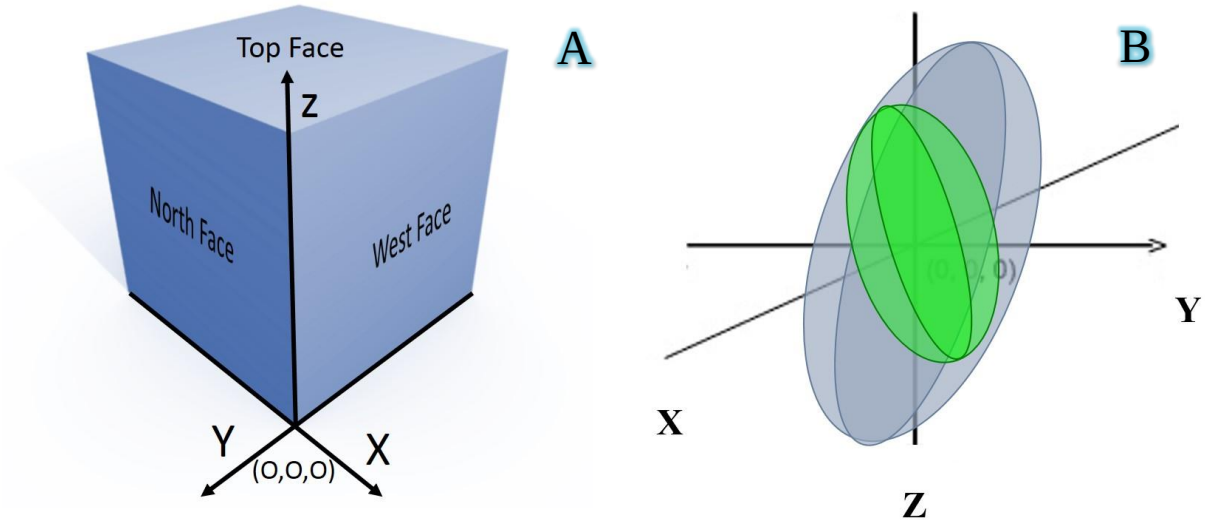

Figure 38. (A) Sketch of SEM analysis plane orientations with (x, y, z) axis. (B) Two (blue, green) overlain representative pore sizes with orientation. The pore orientation, long, and short axis lengths from Table 5 can be used to predict pore shape (saucer or elongated spheroid) or mechanical properties (compliancy along short axis).

3.2 COMPUTED 3-D TOMOGRAPHY CHARACTERIZATION AND ANALYSIS

3.2.1 4th Generation CT Scanner

The Universal Systems HD-350E Computer Tomography scanner (140 kV source) at the NETL Laboratory was used to observe the pore structure of the low porosity limestone core (Figure 39). The resolution and power of this scanner is best applied to core imaging of cores with diameters greater than two inches. This fourth generation CT scanner bridges the resolution gap from the micron to centimeter scale.

Figure 39. Universal HD-350 Petrophysical Computed Tomography System (www.universal-systems.com/HD_350.php#house1)

Figure 40 helps convey that as the observer magnifies, classification of a "porous zone" is more practical than describing individual pores. In comparing the SEM slice to the 4th generation CT images (A), heterogeneous pore density is observed in both. The SEM data show that pores of varying sizes can have a specific orientation in the matrix. Rose diagrams (Figure 36) of pore

orientations reveal slight orientation directions. On the "West" plane, the largest pores had an orientation of ~ 23° and 100° and the smaller pores were offset about 30°. Brajanovski suggests orientation and size of voids is related to sonic frequency attenuation (Brajanovski et al. 2005). The CT images in Figure 40 (A) show that larger scale density zones exist that can further influence wave mechanics. The advantage of the CT scan is that the process is non-destructive and in situ measurements and experiments can be performed simultaneously. Conversely, the scanner cannot resolve common 100 micrometer diameter pores.

The CT observations are used in conjunction with velocity measurements to understand the effects of porous zone orientation on mechanical properties. Velocity changes are measured as the wave pathways are manipulated to find velocity anisotropy values. In the medical CT scan of the low porosity limestone, colored areas represent groups of porous zones in the core (Figure 40). The diagonal low-porosity zone can be seen in the cloud of pore orientation cross hairs overlain on the SEM image to the right. P-wave velocity anisotropy caused by bands of low porosity cannot be observed with current laboratory experimental setup as the source-receiver path remains along the same axis as the core is rotated. To observe p-wave anisotropy experimentally, the source-receiver beam must be normal to the axis of rotation instead of parallel. S-wave anisotropy is, however, observable. Figure 41 shows S-wave anisotropy of about 250 m/s in the 6.6% limestone core. These measurements were taken at rotation increments of 0°, 45°, 90°, 135° and symmetrically copied to finish 360° the rotation (Purcell 2012). The sinusoidal behavior signals that the orientation of the dipping plane of low porosity disperses the planar S-wave as it passes through the sample.

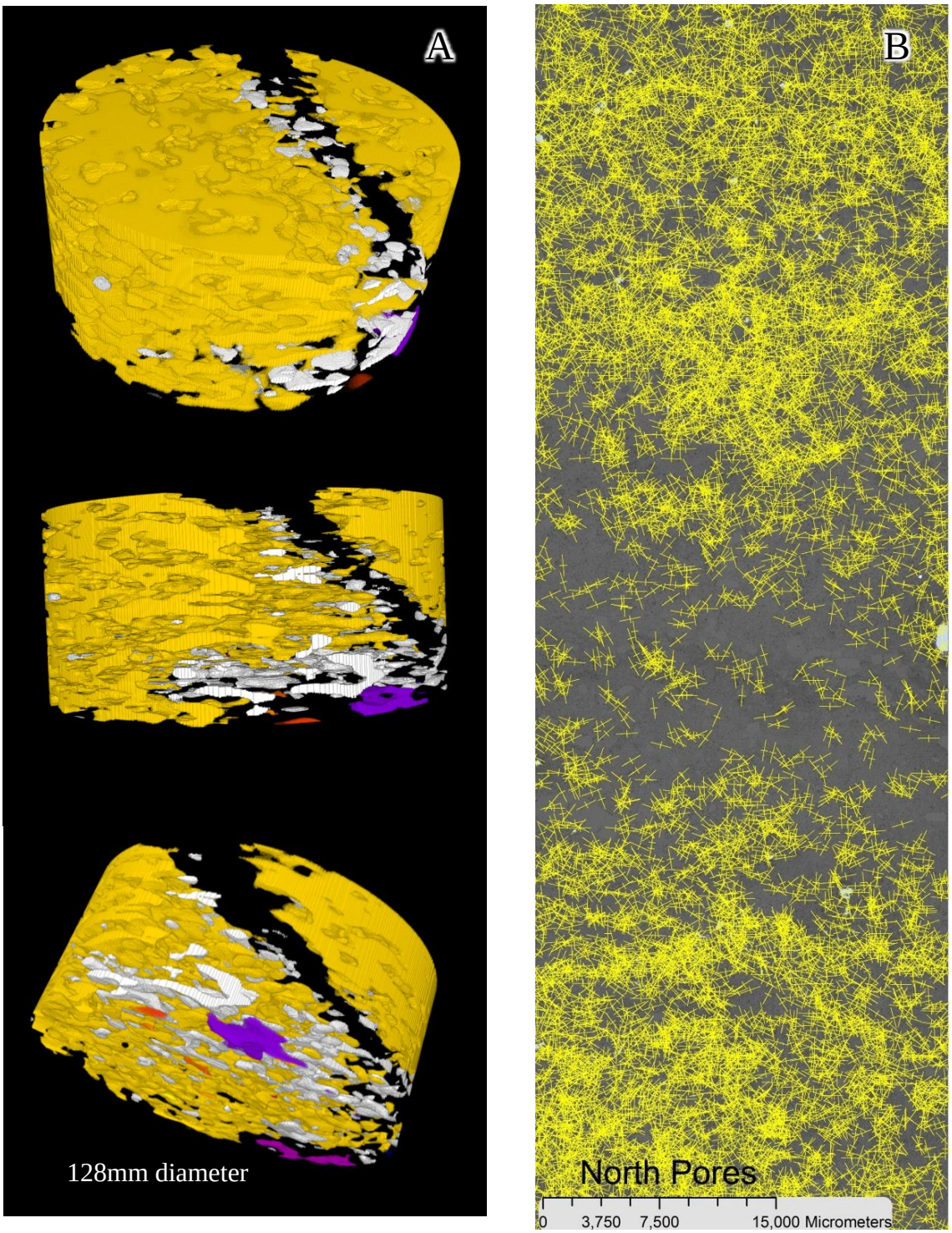

Figure 40. 4th generation medical CT scanner (A) and SEM montage (B). Porous zones defined by colors on left and actual pore data points displayed as yellow crosses. Low porosity domains are visible on both scales.

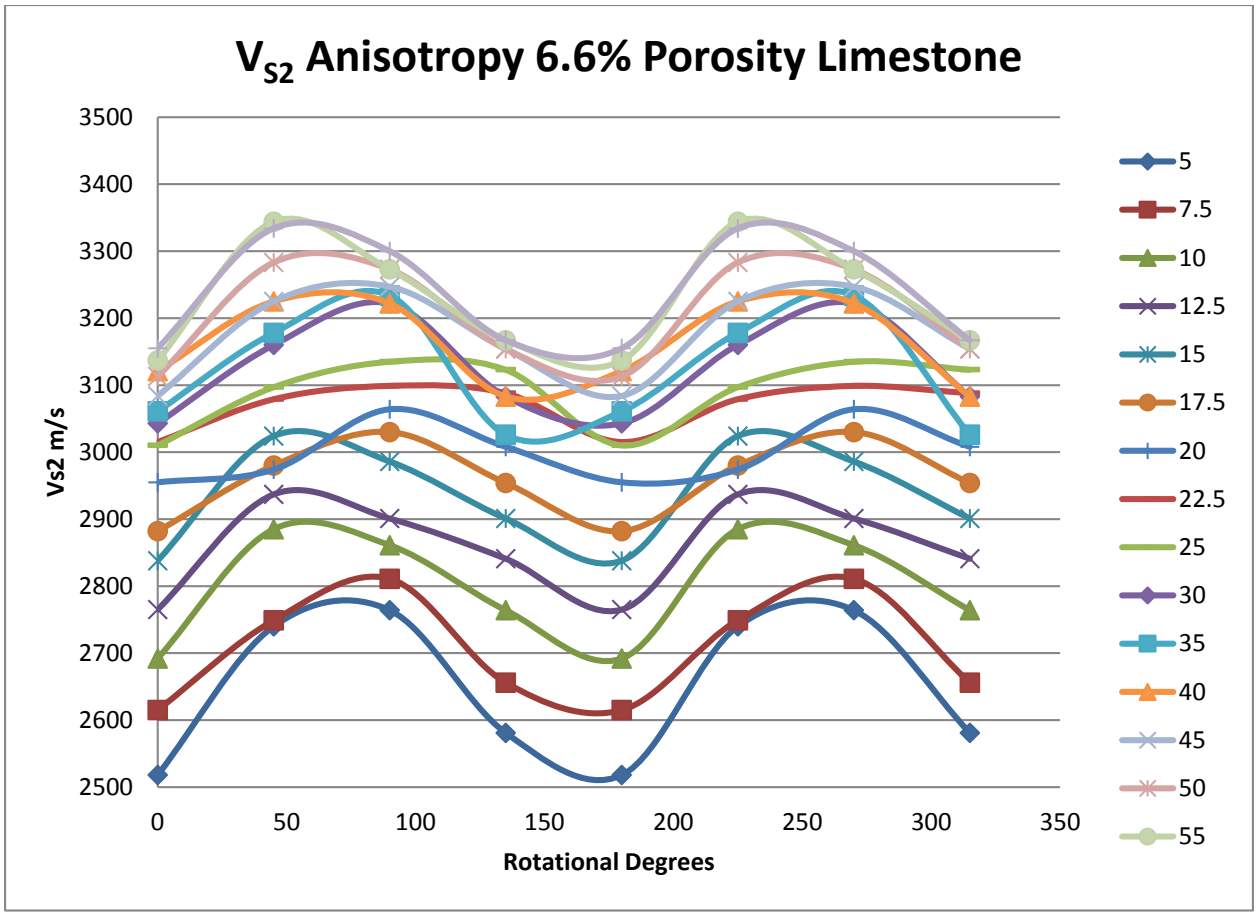

Figure 41. S-wave anisotropy observed in the 6.6% porosity limestone core (Purcell 2012). Abscissa shows the rotation of the core around the long axis, ordinate shows slow S-wave velocities. Colors represent the effective pressure at which the measurement was taken.

3.2.2 Micro CT

Non-destructive, x-ray computed tomographic analysis were performed using an XRadia-400 Micro-XCT scanner at the Pittsburgh and Morgantown NETL laboratories. The device uses a closed tube x-ray source and a multiple lens detector system to collect image slices through the axis of a rotating cylinder. Raw data is exported as sequential 2-D slices normal to the cylinder

axis. Pixel spacing is equal to slice spacing, so when data is reconstructed, there are voxels with three equal length sides. The Micro-XCT (μCT) scanner has a maximum spatial resolution to less than 1 μm and 0.56 μm pixel size. The scans produced at NETL were datasets of ~1000 .tif files with 4X magnification at resolution of 3.9 μm/pixel, 10x magnification at 2.242 μm/pixel, and 20X magnification with resolution of 1.3 μm/pixel. These slices can be visualized in 3-D to investigate sample structures: e.g. identify fossils, and visualize changes in porosity (Figure 42). In Figure 43, slices of the same area in the high porosity limestone at the two different magnifications can be seen.

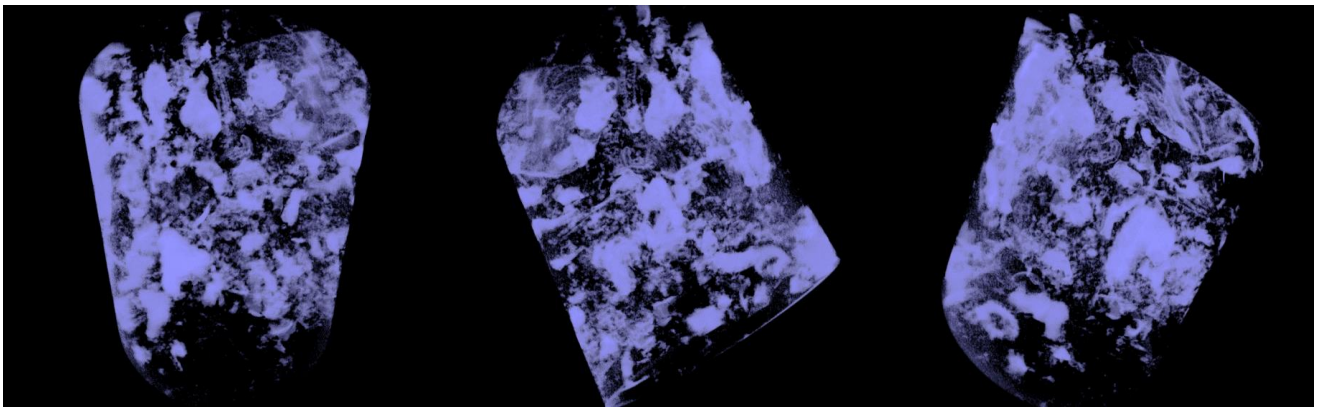

Figure 42. Multiple 3D views of 4x low porosity limestone samples showing pore structure. In processing the CT data, matrix has been defined as transparent to clearly show the porosity structure and topology. Sample diameter is equal to 1.2 mm.

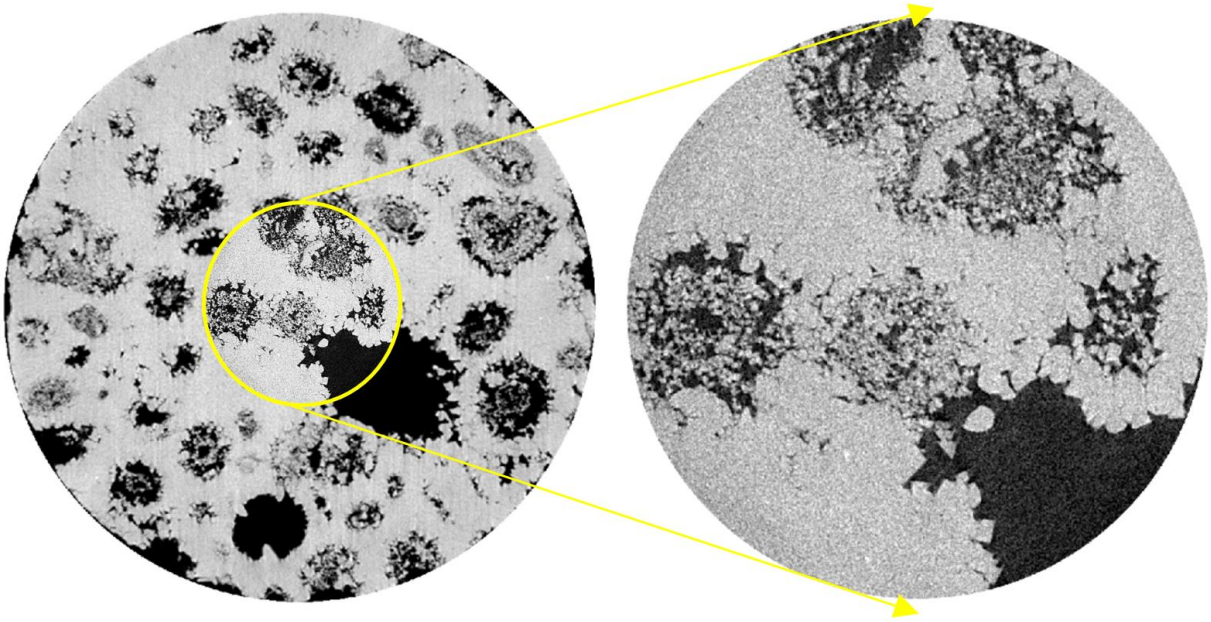

Figure 43. 3-D µCT scans of 18% porosity limestone. Left: 4x, 1.2 mm diameter. Right: 20x subset, 1100 µm diameter.

Fiji/ImageJ was used for analysis of these data. In order to quantify rock properties from µCT scans, the following steps are followed:

1. Enhance contrast of volume
2. Remove washed out frames at beginning and end of volume
3. Threshold to differentiate pores and grains
4. Run 3D object counter process
5. Run thickness process

Select slices from the µCT image stack were analyzed with the previously described Fiji-ArcMap tool (Section 3.1.2). The grayscale images are segmented into three categories: pore, matrix, and bright grains (likely dolomite), converted the classes to polygons and exported the pore class as a binary image. Using Fiji to analyze the pore image, ellipses were best fit around the pores and a dataset with values for spatial location, area, major/minor axis lengths, angle of

major axis from x-axis, aspect ratio, and solidity for 165 pores was produced. I imported the data back into ArcMap and produced a map with the three classifications and the orientation of each pore (Figure 44).

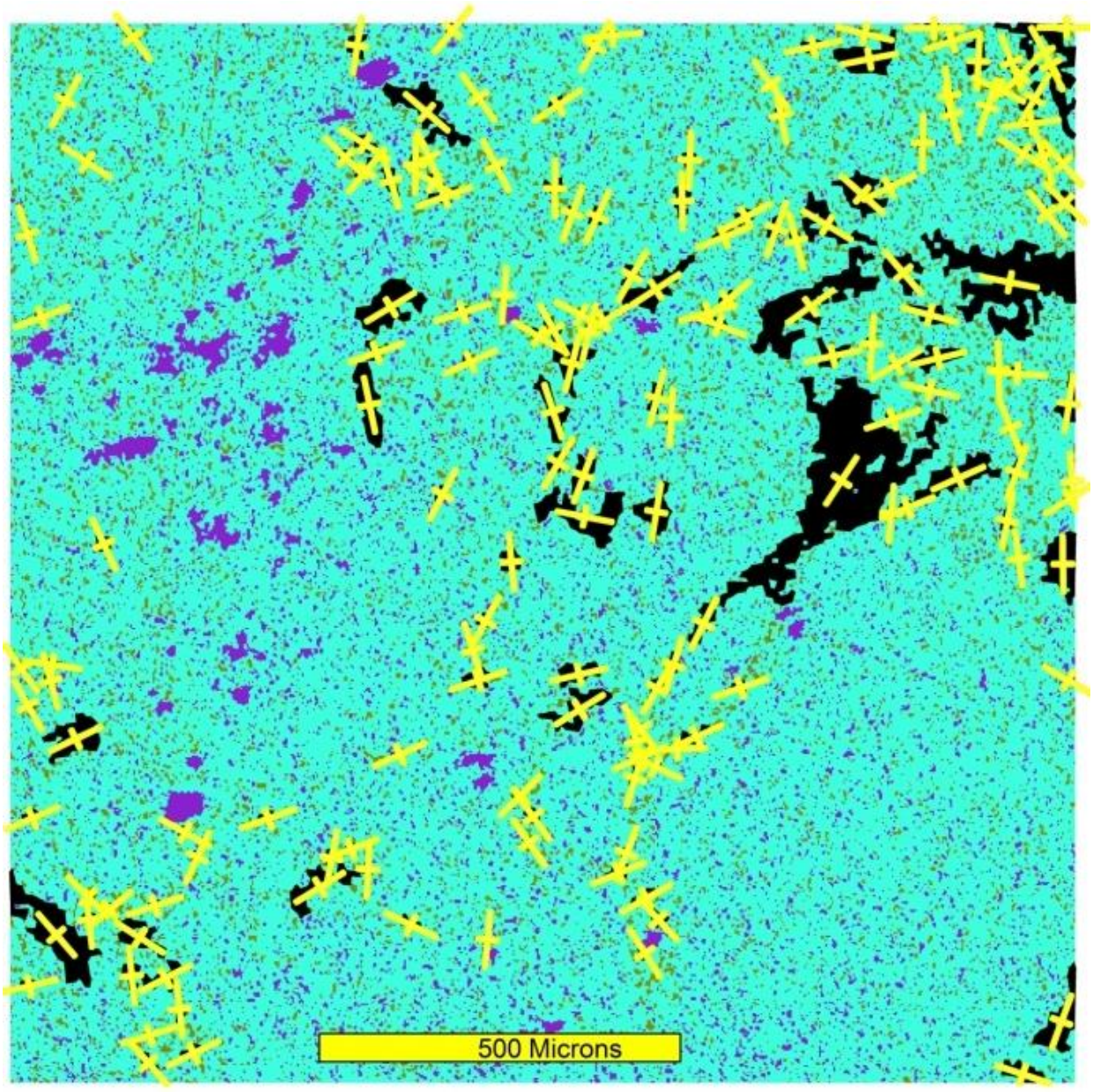

Figure 44. Pore orientations with cross sectional area greater than 130 μm^2 observed in slice of μCT volume of low porosity carbonate reservoir material. Black is the analyzed pore space, green is porosity under the pore size threshold, teal and purple are calcite and dolomite matrix.

The CT dataset was cropped with Fiji, to a 686 x 626 x 499 pixel (1.54 x 1.40 x 1.12 mm) volume and the 3-D Object Counter plug-in (Figure 45) was run. The 3D object counter and thickness process are memory intensive and produce large datasets that provide a significant set of pore measurements. This plug-in finds user defined threshold and minimum/maximum groupings of pixels in each slice of the stack, groups them with neighboring groups in above and below slices, and associates touching groups through the volume (Figure 46) (Abramoff et al. 2004, Bolte et al. 2006).

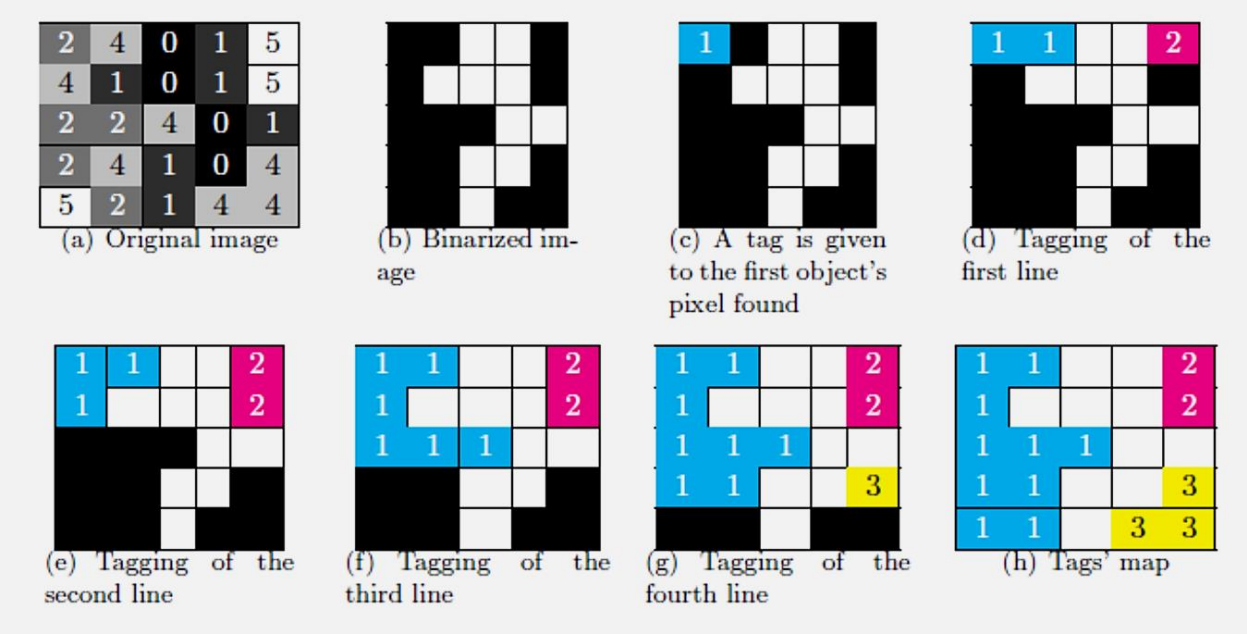

Figure 45. 3D object counter process: Steps a-h are performed on each slice so that neighboring pixels within threshold are tagged as pore 1, 2, 3 etc. The numeric process then unites neighboring pixel tags from slide to slide, giving 3-D voxel groups (Bolte et al. 2006).

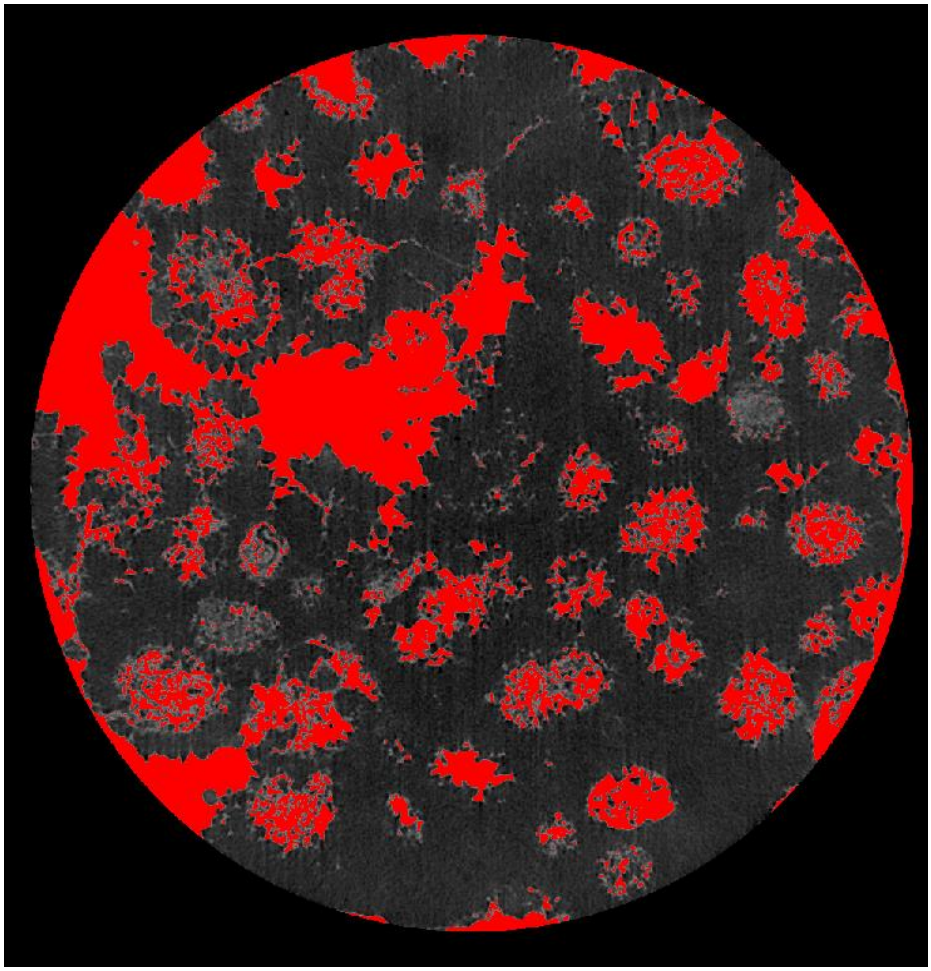

Figure 46. 3-D object counter thresholding process. Porosity determined to be pixels with grayscale value greater than 127. Red represents pore area to be analyzed in the process (calcite-dolomite matrix remain visible). Minimum (15 pixel groups in this case) and maximum pixel size for particles is defined.

Run time of this analysis took over twelve hours with a 2.67 GHz Intel i7 CPU with 21 GB of RAM allocated to the processing program. This tool produces pore volume, surface area, volume coordinates, bounding box dimensions, centroid/center of mass and associated distances to pore surfaces. The colorized numbered pores through the volume allow visual aid in understanding pore connectivity. Figure 47 shows a large network of pores in white and unconnected pores in red.

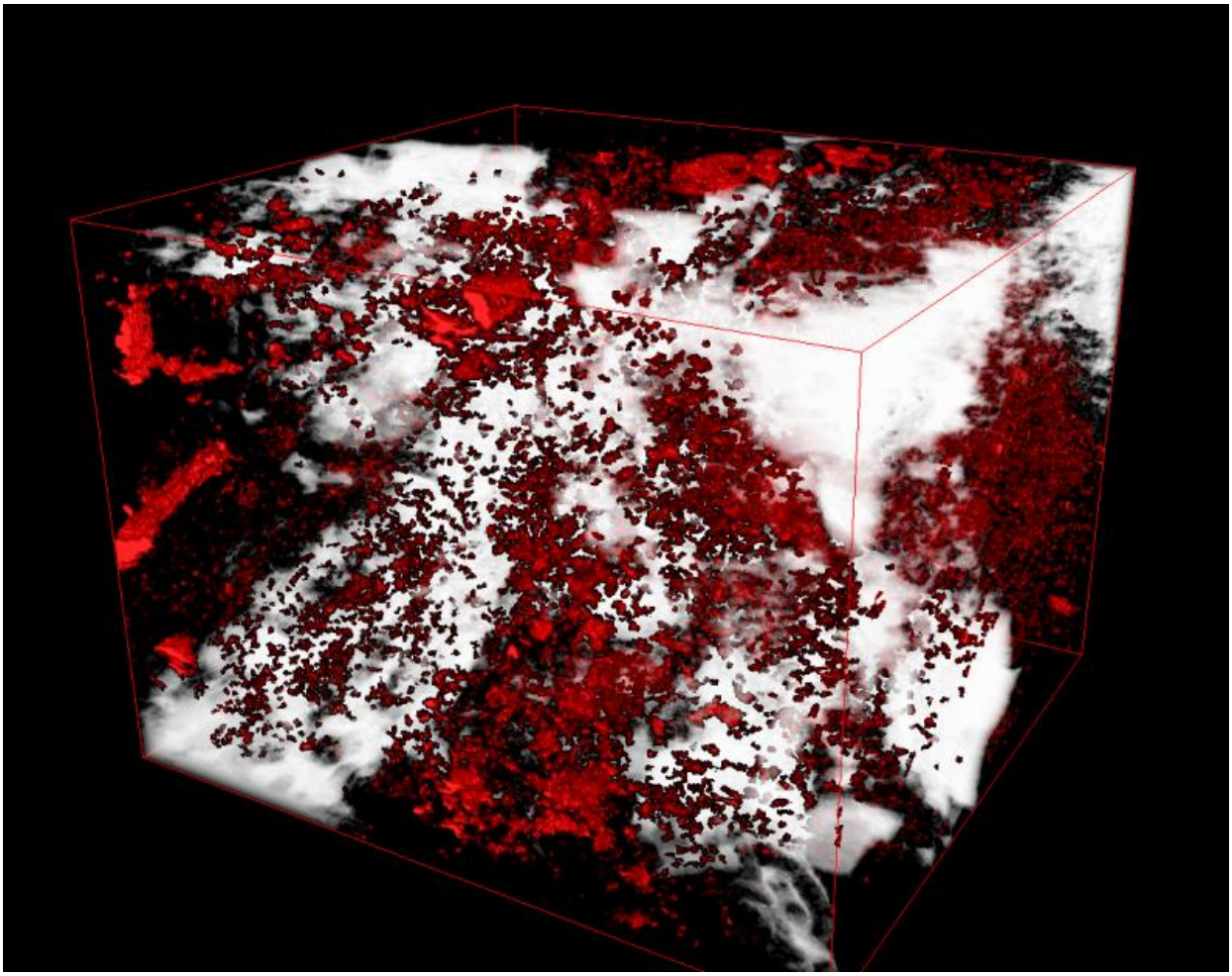

Figure 47. Network of connected and unconnected pores in 6% porosity limestone sample(Volume size 1.54 x 1.40 x 1.12 mm).

Using the volume analysis and previously measured values for density and porosity, I find that core #1 has 175 cm^2 of pore surface area per gram between the pore volume sizes from $2.8*10^2$ μm^3 to $2.8*10^8$ μm^3. Of the 11,089 pores analyzed, pore volume distribution grows to 500 μm^3 and then decreases exponentially. A large connected pore network exists in the sample and produces outlying large volume values.

Finally, local thickness is used to characterize porosity. The process, depicted in Figure 48, draws a multitude of straight lines from a pore pixel to the wall of the pore (A). The pixel is

then colored by the average length of the lines to the pore walls (B). In Figure 48 (B) blue shades define compliant porosity.

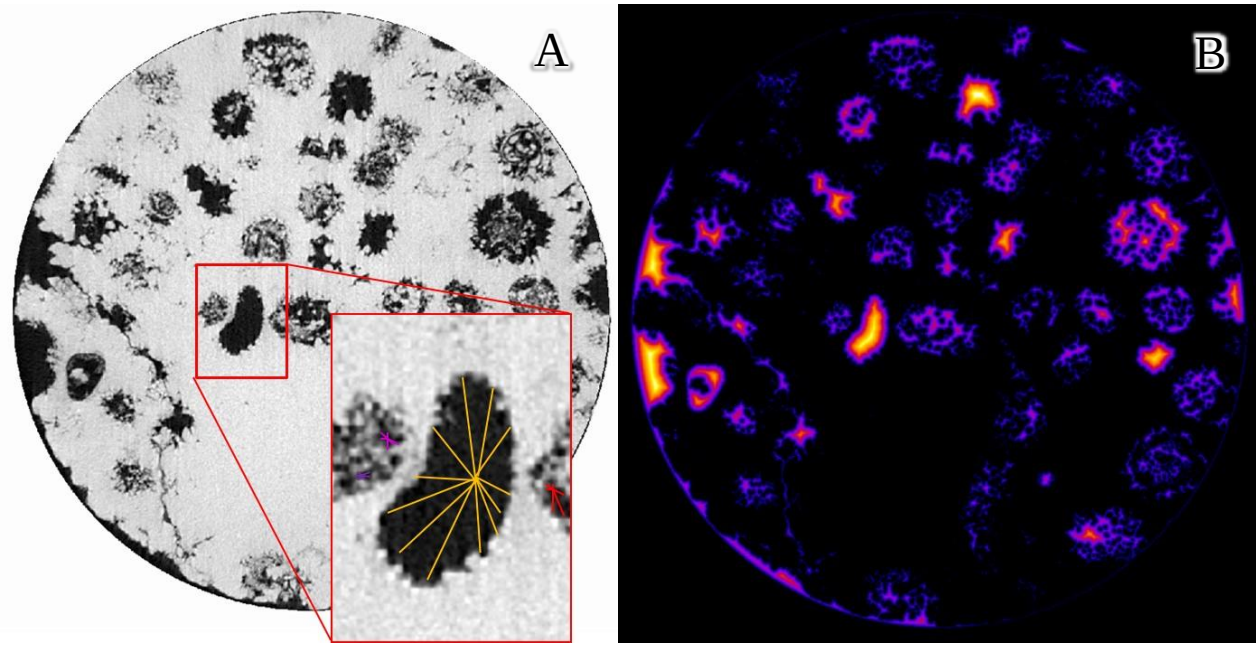

Figure 48. Thickness mapping in ImageJ. Average distance from pore pixel to pore wall is found (A). Bluer colors represent relatively more closeable, compliant pore space (B).

The results of these analysis are used as inputs to the described rock modulus model (from which P and S-wave velocities are calculated). Digital porosity segmentation methodology was refined by comparing laboratory velocity measurements to predicted velocities from the digital rock model (see section 2.2).

3.2.2.1 Digital Wave Propagation Development

For the continued analysis of μCT rock scans, we are developing a Python program that uses central differences to approximate a wave through rock. The program propagates a wave through 2D slices of porous rock with assigned bulk and shear moduli, density, pore filling fluids, and wave attenuation values. The program maps wave displacement and will eventually map stress throughout the volume. We hope to understand, at the micron scale, the effects of local stresses induced by passing seismic waves and relations to small scale rock properties and structures. Figure 50 and Figure 49 show two time slices of a wave passing through a porous limestone.

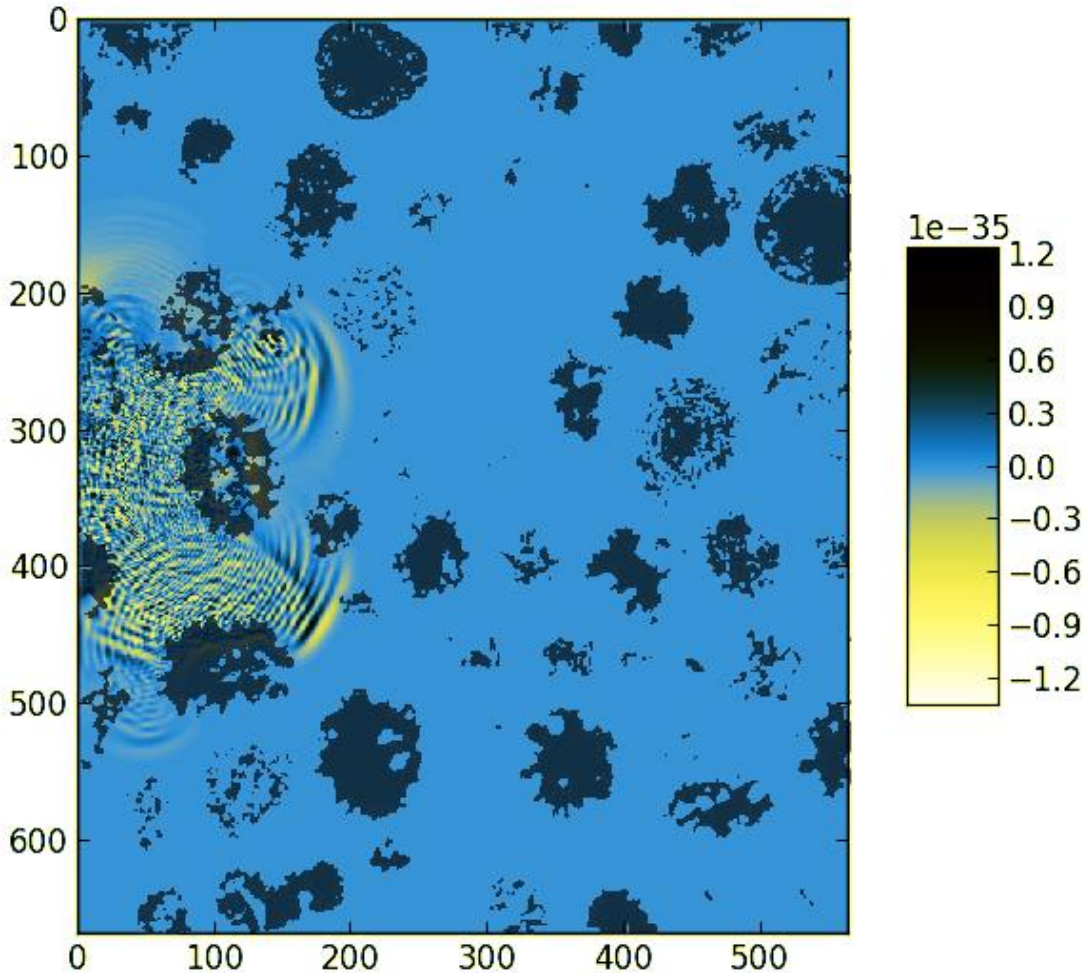

Figure 49. 22nd time step, false color displacement.

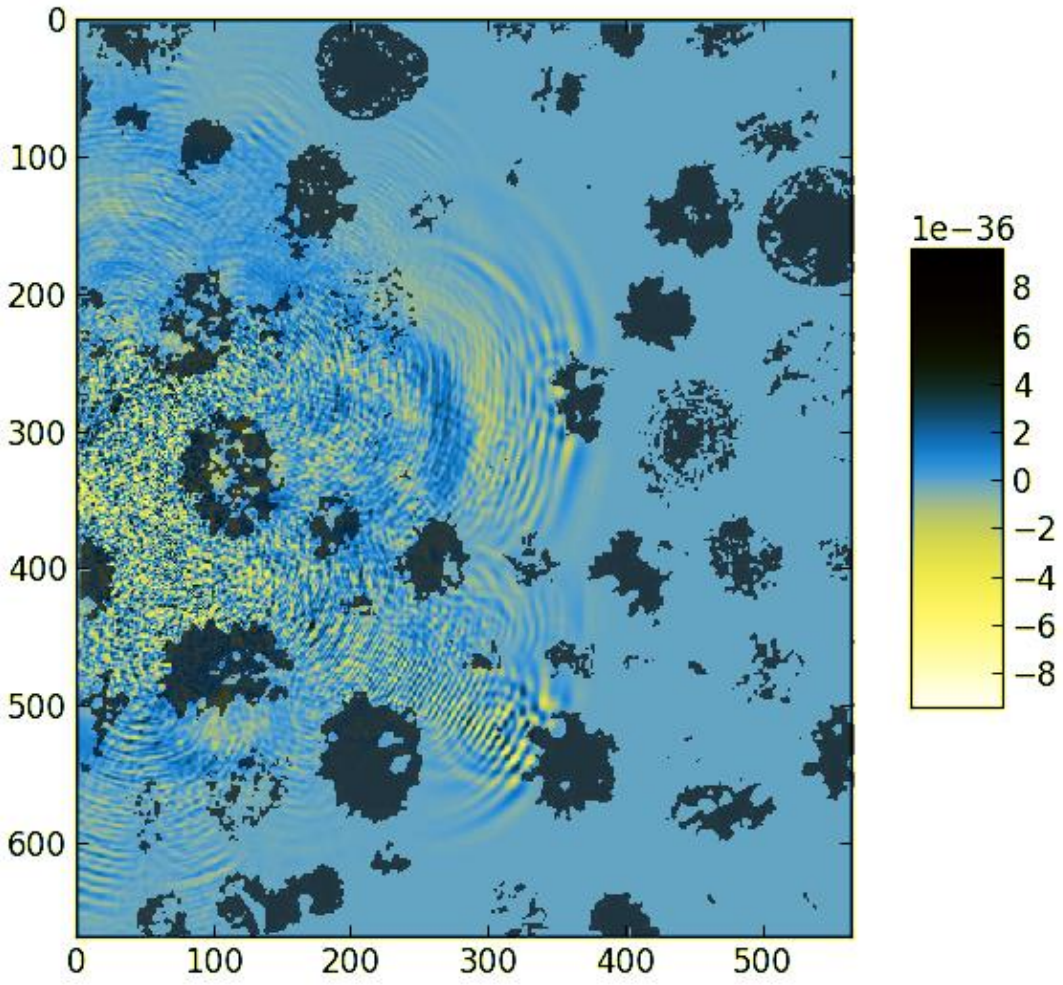

Figure 50. 43rd time step, false color displacement.

3.2.3 Compliant Porosity Analysis

Laboratory observations reveal dramatic P-wave velocity increases over the lower effective pressure range (to ~15 MPa) and are less variable at higher effective pressures. Velocity increase is attributed to increasing bulk modulus (resistance to uniform compression). Bulk modulus increases through the rock over low pressure ranges because compliant porosity is closing (Shapiro

2003). Two theories are used to define compliant porosity in the image data: One is that pores with high aspect ratio close more easily under pressure and the other is that complex cracks on the edges of large pores, although not separate pores, will close first (Figure 14).

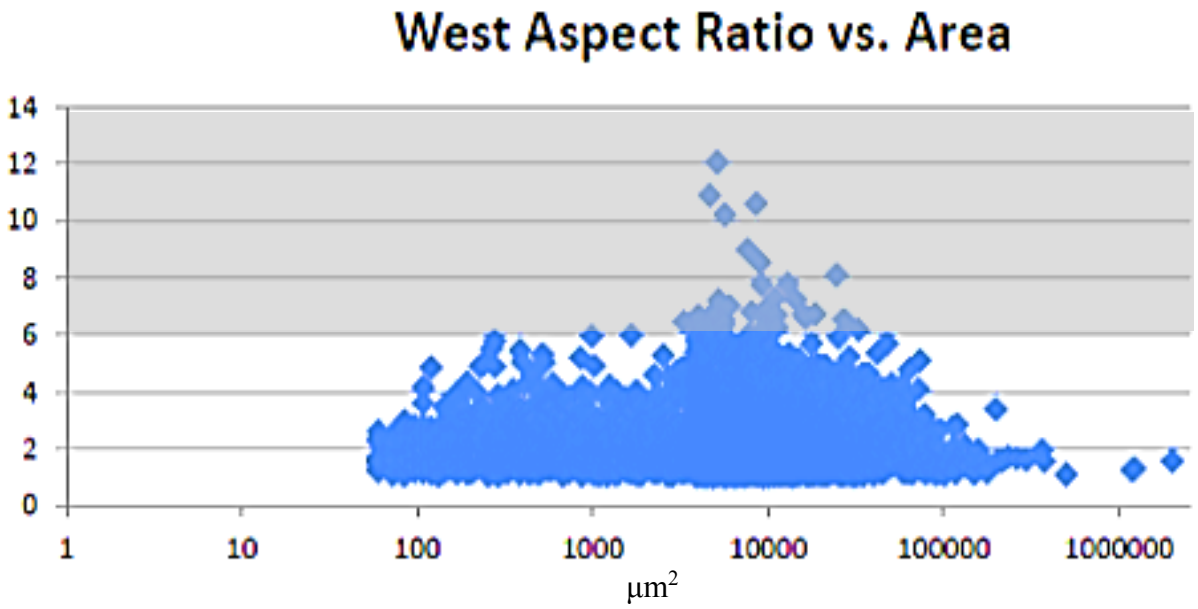

Figure 51. Aspect ratios (long axis of ellipsoid/short axis of ellipsoid) of SEM "West" mosaic versus the pore areas in square micrometers. Elongation is seen around the 10000 μm^2 range. Points inside of the shaded box are relatively more elongated and thus more compliant.

The image processing techniques used have produced best fit ellipsoid descriptors that include length and orientation of long and short axis. Figure 51 suggests that there are a concentration of easily closeable, high aspect ratio pores in the upper thousand μm^2 to ten thousand μm^2 cross sectional pore area range.

In the analysis of higher magnification and µCT data volumes, it becomes difficult to differentiate individual pores. This calls for another method of classifying compliant porosity, which can also be used to confirm the aspect ratio method. A local thickness map is a better tool for high magnification samples. Local thickness was computed on images to determine compliant

porosity (Dougherty et al. 2006). This image-processing tool allows high aspect ratio areas of a given pore to be recognized by rating pixels based on minimum distance to pore walls. Figure 52 is an example of the process: The black inclusions represent 16.8% porosity, the colored image and histogram show the distribution of the local thickness calculated pixels. In this figure, the blue and purple colors represent relative compliant porosity, which is more sensitive to applied load than stiff porosity (represented by yellow and red shades). In (C), compliant porosity color values are segmented from the image. The percentage of white pixels calculated as the percent value for compliant porosity.

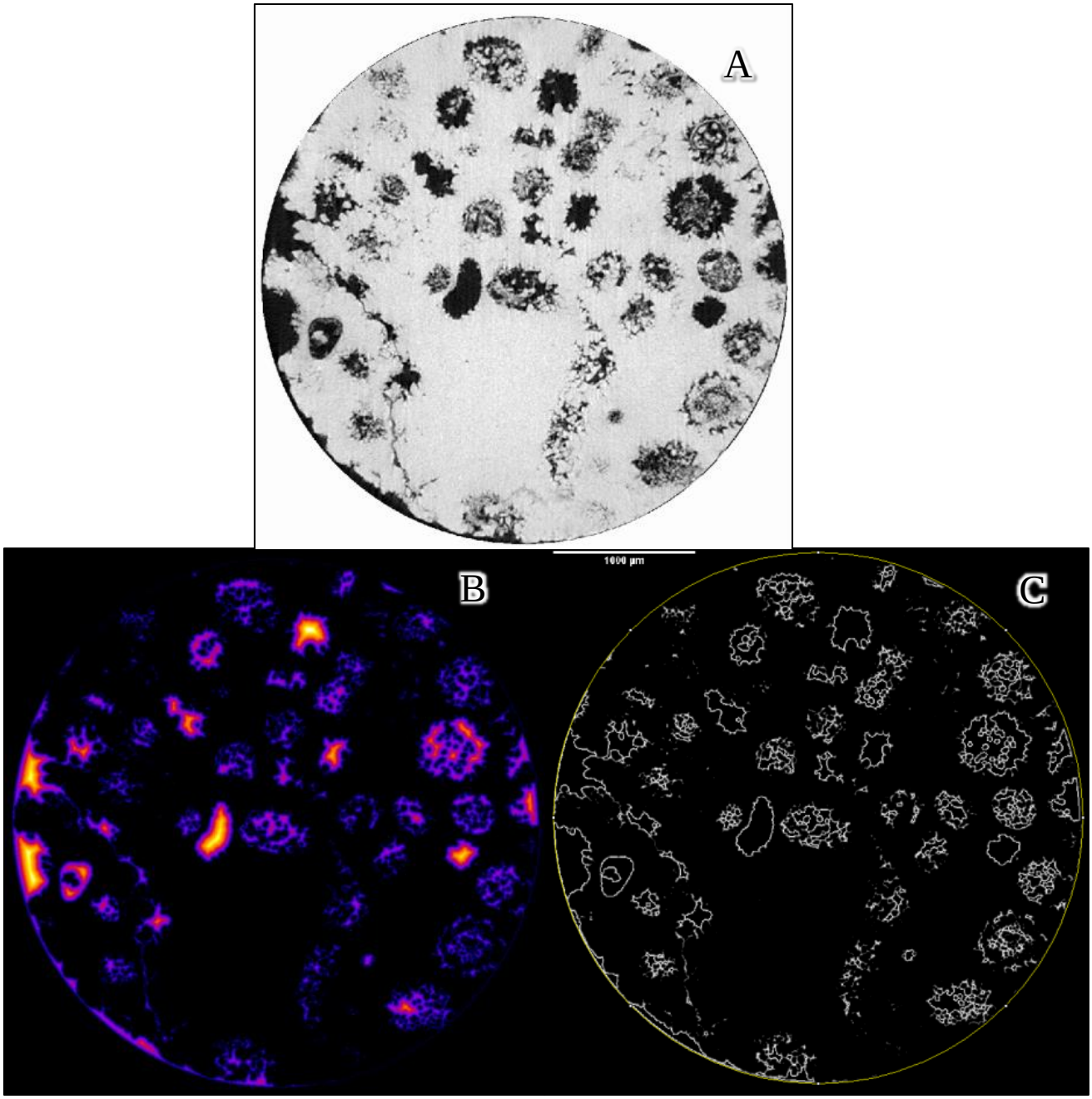

Figure 52. 4x high porosity sample, local thickness processing. (A) original slice, (B) processed slice, (C) compliant porosity segmented by displaying the lowest blue values from (B).

3.3 SUMMARY

The three scale digital analysis of the rock material revealed porosity values and changes with chemical exposure. These methods lend input values to rock sonic velocity models, chemical reactivity models, and wave propagation simulations which must be scale dependent to produce realistic results (due to attenuation, pore size, frequency, and wavelength interactions). Large area 2-D micron scale imagery revealed mineralogy and discreet pores. This was cause to develop the aspect ratio method which describes individual pores and is useful on low magnification where pores are distinct. With greater than 10,000 pores described from a given SEM mosaic, this method would easily detect statistically significant pore orientation trends in a sample. The carbonate, however, had only subtle pore elongations. The "thickness method" is most useful at the small volume 3-D micron scale (μCT) where pore pixels are rated by their relation to nearby matrix pixels, thereby subdividing individual pores. At this scale repeat, non-destructive scans can be made to directly observe the results of fluid exposure experiments (Results in Chapter 4.1). It should be noted that the size of compliant pores are determined by the compliant porosity percentages used in the rock velocity predictions and since values are sometimes extremely low, it may be necessary to have very high magnification datasets with millions of voxels to directly quantify compliant porosity.

At the multi-centimeter core diameter 3-D scale, 4^{th} generation CT scans show zones of relatively greater and lesser porosity over larger rock volumes. The volume produced is a useful space to scale-up the results of the higher magnification observations. It is also a space in which movement of in situ fluids can be detected (Alemu et al. 2013).

4.0 REPEAT CT ANALYSIS OF CO_2 EXPOSED LIMESTONE MATERIAL

The Lu et al. (2012) study of the Cranfield sandstone reservoir showed that CO_2 injected, acidified waters do not have short-term effects on the sandstone. The potential for geochemical reactivity of calcite to acidic solutions requires further investigation of the Permian basin limestone as rock matrix changes affect seismic monitoring. The advantage of having μCT scans is that 3-D surfaces can be characterized in terms of chemical reactivity. Similar to compliant porosity analysis, there are the disadvantages of digital resolution limits (the cubic natures of voxels influence area and volume analysis). To overcome these resolution disadvantages, samples were exposed to reactive fluids for varying time periods and the mass change along with before and after μCT scans were used to calibrate reactive surface area calculations.

4.1 LIMESTONE REACTION RESULTS

It is expected that injecting CO_2 into a partially water filled reservoir would acidify the pore waters and cause some degree of dissolution in a carbonate reservoir matrix. Toews (1995) shows that the prediction models are not accurate for the dissolution of CO_2 into water and the subsequent acidification is as low as pH = 2.80 under pressures of 7-20 MPa (Toews et al. 1995) The injection pressures of CO_2 in reservoirs are on this order of magnitude and greater, so it is likely that water will be well inundated with CO_2. As a preliminary experiment, the mass of desiccator dry piece of the limestone was measured (0.646g), submerged in a small beaker of deionized water, and

placed it in a reactor vessel for 95 hours at 50°C with CO_2 maintaining reservoir pressure of ~2000 psig (pound per square inch gauge = absolute pressure minus atmospheric pressure of 14.7 psi). In this 20% porosity limestone sample, 3% (0.021g) of the rock mass was dissolved. To understand the nature of this dissolution process, the experiment was continued with three small cores of the same material exposed to CO_2-water mixes at reservoir pressure and temperature over extended periods of time. μCT scans of the samples were taken before and after exposure to determine how mass distribution changed.

The μCT scanned samples were approximately 1 cm diameter, 2-3cm long cores that were mounted on aluminum posts of the same diameter. A beaker with a known volume of water was placed inside of the reactor vessel. To suspend the limestone sample in the vessel, an aluminum cross bar that spans the beakers mouth with a locking mechanism to hold the sample's aluminum posts was constructed (see Figure 53). After the apparatus was prepared, the first of three limestone samples was weighed, soaked in a known volume of deionized water, weighed again, and secured in the reactor vessel (see Figure 54). These reactor vessels have a drain on the bottom, but as the sample is in a beaker in the vessel, fluids are not drained during the experiment. Therefore, water pH was not measured through the course of the reaction. However, previous experiments on dissolution of supercritical CO_2 into water show acidification with pH values as low as 3.

Exposure temperature and pressure conditions were 50°C/2000 psi. After a 24 hour exposure, the reactor vessel was degassed and sample removed and weighed. The surface pores of the sample appeared visibly larger. The limestone sample was then scanned again using the XRadia μCT scanner. The before-exposure scans were analyzed to determine pore volume and pore surface area. The after-exposure scans were processed in the same manner. The before/after

volumes were registered (physical reference frame shifts were corrected so that the switch between two voxels occupying the same space represents movement in the time dimension only) and compared to reveal pore size and characteristic changes. Comparison of the before CO_2 exposure and after CO_2 exposure measurements revealed a 0.15% to 1% internal porosity gain, accompanied by a decrease in pore surface area to volume ratios. In Figure 55, the slices from a pre and post exposure show dissolution along a preferred pathway. Note that the water in the reactor vessels is static and therefore all pore fluid flow is diffusion based. Also shown are thickness maps which are used in the section 2.3 P and S-wave velocity model.

Table 6. Exposed limestone masses, pressures, and exposure times.

Experiment	Rock mass (g)	Sat mass (g)	Tot H_2O mass (g)	Temp (°C)	CO_2 pressure (psig)	Exposure time (hours)
HP-L (2 in Core)	294.65	311.51	467.26	50	1950	958.58
HP-1 (w/rod)	1.36	1.37	3.72	50	1950	27.05
Hp-2 (w/rod)	1.26	1.35	3.75	50	2000	722.45
HP-3 (w/rod)	1.43	1.50	3.78	50	2000	331.50

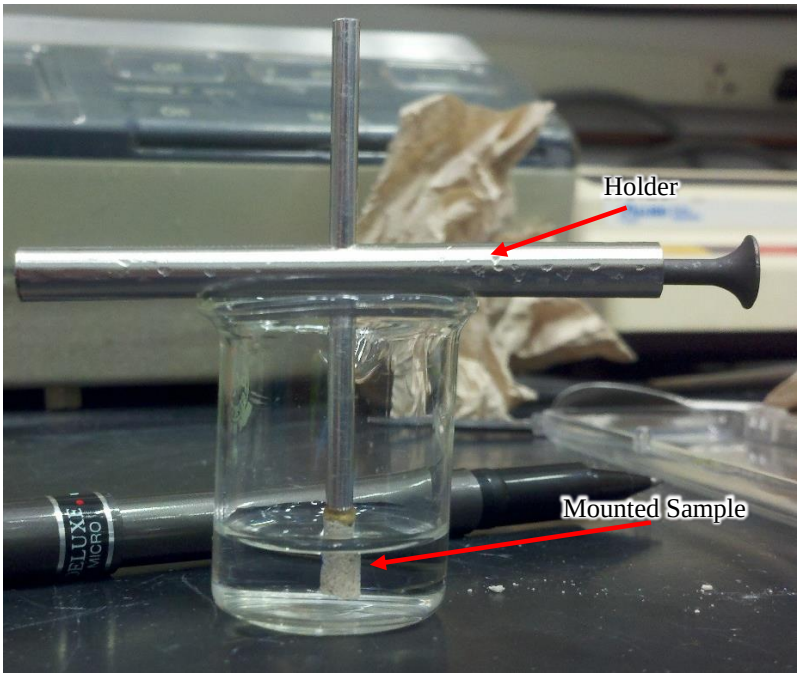

Figure 53. Sample core holder. The sample remains suspended and submerged in deionized water. Beaker approximately 1 inch in diameter.

Figure 54. Static reactor vessel holds pressure and temperature conditions for the experiment (2000 psi at 50°C).

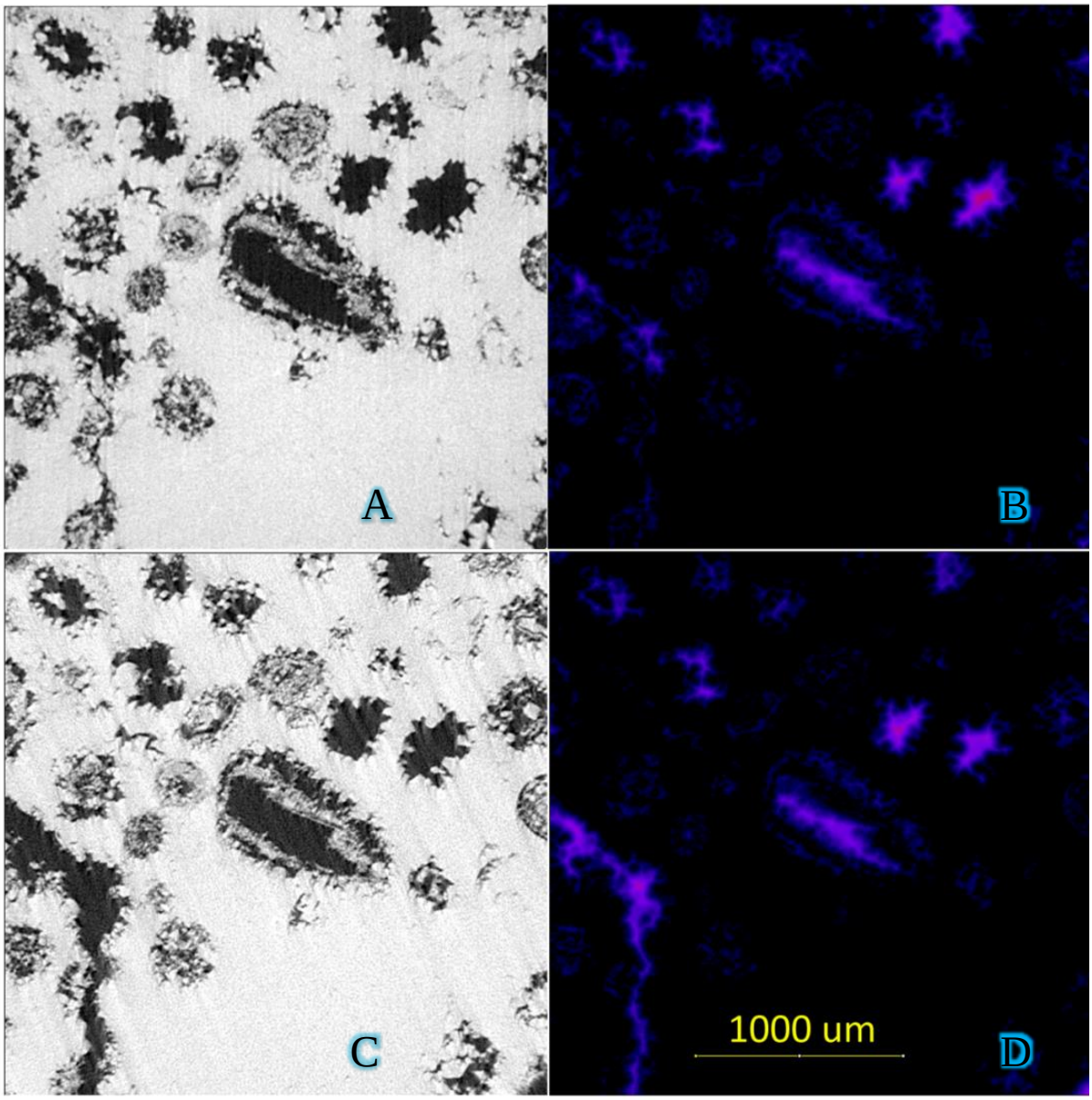

Figure 55. Before and after a 27 hour, 1950 psig at 50°C CO_2 exposure, µCT HP-1 sample slices (A, C) and thickness analysis of the respective slices (B, D). Dissolution along fluid pathways is visible in (C, D) of the sample slices. Thickness maps (B, D) are thresholded to isolate porosity classes (compliant and stiff).

4.2 CHEMICAL REACTIVITY

This study has revealed that a distinction should be made between internal matrix surface area and fracture surface area. The permeability measurements made in the lab are much smaller than reservoir permeability (Table 1) showing that as no non-fractured samples measure in the Darcy range, fluids must primarily move through larger fracture paths in the reservoir.

As an interest to CO_2 injection studies, the effects on limestone permeability of a 959 hour exposure to a CO_2-water mixture at a pressure equal to 1950 psig and a temperature equal to 50°C were studied (Sample HP-L, Table 6). The use of a static reactor vessel in the experimental setup dictates that transportation of H^+ into and mobilized ions out of the internal pore space is diffusion based. Even with diffusion based ion transport, μCT observations suggest that a large internal pathway experienced significant dissolution and pore wall smoothing. The primary dissolution location, however, was on the external sample surfaces. By measuring the volume lost from particularly the outer surfaces, a fracture surface analog is produced. The chemical system of the large core sample reactions is explored, as the μCT samples differencing quantification comes very close to resolution limits. The kinetic approach developed in (Lasaga et al. 1981, Lasaga 1984) works well. For the dissolution of calcite, H^+ ion concentration controls the probability of interaction:

$$\boldsymbol{CaCO_3 + 2H^+ \rightarrow Ca^{2+} + H_2CO_3} \quad \textbf{(58)}$$

$$\boldsymbol{E_a = 35\ kJ/mol\ (5 - 50°C)} \quad \textbf{(59)}$$

The H^+ ions in Equation 58 are produced by the proton dissociation of carbonic acid in the speciation of dissolved CO_2 in water:

$$H_2O + CO_2 \underset{k_{-1}}{\overset{k_1}{\leftrightarrow}} H_2CO_3 \overset{fast}{\leftrightarrow} H^+ + HCO_3^- \quad \textbf{(60)}$$

In sample HP-L, 1.72g of limestone were lost: 0.0172 mol of calcite were assumed dissolved into 467.26 cc of H_2O. As no fluid flow through the core samples exists in the static reactor vessel, ions are left to diffuse into and out of the pore space. Therefore, the dissolution observed in the laboratory experiments is subject to two chemical rates. One rate is on the surface of the core where freed calcium ions escape from the proximity of the core surface into the volume of the solution,

$$\frac{dc_i}{dt}\Big|_{diss} = \frac{A_\theta}{V} k_{i\theta} \quad \textbf{(61)}$$

where dc_i/dt is the change in concentration of calcium ions in the fluid due to dissolution. A_θ is the mineral surface area, V is the volume of solution in contact with the mineral, and $k_{i\theta}$ is the rate constant. However, inside the pore network, fluids are locally buffered and the supply of H^+ is decreased. So, one explanation for the velocity increase in the low effective pressure regime is that stiff calcite crystals have been precipitated in the compliant porosity space. It is possible that dissolution followed by recrystallization is occurred inside of the pore space although no major mass addition was observed in samples HP-1, HP-2, or HP-3. The equation:

$$\frac{dc_i}{dt}\Big|_{diss} = \frac{A_\theta}{\phi} k_{i\theta} \quad \textbf{(62)}$$

describes the internal dissolution rate of the limestone (Lasaga 1984).

To simplify this calculation, the dissolution rate is calculated assuming the reactive surface is only the outside of the cylindrical core. In this approach, the surface of the core has a calcite matrix surface area with the addition of the intersecting surficial pores. The external surface area is equal to the sum of the two circular area top and bottom surfaces plus the surface area of the

cylindrical outer surface. The surface area of the pores exposed on the outside of the core is calculated:

$$A_T = (A_S - A_S\phi) + 1/2\, G_\phi(A_s\phi) \quad (63)$$

where A_T is the total surface area, A_s is the macro surface area, φ is porosity, and G_φ is a surface area/surface area value that translates two dimensional porosity exposure to three dimensional pore wall surface area using SEM imagery. In SEM sample "West," most porosity occurs in the 10000 μm^2 to 100000 μm^2 surface area range. From SEM analysis, it was found that the average pore surface area coverage in this pore range is 1913.2 μm^2. Figure 56 shows the SEM results that compare the perimeter to the area of the pores. Variance from the red curve represents pore wall complexity.

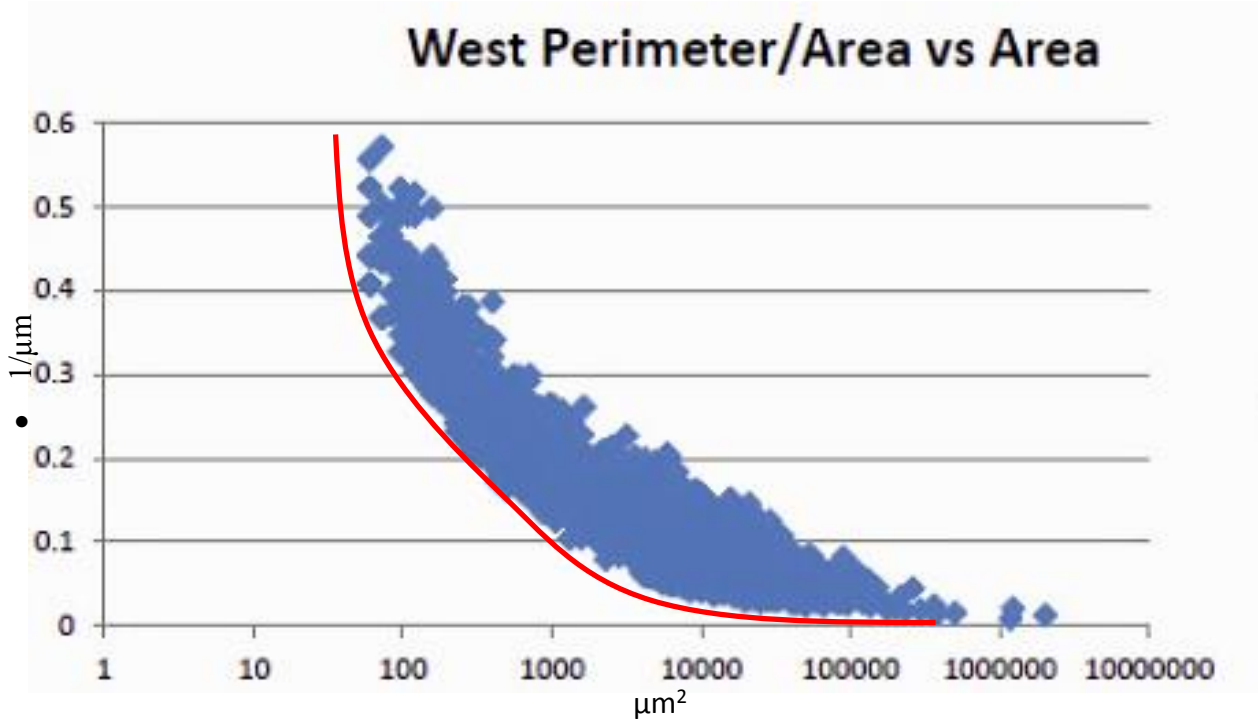

Figure 56. Pore complexity visualization: ratio of pore perimeter and area (1/μm) versus area (μm^2) (values for a circle (minima) are represented by the red arc along the field of points). Any movement above the red line represents irregular pore surfaces.

The average ratio of area to perimeter is 15.2 in the 10000 μm^2 to 100000 μm^2 surface area range. A sphere of that cross sectional surface through its hemisphere has an area-to-perimeter ratio of 39.6. The quotient of the two ratios gives us a multiplier to correct the spherical surface area to pore surface area value. If an estimate is made that the average pore has a cross sectional area of 1913.2 μm^2, then the area of that spherical pore is 78852.6 μm^2. The pore complexity multiplier is 39.6/15.2 = 2.6. Therefore, I will assume that the average pore has 204944.3 μm^2 of total surface area. This gives us the value:

$$G_{\phi} = \frac{204944.3\ \mu m^2}{1913.2 \mu m^2} = \mathbf{107.1} \qquad \textbf{(64)}$$

For sample HP-L, the total surface area is $1.5*10^2 cm^2$. Before the correction, the outer surface area of the cylinder is $1.5*10^1 cm^2$. If dissolution primarily occurred on the outside surface of the sample, Equation 61 can be rearranged to solve for the rate of calcite release, $k_{i\theta}$:

$$k_{i\theta} = \frac{dc_i}{dt}|_{diss} \frac{V_{H_2O}}{A_{\theta}} \qquad \textbf{(65)}$$

$k_{i\theta}$ = (0.0172 mol/L/$3.45*10^6$s)*($467.26*10^{-6} m^3$H2O/$1.51*10^{-2}$ m^2)= $5.6*10^{-9}$mol/m^2/hr

=$1.54*10^{-10}$mol/m^2/s

This value is particular to a sample surface that is exposed. Using this rate, the chemical system is further explored to understand how rapidly species are produced. To determine the concentrations of the species, I start by calculating the amount of dissolved CO_2

$$m_{CO_2} = k_H P_{CO_2} = \mathbf{10^{-1.5}} P_{CO_2} \qquad \textbf{(66)}$$

m_{CO2} is the molality of CO_2 in the solution and P_{CO2} is pressure in Pascals. To calculate Henry's constant at 50° C using the van't Hoff equation:

$$k_{H(T)} = k_H(T^{\theta}) e^{\left[-C\left(\frac{1}{T}-\frac{1}{T^{\theta}}\right)\right]} \qquad \textbf{(67)}$$

We find k_H=1.78*10^{-1} mol/(L*MPa) when P_{CO2}=13.79 MPa. The amount of CO_2 dissolved in solution is: m_{CO2}=2.48*10^3 mol/m^3

Experimental rates for production of H_2CO_3 from CO_2 pressure 298K are:

$$\boldsymbol{k_1 = 4.37 * 10^{-2} s^{-1}} \quad \textbf{(68)}$$

$$\boldsymbol{k_{-1} = 19.2 s^{-1}} \quad \textbf{(69)}$$

$$\boldsymbol{m_{H_2CO_3} = 0.0023 m_{CO_2(aq)}} \quad \textbf{(70)}$$

(Van Eldik et al. 1982)

The rate of H^+ generation is then determined by:

$$\boldsymbol{\frac{dm_{H_2CO_3}}{dt} = k_1 m_{CO_2} = (4.37 * 10^{-2} s^{-1}) \cdot (2.48 * 10^3\ mol/m^3) = 10.84\, mol/m^3/s} \quad \textbf{(71)}$$

This suggests that CO_2 injected into the reactor vessel continuously provides the solution with carbonic acid, so that no reaction rates are limited by the amount of CO_2 in solution. The rate of H^+ demand from calcite dissolution is computed from

$$\boldsymbol{rate_H = \upsilon_{H^+} \frac{A}{V} k_{i\theta}} \quad \textbf{(72)}$$

υ is the stoichiometric number of H^+ needed to dissolve calcite (2 mol H^+ per 1 mol $CaCO_3$), A/V is the surface area (A) of the mineral per volume (V) of solution and $k_{i\theta}$ is the rate of mineral dissolution found in Equation 65. I find that demand of H^+ is equal to 9.91*10^{-9} mol/m^3/s which is far less than that of the production of H^+ calculated in Equation 71. Because no water chemistry measurements were made over the period of exposure, equilibrium status is not known. It is possible that dissolution occurs much faster under these conditions and a steady, buffered, dissolution-precipitation state is reached quickly; the dissolution rate could be masked by the long time interval over which the dissolution rate is calculated. We do know, however, that the production of H^+ is not limiting.

4.2.1 Discussion of Chemical Reactivity Results

Geochemical modeling can determine the effect of CO_2 injection on both the limestone internal matrix porosity and permeability as well as the large scale reservoir permeability. As none of the core exposure experiments resulted in more than a 1% mass loss, it may be that the irregularity of the initial rock sample (irregularly fractured) caused accelerated dissolution due to its uncut, unpolished surface. However, the exposure experiments performed on the HP-L core determined that with a very slight mass loss from exposure, there were notable permeability changes. Figure 57 shows a three channel registration in which slices of the same subject before and after CO_2 exposure occupy different color channels and the mixture of color reveals where the mineral matrix has changed. In the μCT composite, a fluid pathway that was susceptible to dissolution is shown in red. The sample experienced external dissolution, but along the internal pathway, experienced almost equal dissolution. Comparison of before and after uCT volumes showed for HP-1 show that the unconnected pore space displayed minimal dissolution. Assuming that pore-throat blocking particles expose significant surface area to the reactive pore fluids and will therefore be selectively dissolved or removed from pore throats, an increase in permeability is an expected consequence. It should be noted that in cases where reactive fluids are forced through permeable networks at high pressures, freed particles can be mobilized and block pore throats, decreasing permeability. The distinction between forced flow reactivity and static reactivity is important. Forced flow reactivity is most likely to occur at the injection site. Therefore these experiments are applicable to the regions in the reservoir away from the injection point where injection from fluid flow is slow and ion transport is more diffusive.

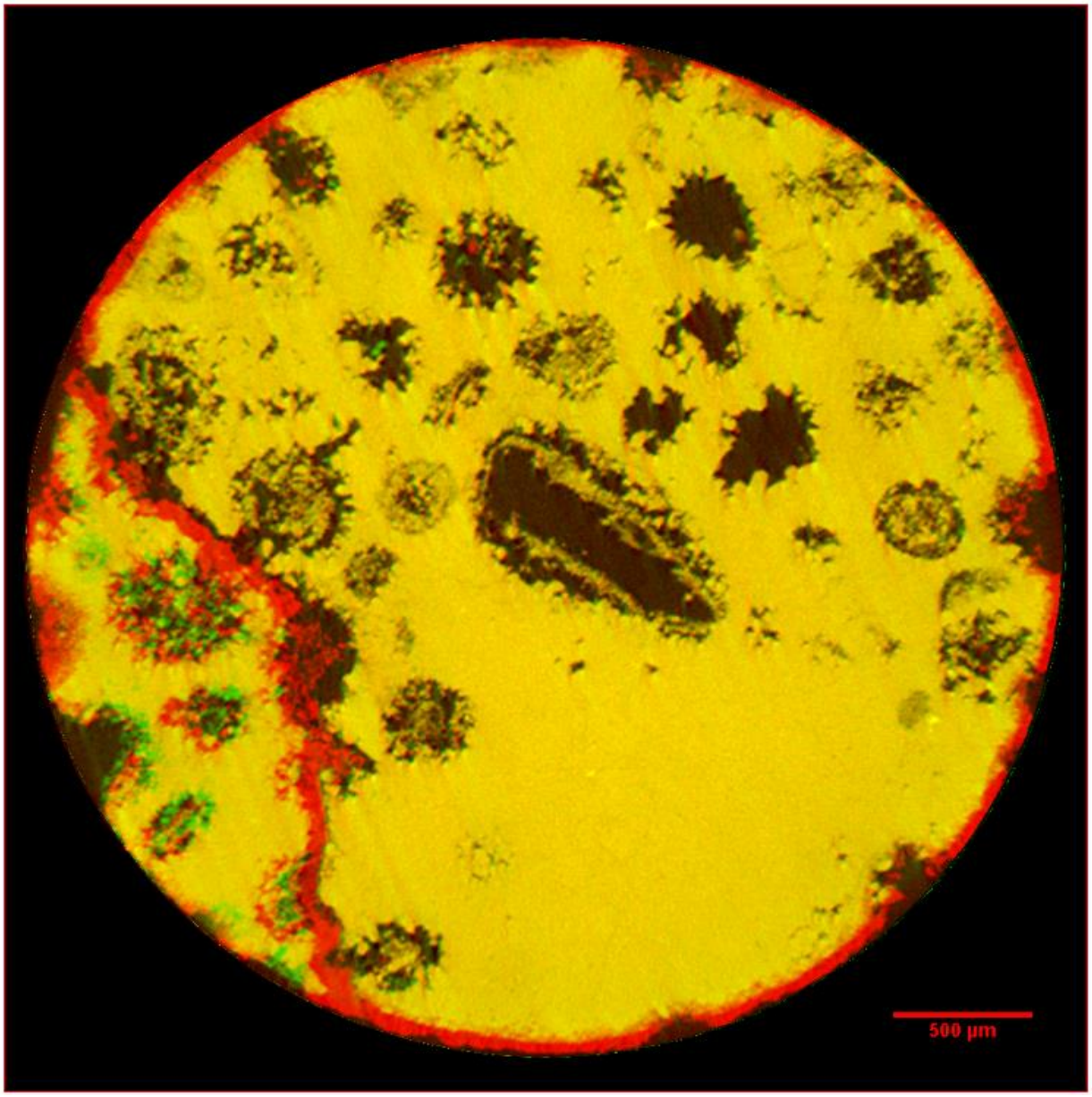

Figure 57. Three-channel, before and after a 27 hour, 1950 psig CO_2-Water exposure at 50°. The original slice occupies the red channel and the exposed sample occupies the green channel. In this µCT sample slice composite, yellow indicates no change from exposure and red indicates dissolution of limestone. Some green can be seen from the post exposure slice as there was a slight translation of material.

4.3 RESERVOIR PERMEABILITY CHANGE

Permeability measurements were performed, using an Ultra-Perm 500 device, before and after a 45-day exposure to a CO_2 water mixture. These experiments were performed by varying the differential pressure of the limestone core ends and measuring the flow rate of nitrogen through the core. Permeability was determined by using the measured physical parameters of diameter and length along with Darcy's Law (Darcy 1856):

$$\boldsymbol{k = \frac{-Q\mu L}{\Delta P A}} \qquad \textbf{(73)}$$

where L is the length of the sample, A is the cross sectional area, Q is the flow rate, ΔP is the differential pressure, and μ is the viscosity. The measurements were taken at varying confining pressures and flow rates (corrected with bubble flow meter). Figure 58 shows permeability before and after CO_2 exposure for sample HP-L. Pale colors are the equivalent effective pressures post CO_2 exposure. The x-axis describes the flow rate induced by the differential pressure.

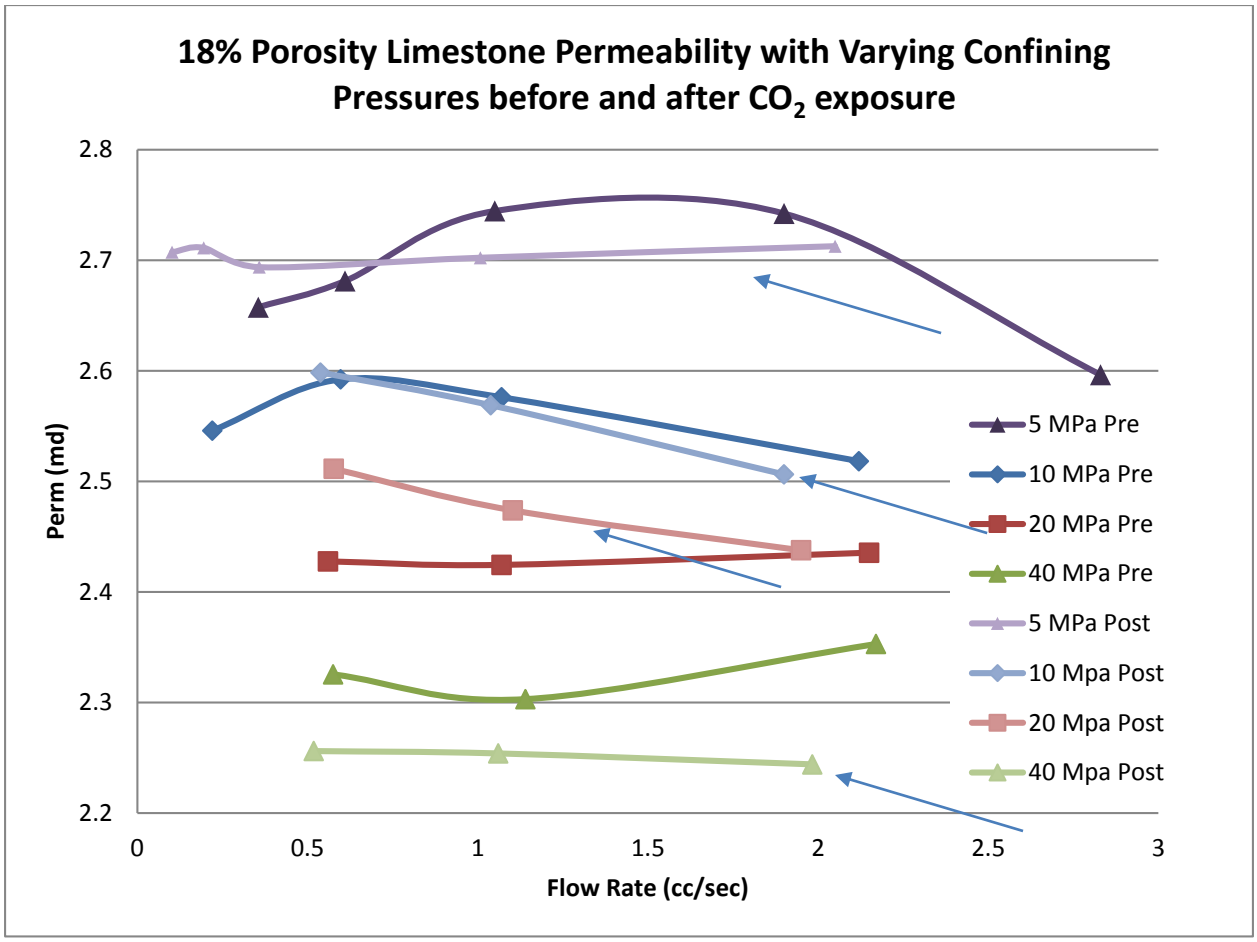

Figure 58. Permeability (y axis) measurements at increasing effective pressure (color) and flow rate (x axis). Pale colors are the equivalent effective pressures post CO_2 exposure (indicated by arrows). A trend of decreasing permeability with dissolution is observed at increasing effective pressures. Permeability tends to decrease with increased flow rate.

4.3.1 Results of CO_2 Exposure

The change in permeability of limestone sample HP-L in response to different effective pressures and induced flow rate was measured. The sample was exposed to a CO_2 - H_2O mixture for 959 hours (40 days) and then re-measured. Figure 59 and Figure 60 show the results of these experiments on a 3 dimensional plot with a simple linear interpolation used to fit a plane to the

points; Figure 61 shows the surface interpolation of four best-fit polynomial lines of permeability versus flow rate, constant pressure permeability curves for the pre-exposure experimental measurements for sample HP-L.

It was expected that with CO_2 exposure and subsequent mineral framework dissolution, permeability would increase as pores and pathways were enlarged and connected to flow. However, increased permeability was only observed at low confining pressure (~5 MPa) and low flow rate (< 0.5 cc/sec). Sample HP-L trends toward permeability *loss* with increased confining pressure in fact, for this sample, post exposure. As velocity measurements (2.2) suggest that compliant porosity has become more sensitive to stress in the lower effective pressure ranges, the permeability loss could be explained by gains in the compliant porosity regime, associated with rock framework. Stiff rock material that had been holding fluid pathways open was dissolved, so with pore pressure decrease (effective pressure increase) compliant pores are no longer held open and fluid pathways are lost.

The velocity model developed in section 2.2.2 can use these dynamic permeability and effective pressures to determine velocity at seismic to ultrasonic frequencies throughout the reservoir, further defining relationships between pore pressure, attenuation, exposure time, and injection rate that can be used to create reservoir property predictions through reflection seismic data inversions.

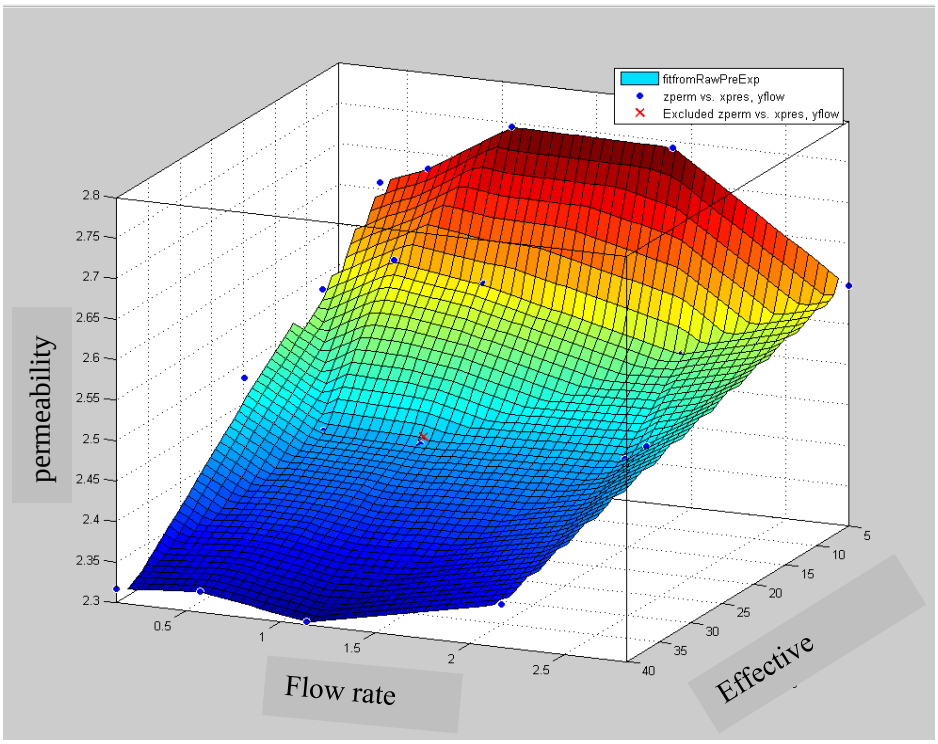

Figure 59. Sample HP-L, Pre-CO_2 exposure permeability, flow rate, effective pressure surface.

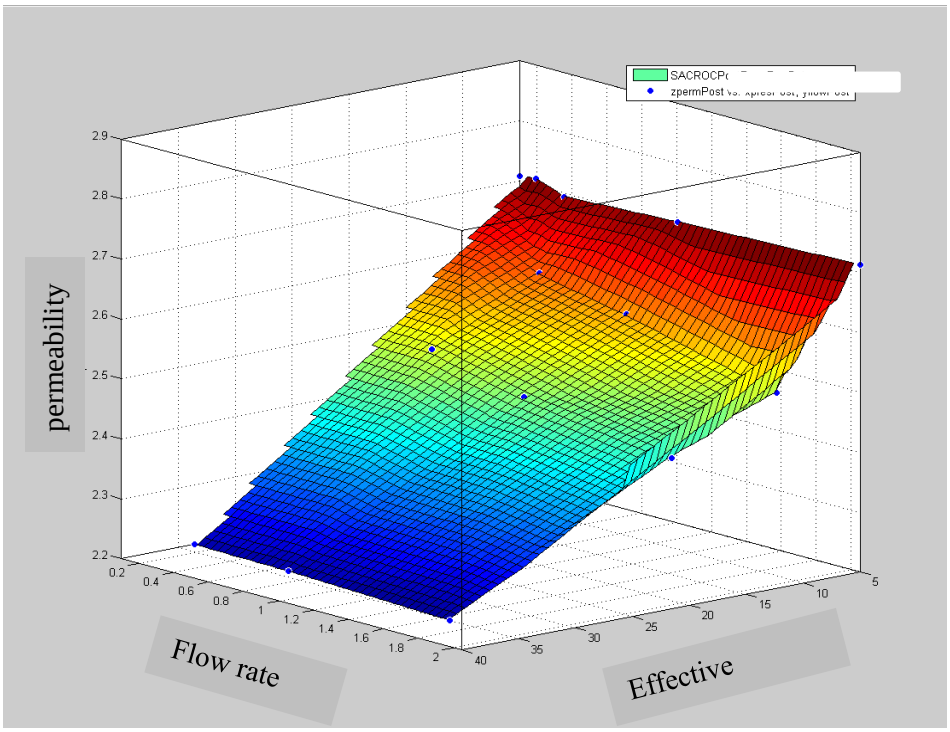

Figure 60. Sample HP-L, Post-CO_2 exposure permeability, flow rate, effective pressure surface.

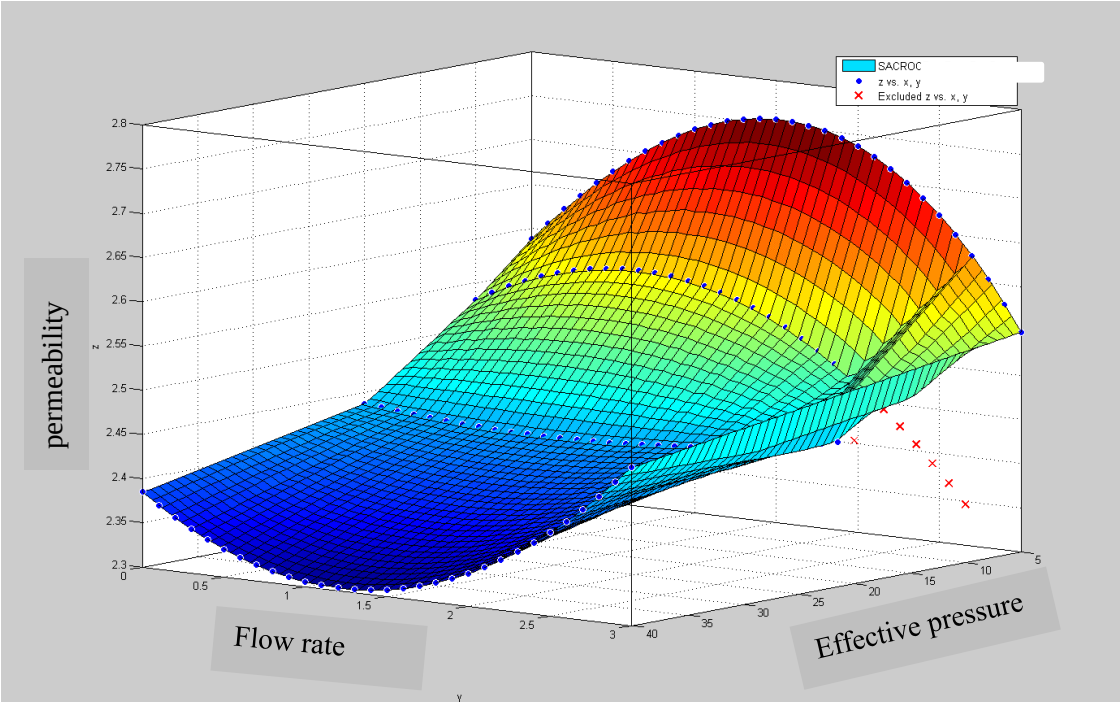

Figure 61. Sample HP-L, Pre-CO_2 exposure permeability, flow rate, effective pressure. interpolation done on polynomial fit lines made from runs varying only flow rate.

4.3.2 Discussion of Permeability Data

By measuring reservoir permeability as well as matrix permeability, fracture diameter can be approximated. (Chilingarian et al. 1992) cites (Huitt 1956, Parsons 1966) methods for determining permeability values in a horizontal direction through an idealized fracture-matrix system with:

$$k_H = k_m + 8.44 \times 10^7 w^3 \cos^2 \frac{\alpha}{L} \qquad (74)$$

where k_m is the matrix permeability (mD), w is the fracture width (mm), L is the distance between fractures (mm), and α is the angle of deviation of the fracture from the horizontal plane in degrees.

If fracture orientation and spacing can be predicted, through seismic attribute analysis for instance, the fracture width can be better constrained:

$$w = \sqrt[3]{\frac{k_h - k_m}{8.44\times10^7 \times \cos^2\frac{\alpha}{L}}} \quad (75)$$

By assuming that the orientation of the fractures are aligned with the horizontal plane (α=0, thus $\cos^2(0)=1$), the equation can be solved for fracture width of the reservoir permeability as the matrix permeability is known:.

$$w = \sqrt[3]{\frac{k_h - k_m}{8.44\times10^7}} \quad (76)$$

Using the laboratory measured permeability along with the injection-production measured permeability, we can determine a range of fracture width distributions (31 μm using observed fracture and matrix values from Table 1) and thus calculate an average volumetric surface area which can be interpreted as the reactive surface area per volume (m^2/m^3). This value is used as the input for the chemical reactivity calculations along with the observed sample surface dissolution for property perturbation throughout the reservoir model where these characteristics.

4.4 CONCLUSIONS

That permeability itself is a scalable value adds further complexity to the velocity-permeability relationship. The laboratory measurements of the low and high porosity limestone are between 2 and 4 millidarcies (mD) in general. However, measurements of the reservoir permeability range from tens of millidarcies in cracks and up to 2,500 mD in fractures. Methods have been developed to use the discrepancy of discreet sample matrix permeability and large scale reservoir permeability to determine fracture width, spacing, and orientation (Chilingarian et al. 1992). This topic is discussed in conjunction with the chemical reactivity of fracture faces (see 4.2).

For sequestration and EOR applications in limestones, CO_2 injection pressure must be maintained in order to keep pore pressure levels high enough to prop open compliant cracks. Over time, dissolvable reservoir space will be more easily closed off with the loss or dissipation of pore pressure, decreasing "available" porosity for storage of CO_2. Permeability could be regained over time as pore pressure slowly increases, but caution must be taken to not block pore throats with freed rock material as observed by with "near borehole" type rates of injection (Izgec et al. 2008).

The simplification of pore wall complexity effects both chemical reactivity and rock compressibility. As reactive surface area decreases, H^+ ions are less likely to interact with mineral surface calcite molecules, so decreasing surface area contributes to slow rates of dissolution. As vugs tend to get larger with dissolution, smaller porosity is converted into larger porosity. Stress will be distributed to remaining grain contacts. Due to time limitations, the experiments performed did not focus on mineralization rates, which will also contribute to pore space texture and mechanical properties over hundreds of years. Mineralization is the ultimate end goal of sequestration scenarios after thousands of years.

Thickness analysis (Figure 57) show that the lower 15% of porosity size distribution accounts for 4-6% of total rock porosity in the 18.5% porosity limestone samples and 3% total rock porosity in the 6.4% limestone samples. As the smallest pore diameter bins on all samples account for, at minimum 1% of total porosity in a given sample; the compliant porosity is either smaller than the resolutions at which these CT scans were taken, or the model is over-sensitive to compliancy. In this case, the smallest porosity bin observed was about 1% whereas compliant porosity values needed for model accuracy range in the hundredths of a percent (0.025-0.075% range in this case). Figure 22 shows the sensitivity of compliant porosity perturbations (+/- 0.5%).

Problems with the petrophysical model sensitivity could be attributed to the use of penny-crack shaped pore geometry as the implied shape of compliant pores or the sphere shaped pores as the implied shape of stiff pores. Further, aspect ratio has a very large effect on the calculations. In the 20X magnification limestone samples for both porosities, calcite crystals are visible, but finding a unique or even statistically significant "aspect ratio" of the exo-crystal space poses a challenge. As compliant porosity is the volume of porosity with a certain range of aspect ratios, the model is simplifying a distribution into a single value. When the pressure dependent rock model developed in chapter 2.0 is recalibrated to fit repeat velocity measurements, the changed parameters are tied to changes observed in digital rock analysis. Figure 62 highlights, in blue, the change in P-wave velocity in the low effective pressure range caused by dissolution. As compliant porosity adjustments to the rock model are very small and the subtle changes observed in thickness analysis occur in the lower resolution limits of the μCT scans, caution still must be taken in producing velocities directly from digital rocks. So, although the rock model is a good predictor of velocities and is used to implement theoretical dissolution scenarios to reservoir scale 4-D carbon sequestration models, digital analysis still requires laboratory calibration on a rock by rock basis.

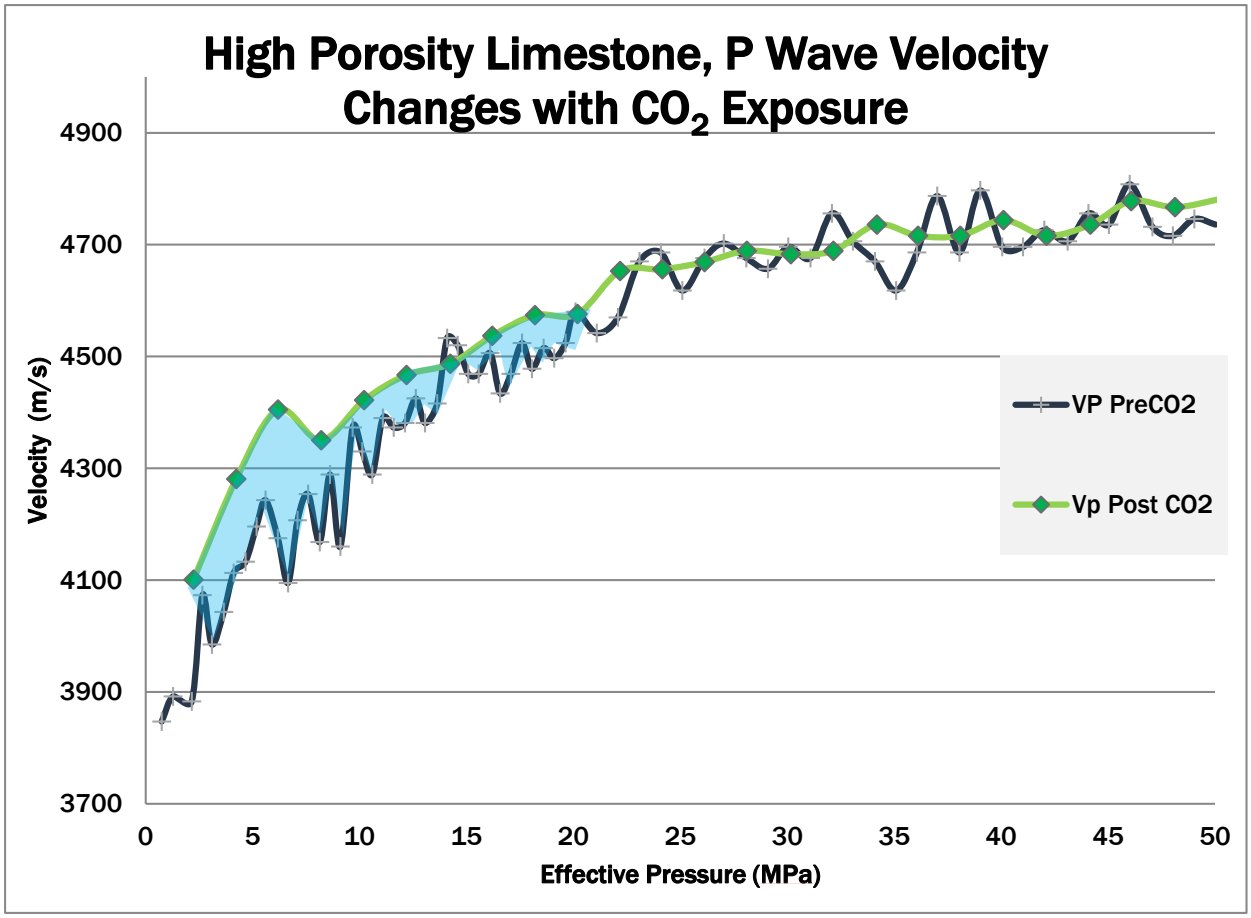

Figure 62. P-wave velocity with respect to effective pressure for the 18% porosity limestone sample before and after CO_2 exposure. Up to 10% change in velocity in the low (0~20) effective pressure ranges.

5.0 SEISMIC RESPONSE OF LONG-TERM CO_2 SEQUESTRATION

When an incident traveling wave meets the interface between two units with differing acoustic impedances, part of the wave energy is reflected and the remaining energy is refracted. Note that acoustic impedance, Z, is defined as the product of the rock density (ρ) and velocity (V):

$$\boldsymbol{Z = \rho V} \qquad \textbf{(77)}$$

Often times when working with well logs, a synthetic seismic trace is made from available data. Reflection coefficients (R) are produced along the well by repeating the following method incrementally down through the well:

$$\boldsymbol{R = \frac{Z_2 - Z_1}{Z_2 + Z_1}} \qquad \textbf{(78)}$$

This reflection coefficient is for a normally incident wave. At different offset angles of incidence, Snell's law is used to determine reflection angles:

$$\boldsymbol{\frac{sin\theta_1}{V_{P1}} = \frac{sin\theta_2}{V_{P2}} = \frac{sin\phi_1}{V_{S1}} = \frac{sin\phi_2}{V_{S2}}} \qquad \textbf{(79)}$$

Figure 63 shows a simple visualization of Snell's law as well as P-wave to S-wave conversion and defines θ_1, θ_2 , ϕ_1, ϕ_2, V_{P1}, V_{P2}, V_{S1}, V_{S2} used in Equation 79. The change in wave propagation angle ($\phi_2 < \theta_1$) of the produced S-wave is due to $V_{S2} < V_{P1}$. This theory is used to combine the multitude of traces acquired in a 3-D seismic reflection survey.

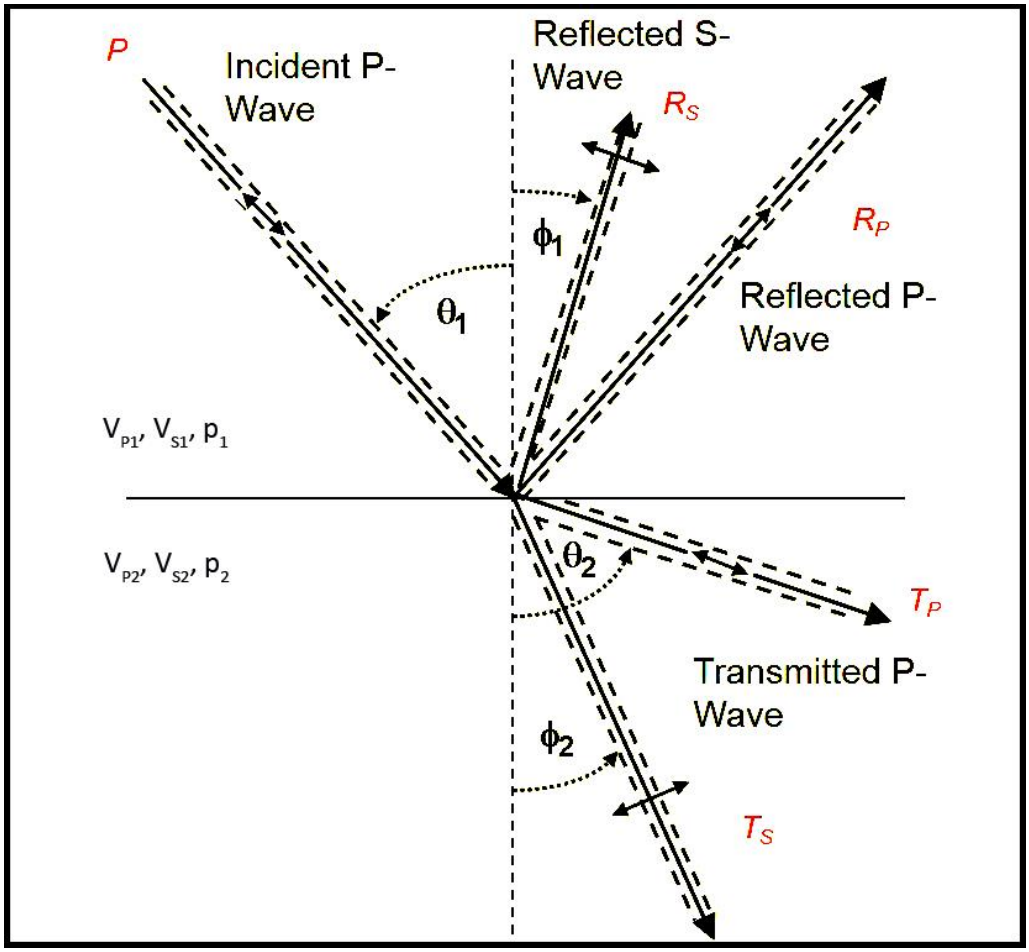

Figure 63. Reflection transmission system in layered media. The material layer numbered from top (1) to bottom (2) is used in the subscripts of V_P (P-wave velocity), V_S (S-wave velocity), and ρ (material density).

To interpret seismic reflections, common reflection point data is gathered from midpoint (CMP) data (Figure 64). The common midpoint gather combines multiple source and receiver paths that share a common midpoint. To get a clear image of the subsurface, trace records of small seismic signals are summed over many times. To find a common space to sum these signals, the distance they travel is corrected to that of the least distance. This vertical incidence (straight down/up path) is known as the incident angle. With increasing offset, the incidence angle (θ_i) increases result in a longer travel distance overall. The relationship between incidence angle and

elastic wave travel time is referred to as normal move-out (NMO). Once NMO has been corrected (Figure 65), the reflections are enhanced by the signal to noise ratio increase.

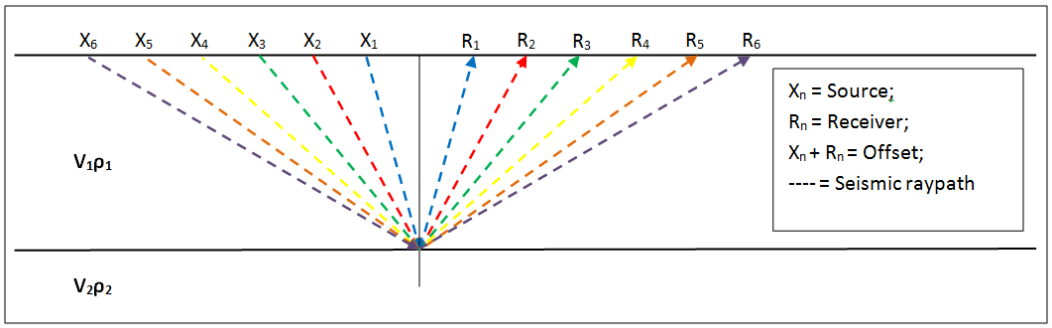

Figure 64 Common Midpoint (CMP) on a flat-lying reflector. Source-receiver pairs, X_nR_n, with increasing offset, n, are shown. Common reflection point data is gathered to enhance reflection signal **(**Wikipedia_Commons**)**.

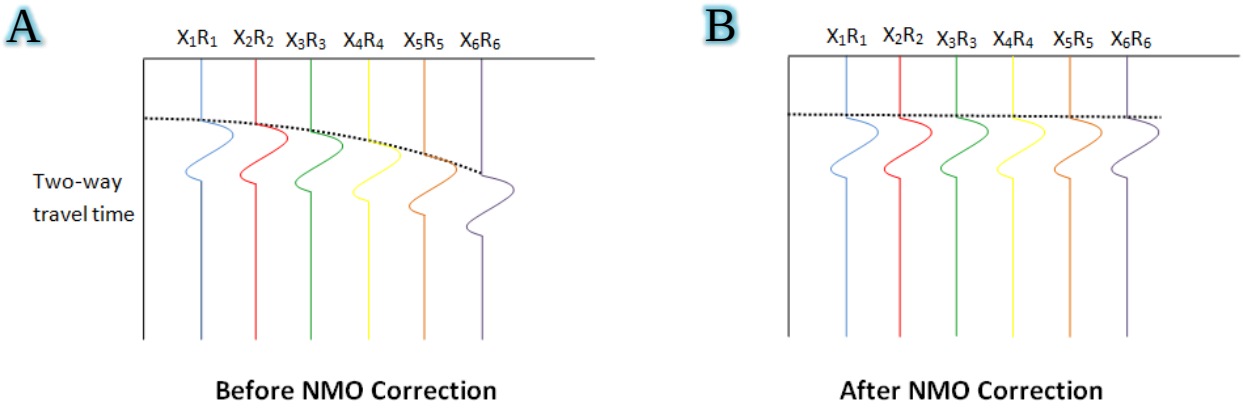

Figure 65. Normal moveout (NMO) correction of Figure 65 allows reflections from a common reflection point to be positioned at common two-way travel times. The sinusoidal reflection signal is seen at increasingly later two-way travel time arrivals X_nR_n with increasing n in (A). After NMO correction (B), the reflection occurs at the same two-way travel time at all offsets **(**Wikipedia_Commons**)**.

After velocity analysis, NMO correction, deconvolution (rigorous noise removal technique), and stacking, cross sections are made from the reflection volumes and are interpreted for stratigraphy and structure as can be seen in Figure 66.

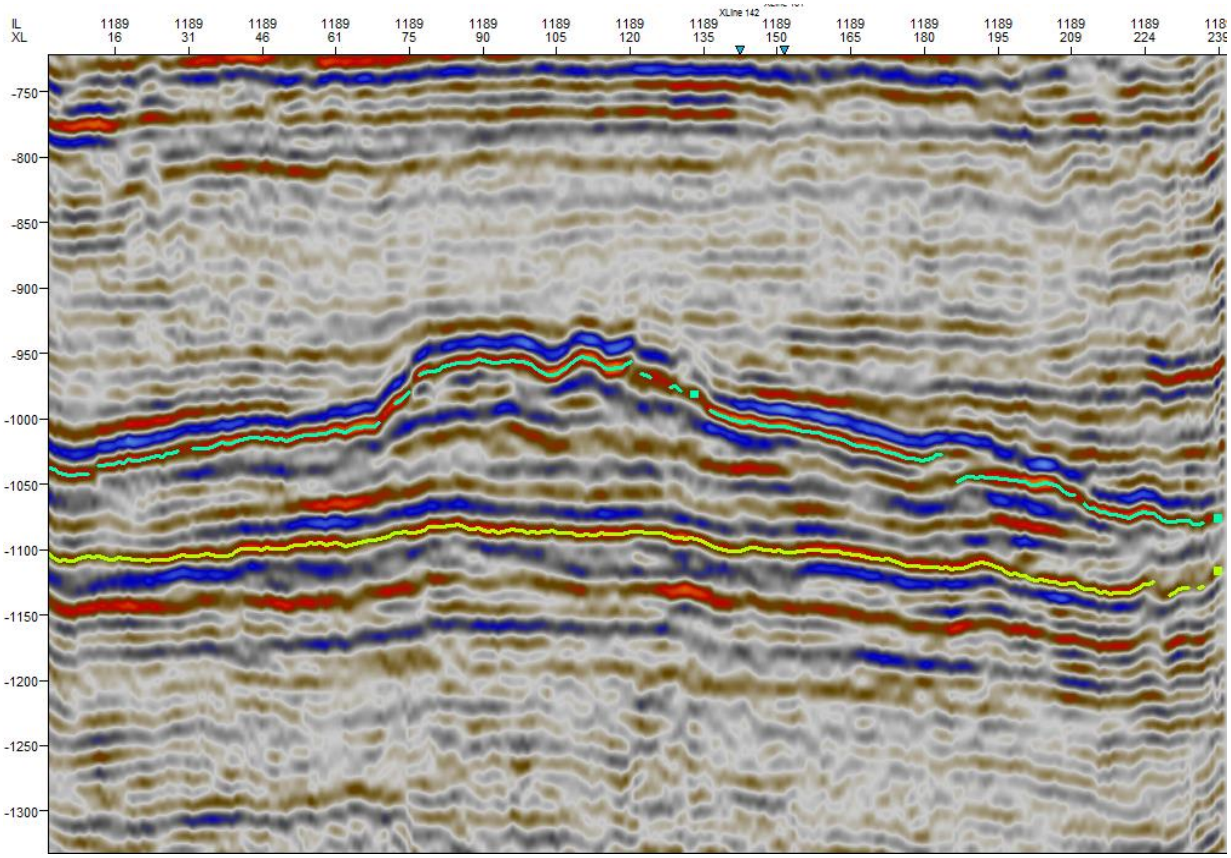

Figure 66. Cross section of the interpreted carbonate reef post-stack reflection seismic data. Vertical axis is time, horizontal axis is ground position, colors are US positive (red) and negative (blue) amplitudes. The reef topography is highlighted with the green line.

Although stacked data is primarily used for structural interpretation, pre-stack data still exist and are used for wave analysis purposes. Further, subsets of the prestack data can be stacked and interpreted (e.g. in the sandstone analysis, "Far-Offset" stacks are produced from 30°-38° offsets, "Mid-Far-Offset" stacks are produced from 24°-32° offsets, "Mid-Offset" stacks are produced from 17°-26° offsets, "Near-Mid-Offset" stacks are produced from 9°-19° offsets, "Near-Offset" stacks are produced from 1°-12° offsets).

5.1 WAVE AMPLITUDE VERSUS OFFSET FITTING PARAMETERS

The presence of a reflection interpreted for geologic structures, but the recorded reflections have signature amplitudes reveal a good deal about the rock properties. Large numbers of source and receiver combinations sharing a common midpoint not only increase signal to noise ratio, but also allow the reflection to be characterized at a number of different incident angles. Amplitude variation with offset (AVO) theory allows the reflection to then be categorized based on previous observations and theoretical models. Karl Zoeppritz described the partitioning of seismic energy at an interface (Zoeppritz 1919). A number of modifications have been made to the original Zoeppritz equations. To demonstrate wave amplitude behavior at a given incidence angle, the arrangement utilized in the Rock Physics Handbook is implemented (Zoeppritz 1919, Aki et al. 1980, Hilterman 1983, Mavko et al. 1998):

$$\begin{pmatrix} \downarrow\uparrow & \downarrow\uparrow & \uparrow\uparrow & \uparrow\uparrow \\ \boldsymbol{PP} & \boldsymbol{SP} & \boldsymbol{PP} & \boldsymbol{SP} \\ \downarrow\uparrow & \downarrow\uparrow & \uparrow\uparrow & \uparrow\uparrow \\ \boldsymbol{PS} & \boldsymbol{SS} & \boldsymbol{PS} & \boldsymbol{SS} \\ \downarrow\downarrow & \downarrow\downarrow & \uparrow\downarrow & \uparrow\downarrow \\ \boldsymbol{PP} & \boldsymbol{SP} & \boldsymbol{PP} & \boldsymbol{SP} \\ \downarrow\downarrow & \downarrow\downarrow & \uparrow\downarrow & \uparrow\downarrow \\ \boldsymbol{PS} & \boldsymbol{SS} & \boldsymbol{PS} & \boldsymbol{SS} \end{pmatrix} = \boldsymbol{M^{-1}N} \qquad \textbf{(80)}$$

in which the letter P or S is the type of wave, incidence or reflected (read left to right), and the direction of wave travel from the interface are shown for each incident and reflected wave phase pair combination. The material layer numbered from top (1) to bottom (2) is used in the subscripts of V_P (P-wave velocity), V_S (S-wave velocity), ρ (material density), θ (P-wave angle to incidence), and ϕ (S-wave angle to incidence) as in Figure 63. M and N are defined as:

$$M = \begin{bmatrix} -sin\,\theta_1 & -cos\phi_1 & sin\theta_2 & cos\phi_2 \\ cos\,\theta_1 & -sin\phi_1 & cos\theta_2 & -sin\phi_2 \\ 2\rho_1 V_{S1} sin\phi_1 cos\theta_1 & -\rho_1 V_{S1}(1-2\sin^2\phi_1) & -\rho_2 V_{S2} sin\phi_2 \cos\theta_2 & -\rho_1 V_{S2}(1-2\sin^2\phi_2) \\ -\rho_1 V_{P1}(1-2\sin^2\phi_1) & \rho_1 V_{S1}(1-2\sin^2\phi_1) & -\rho_2 V_{P2}\sin^2\phi_2 & -\rho_2 V_{S2} sin2\phi_2 \end{bmatrix}$$

$$N = \begin{bmatrix} \sin\theta_1 & \cos\phi_1 & -\sin\theta_2 & -\cos\phi_2 \\ \cos\theta_1 & -\sin\phi_1 & \cos\theta_2 & -\sin\phi_2 \\ 2\rho_1 V_{S1} \sin\phi_1 \cos\theta_1 & -\rho_1 V_{S1}(1-2\sin^2\phi_1) & -\rho_2 V_{S2} \sin\phi_2 \cos\theta_2 & -\rho_1 V_{S2}(1-2\sin^2\phi_2) \\ -\rho_1 V_{P1}(1-2\sin^2\phi_1) & \rho_1 V_{S1}(1-2\sin^2\phi_1) & -\rho_2 V_{P2}\sin^2\phi_2 & -\rho_2 V_{S2}\sin 2\phi_2 \end{bmatrix}$$

(81)

and are used to model the wave amplitude at a specified wave angle and direction (i.e. Equation 79: the reflected P-wave from an incoming P-wave is at position (1,1) in the matrix). This allows the amplitudes of the wave paths in Figure 63 to be determined at varying incidence angles. The Zoeppritz Explorer (Margrave et al. 2001) is a free online application that produces graphs of a specified wave's magnitude from 0° to 90° of incidence. Figure 67 demonstrates the behavior of the reflected and transmitted waves of an incident P-wave at an interface of a relatively more dense and fast rock on top of a relatively less dense and slower rock ($\rho_1 > \rho_2$, $V_{P1} > V_{P2}$, and $V_{S1} > V_{S2}$).

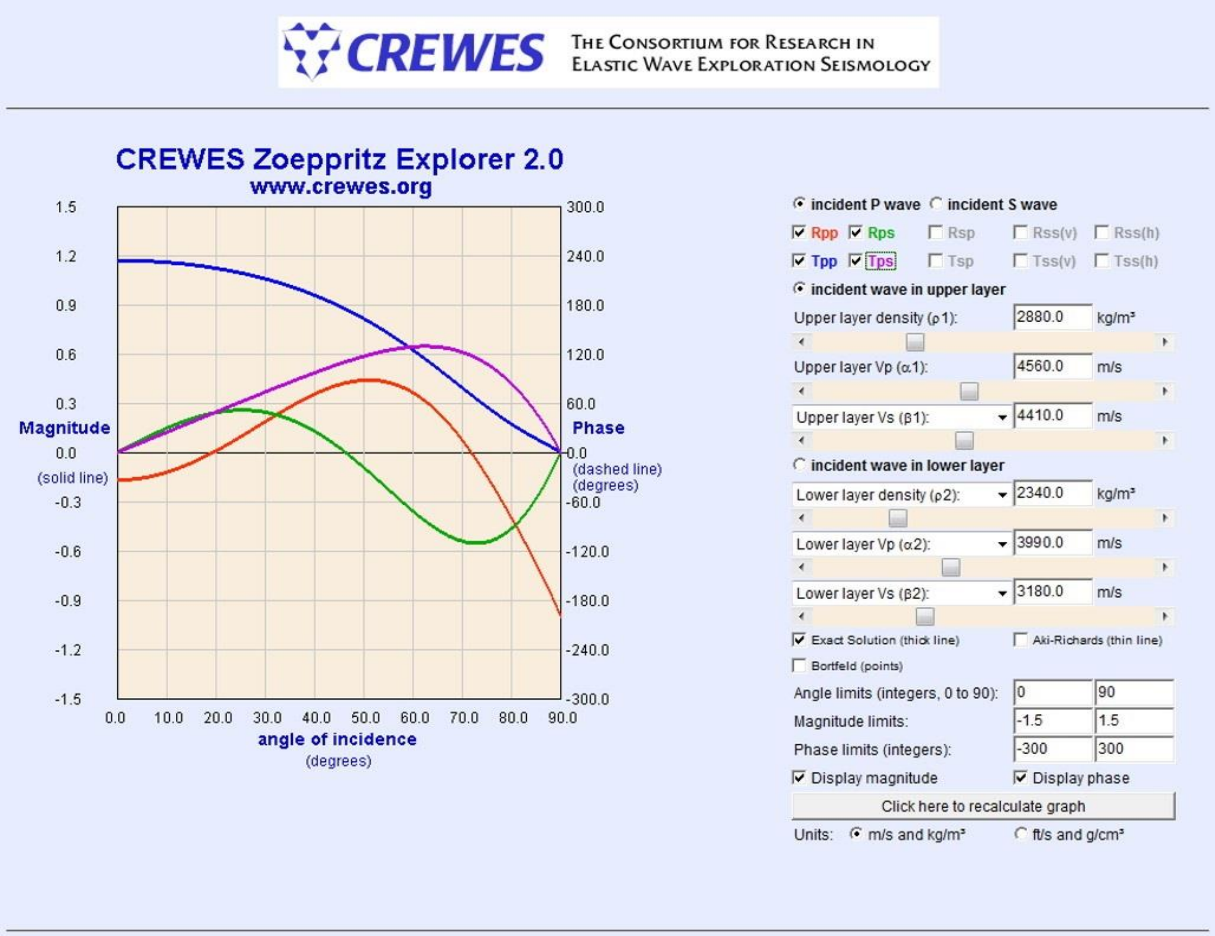

Figure 67. Example of incident P-wave P-P and P-S converted reflection and transmission magnitudes at increasing offset with the Zoeppritz Explorer (Margrave et al. 2001), (http://www.crewes.org/ResearchLinks/ ExplorerPrograms /ZE/ZEcrewes.html). Red is reflected P-wave from incident P-wave, blue is transmitted P-wave from incident p-wave, green is reflected S-wave from incident P-wave, purple is transmitted S-wave from incident P-wave. The interface impedance contrast is defined by the upper and lower layer rock density, P-wave velocity, and S-wave velocity.

Note that the reflected $PP_{reflected}$ wave (shown in red) has a negative magnitude (or amplitude) at a zero degree angle of incidence and becomes positive as the angle of incidence increases until at about 70° where it becomes negative again. Mathematical fluid substitutions to the reservoir rock are made and the differing wave responses were evaluated (Purcell 2012). Figure 68 shows that the presence of CO_2 caused the reflection to move to the negative amplitude range at zero incidence. With repeat, multi-fold seismic surveying, common mid-point stacks (CMP), can be compared before and after fluid injection to determine fluid density signatures. The changes in amplitude with variation in offset signatures (AVO) can be an indicator of pore filling fluid changes. Three methods were implemented to model reflected wave amplitudes at increasing offset angle in these reservoir studies, Shuey two-term, Shuey three-term, and Aki-Richards methods.

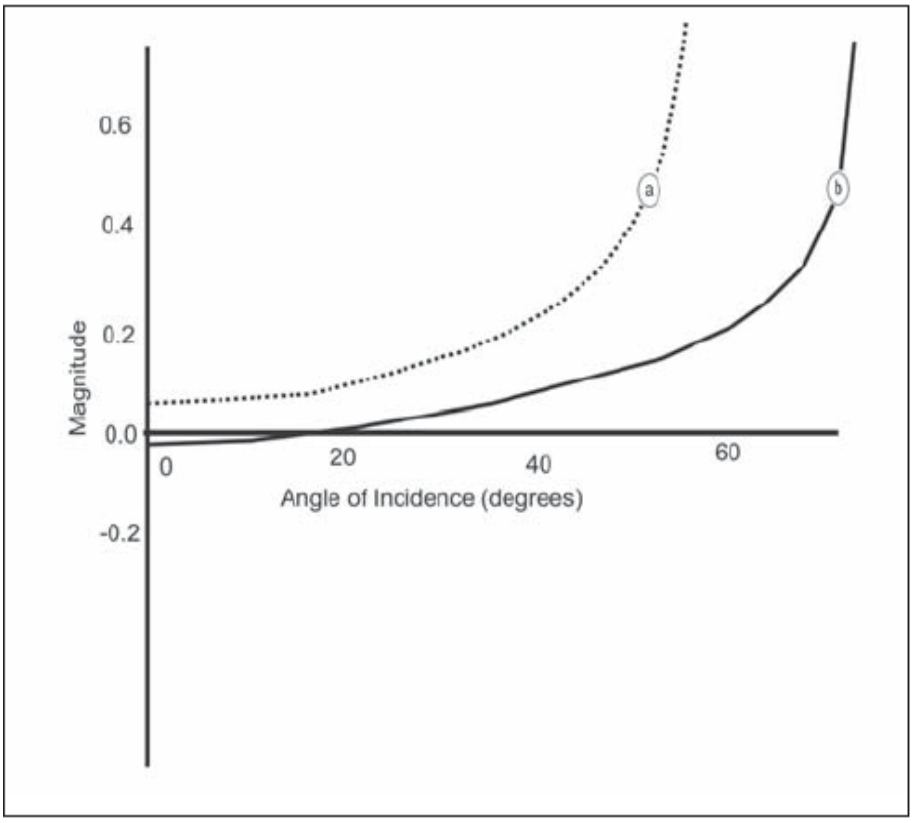

Figure 68. Effects of CO_2 fluid substitution in limestone on reflection magnitude at 0° to 70° incidence at shale/limestone interface. (a) is the brine-saturated reflection behavior and (b) is a fluid substitution to 100% CO_2 saturation (Purcell 2012).

5.1.1 Shuey: Zoeppritz Approximation Method

The amplitudes of a common midpoint gather show a series of reflections at increasing offsets. Instead of using the full Zoeppritz equations, it is convenient to use fitting parameters that are physically based (Shuey 1985). (Shuey 1985) simplified the Zoeppritz equations to

$$\boldsymbol{R(\theta) = R(0) + \left[a(0)R(0) + \frac{\Delta\sigma}{(1-\sigma)^2}\right] sin^2\theta + \frac{1}{2}\frac{V_p}{V_p}(tan^2(\theta) - sin^2(\theta))} \quad \textbf{(82)}$$

Where a(0) is equal to the incident reflection amplitude, σ is equal to Poisson's ratio at the reflecting interface, V_p and V_s are P and S-wave velocities, and R(θ) is the reflection coefficient at

offset angle, θ. The application of this theory to actual reflection seismic survey analysis solves the system so that V_p, V_s, and Poisson's ratio relationships reproduce true reflection coefficients at all angles. The values are often folded into fitting parameters that can be mapped to reveal anomalies. For surveys with offsets less than 30°, a Shuey two-term approximation is used,

$$\boldsymbol{R(\theta) = A(0) + Bsin^2(\theta)} \qquad \textbf{(83)}$$

to determine linear fitting parameters A (intercept) and B (gradient). Common midpoint (CMP) volumes can be classified in this manner to produce intercept and gradient volumes that can have traditionally been used as exploration tools. Figure 69 shows the two term approximation to a CMP stack. The two term method is a fast linear approach but is not effective at high angles (>35°).

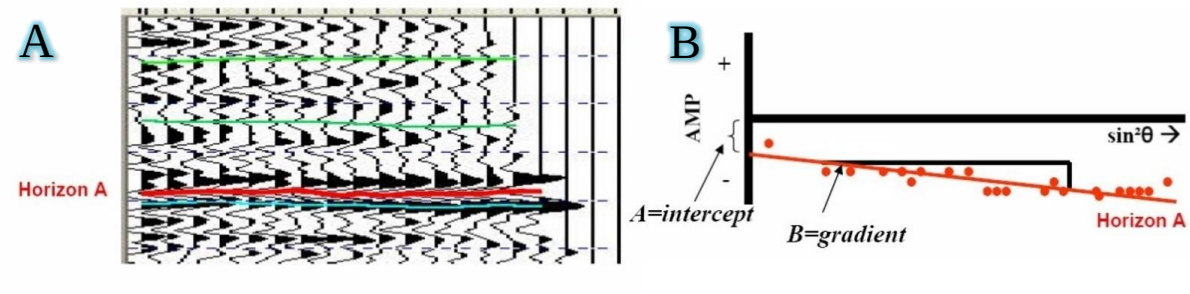

Figure 69. Zoeppritz Approximations: Shuey 2 Term Approximation (Roden 2008). With increasing offset, amplitude of horizon A (A) is described by a linear intercept and gradient fit in (B).

The Shuey three term adds a curvature fitting parameter, C, to fit to the CMP points following the formula:

$$\boldsymbol{R(\theta) = A(0) + Bsin^2(\theta) + C(\tan^2(\theta) - \sin^2(\theta))} \qquad \textbf{(84)}$$

Figure 70 shows the three term method applied to a CMP stack from the limestone reservoir. An offset gather in the lower window (A) with a horizon picked across the reflection. The amplitude values at which the horizon touches the signal trace is shown in (B). The input angle

is the on the abscissa of the graph. The fitting parameters are determined for all the reflections of a given volume of interest and can be mapped and interpreted.

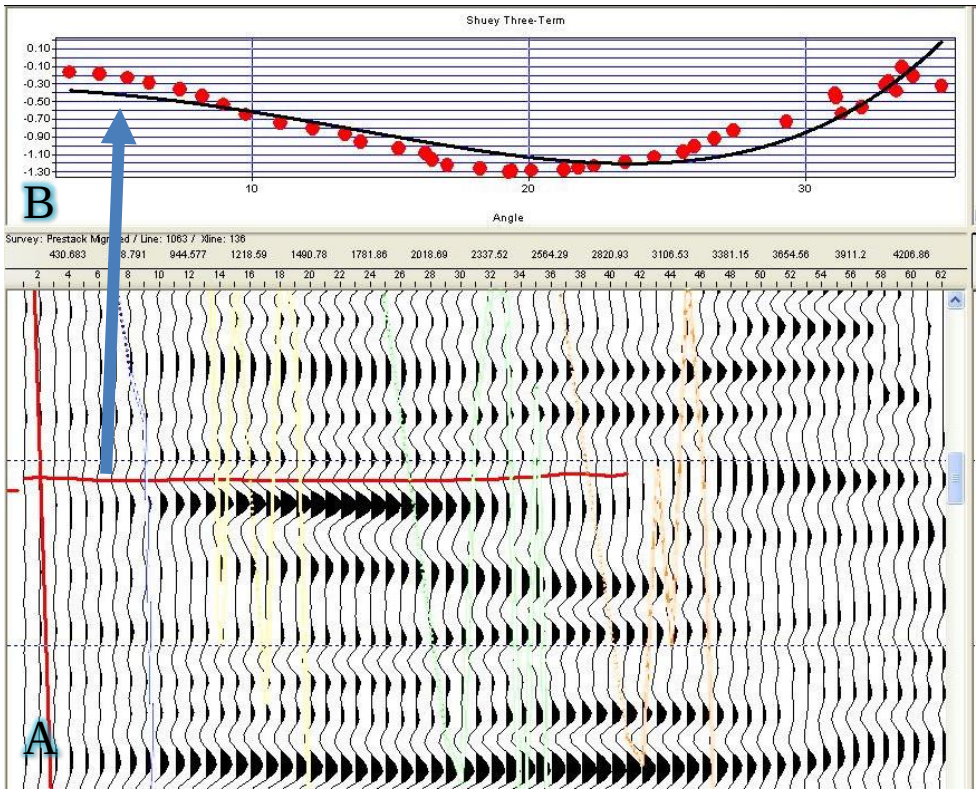

Figure 70. Shuey three term parameter fitting. In (A), the limestone reservoir is identified with a horizontal red line in a CMP stack with the vertical incident on the left and increasing offset moving right. The blue arrow indicates the amplitudes in (B) of the red line along the increasing offset angle. The black fit line in (B) uses the Shuey three term parameters A, B, and C to define the curve. These parameters are then assigned to the zero offset stack volume position at each specific time or depth.

5.1.1.1 Carbonate AVO Response

Amplitude variation with offset (AVO) is a general study of reflected wave amplitude at increasing angle. The classification methodology was originally developed by Rutherford for hydrocarbon location in gas sands (Rutherford et al. 1989), but the use of methodology in the current study is

unorthodox. Therefore, the AVO classification system (Figure 71) for sandstones in which Class 1 is a sand with higher impedance than the encasing shale, Class 2 is a sand with nearly the same impedance as the encasing material, Class 3 is a sand that has a lower impedance than the encasing material, and Class 4 (Castagna et al. 1998) is a porous sand encased by a high-velocity, hard shale, siltstone, tight sand, or carbonate can be loosely applied to the reservoirs in question. Crossplots using the calculated gradient (A) versus intercept (B) (Figure 72) have been used empirically by quadrant point grouping to predict trends such as: increasing cement, hydrocarbon, pore pressure, shaliness, or porosity. (Purcell 2012) determined that the limestone reservoir had a Type III AVO response. As the industry has not rigorously applied such resources to carbonate reservoirs and especially not to finding "increasing CO_2" trends, we use the four case sandstone classification scheme to the logical limits, but we leave the traditional schemes to further explore the special case of CO_2 and carbonates.

The mapping of intercept (A) and gradient (B) relationships is particularly useful in understanding the effects of CO_2 injection, especially when injection location is known. Table 7 lists the various combination of intercept, slope, and gradient fitting parameters that are used for attribute analysis. The volumes produced by these calculations are reviewed and interpreted for evidence of CO_2 anomalies. The images presented feature stacked reflection wiggles (black peaks) overlying AVO parameter calculations from Table 7 visualized with color gradients.

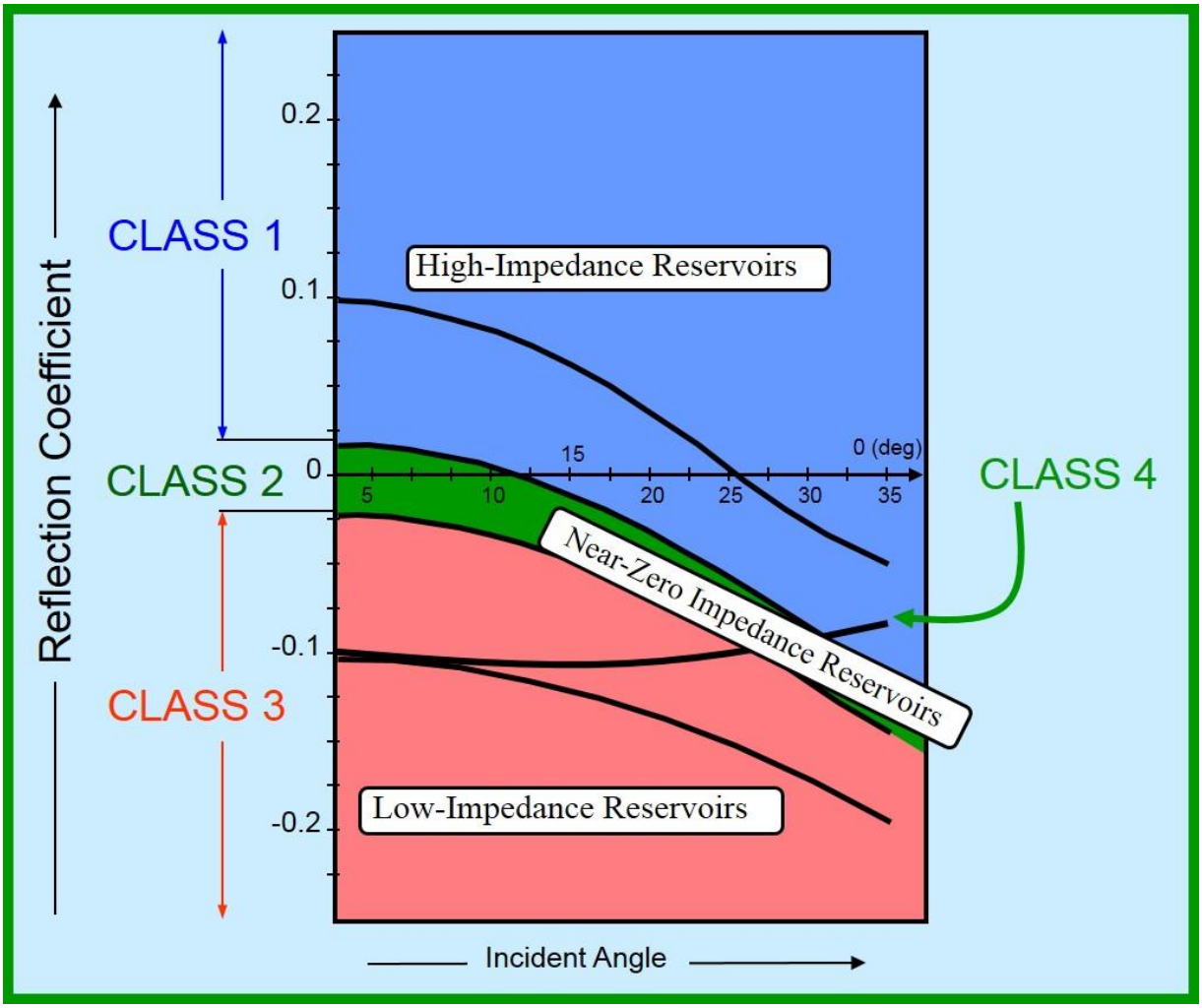

Figure 71. AVO classifications for a shale-gas sand interface (Hilterman 1983, Rutherford et al. 1989, Ross et al. 1995, Castagna et al. 1998).

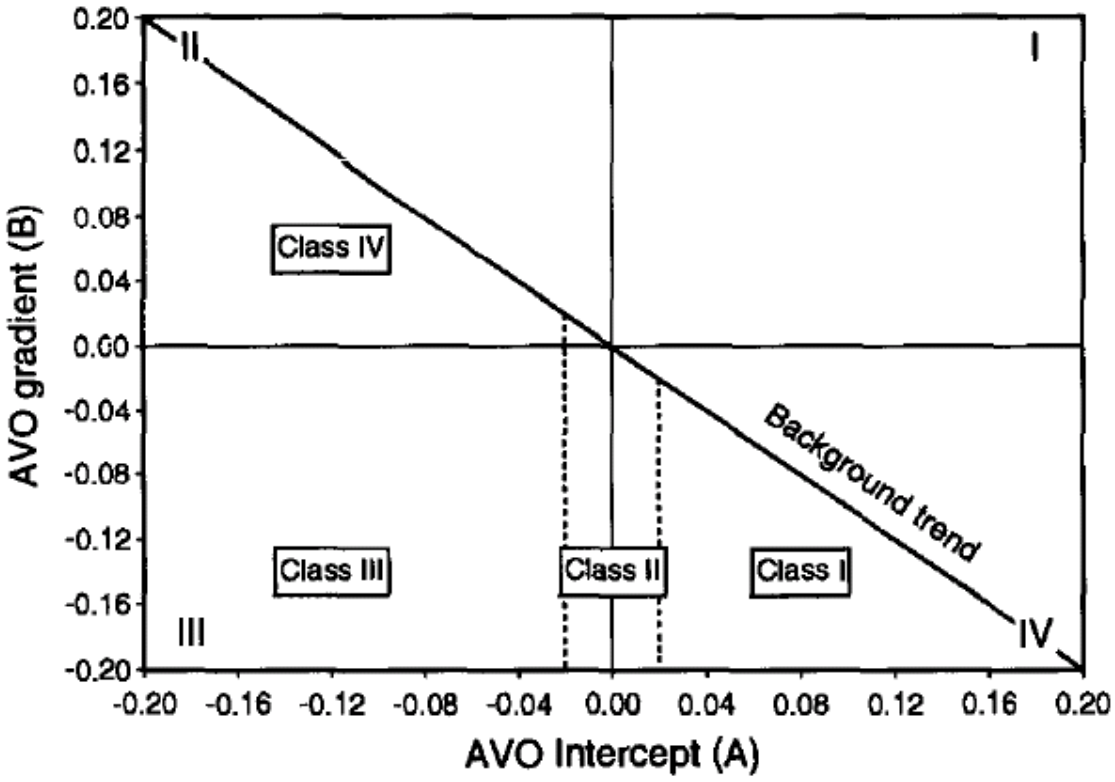

Figure 72. AVO crossplot classes (Castagna et al. 1998). This crossplot of fitting parameters intercept (A) and gradient (B) (from Equations 83 and 84) show the reflected wave behavior at increasing offset (shown in Figure 71) in a space that has allowed trends (Classes I-IV) to be observed for various situations. The background trend is the result of linear V_p/V_s ratio and constant density. The classes are determined by the quadrant (I-IV) location of parameter plots.

Table 7. List of useful attributes calculated from Shuey 3-Term coefficient data cubes (RockSolid, Seismic Micro Technologies, 2008).

Attribute	**Description**
½(A+B)	Estimate of P Reflectivity – Shear Reflectivity (R_P-R_S)
½(A-B)	Estimate of Shear Reflectivity
A*B	Intercept * Gradient
A-C	Intercept - Curvature
Err	Standard Error
r^2	Goodness of fit

At the carbonate reef site, AVO anomalies of the three term Shuey approximation derived attribute of ½ (A+B) (Figure 73) post-injection prestack reflection seismic were observed. The anomalies in the calculated AVO attribute of ½ (A+B) highlight P-wave reflectivity changes. The stacked reflection seismic is overlain for reef structure. Anomalies appear in red and are interpreted to be CO_2 pools. There seems to be a density effect present, pushing the fluid downward on the right side of the anomaly. We may be seeing intrusion into a high pressure fluid updip.

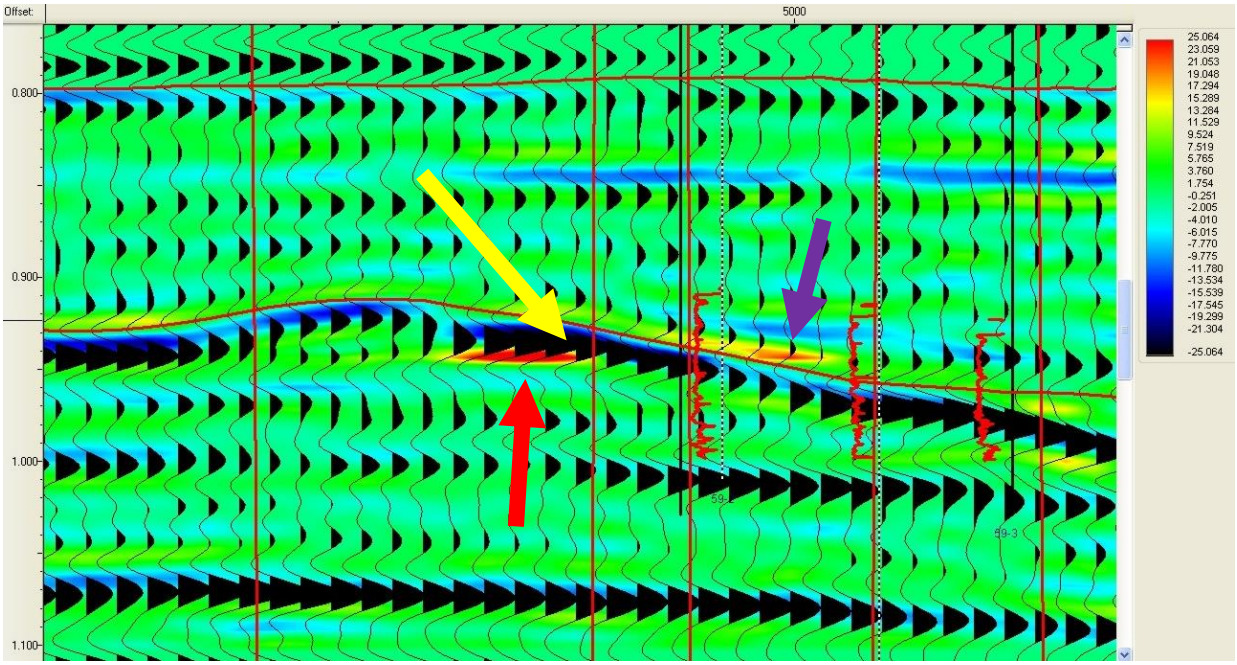

Figure 73. Shuey 3 Term Zoeppritz Approximation Method using the combination of fitting parameters intercept, (A) and gradient, (B): ½(A+B). Attribute is an estimate of P reflectivity minus shear reflectivity. Arrows indicate possible locations of injected CO_2, which has caused relative increases in P-wave reflectivity. The red arrow points to the Canyon limestone and the purple arrow points to the Cisco limestone. The injection of CO_2 caused the yellow-red anomalies. CO_2 pressure increases could be localized due to permeability heterogeneities or buoyancy effects. Consequently, non-structural trapping type pooling is observed (Purple Arrow). An alternative interpretation is that the injection of CO_2 causes brightening (more positive ½(A+B)) above and fluid location, so that low reflectivity values bounded by anomalously high values indicate the presence of CO_2. In which case the yellow arrow indicates the location between the yellow-red anomalies which contains the CO_2.

5.1.2 Aki-Richards: Zoeppritz Approximation Method

Similar to the methods used in carbonate reservoir, a reflection seismic amplitude analysis technique was used with the Cranfield sandstone reservoir. Prestack data in this case was stacked into sub gathers that represent an average offset value. The gathers were processed using the three

term Aki-Richards equation (Aki et al. 1980). This is a similar approach to the Shuey method, but the ratio of velocity (V_p, V_s) or density (ρ) change is highlighted. The attribute volumes calculated are:

$$\boldsymbol{Density\ Reflectivity} = \frac{\Delta\rho}{\rho} \quad \textbf{(85)}$$

$$\boldsymbol{P\ Reflectivity} = \frac{1}{2}\left(\frac{\Delta V_p}{V_p} + \frac{\Delta\rho}{\rho}\right) \quad \textbf{(86)}$$

$$\boldsymbol{S\ Reflectivity} = \frac{1}{2}\left(\frac{\Delta V_s}{V_s} + \frac{\Delta\rho}{\rho}\right) \quad \textbf{(87)}$$

Which are determined by calculating the reflection coefficient, R, at multiple angles (θ).

$$\boldsymbol{R(\theta) = a\frac{\Delta V_p}{V_p} + b\frac{\Delta\rho}{\rho} + c\frac{\Delta V_s}{V_s}} \quad \textbf{(88)}$$

In which

$$\boldsymbol{a} = \frac{1}{2\cos^2(\theta)} \quad \textbf{(89)}$$

$$\boldsymbol{b} = \frac{1}{2} - 2\sigma\sin^2(\theta) \quad \textbf{(90)}$$

$$\boldsymbol{c} = -4\sigma\sin^2(\theta) \quad \textbf{(91)}$$

$$\boldsymbol{\sigma} = \left(\frac{V_s}{V_p}\right)^2 \quad \textbf{(92)}$$

In order to determine the proper reflectivity values, a prestack reflection seismic volume is divided into three offset groups to determine R(θ): near, mid, and far. The system is then solved so that V_p, V_s, and ρ reflectivity (Equation 78 modified to highlight attribute contrasts) values reproduce true reflection coefficients at all angles.

5.1.2.1 Sandstone AVO Response

Figure 74 shows the input parameters used for all six volumes that were produced. The pre and post injection pre-stack data were sub-stacked to Near, Mid, and Mid-Far stacks and offset angles were calculated. A consistent V_P/V_S ratio was used for all sets.

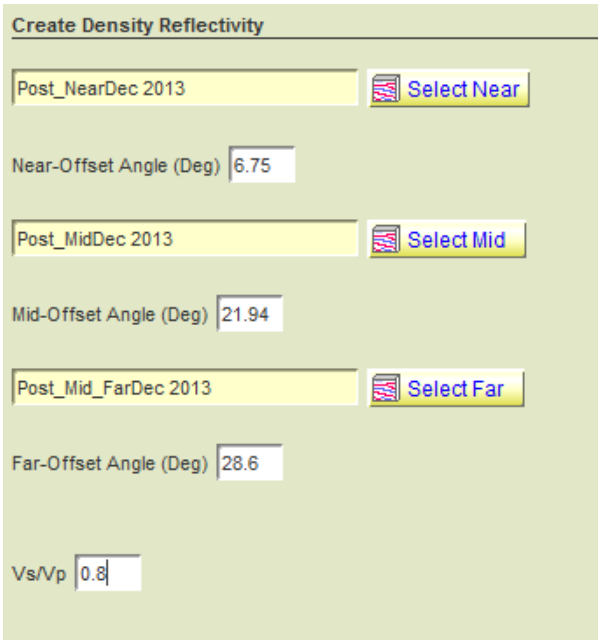

Figure 74. Input parameters for Aki-Richards attributes. "Mid-Far-Offset" stacks are produced from 24°-32° offsets and averaged to 29°, "Mid-Offset" stacks are produced from 17°-26° offsets and averaged to 22°, "Near-Offset" stacks are produced from 1°-12° offsets and averaged to 7°. V_S/V_P is held constant at 0.8.

The reflectivity volumes (Appendix A: Figure 105, Figure 106, Figure 107) were differenced to highlight changes in the wave reflectivity after injection (Figure 77, Figure 75, Figure 76). The changes in density and S-wave are dramatic. S-waves should not be changed due to fluid replacement, but reservoir pressure increase may open reservoir compliant pore space and press on the surrounding units, causing density and matrix wave sensitivity changes.

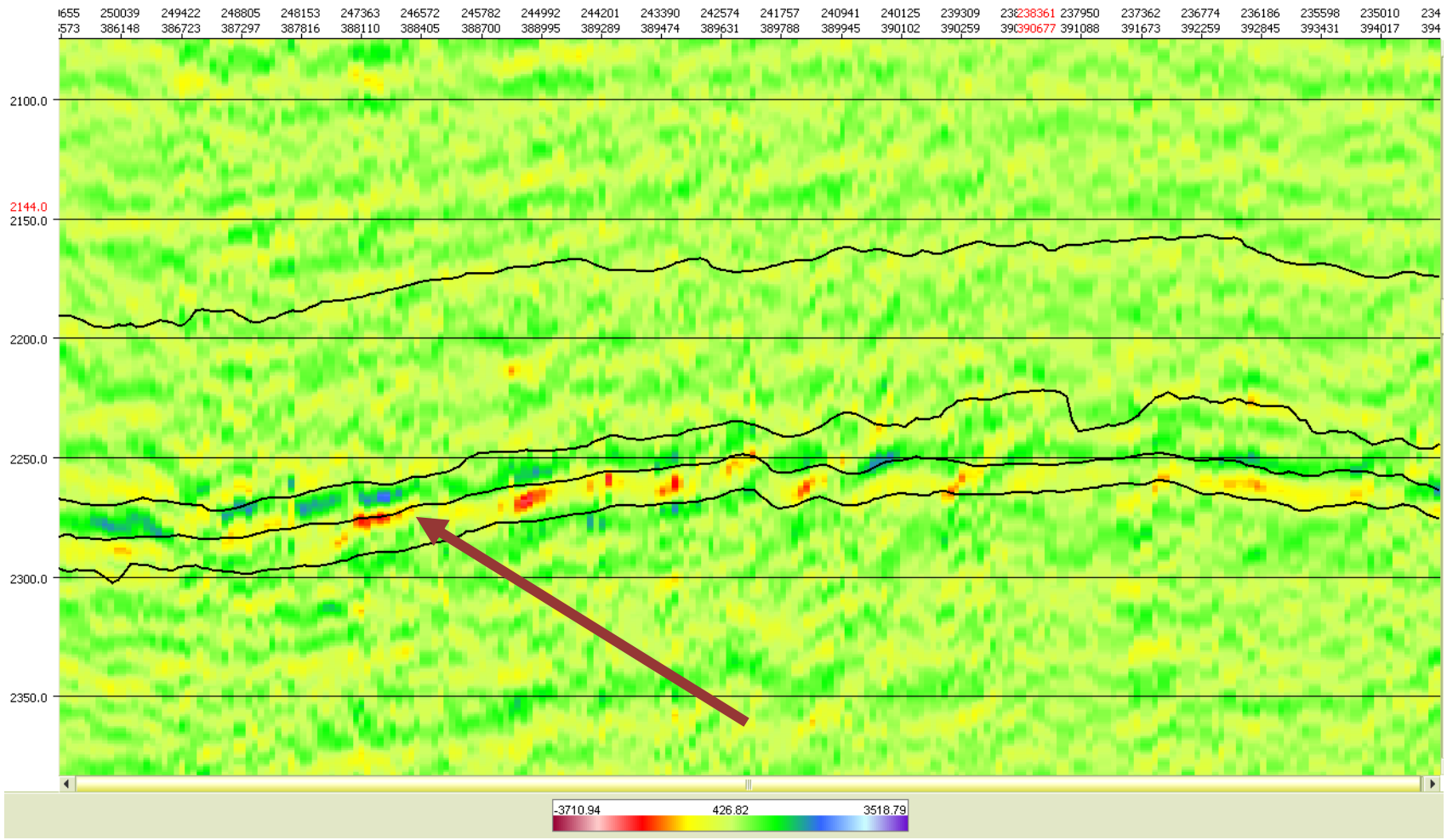

Figure 75. P-wave reflectivity difference volume. Arrow indicates reservoir unit. Subtle changes can been seen due to injection of CO_2. The red coloration indicates a negative shift in P-wave reflectivity which agrees with fluid substitution modeling.

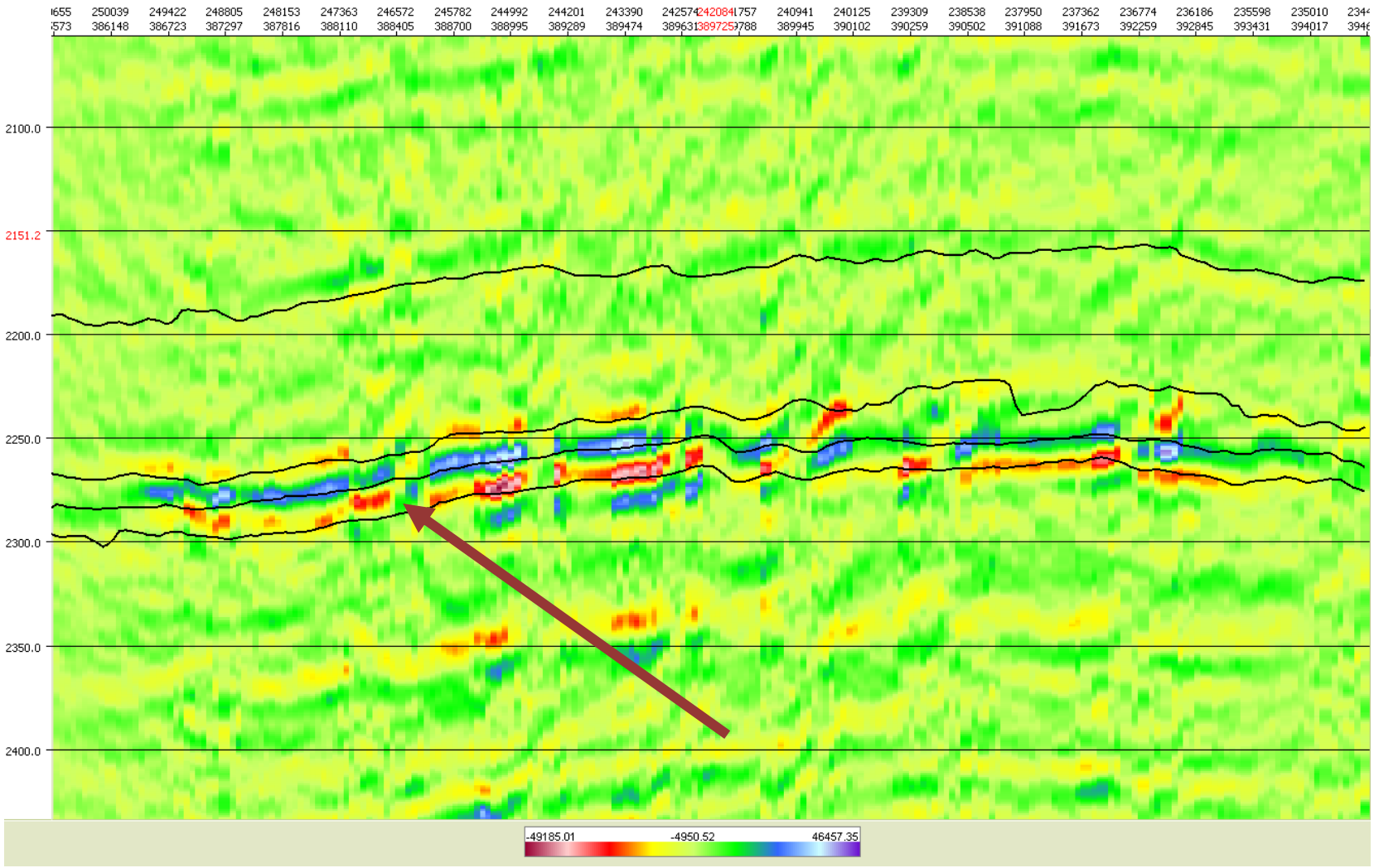

Figure 76. S-wave reflectivity difference volume. Arrow indicates reservoir unit. The injection of CO_2 has had significant effect on the sandstone reservoir S-wave reflectivity. This is likely due to pressure effects and not fluid effects.

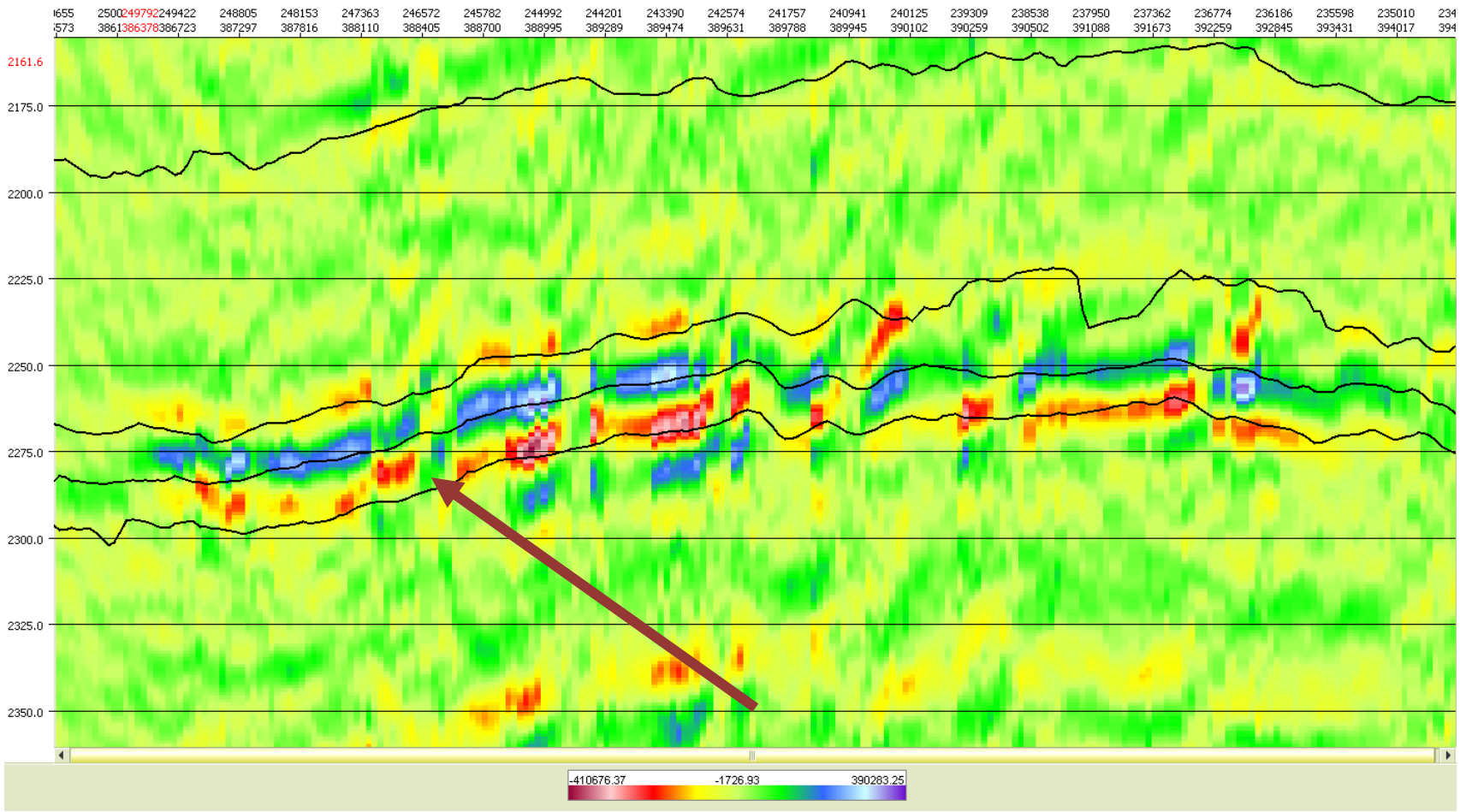

Figure 77. Density reflectivity difference volume. Arrow indicates reservoir unit. Density effects can be caused by both fluid substitution and the effects of pressure on the matrix.

5.2 CARBONATE RESERVOIR MODEL

Models were produced with varying levels intricacy (e.g. onlap sequences versus variable thickness strata) to reproduce the reflection seismic response of the reservoir. Horizons interpreted on the original seismic were used as boundaries to distribute acoustic properties (Figure 79). These geological models were simplified and fluid substituted well logs were used to distribute new rock properties to the units. A statistical wavelet was extracted from the seismic for convolution purposes (Figure 78). Convolution consists of producing the area overlap between a reflection coefficient function (R_c) and a wavelet as a function of the translated wavelet in the domain of R_c (time or depth).

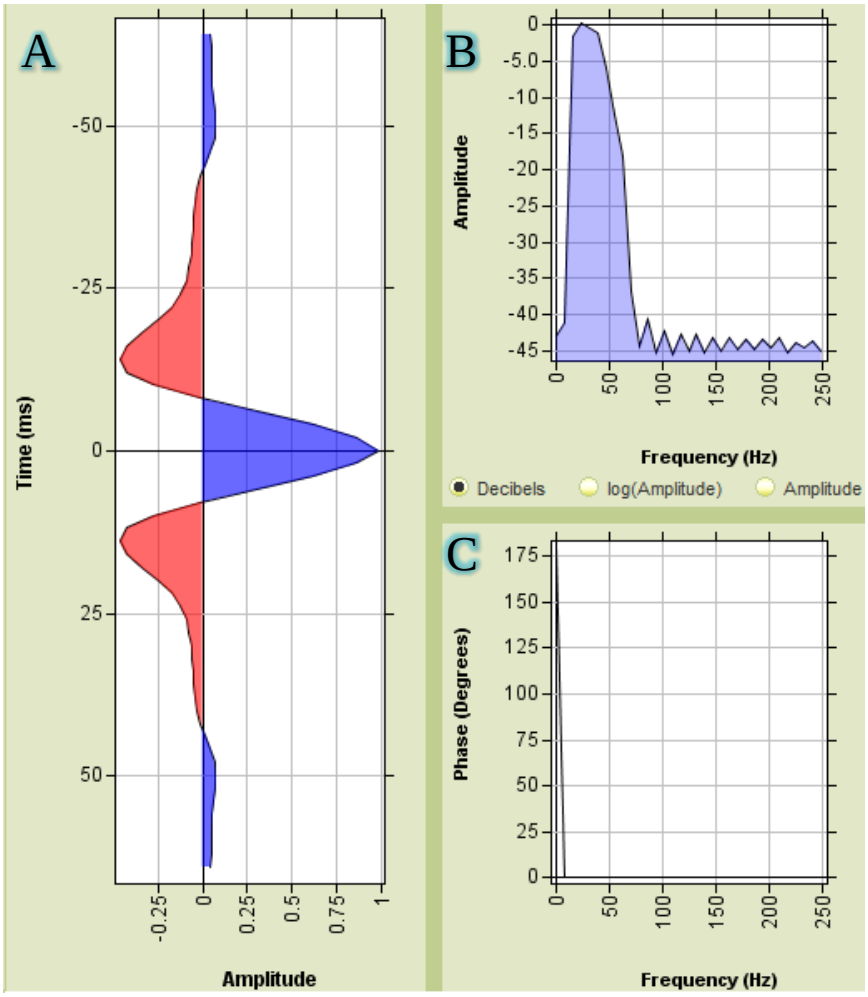

Figure 78. Extracted wavelet from seismic trace nearby reef carbonate well used for convolution in later models. (A) shows the wavelet, (B) shows the frequency spectrum (frequency most effective between 5 and 125 Hz) and (C) shows the wave phase (in this instance, the wavelet is zero phase).

The wavelets presented in this thesis are in the seismic frequency band and are either statistically derived from near well seismic stacks or produced in a wavelet editor. Figure 80 shows the model derived reflectance overlying the original seismic. Figure 81 shows the model as a seismic cross section along with a previous example of the actual seismic (Figure 82). Finally, Figure 83 shows the subtle (change of 1-3%) density effects of the fluid substitution

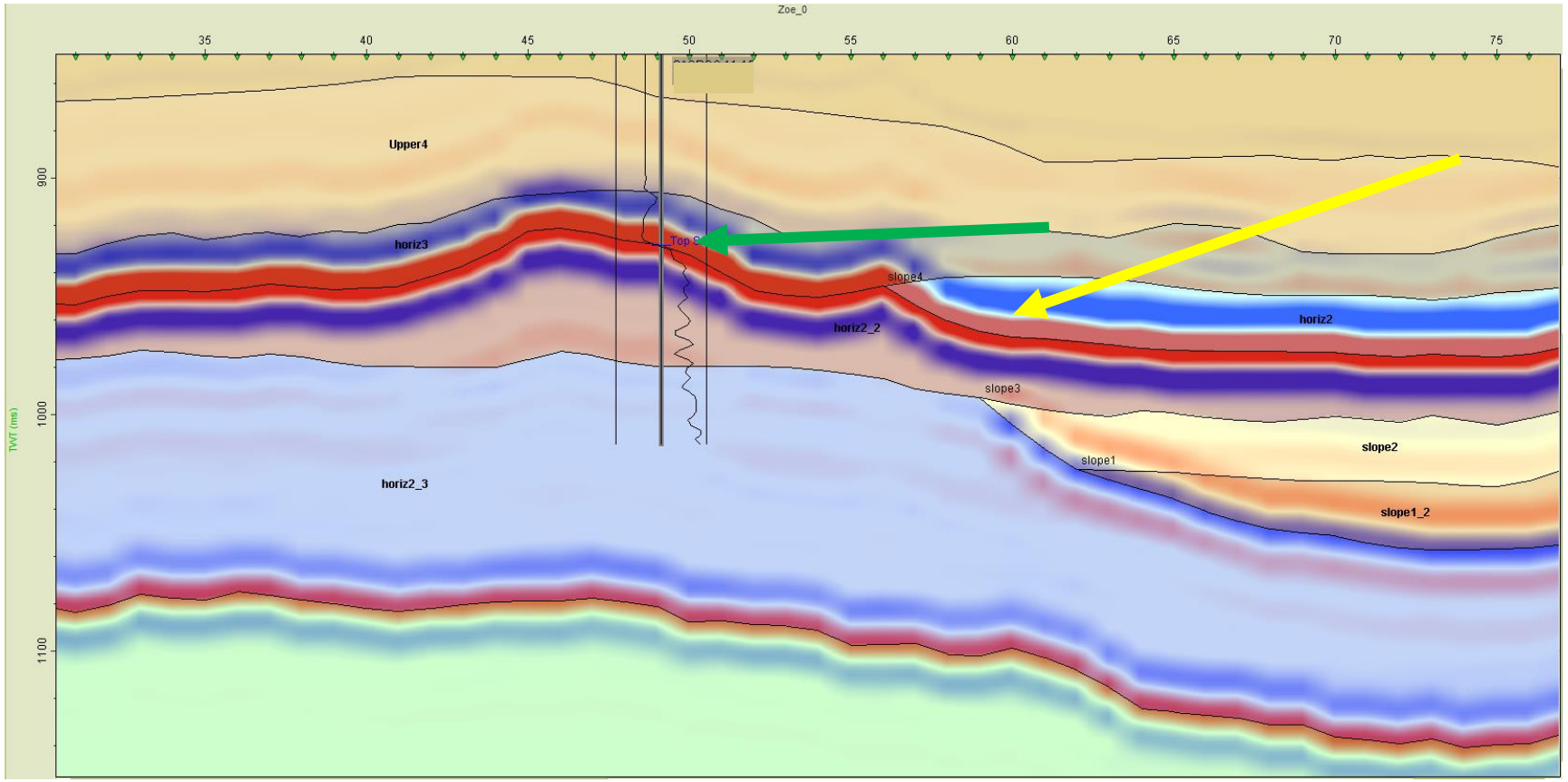

Figure 79. Original, more intricate model of carbonate reef produced from structural interpretation horizons from reflection seismic interpretation. Green arrow points to top of carbonate reservoir unit. Yellow arrow points to top onlapping sequence package. Each discreet packet must have assigned rock properties (V_p, V_s, ρ) to determine reflection coefficients at interfaces.

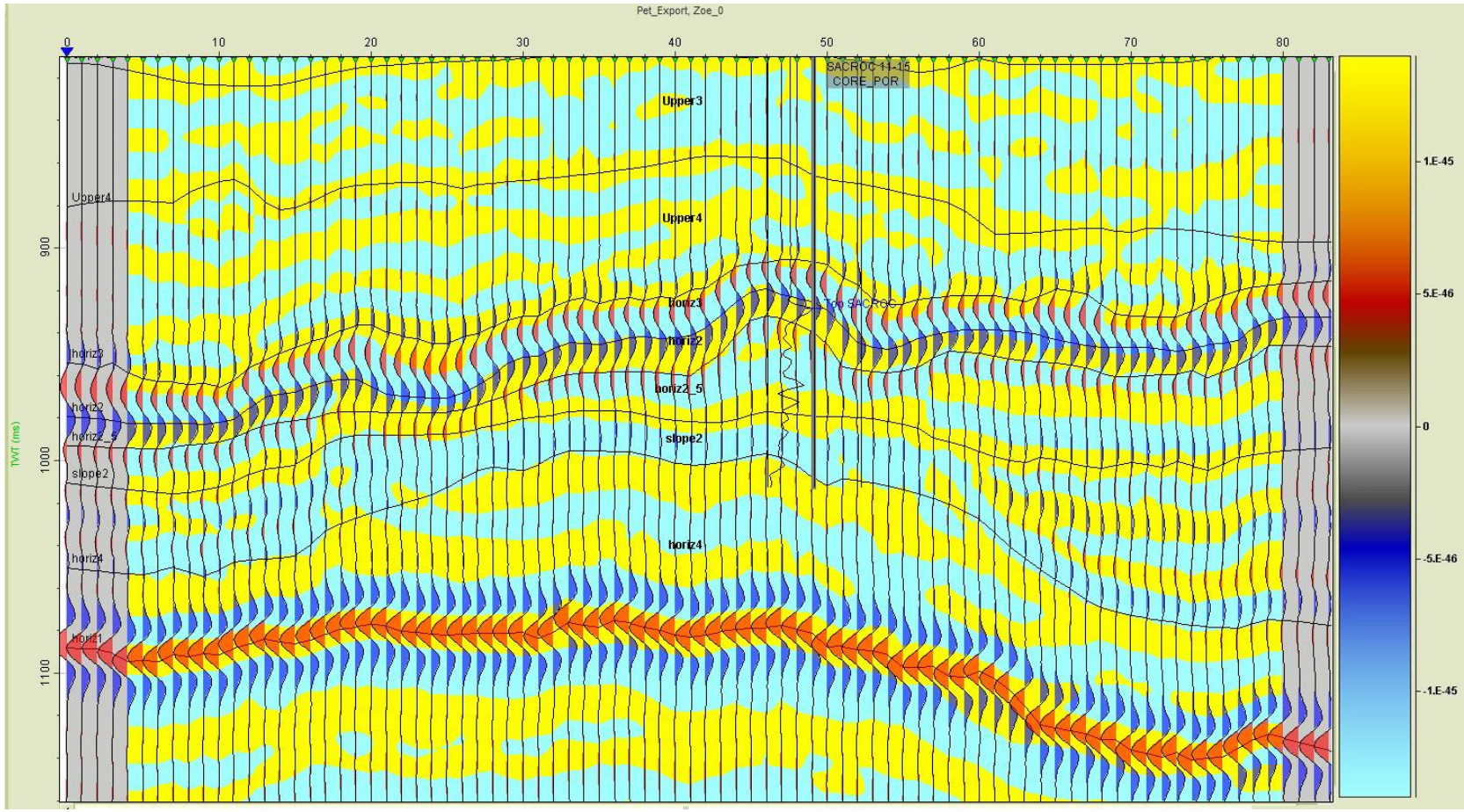

Figure 80. Synthetic reflectance overlying original seismic (blue/yellow). Surfaces are simplified to reproduce observed basic seismic reflection structure.

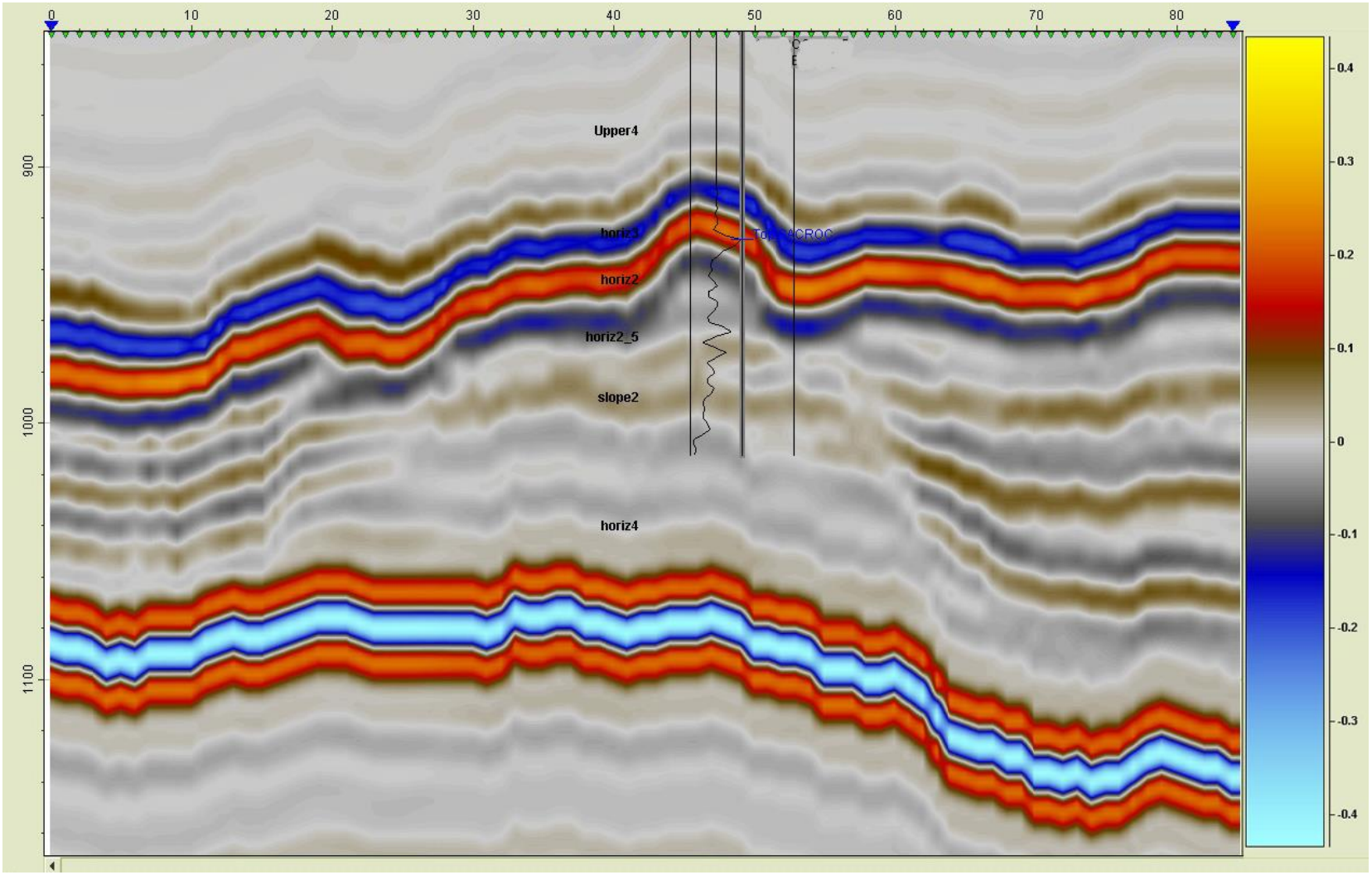

Figure 81. Synthetic seismic cross section produced from simplified model.

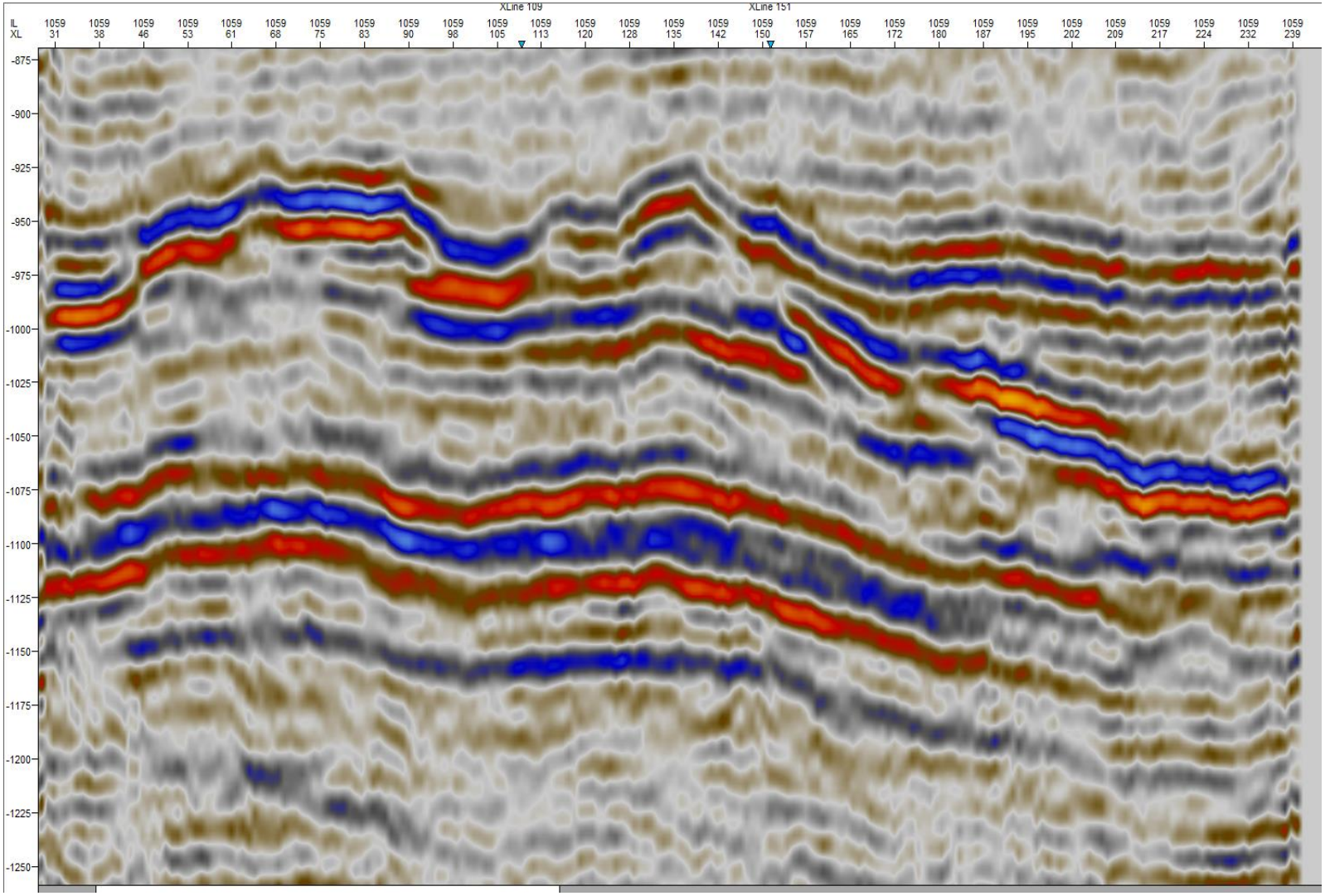

Figure 82. Reference seismic image. Sloping reef material (off-center right) stands out with stronger reflectors than in the model. However, as no wells exist in the area to the right, the model agreement is acceptable

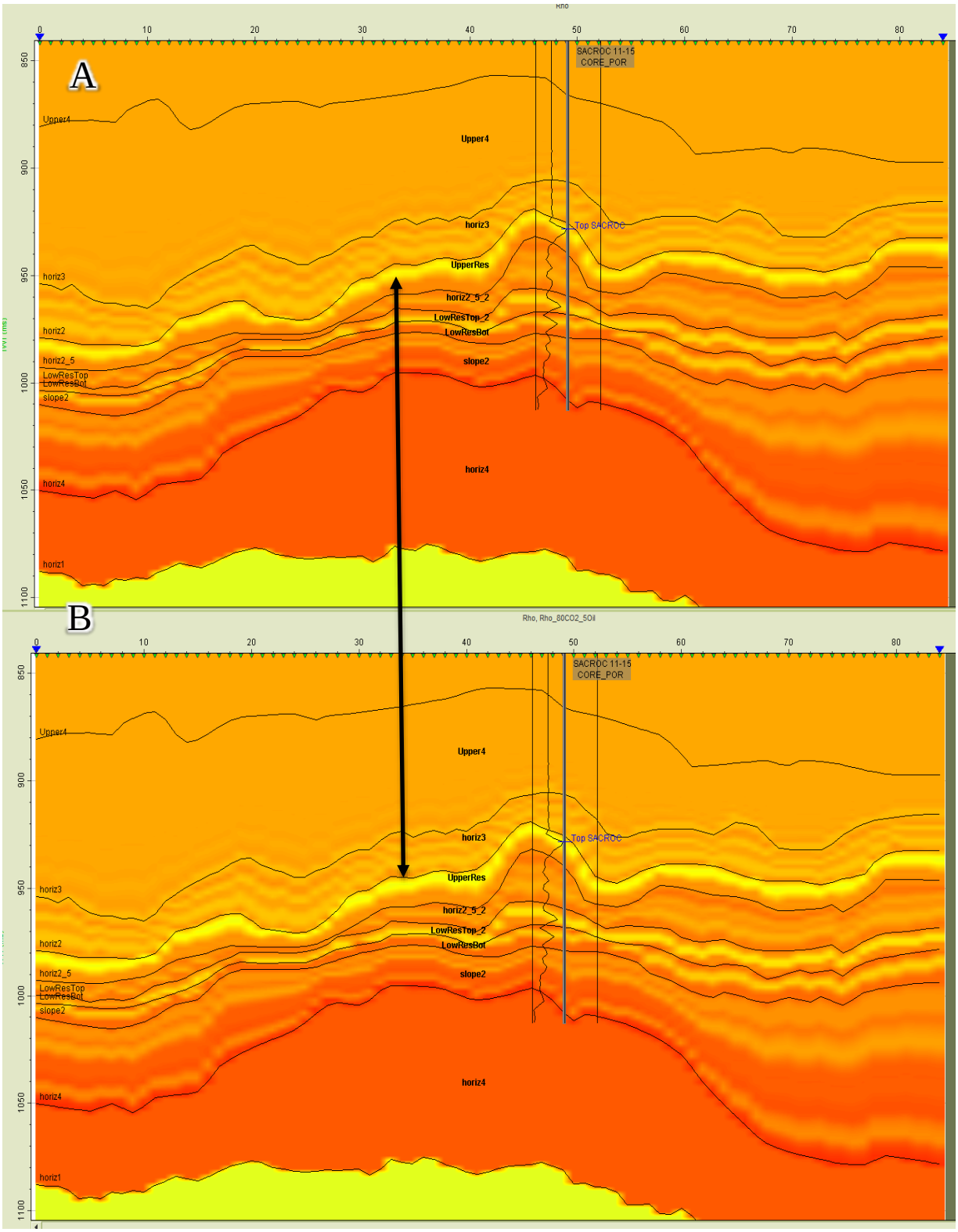

Figure 83. Fluid substitution (to 80% CO_2) in the reservoir unit reveals only slight density changes.

5.3 SANDSTONE RESERVOIR MODEL

Using multiple 3-D seismic pre and post stack volumes and well logs from a sandstone reservoir, we modeled the reservoir seismic response of CO_2 substitution and fluid replacement as a component of the pore filling fluid mix in a reservoir. Repeat seismic surveys reveal amplitude changes in the Sand "D-E" reservoir unit after CO_2 injection.

Figure 84 is a fluid substitution workflow that describes the input and modeling steps. Well log data are used to determine the rock and fluid properties through the geologic strata. Resistivity and neutron porosity logs are used in conjunction with Archie's law to determine fluid volume and saturation. The gamma ray log is used to determine clay content and differentiate sandstone and shale mineralogy. P-wave sonic, density, and mineralogy logs are used with rock physics models to predict S-wave velocities. Using density, P and S-wave logs, acoustic impedance and reflection coefficient logs are produced. A wavelet chosen based upon seismic survey parameters and convolved with the reflection coefficient log to produce synthetic seismic response logs. Once synthetic seismic matches actual seismic, the rock physics properties are distributed through the reservoir model and synthetic seismic volumes produced.

Once an accurate reservoir model exists, fluid substitutions and porosity perturbations can be mathematically performed to generate synthetic seismic scenarios. Fluid substitutions are performed using fluid properties calculated at the reservoir temperature and pressure conditions (standard fluid mixing models are used in the case of multiple fluid types).

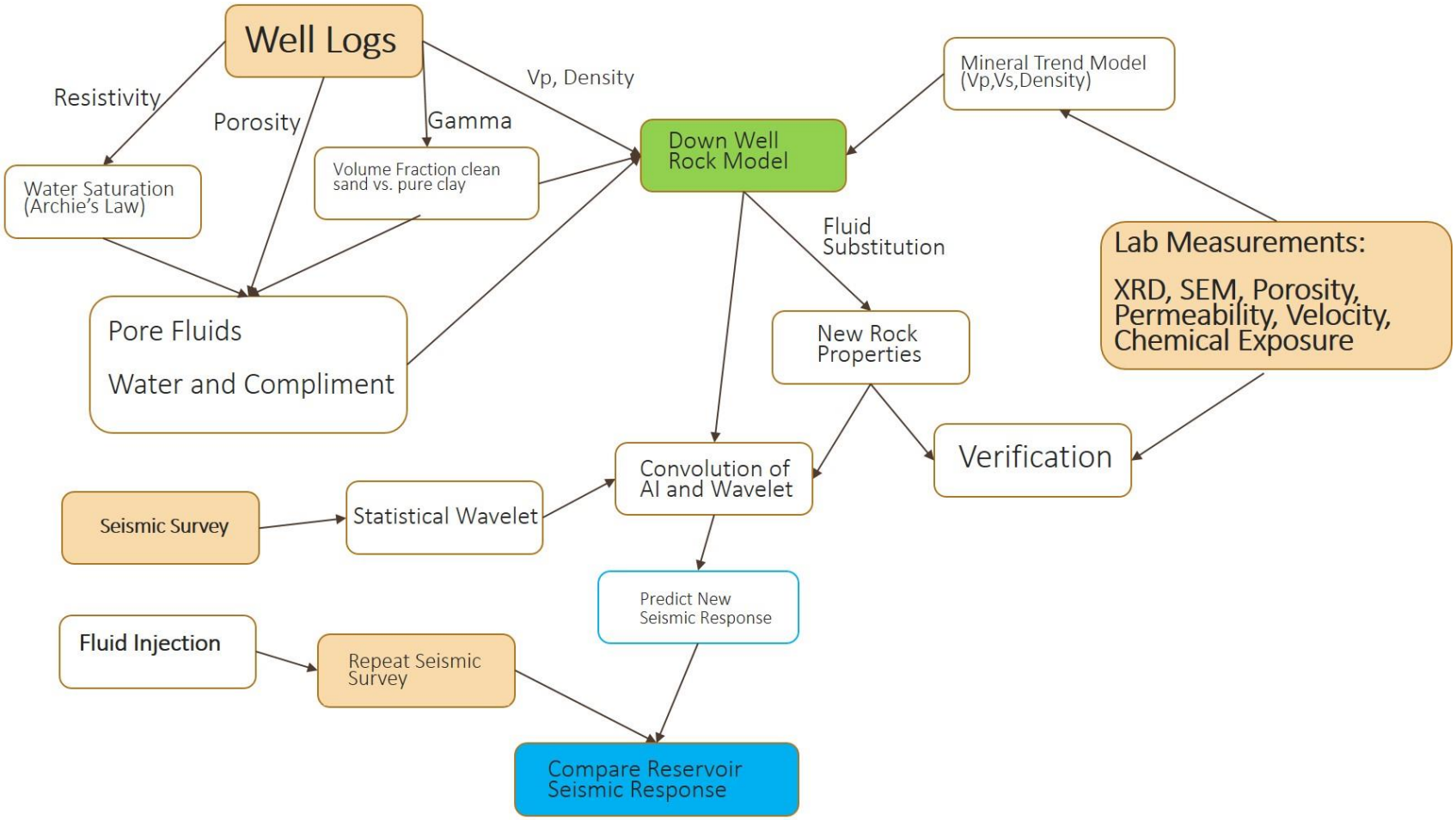

Figure 84. Synthetic seismic generation and scenario comparison workflow. Three input data types: Well logs, laboratory measurements, and multiple seismic surveys

Previous mineralogical analysis (Lu et al. 2012) are used to derive the matrix mineral properties. Table 8 data show XRD mineral percentages from a well 68 meters east of the full well data. The sampling interval of XRD is approximately 0.5 meters and correlates well with gamma ray signature matching with a clay spike at 3195.5 meters depth. The point data are interpolated (spline) over the reservoir unit to create a volume fraction log. The volume fraction log is used to determine the required Voigt-Reuss-Hill mineral bulk and shear moduli to the Gassmann fluid substitution model. The Gassmann fluid substitution model produces V_S values over the reservoir which are then used to improve empirical V_P-only input based V_S model which are then applied over the entire well. It was observed that the (Han 1987) <15% porosity V_S prediction method, which is an empirical relationship which uses the sonic P-wave values to produce S-wave values, matched very well with the S-wave velocities produced by XRD analysis (Lu et al. 2012) and was thus used throughout the other Cranfield reservoir units. This relationship of V_S and V_P is:

$$\mathbf{V_S = 0.7563*V_P - 662.0} \qquad \mathbf{(93)}$$

Once a full-well V_P-V_S-ρ set is produced, the seismic response of various fluid mixes are modeled into the pore space of the reservoir. The models appear in the form of common midpoint gathers, which show reflection amplitude and polarity at increasing source-receiver offsets. This is achieved by convolving a wavelet with the reflection coefficients generated by the V_P-V_S-ρ set. Convolution consists of producing the area overlap between a reflection coefficient function (R_c) and a wavelet as a function of the translated wavelet in the domain of R_c (time or depth). It is important to note that the frequency of the convolved wavelet can be set to reveal both land source-receiver based 3-D seismic survey resolution bedding features and vertical seismic profile (VSP) survey level resolution bedding features. VSP surveys can have a higher frequency and consequently higher resolution.

Models reveal that seismic amplitude variations with offset occur with different pore filling fluid mixes (Water-Oil, Water-CO_2, and Water-Oil-CO_2). The models are compared to the before-and-after CO_2 injection 3-D seismic surveys that were done on the reservoir to test the prestack seismic sensitivity of the AVO modeling. In Figure 89 and Figure 90, the product of these models: two mid offset synthetic traces produced by convolving an extracted wavelet with the reflection coefficients derived from V_P-V_S-ρ logs of the original well data (right) and a CO_2 substituted set (left) can be seen.

Table 8. Cranfield Reservoir Sand D-E XRD analysis from Lu et al. (Lu et al. 2012).

Depth (m)	Quartz	Kaolinite	Chlorite	Illite	Albite	Calcite	Dolomite	Anatase
3178.1	77.9	5.1	11	1.3	0	0.5	0	4.2
3178.9	73.7	4.3	13.8	1.9	2.5	0	0	3.7
3179.8	66.9	5.1	18.4	2.8	2.9	0	0	4
3180.1	77	6	18.8	2.9	1	0	0	4.3
3181.1	79.4	3.9	11	2	0.9	0	0	2.8
3181.7	78.6	4	11.1	2.1	1.1	0	0	3.1
3182	74.7	4.6	14.4	2.3	0	0	0	4.1
3183	82	3.3	9.7	1.8	0	0	0	3.2
3183.8	81.5	3.7	10.1	1.8	0	0	0	2.9
3184.4	85.8	3.3	7.3	1.2	0	0	0	2.5
3184.8	83.9	3.4	8.4	1.3	0	0	0	3
3185.2	83.5	3.4	9	1.6	0	0	0	2.5
3185.8	83.2	3.3	9.1	1.1	0	0	0	3.3
3187	79.3	4.2	11.2	1.2	0	0	0	4.1
3187.6	79.3	3.3	13	0.9	0	0	0	3.4
3188.3	80.7	3.1	12.6	1.2	0	0	0	2.5
3188.8	82.3	2.1	12.2	1	0	0	0	2.5
3189.3	81.3	2.6	12	1	0	0	0	3.1
3189.6	82.5	2.7	10.7	1.2	0	0	0	2.9
3190	78.8	2.7	14	1.3	0	0	0	3.2
3190.1	83	2.4	10.7	1.3	0	0	0	2.7
3190.8	81	1.5	13.4	1.2	0	0	0	2.9
3190.9	80.7	1.7	14.1	0.8	0	0	0	2.6
3191.2	75.6	2.5	17.1	1	0	0	0	3.7
3191.5	77.9	2.8	15.3	0.9	0	0	0	3.2
3193.2	55.2	1.2	4.7	0.6	0	36.8	0	1.5
3193.6	84.6	3	8.8	0.8	0	0	0	2.8
3193.9	81.4	2.2	12.8	0.4	0	0	0	3.3
3194.2	85.5	2.5	8.7	0.4	0	0.5	0	2.4
3194.9	85.1	2.2	10.1	0.3	0	0	0	2.3
3195.6	85.7	2	9.2	0.5	0	0.6	0	2
3195.9	80.8	2.1	14	0.3	0	0	0	2.9
3196.1	82	2.2	13.1	0.1	0	0	0	2.7
3196.8	81.9	2.2	12.5	1.2	0	0	0	2.2
3197.7	83.6	1.7	10.5	1.4	0	0.5	0	2.3
3199.7	71.2	4.8	10.6	1.9	0	0	9.8	1.8
3200.3	70.5	4.7	13.1	1.5	0	0	6.5	3.7

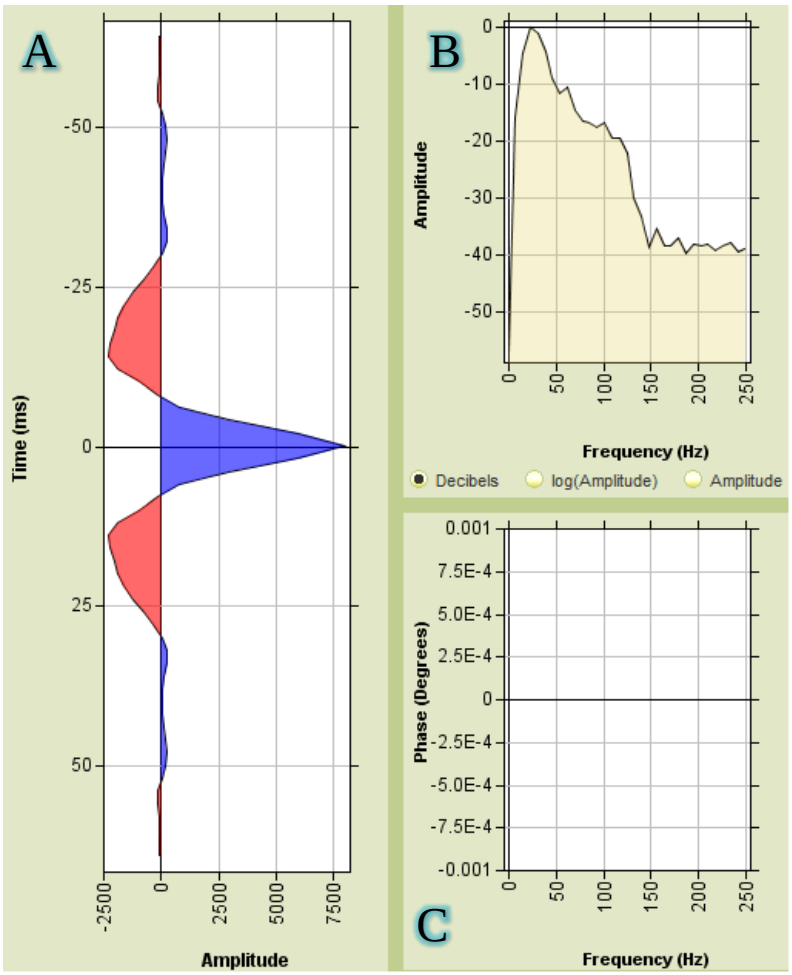

Figure 85. Wavelet extracted from Cranfield pre-injection stacked data nearby the modeled well. (A) shows the wavelet, (B) shows the frequency spectrum (frequency most effective between 5 and 125 Hz) and (C) shows the wave phase (in this instance, the wavelet is zero phase).

5.3.1 Fluid Properties and Reservoir Pressure

Reservoir fluid properties were calculated using the 2011 FLAG fluid models (Batzle et al. 1992, Han 2011). Density, P-wave velocity, and bulk modulus of the desired fluids are calculated at observed pressure and temperature conditions or at calculated pressure and temperature from depth-pressure/temperature gradients. Figure 86 shows the input calculator and calculated water,

oil, gas, and CO_2. Water is calculated by concentration of sodium, potassium, and calcium, oil is calculated by dissolved gas/oil ratio, API, and gas gravity, gas is calculated with gas gravity, and CO_2 needs only pressure and temperature.

For the sandstone reservoir, salinity value of 150,000 mg/L TDS of dominantly Na-Ca brine, and pre-injection reservoir temperature and pressure values of 125°C and 32.4 MPa (at 3040 m depth) are used (Lu et al. 2012). Figure 87 and Figure 88 show the mixing models the defined CO_2 with the defined brine and the defined oil with the defined brine; the graphs show the various mixing models that can be used for later fluid substitutions: the Voigt line (parallel arrangement of mineral mixing – Equation 24), VHR or Voigt-Reuss-Hill line (average of parallel and series mineral mixes – Equation 26), and the Woods line (inverse bulk modulus average).

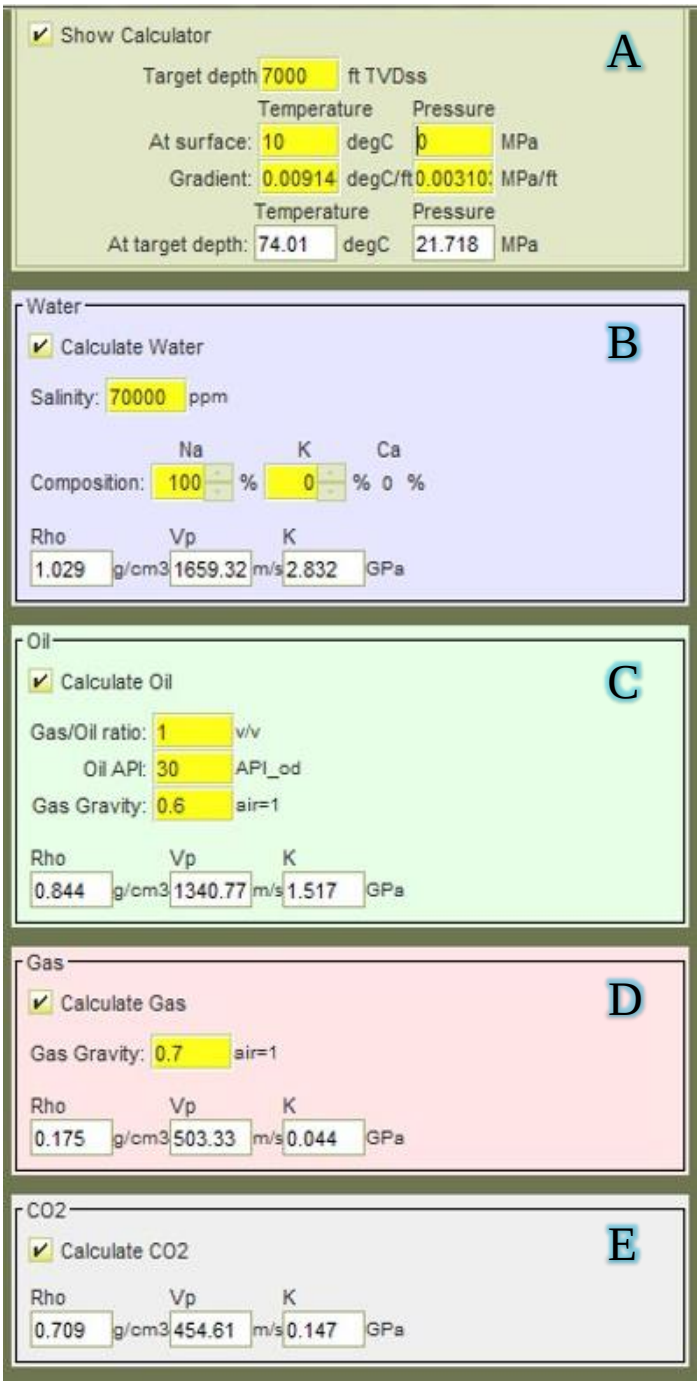

Figure 86. FLAG Fluid Calculator, showing the input parameters used to determine fluid properties. Here, using a reservoir depth and temperature gradient (A), water (B), oil (C), gas (D), and CO_2 (E) fluid properties are calculated (Han 2011).

Table 9. Sandstone reservoir fluid properties calculated with FLAG calculator (Batzle et al. 1992, Han 2011).

Fluid Type	**ρ**	**V_P**	**K**
Water	1.062	1712.358	3.114
Oil	.777	1167.941	1.06
CO_2	.612	442.787	0.12

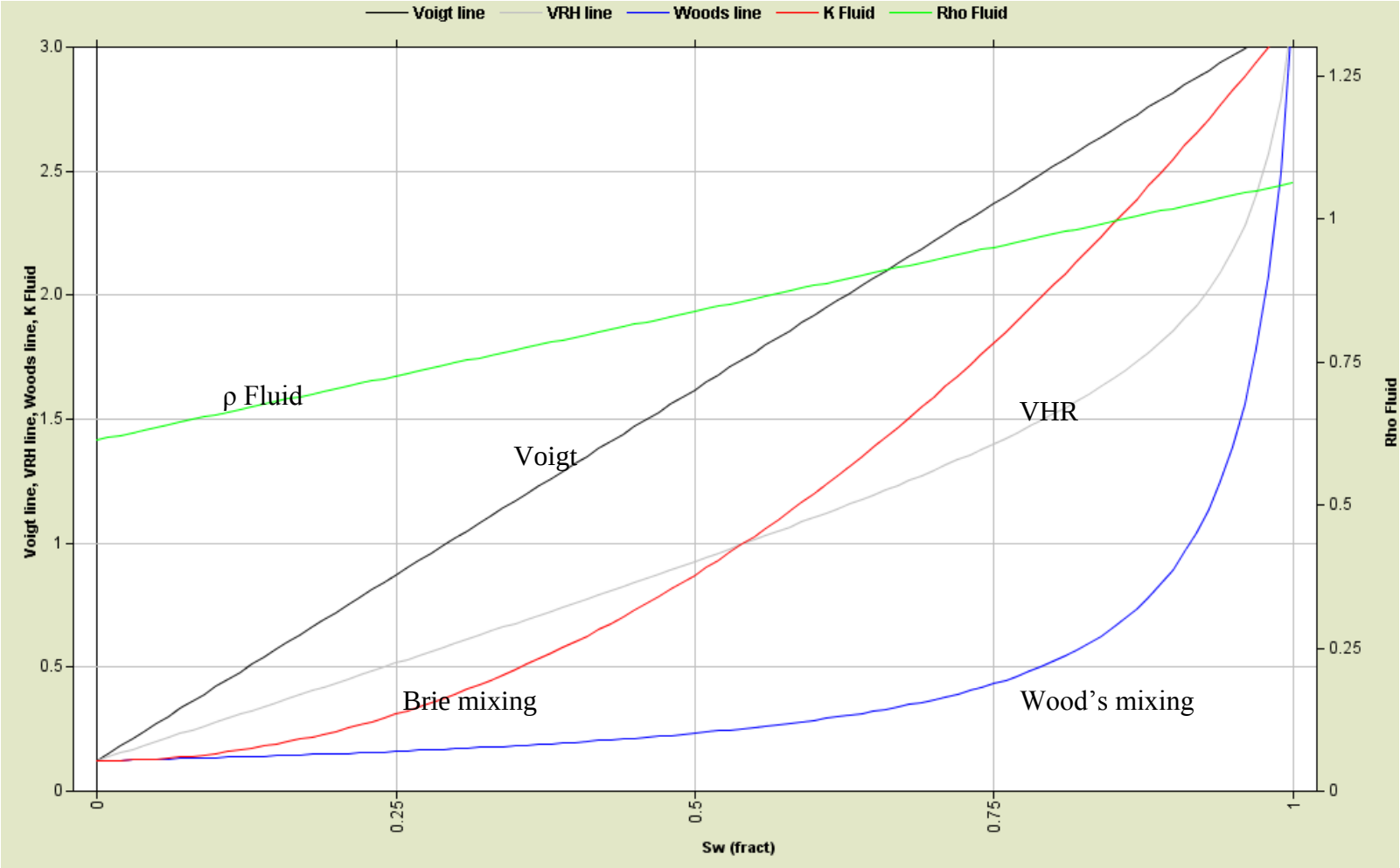

Figure 87. CO_2-Brine Mixing models. The bulk modulus and density (green) at varying CO_2-Brine fractions are shown. The Voigt (black), VHR (grey), Brie (red) and woods (blue) lines show the various mixing techniques effects on fluid bulk modulus.

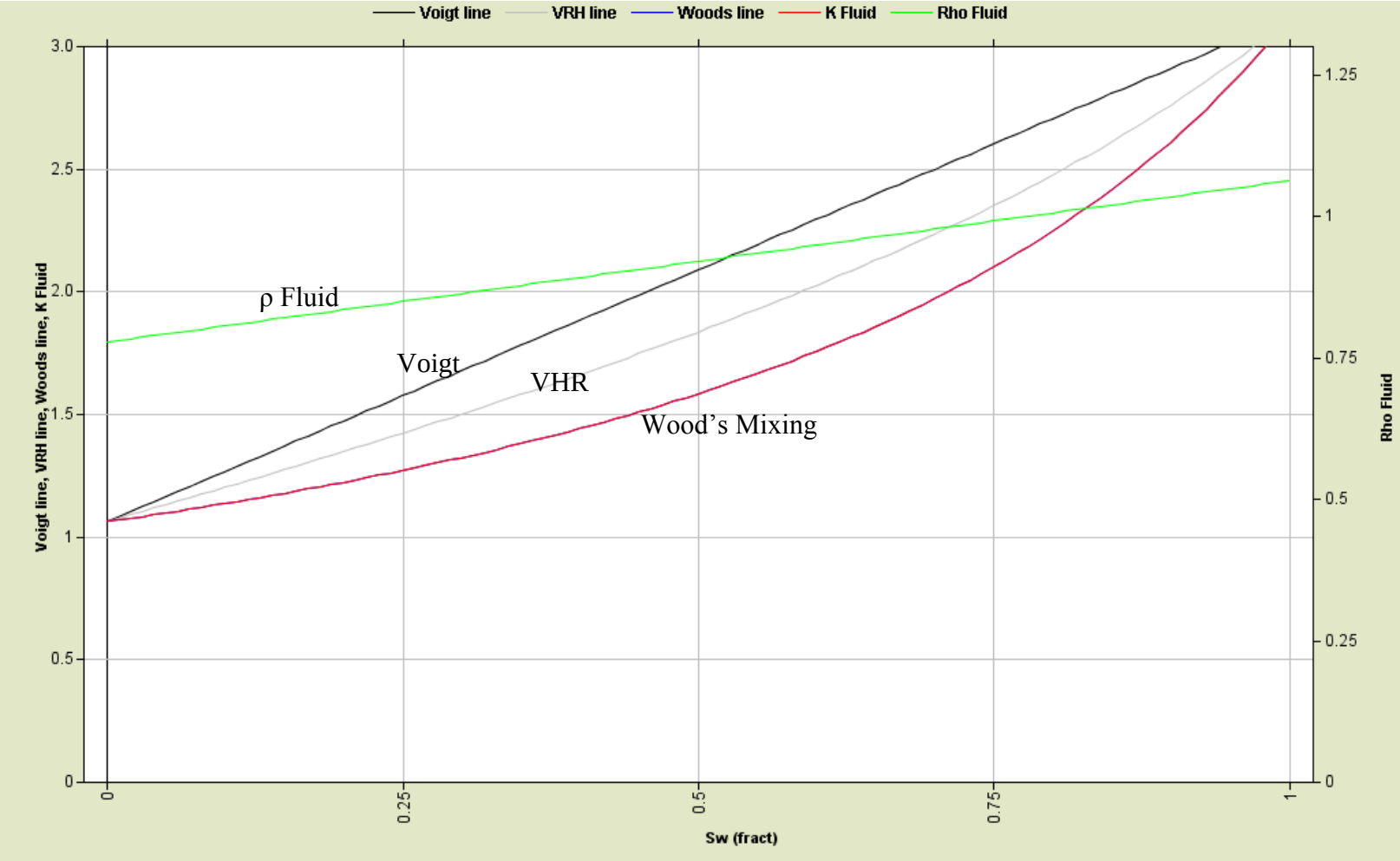

Figure 88. Oil-Brine Mixing Models. The bulk modulus and density at varying Oil-Brine fractions are shown in red and green. The Voigt (black), VHR (grey), and woods lines (here, red) show the various mixing techniques effects on fluid bulk modulus. Wood's mixing model has been chosen in this instance.

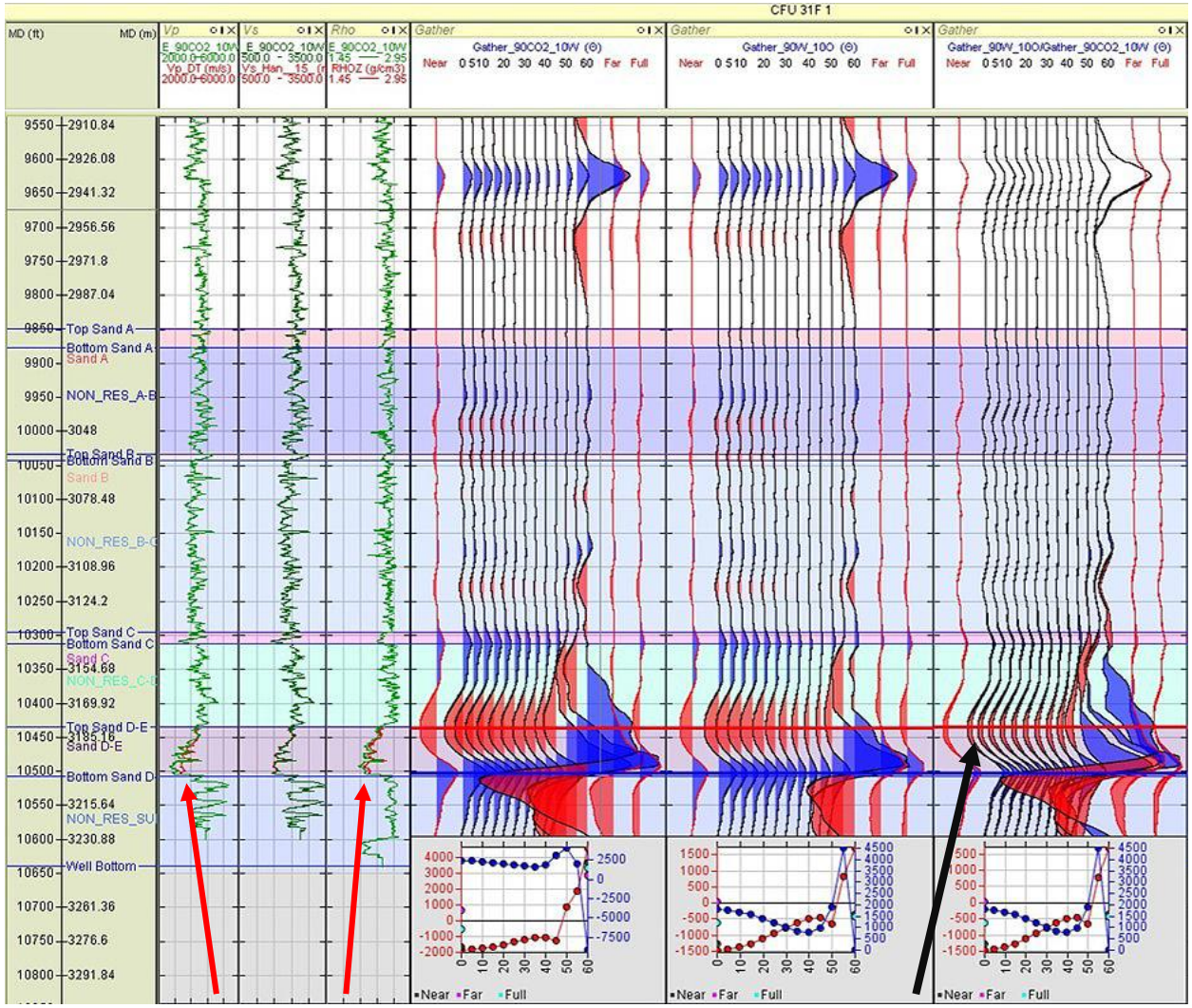

Figure 89. Well log with fluid substitution results: V_p, V_S, ρ, and gathers. The red arrows point to fluid substitution effects (shown in red) on the V_P and ρ curves (V_S is unaffected by fluid substitution). The black arrow points to difference of before and after gathers and shows large amplitude anomaly at high angle.

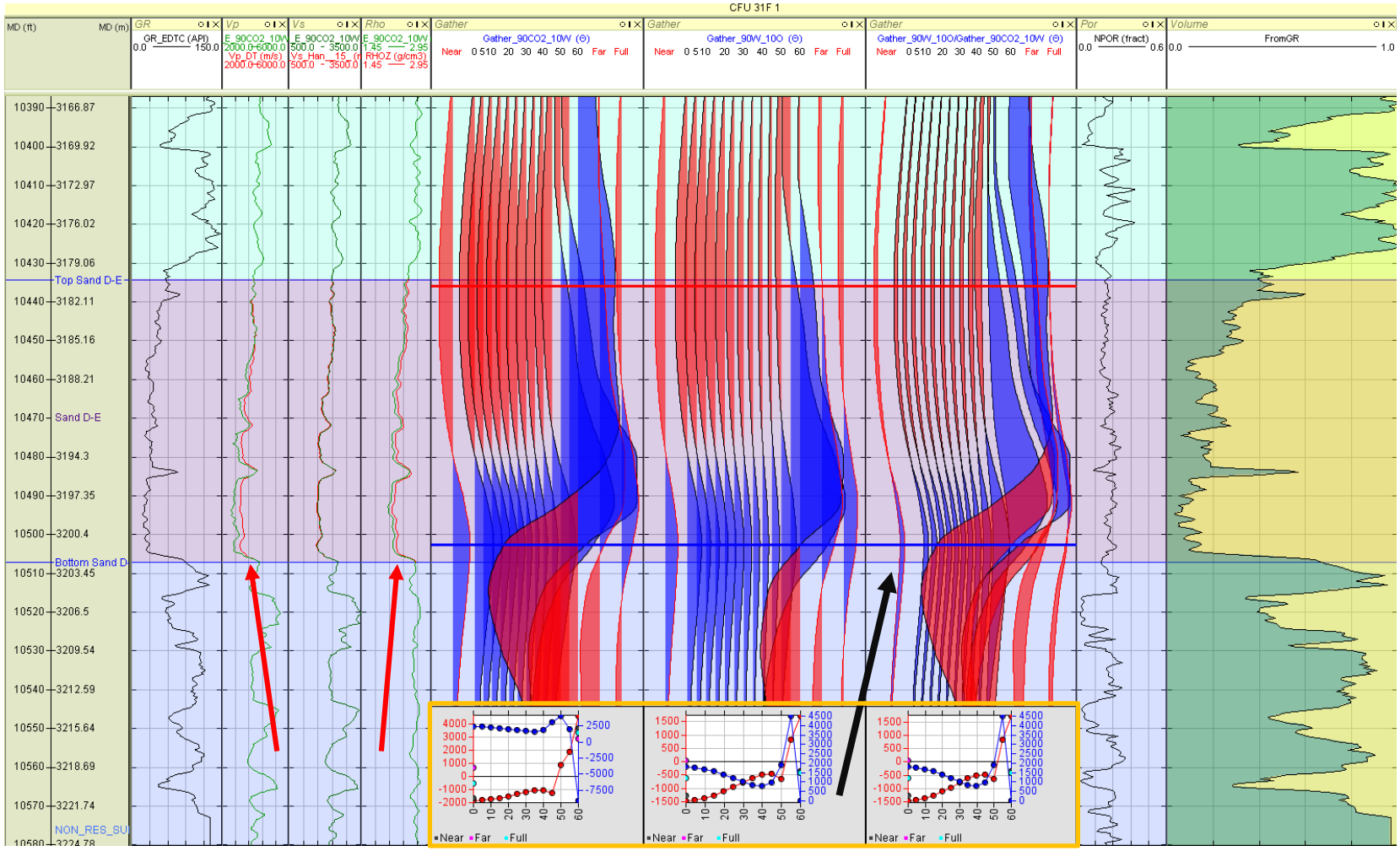

Figure 90. Magnification to reservoir unit. In this image, the volume fraction of sand (yellow) to shale (green) is shown in the far right column. The red arrows point to fluid substitution effects (shown in red) on the V_P and ρ curves (V_S is unaffected by fluid substitution). The black arrow points to full stack trace difference of before and after gathers and shows large amplitude anomaly at high angle. In the orange box, reflection amplitudes with increasing offset are depicted.

Figure 91 and Figure 92 show the impedance models at Cranfield revealing a potential 10-25% acoustic impedance decrease with the substitution of 75% CO_2 - 15% brine - 5% oil in place of the estimated 80% brine - 20% oil occupying the D-E reservoir unit. This significant impedance difference leads to the increased reflectivity in the zero offset model seen in Figure 93.

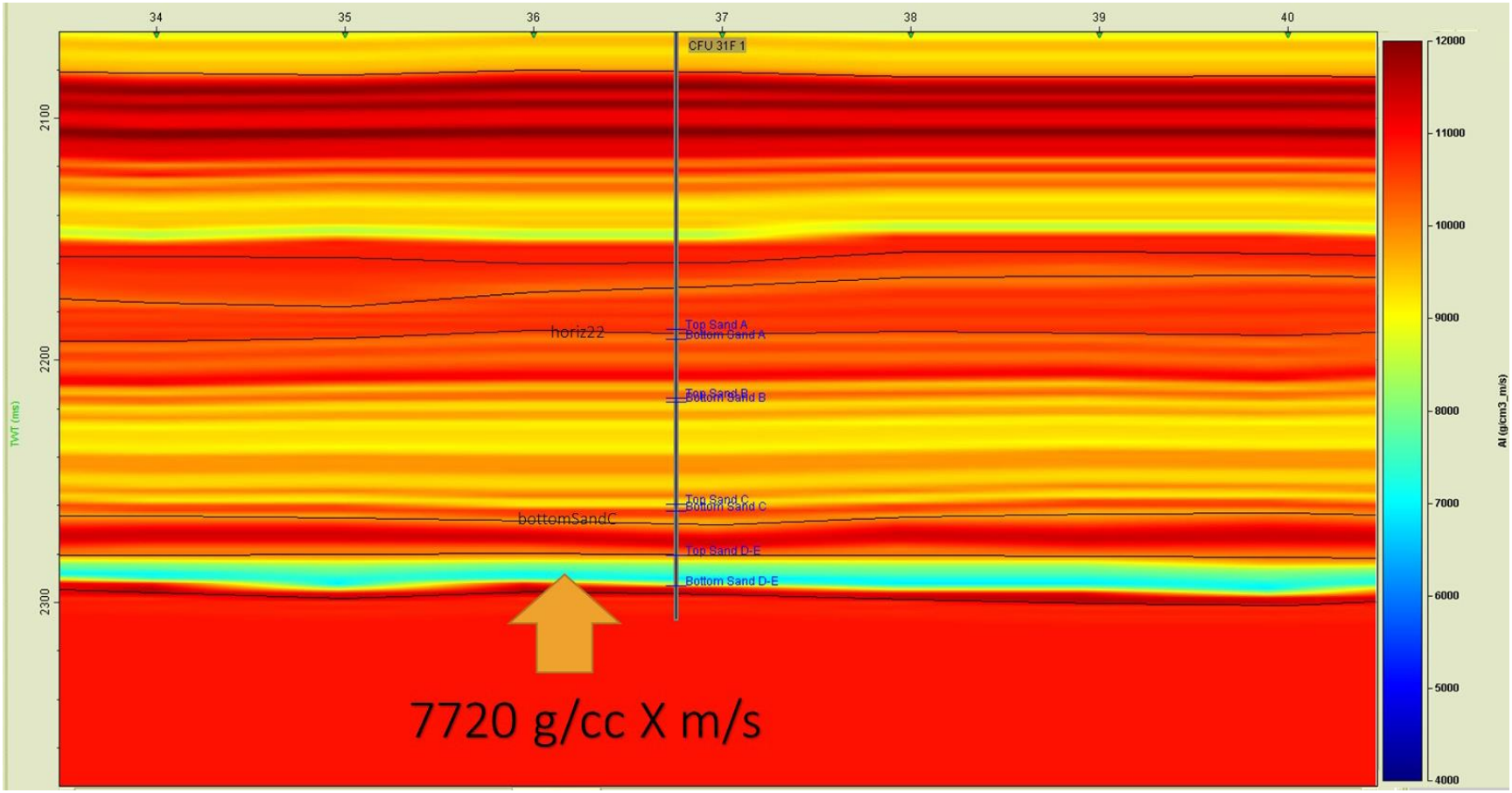

Figure 91. Cranfield well CFU 31F Reservoir Model Acoustic Impedance (g/cc*m/s) (PreCO_2 substitution).

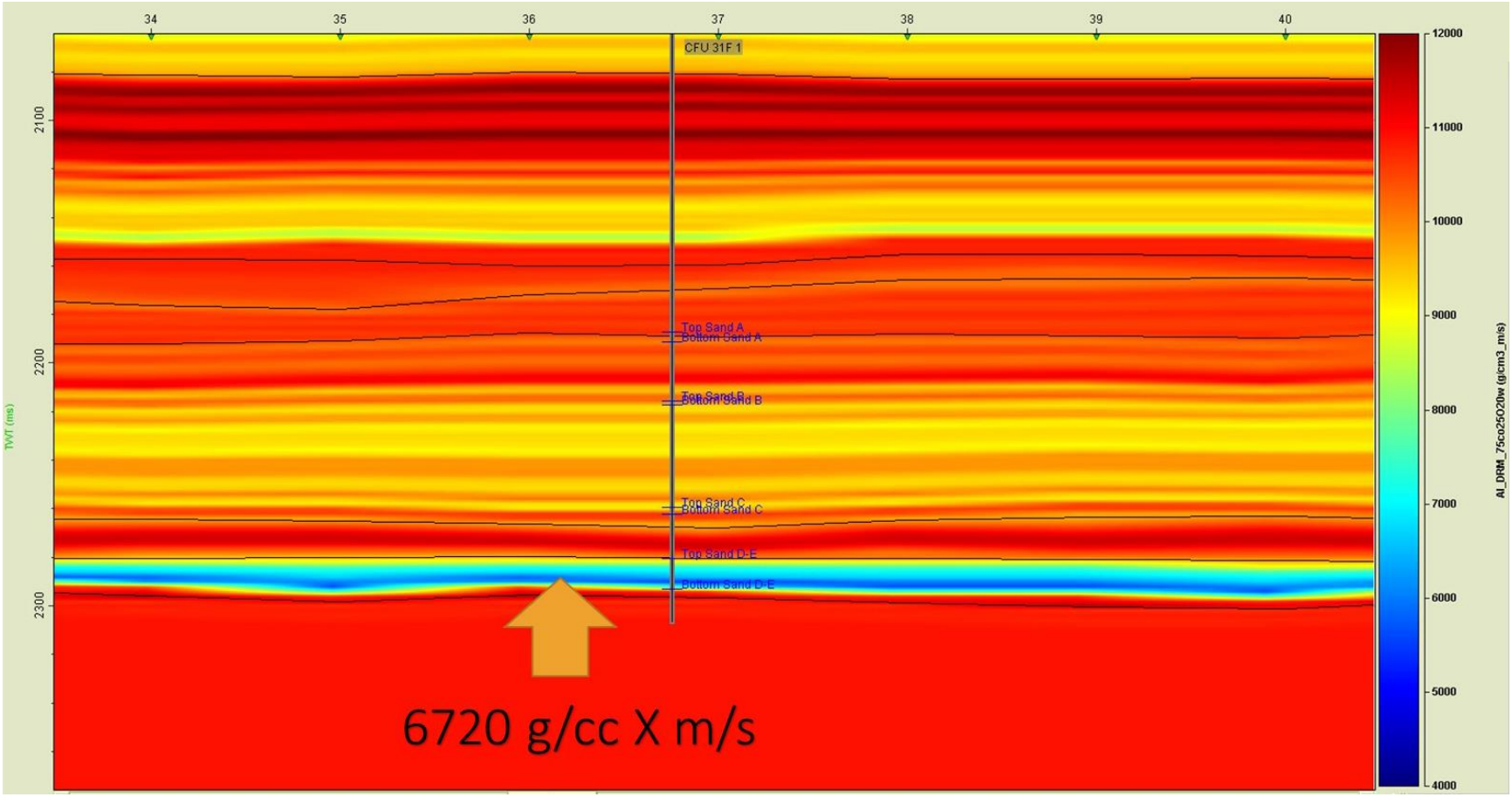

Figure 92. Cranfield well CFU 31F Reservoir Model Acoustic Impedance (g/cc*m/s) (Post CO_2 substitution). Fluid replaced value represents a 13% decrease in acoustic impedance in the unit. This model therefore predicts significant increases in reflectivity from fluid replacement due to CO_2 injection.

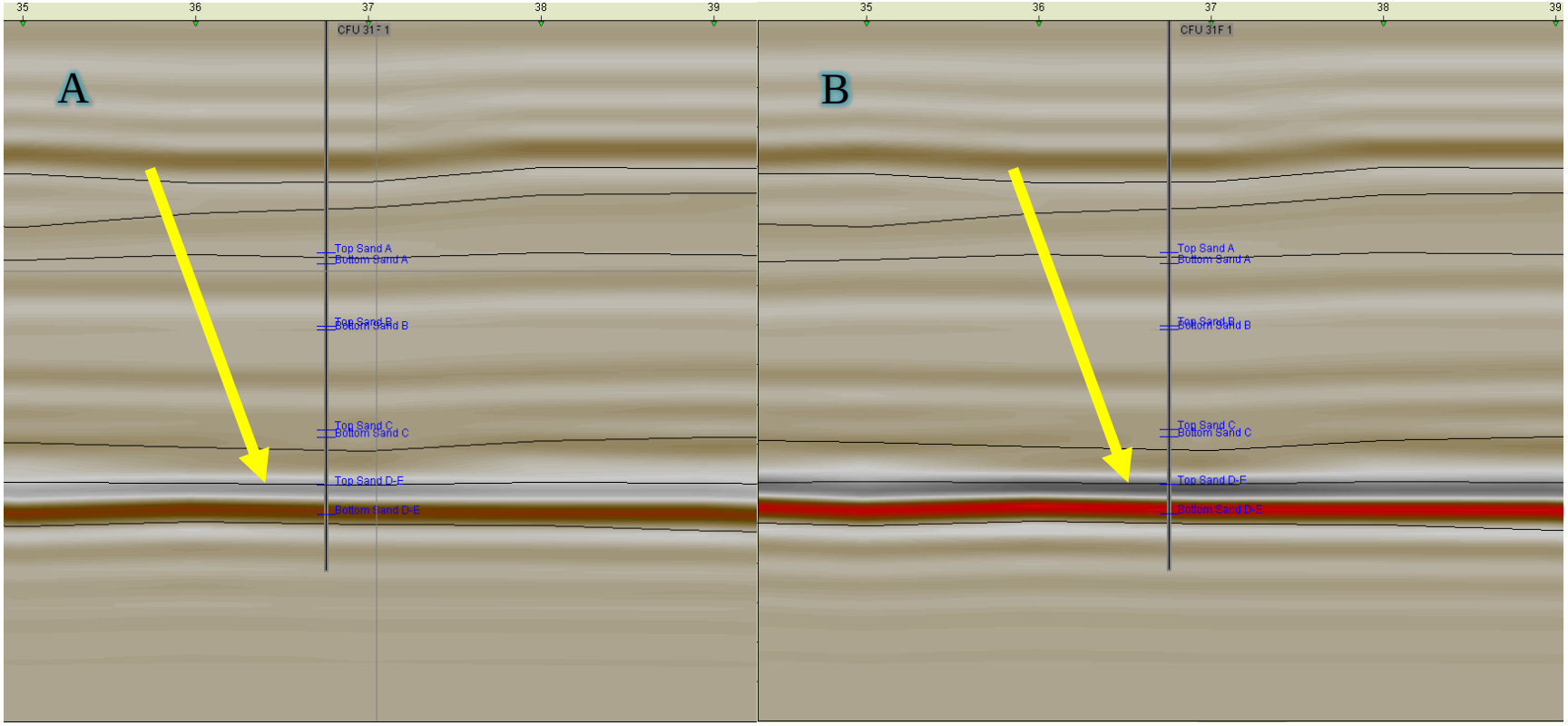

Figure 93. Cranfield Pre injection (A) and Post injection (B) reflection modeling. 13% decrease in acoustic impedance from CO_2 substitution causes increased reflection amplitudes as highlighted by the yellow arrows. The greater impedance contrast leads to greater negative reflections at the top of the sand unit and greater positive reflections at the lower sand unit.

5.3.2 Porosity Analysis

An acoustic impedance to porosity transform was produced by cross plotting the Cranfield well log acoustic impedance and porosity values. The well log porosity and acoustic impedance values were colorized by gamma ray and using known high gamma ray values greater than 80 API (standard measure of natural gamma radiation measured in a borehole) for shale and less than 45 API for sandstone, two curves were produced (Figure 94). A 5-iteration stochastic inversion using the seismic horizons, stacked seismic, extracted wavelet, and impedance log were used to create an impedance volume (cross section shown in Figure 95) to which the impedance to porosity transform is applied. Figure 96 and Figure 97 show the impedance to porosity transform applied to the reservoir. The lower injection sand unit, having different transform rules, has been merged back onto the shale cross section (with proper color scaling). These porosity models, in conjunction with seismic anomaly analysis, can allow reasonable volume calculations of injected CO_2 by overlapping with 3-D porosity and anomaly volumes.

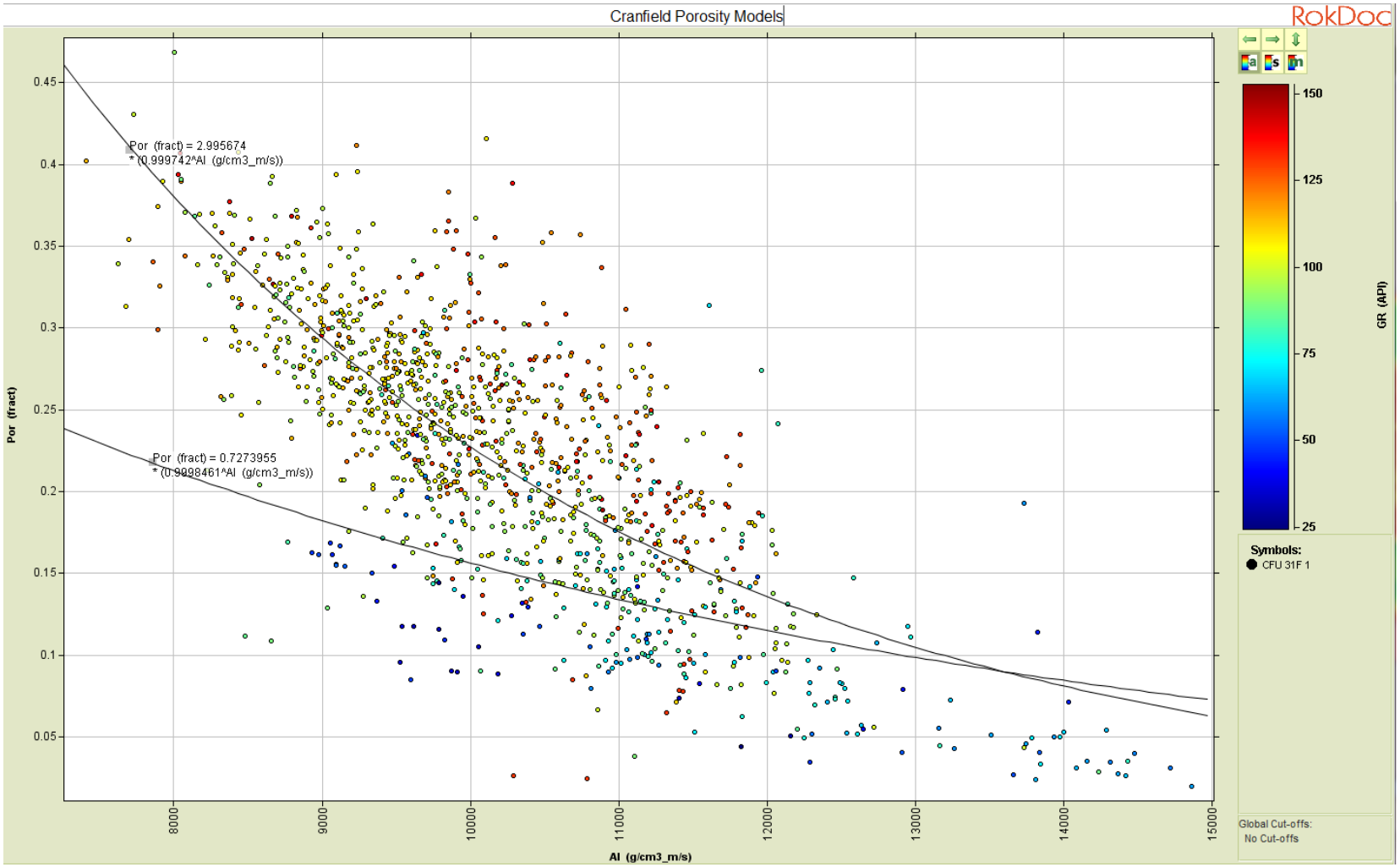

Figure 94. Acoustic impedance (segmented by gamma ray) to porosity transforms for Cranfield sand (GR<45API) and shale (GR>80API).

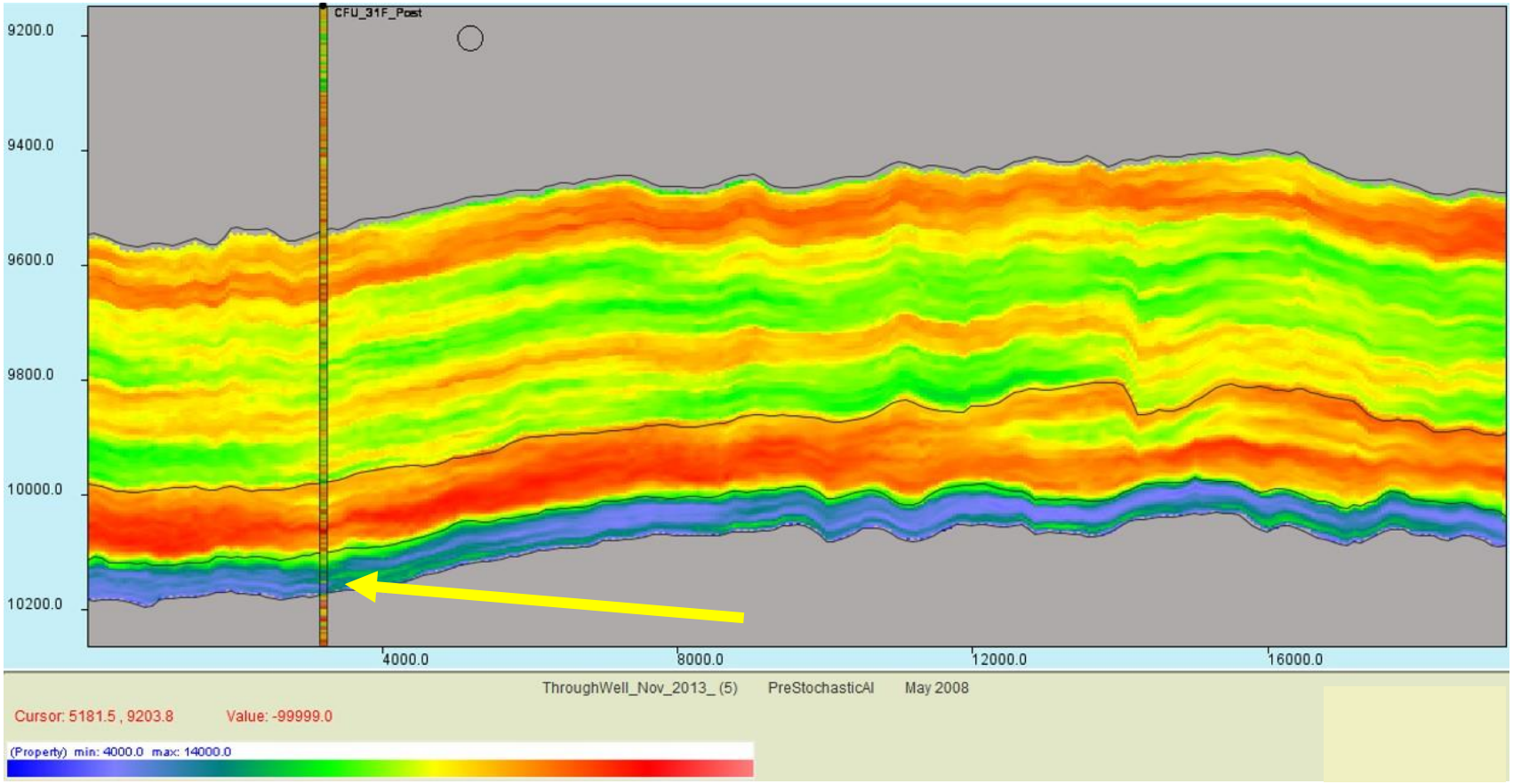

Figure 95. Stochastic inversion impedance product (average of 5 iterations). This inversion matches well with the model in relative layer to layer impedance model (Figure 91). The yellow arrow points to the reservoir unit.

.

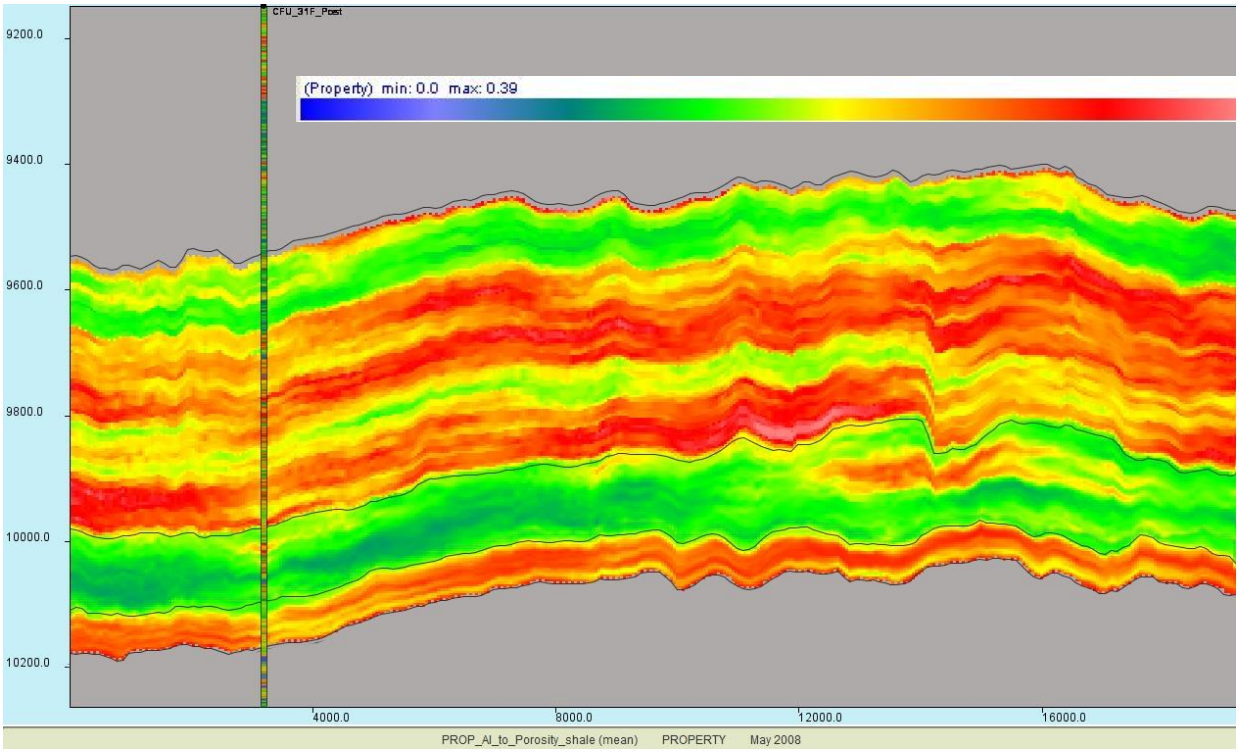

Figure 96. AI to porosity cloud transform (Sand D-E added to shale section) applied to stochastic inversion of preinjection reservoir stacked seismic and VP-RHOZ logs.

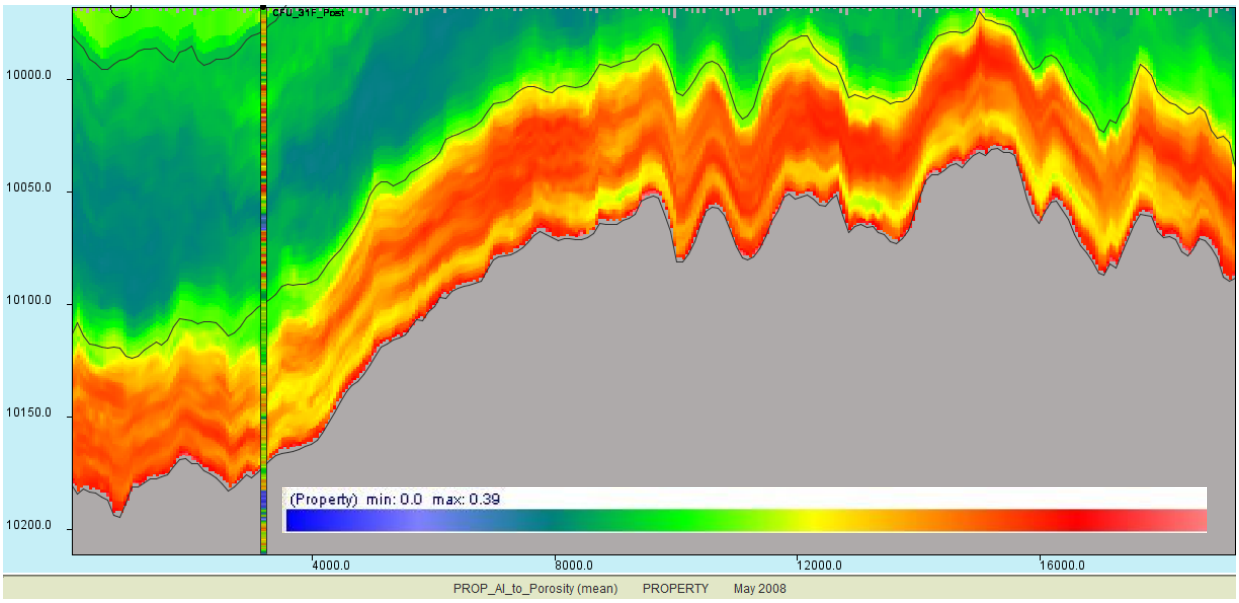

Figure 97. Magnified to reservoir unit: AI to porosity cloud transform (for Sand D-E) applied to stochastic inversion of preinjection reservoir stacked seismic and VP-RHOZ logs.

6.0 CONCLUSION

This study has explored sample mechanics across the micron to kilometer scales as well as reactivity to acidified water over time. Frequency and stress dependent rock models that include permeability, pore stress sensitivity and pore orientation observations were produced.

Crack orientation effects on rock compressibility and velocity anisotropy as well as the diffusion of wave energy were observed. Zones of more dense rock, observed with the medical CT scanner, in the 6.6% porosity limestone core (see Figure 40) have caused S-wave anisotropy that could not be observed by the P-wave measurements due to the polar nature of the S-waves.

Chemical experiments revealed that in the carbonate reservoir material, small mass losses due to exposure to acidic CO_2-water mixes caused changes in ultrasonic velocity and permeability. Dissolution rate, $k_{i\theta}$, for sample HP-L, having the total external surface area of $1.5*10^1$ cm^2 was calculated $k_{i\theta}=1.54*10^{-10} mol/m^2/s$, which is predictably faster than surface water-calcite dissolution rates (Van Eldik et al. 1982) and up to four orders of magnitude faster than silica release from quartz in similar conditions (Lasaga 1984). Without pressure driven fluid reaction experiments, surficial exposure experimental results best represent fracture network chemical exposure, not internal matrix pore surface exposure. Equation 76 and matrix and reservoir permeability measurements are solved for a minimum fracture width of 31 μm in zones of 2500 mD permeability. μCT observations revealed an internal fracture path of similar width characteristics (Figure 57) and the effects of CO_2 dissolution on the fracture.

The low confining pressure permeability increases confirm that flow path widths are potentially increased. The sensitivity to effective pressure is also increased with dissolution, as

velocity measurements show increases in the low effective pressure regimes (5-10 MPa) P-wave velocity increases up to 10% (Figure 62). As effective pressure increases, permeability decreases up to 5% at 40 MPa confining pressure and high flow rates (Figure 58).

Injection increases pore pressure and thus decreases effective pressure. The dissolution of reservoir limestone causes increased low effective pressure permeability leading to low-frequency wave attenuation increases and velocity decreases (rock model described in Section 2.2.2) in reflection seismic observations of the carbonate reservoir with continued CO_2 injection. Conversely, if injection were to cease or production increased, the model predicts that compliant pores and cracks will close due to increased effective pressure resulting in permeability losses, velocity increases, and attenuation decreases. This understanding of reservoir pore pressure, permeability, and injection rate relationships will aid injection scenario planning to maximize fluid injection volumes without losing permeability and valuable pore space.

For the sandstone reservoir, fluid substitution modeling and pre and post injection reflection seismic prestack wave observations were used to better understand the effects of CO_2 injection. Figure 91 and Figure 92 show the impedance models at Cranfield revealing a potential 10-25% acoustic impedance decrease 13% with the substitution of 75% CO_2 - 15% brine - 5% oil in place of the estimated 80% brine - 20% oil occupying the D-E reservoir unit. This significant impedance difference leads to the increased reflectivity in the zero offset model seen in Figure 93 shows the result of a an acoustic impedance to porosity transform performed on acoustic impedance inversions.

Fluid injection causes increased pore pressure (lower effective pressure) in reservoir units and increased confining (effective) pressure on neighboring rock unconnected by permeability. These effective pressure changes affect rock velocities. Once these rock velocity effects are

accounted for in 4D difference volumes, the subtle fluid bulk and density properties can be interpreted. Proper interpretation requires knowledge of solubility, miscibility, and reactivity of the fluid mixtures created in a given reservoir. Much work must be done at all model and observation stages to quantify directly, pore-filling fluid changes. The most successful method merges strong porosity models with anomaly volumes and measures the pore volume that the anomaly effects. As the understanding of how limestone and sandstone rocks behave under stress, when filled with different fluids continues to improve, and computer processing power increases, cost effective integration of orthorhombic or Thomsen's anisotropy parameters to the velocity modeling process from pre-stack to attribute analysis, stress sensitive pore pressure models, and effective fluid substitution methods will give a space in seismic models for more complete rock frame properties, producing realistic pore filling fluid interpretations.

APPENDIX A

POST EXPOSURE VELOCITY MEASUREMENT REPORT

Sample and Experiment Information for File 1349983779			
Well:		Organization:	National Energy Technology Lab
Depth:	2000.0 m	Transducer:	NETL_2.0inch_male_with_perm
Formation:		Rock type:	Limestone
Dry bulk density:	2.220 gm/cm^3	Porosity:	16.0%
Sat. bulk density:		Pore fluids:	Air
Diameter:	50.10 mm	Entered Length:	67.00 mm

Comments:	User: igor on al1500 at Thu Aug 9 17:23:36 EDT 2012
Expt name:	1349983775
Expt date:	Thu Oct 11 15:39:49 2012
Print date:	Fri Oct 12 13:37:44 2012
A2D File:	

Table 10. Event Picks for experiment 1349983779

Event	Conf	Pore	Diff	Temp	t_p	$t_s^{(1)}$	$t_s^{(2)}$
	MPa	MPa	MPa	°C	μsec	μsec	μsec
0	2.3	0.1	-0.1	22.9	27.475	50.848	50.347
1	4.3	0.1	-0.1	23.0	26.790	50.848	50.096
2	6.3	0.1	-0.2	23.4	26.348	50.096	49.637
3	8.3	0.1	-0.1	23.5	26.540	49.595	48.994
4	10.3	0.1	-0.3	23.7	26.289	49.770	48.776
5	12.3	0.1	-0.2	23.8	26.139	49.520	48.342
6	14.3	0.1	-0.3	23.9	26.072	49.144	48.066
7	16.3	0.1	-0.4	23.9	25.905	48.914	48.054
8	18.3	0.1	-0.6	24.0	25.788	48.664	47.891
9	20.3	0.1	-0.7	24.0	25.780	48.580	47.657
10	22.3	0.1	-0.8	24.1	25.537	48.413	47.590
11	24.3	0.1	-0.7	24.1	25.529	48.309	47.490
12	26.2	0.1	-0.9	24.1	25.487	48.183	47.427
13	28.2	0.1	-0.9	24.0	25.429	47.974	47.277
14	30.3	0.1	-1.0	24.1	25.445	47.954	47.198
15	32.3	0.1	-1.1	24.2	25.429	47.870	47.189
16	34.3	0.1	-1.4	24.2	25.287	47.724	46.939
17	36.2	0.1	-1.1	24.2	25.345	47.599	47.005
18	38.2	0.1	-1.4	24.1	25.345	47.473	46.838
19	40.2	0.1	-1.4	24.2	25.262	47.340	46.730

Event	Conf	Pore	Diff	Temp	t_p	$t_s^{(1)}$	$t_s^{(2)}$
	MPa	MPa	MPa	°C	μsec	μsec	μsec
20	42.2	0.1	-1.6	24.2	25.345	47.327	46.730
21	44.3	0.1	-1.6	24.2	25.287	47.243	46.605
22	46.2	0.1	-1.7	24.3	25.161	47.089	46.605
23	48.2	0.1	-1.6	24.2	25.195	47.089	46.563
24	50.2	0.1	-1.7	24.4	25.153	47.077	46.738
25	48.3	0.1	-1.6	24.1	25.136	47.160	46.567
26	46.3	0.1	-1.6	23.7	25.161	47.243	46.605
27	44.2	0.1	-1.7	23.6	25.086	47.160	46.563
28	42.3	0.1	-1.5	23.3	25.161	47.223	46.521
29	40.3	0.1	-1.5	23.0	25.095	47.411	46.646
30	38.3	0.1	-1.3	23.1	25.195	47.411	46.688
31	36.3	0.1	-1.3	23.0	25.287	47.411	46.813
32	34.3	0.1	-1.2	22.9	25.387	47.578	46.980
33	32.3	0.1	-1.2	23.0	25.345	47.661	46.838
34	30.3	0.1	-1.1	22.9	25.387	47.661	46.913
35	28.3	0.1	-0.9	23.0	25.412	47.807	46.980
36	26.3	0.1	-0.8	22.9	25.412	47.841	47.122
37	24.4	0.1	-0.9	22.9	25.412	48.037	47.231
38	22.3	0.1	-0.7	22.9	25.471	48.079	47.164
39	20.3	0.1	-0.6	22.9	25.537	48.225	47.315
40	18.3	0.1	-0.7	22.7	25.805	48.267	47.565
41	16.3	0.1	-0.5	22.7	25.846	48.622	47.565
42	14.3	0.1	-0.6	22.7	25.913	48.872	47.590
43	12.3	0.1	-0.4	22.7	26.055	49.123	48.025
44	10.3	0.1	-0.4	22.7	26.180	49.332	48.192
45	8.3	0.1	-0.2	22.6	26.348	49.666	48.484
46	6.3	0.1	-0.0	22.6	26.414	49.094	49.127
47	4.3	0.1	-0.2	22.5	26.724	50.096	49.808
48	2.4	0.1	0.2	22.5	27.041	50.347	50.531

Table 11. Observed Velocities and Moduli for experiment 1349983779

Event	Conf	Pore	Diff	Temp	V_p	$V_s^{(1)}$	$V_s^{(2)}$	Young's Modulus	Poisson's Ratio
	MPa	MPa	MPa	°C	m/s	m/s	m/s	GPa	
0	2.3	0.1	-0.1	22.9	4101	2245	2291	29.23	0.280
1	4.3	0.1	-0.1	23.0	4281	2245	2311	30.01	0.303
2	6.3	0.1	-0.2	23.4	4405	2303	2348	31.38	0.307
3	8.3	0.1	-0.1	23.5	4350	2343	2402	32.20	0.288
4	10.3	0.1	-0.3	23.7	4422	2329	2421	32.49	0.297
5	12.3	0.1	-0.2	23.8	4467	2349	2460	33.27	0.296
6	14.3	0.1	-0.3	23.9	4487	2381	2485	33.95	0.292
7	16.3	0.1	-0.4	23.9	4537	2400	2486	34.34	0.296
8	18.3	0.1	-0.6	24.0	4574	2422	2501	34.87	0.296
9	20.3	0.1	-0.7	24.0	4576	2429	2523	35.20	0.293
10	22.3	0.1	-0.8	24.1	4653	2444	2530	35.70	0.300
11	24.3	0.1	-0.7	24.1	4656	2454	2539	35.93	0.298
12	26.2	0.1	-0.9	24.1	4669	2465	2545	36.16	0.298
13	28.2	0.1	-0.9	24.0	4689	2484	2560	36.61	0.296
14	30.3	0.1	-1.0	24.1	4683	2486	2568	36.71	0.295
15	32.3	0.1	-1.1	24.2	4689	2494	2569	36.83	0.294
16	34.3	0.1	-1.4	24.2	4736	2507	2594	37.42	0.296
17	36.2	0.1	-1.1	24.2	4716	2519	2587	37.41	0.293
18	38.2	0.1	-1.4	24.1	4716	2531	2604	37.74	0.289
19	40.2	0.1	-1.4	24.2	4744	2544	2615	38.11	0.290
20	42.2	0.1	-1.6	24.2	4716	2545	2615	38.02	0.286
21	44.3	0.1	-1.6	24.2	4736	2553	2628	38.33	0.287
22	46.2	0.1	-1.7	24.3	4778	2568	2628	38.66	0.290
23	48.2	0.1	-1.6	24.2	4767	2568	2632	38.67	0.288
24	50.2	0.1	-1.7	24.4	4781	2570	2614	38.54	0.292
25	48.3	0.1	-1.6	24.1	4786	2561	2631	38.65	0.292
26	46.3	0.1	-1.6	23.7	4778	2553	2628	38.49	0.292
27	44.2	0.1	-1.7	23.6	4804	2561	2632	38.72	0.294
28	42.3	0.1	-1.5	23.3	4778	2555	2636	38.61	0.291
29	40.3	0.1	-1.5	23.0	4801	2537	2623	38.33	0.297
30	38.3	0.1	-1.3	23.1	4767	2537	2619	38.16	0.293
31	36.3	0.1	-1.3	23.0	4736	2537	2606	37.90	0.291
32	34.3	0.1	-1.2	22.9	4702	2521	2589	37.40	0.291
33	32.3	0.1	-1.2	23.0	4716	2513	2604	37.53	0.291
34	30.3	0.1	-1.1	22.9	4702	2513	2596	37.39	0.291
35	28.3	0.1	-0.9	23.0	4694	2500	2589	37.14	0.292
36	26.3	0.1	-0.8	22.9	4694	2496	2575	36.94	0.294
37	24.4	0.1	-0.9	22.9	4694	2478	2564	36.61	0.297
38	22.3	0.1	-0.7	22.9	4675	2474	2571	36.58	0.295

Event	Conf	Pore	Diff	Temp	V_p	$V_s^{(1)}$	$V_s^{(2)}$	Young's Modulus	Poisson's Ratio
39	20.3	0.1	-0.6	22.9	4653	2461	2556	36.18	0.295
40	18.3	0.1	-0.7	22.7	4568	2457	2532	35.57	0.288
41	16.3	0.1	-0.5	22.7	4555	2426	2532	35.19	0.290
42	14.3	0.1	-0.6	22.7	4535	2404	2530	34.85	0.290
43	12.3	0.1	-0.4	22.7	4492	2383	2489	34.03	0.292
44	10.3	0.1	-0.4	22.7	4454	2365	2474	33.55	0.291
45	8.3	0.1	-0.2	22.6	4405	2337	2447	32.79	0.291
46	6.3	0.1	-0.0	22.6	4386	2385	2391	32.64	0.289
47	4.3	0.1	-0.2	22.5	4299	2303	2334	30.91	0.295
48	2.4	0.1	0.2	22.5	4213	2283	2277	29.84	0.293

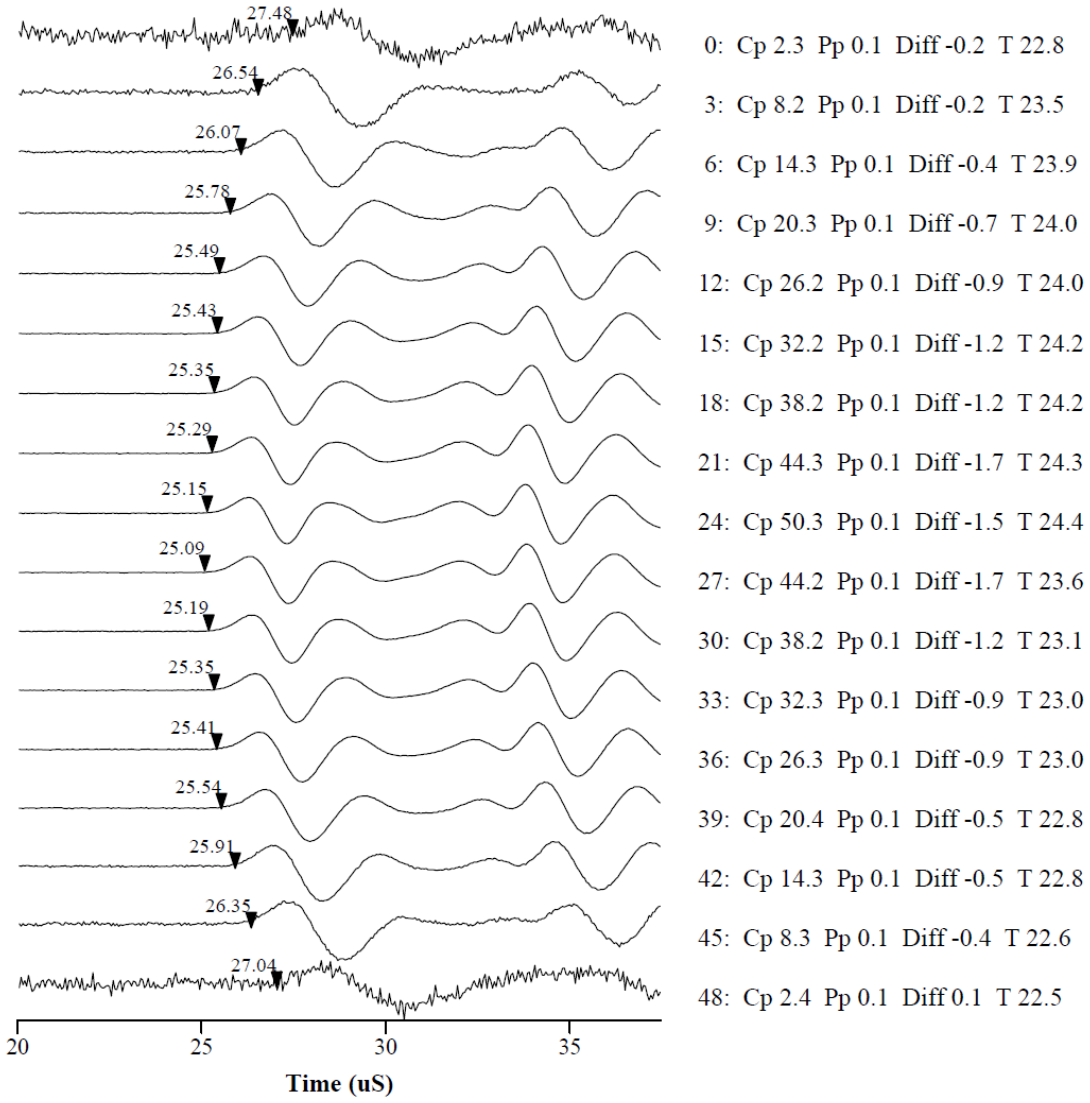

Figure 98. Waveform waterfall for P arrivals for experiment 11349983775, carbonate, 2000m depth.

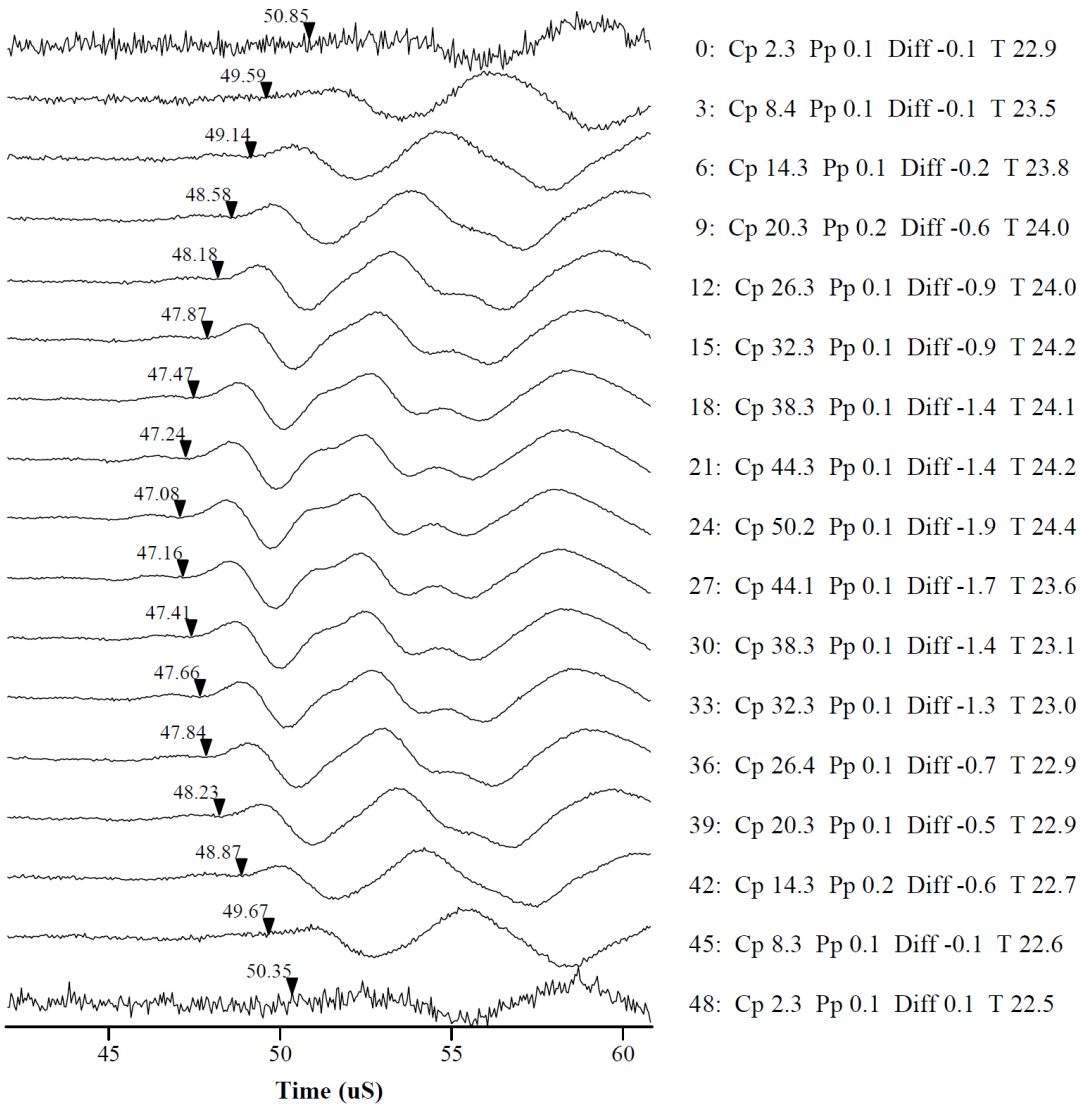

Figure 99. Waveform waterfall for S1 arrivals for experiment 11349983775, carbonate, 2000m depth.

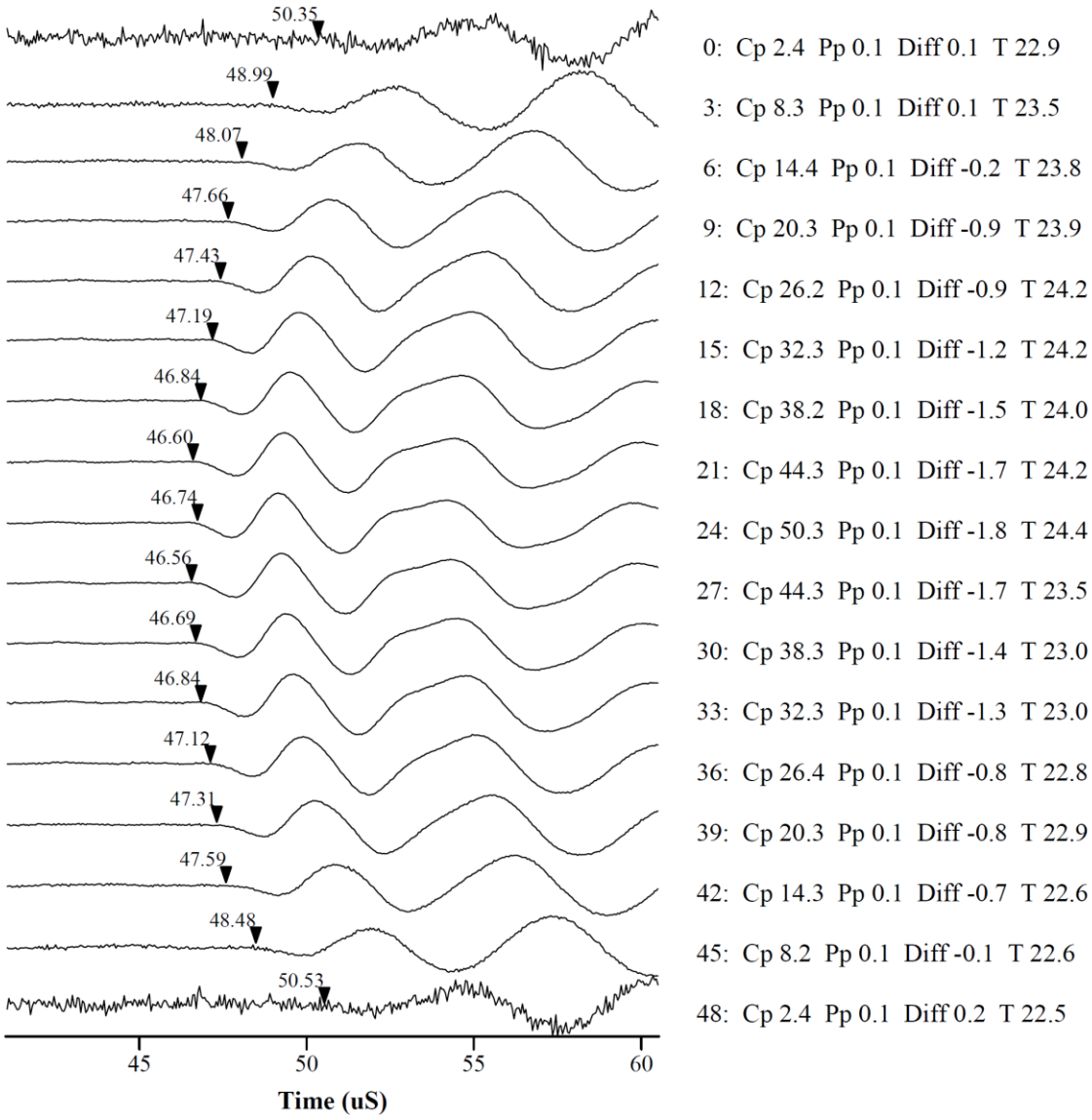

Figure 100. Waveform waterfall for S2 arrivals for experiment 11349983775, carbonate, 2000 m depth.

MATLAB CODE

A.1.1 Complex Velocity as Function of Pressure

```
Pressure=(0.0005:.0005:.05);
PressureMPA=(0.5:0.5:50);
Kgr=74.5;
% Kmt(grain material)
ugr=33;
% umt(grain material)
gamma=.0006;
% aspect ratio
rho_mineral=2.7;
%mineral density
rho_fluid=.001183;
Poiss_Mineral=(3*Kgr-2*ugr)/(2*(3*Kgr+ugr));

VS_Correction=450;
K_fluid=0.101;
phiS=.184625;
%(stiff_unload)
phiC=.000375;
%complient_unload

theta_s=1+(3*Kgr)/(4*ugr);
theta_su=1+(6*Kgr+2*ugr)/(9*Kgr+8*ugr);
theta_c=Kgr*(3*Kgr+4*ugr)/(pi*gamma*ugr*(3*Kgr+ugr));
theta_cu=1/5*(1+(4*(3*Kgr+4*ugr)*(9*Kgr+4*ugr))/(3*pi*gamma*(3*K
gr+ugr)*(3*Kgr+2*ugr)));

KphiS=Kgr*2*(1-2*Poiss_Mineral)/(3*(1-Poiss_Mineral));
uphiS=ugr*2*(7-5*Poiss_Mineral)/(15*(1-Poiss_Mineral));


Kdry=(1/Kgr+phiS/KphiS)^(-1);
udry=(1/ugr+phiS/uphiS)^(-1);

KdryS=Kdry*(1-theta_s*phiS);
udryS=udry*(1-theta_su*phiS);
```

```
rhoP=rho_mineral*(1-phiS-phiC)+rho_fluid*(phiS+phiS);
%bulk density

KdryPeff=KdryS*(1+theta_s*(1/KdryS-1/Kgr).*Pressure-
phiC*theta_c.*exp(-theta_c*(1/KdryS).*Pressure));
KsatPeff=KdryPeff+((1-KdryPeff/Kgr).^2)/((phiS/K_fluid)+(1-
phiS)/udryS-K_fluid/(Kgr^2));
udryPeff=udryS*(1+theta_su*((1/KdryS)-(1/Kgr))*Pressure-
phiC*theta_cu*exp(-theta_c*(1/KdryS)*Pressure));

Vp_calib=1000*sqrt((KsatPeff+udryPeff*4/3)/rhoP);
Vs_calib=1000*sqrt(udryPeff/rhoP)-VS_Correction;

load('HPLS_Air_PreCO2.mat');
%load data
observed(:,1)=observed(:,1)/1000;

figure(1)
plot(Pressure,Vp_calib)
hold on
plot(Pressure,Vs_calib)
xlabel('Effective Pressure (GPA)')
ylabel('Velocity (m/s)')
axis([0 .050 1000 5000])
plot(observed(:,1),observed(:,2),'--
rs','LineWidth',2,'MarkerEdgeColor','k','MarkerFaceColor','r','M
arkerSize',5)
plot(observed(:,1),observed(:,3),'--
rs','LineWidth',2,'MarkerEdgeColor','k','MarkerFaceColor','g','M
arkerSize',5)
plot(observed(:,1),observed(:,4),'--
rs','LineWidth',2,'MarkerEdgeColor','k','MarkerFaceColor','c','M
arkerSize',5)

obsQ=1/15.3;
obsFreq=150000;
Kmin=Kdry;
Emin=KdryS;
pg=2.715;
%density of grain
phiS=phiS;
pf=rho_fluid;
%density of fluid
K=1/(1/Kmin*1+phiS/27.66);
E=1/(1/Emin+phiS/34.70);
```

```
pb=pg*(1-phiS)+pf*phiS;

Lb=(3*K*(3*K+E))/(9*K-E);
%dry Pwave modulus
ab=.5;
%biot-willis coefficient ab=K/H
Mb=2.2;
%fluid bulk modulus
kb=.0023;
%permeability units?
n=1;
%viscosity
Cb=Lb+(ab^2)*Mb;
%H=
Db=kb*Mb*Lb/(n*Cb);
dN=.1
Lowfreqs=(0.0001:.01:100);
Highfreqs=(100:100:100000000);
freqs=[Lowfreqs(:,:) Highfreqs];
%O=2*pi*100;
O=sqrt(freqs*1i);
% O=w*(H*Mb/(2*Cb*Db))^2
Rb=ab*Mb/Cb;


C33=1./((1/Cb)+((dN*(Rb-1)^2))./(Lb*(1-
dN+dN*((O).*cot(Cb/Mb*(O))))));
Vp3=sqrt(C33/pb);
Vp=(real(Vp3.^-1)).^(-1);
%km/s?
Qinv=(2*Vp.*imag((Vp3).^-1));
Lfreq=log(freqs);

figure(2);
semilogx(freqs,Vp)
title('\it(Mavko et al. 1998)','FontSize',16)
xlabel('Frequency')
ylabel('P-wave Velocity km/s')
hold on
%figure(2);
%plot(freqs,Qinv)
figure(3);
loglog(freqs,Qinv)
xlabel('Frequency')
ylabel('Attenuation (1/Q)')
hold on
```

```
plot(obsFreq,obsQ)
```

A.1.2 Fracture Width from Permeability

```
%Calculates fracture width from fracture spacing, angle,
permeability
%Alan Mur 2013
km=2.3
% matrix permeability md
kh=2500
% horizontal permeability md
% w
% fracture width mm
alpha=10;
% angle of deviation of fracture from horizontal plane degrees
L=6;
% distance between fractures mm
w3=(kh-km)/(8.44*10^7);
%w3=(kh-km)/(5.446*10^10*(cosd(alpha/L))^2);
% if alpha and L are known
w=nthroot(w3,3)
```

A.1.3 Sound Study 1

```
t=0:0.001:200;
y=sin(2*pi*t.^2/.1); % notice the dot in the squaring
% t was defined before
sound(1000*y,1000) % to listen to the sinusoid
figure(2) % numbering of the figure
plot(t(1:100),y(1:100)) % plotting of 100 values of y
figure(3)
plot(t(1:100),x(1:100),'k',t(1:100),y(1:100),'r') % plotting x
and y on same plot
y=sin(2*pi*t.^2/.1); % notice the dot in the squaring
% t was defined before
```

```
sound(1000*y,1000) % to listen to the sinusoid
figure(2) % numbering of the figure
plot(t(1:100),y(1:100)) % plotting of 100 values of y
figure(3)
plot(t(1:100),x(1:100),'k',t(1:100),y(1:100),'r')
```

APPENDIX B

SEM AND CT MAPS

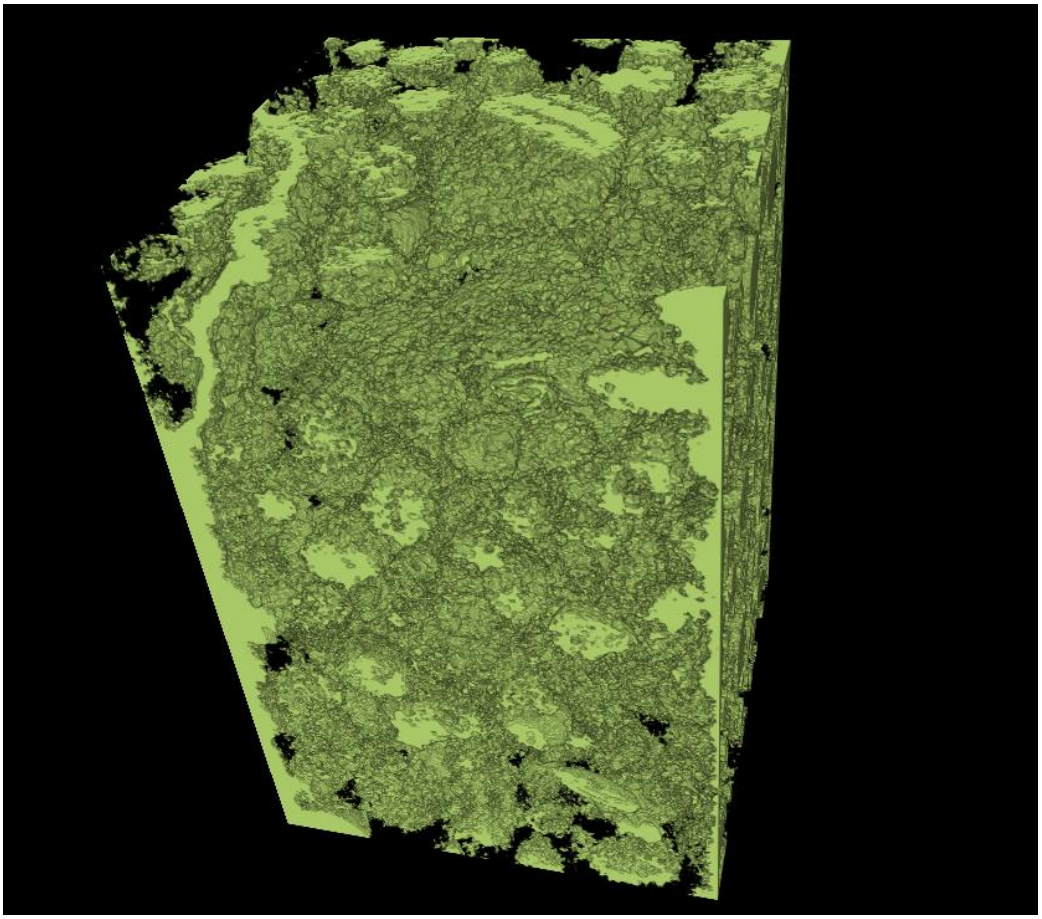

Figure 101 3-D volume of pore space

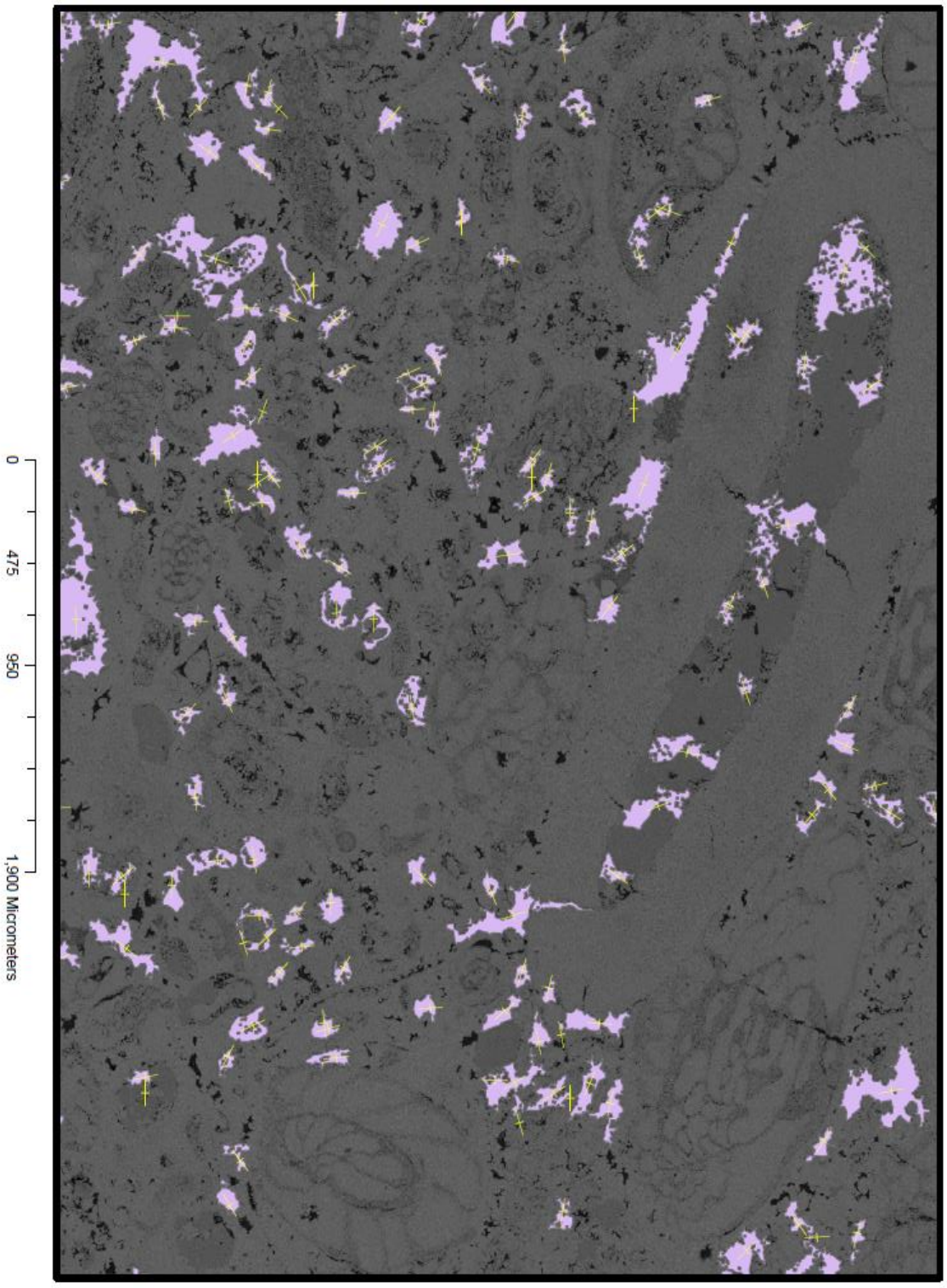

Figure 102 “West” pores and orientations

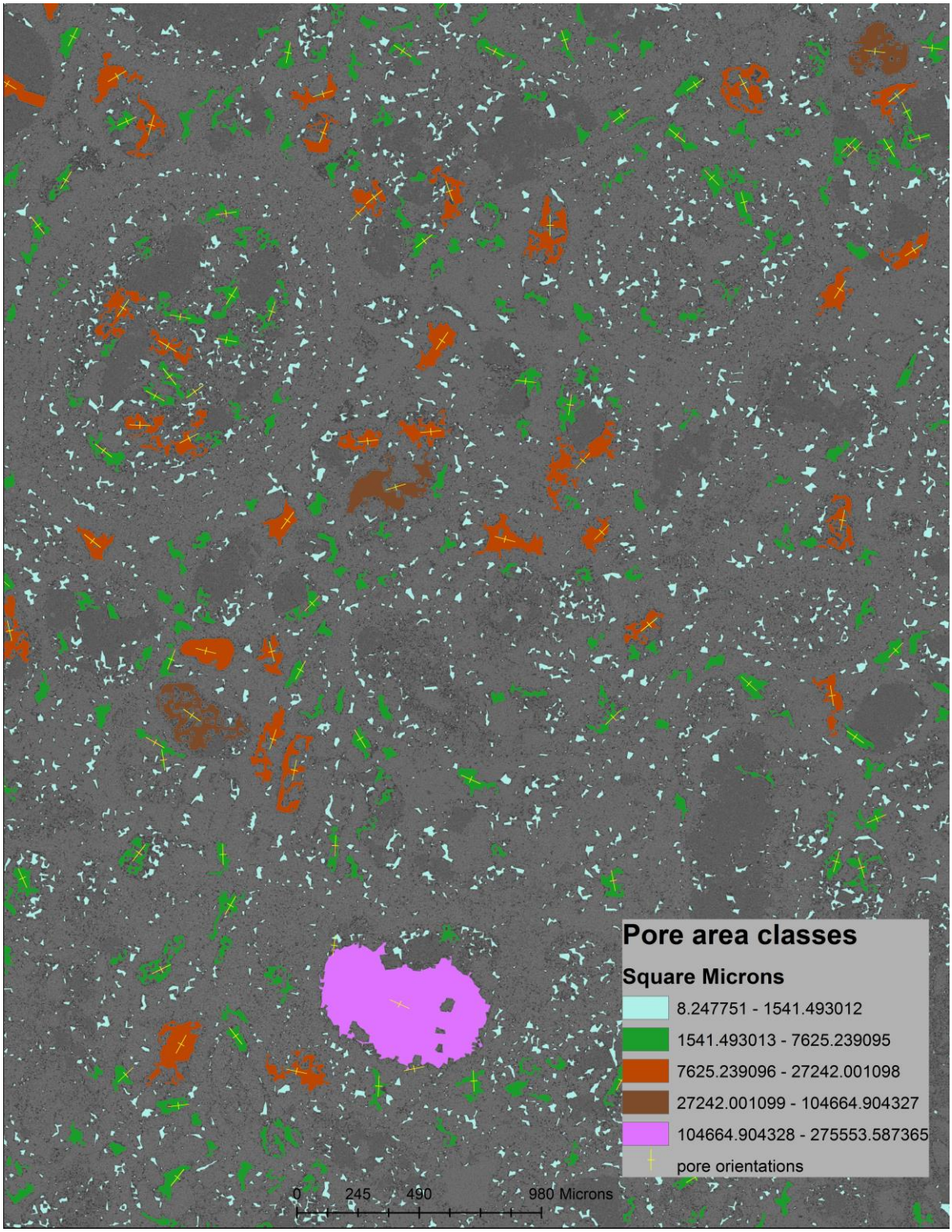

Figure 103 "Top" pore size classes and orientations

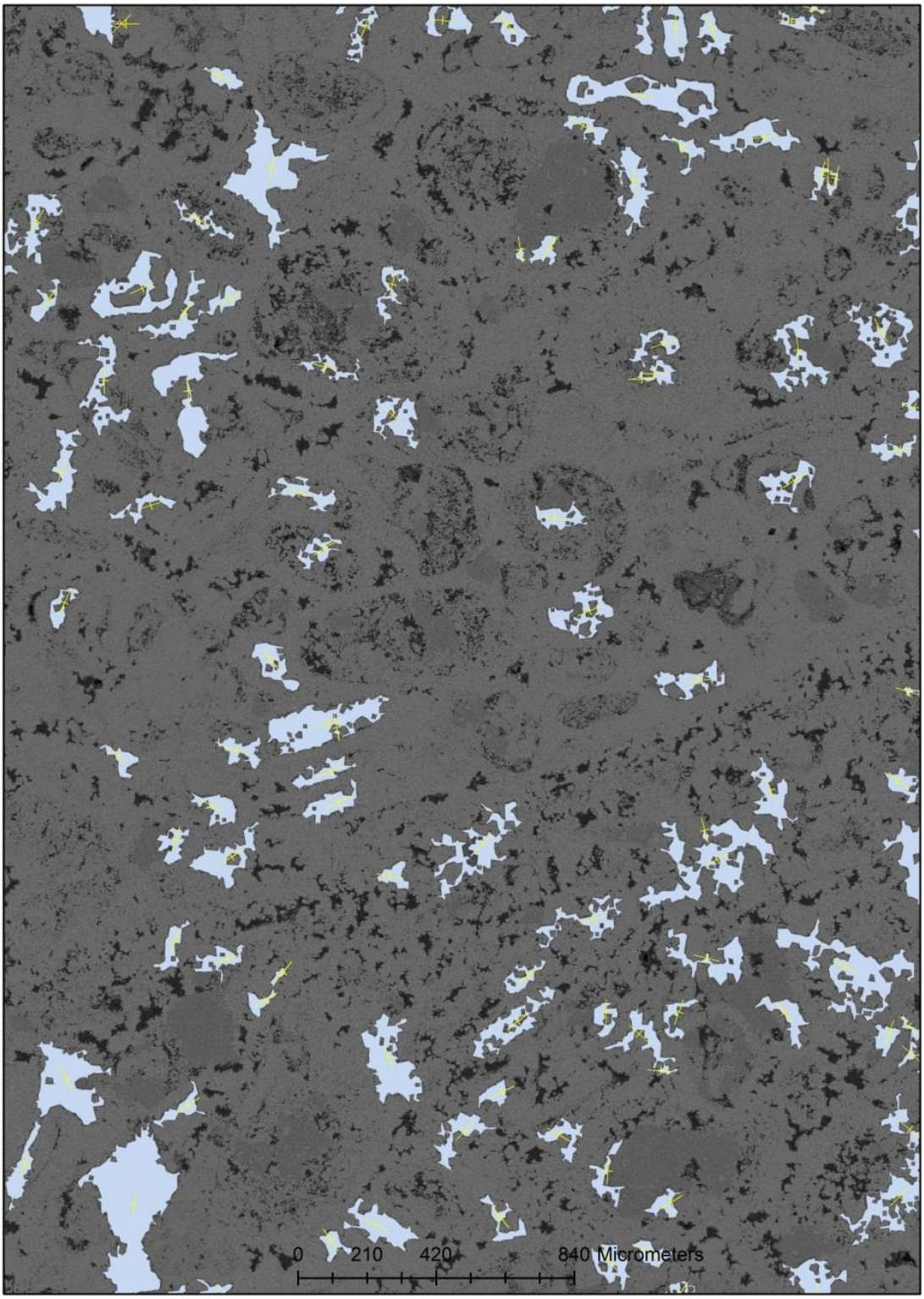

Figure 104 "North" pore map, magnified. 16000µm^3 >Pores >12µm^3

SANDSTONE PRESTACK REFLECTIVITY ATTRIBUTES

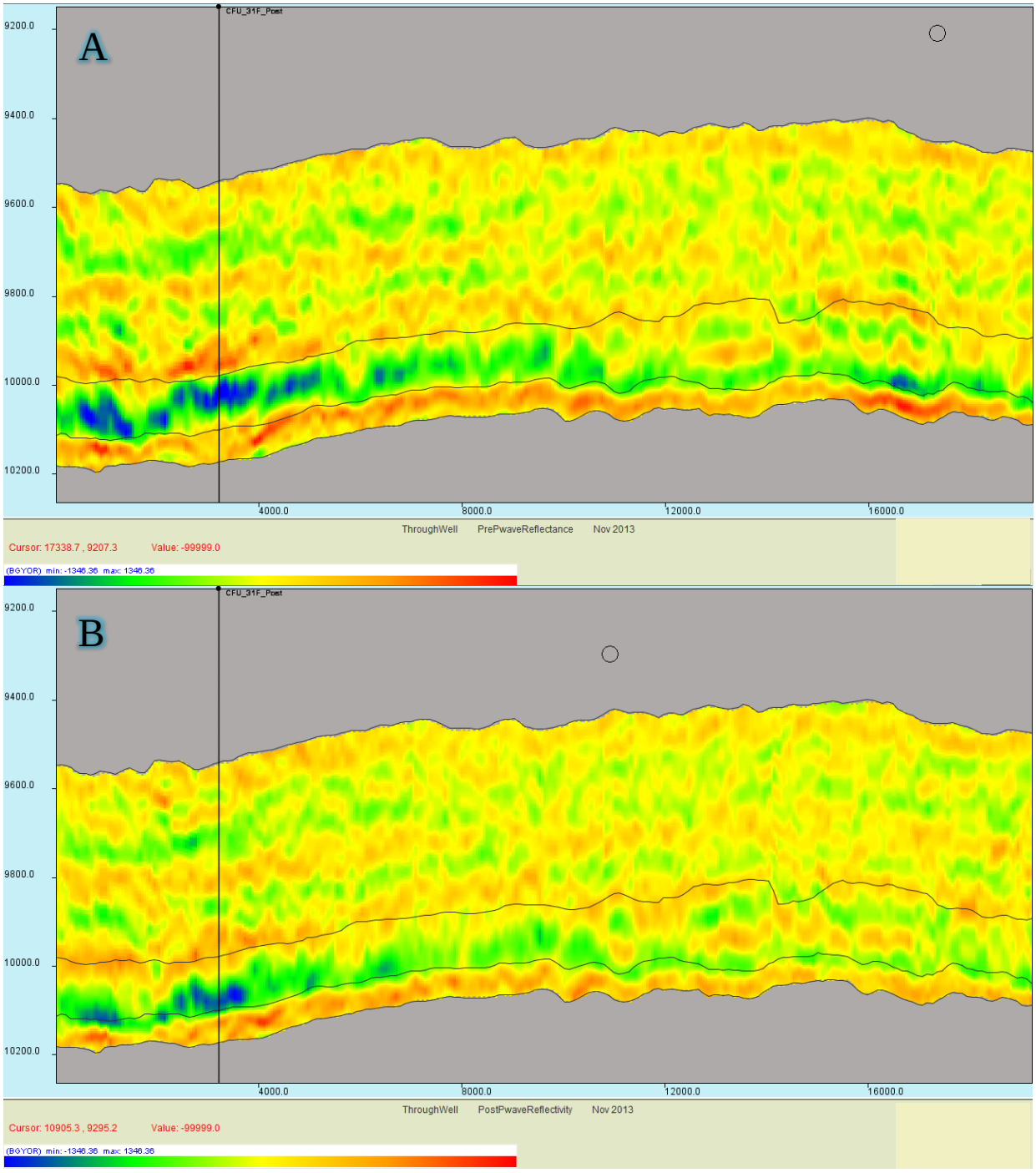

Figure 105. Pre (upper) and post (lower) injection, P-wave reflectance used in differencing operation.

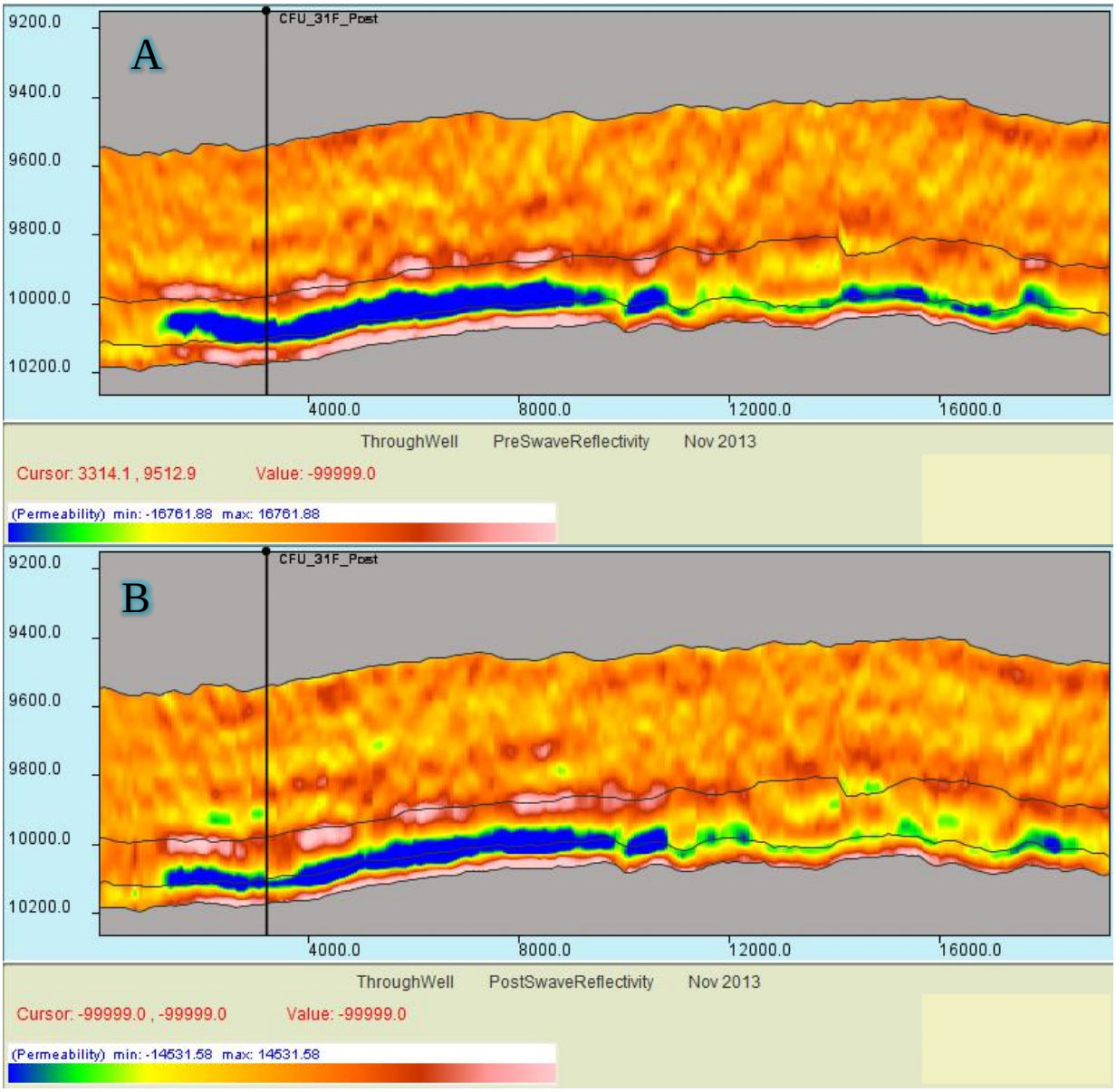

Figure 106. Comparison of pre and post injection S-wave reflectivity used in differencing operation.

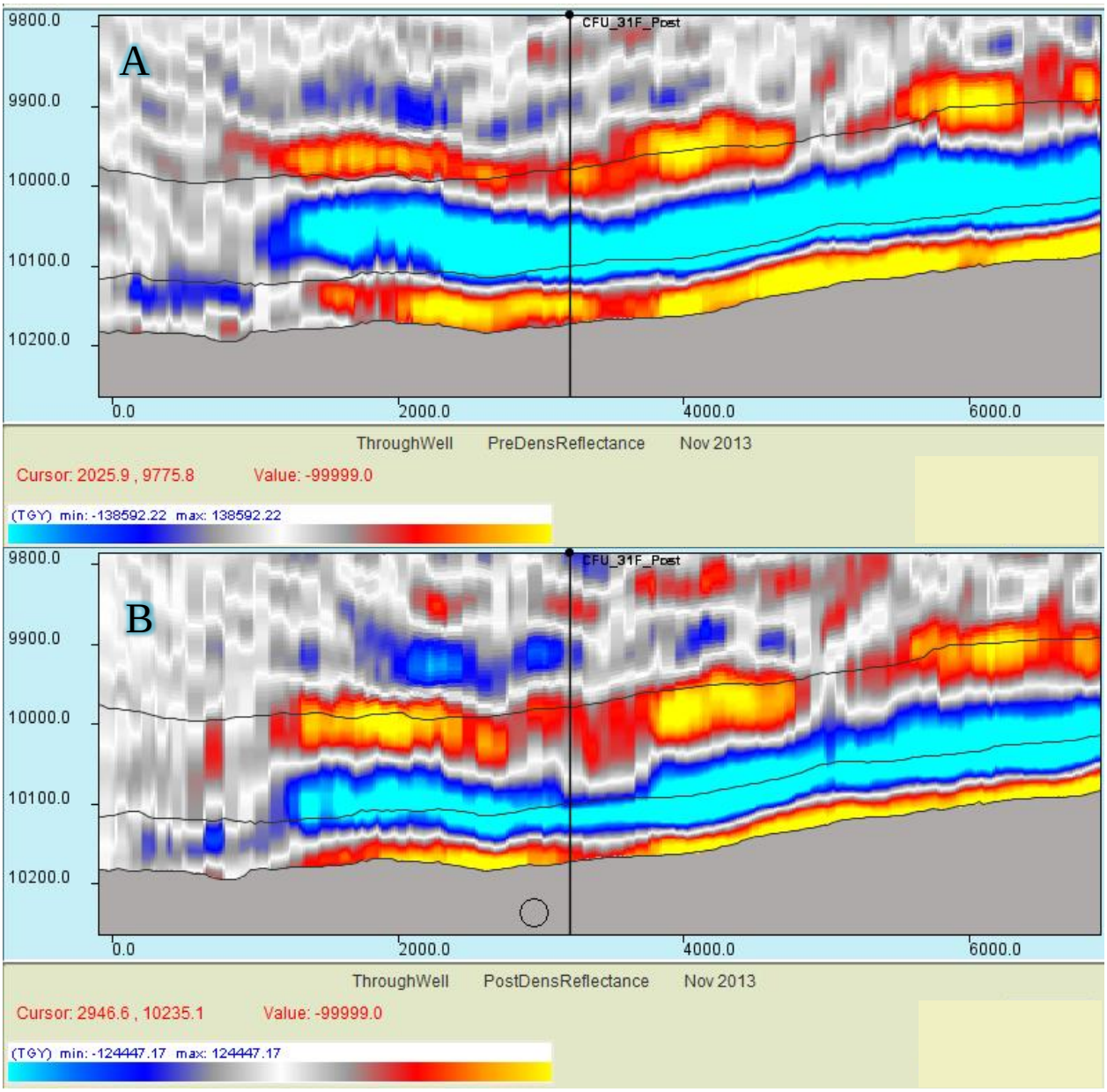

Figure 107. Density reflectance before and after injection used in differencing operation.

CHEMICAL SYSTEM

$$K_{sp} = [Ca^{2+}][CO_3^{2-}] = 6 * 10^{-9} \quad (94)$$

$$[CO_2] = K_{CO_2} P(CO_2) \quad K_{CO_2} = 2 * 10^{-3} \quad (95)$$

$$K_{a1} = \frac{H^+ HCO_3^-}{H_2CO_3} = 4.45 * 10^{-7} \quad (96)$$

$$K_{a2} = \frac{H^+ CO_3^{2-}}{HCO_3^-} = 4.69 * 10^{-11} \quad (97)$$

$$K_w = [H^+][OH^-] = 10^{-14} \quad (98)$$

Activation energy

$$CaCO_3 \rightarrow Ca^{2+} + CO_3^{2-}$$

$$CaCO_3 \rightarrow Ca^{2+} + CO_3^{2-} \quad E_a = 35\ kJ/mol\ (5 - 50°C) \quad (99)$$

APPENDIX C

RJLEE REPORT

March 29, 2010

Dr. Bill Harbert
Department of Geology and Planetary Science Thaw
Hall, University of Pittsburgh

Re: RJ Lee Group Project Number TEH1007704
Limestone

Dear Bill,

RJLG was retained by you to characterize a limestone rock identified by you as. From the original 4 inch diameter oriented core sample you hand delivered, we prepared three mutually perpendicular epoxy impregnated polished samples: Top, North and West (Figure 108). The top side of sample Top, the north side of sample North and the west side of sample West were analyzed. The Top sample measured approximately 40 mm east to west and approximately 45 mm north to south. The North and West samples measured approximately 80 mm top to bottom and 40 mm from side to side. RJLG retained a central column of rock from which the three samples were obtained and returned the cut remnants to you during your visit on November 20, 2009.

Figure 108. Photographs of the trimmed sample. The right image shows the North, Top and West samples analyzed.

Analyses included an optical montage, a scanning electron microscope (SEM) montage in backscattered electron imaging mode, a computer controlled scanning electron microscope (CCSEM) point count analysis and a CCSEM High-Z analysis. Representative particles detected in the high-Z analysis were relocated and documented in the manual SEM (MSEM) mode. Results are briefly summarized in the report, and all raw data will be delivered electronically.

All SEM analysis was performed using an Aspex Personal SEM 75. As oriented in the SEM, the Top sample north side was pointing up and had more positive Y coordinate values. Sample North and Sample West were oriented with the more positive Y coordinate values in the up direction.

Optical Montage

Optical montages were created for the Top, West and North samples. Optical images were acquired using a Keyence digital microscope and stitched together using PanaView. Full bitmap images ranged up to over 400 MB file size and will be provided electronically. Smaller pixel resolution JPG images are included in Appendix A. It should be noted that the color in the West and North montages is close to true, but that of the Top sample is not. Fossils and stylolites are clearly visible.

SEM Montage

SEM montages were created for the Top, West and North samples. Field images of 512 by 512 pixel resolution (3.47266 um/pixel) were acquired at a magnification of 50X. A grid of 20 by 20 images were acquired for the Top sample, and a grid of 15 by 45 images were acquired for the west and north samples. Small resolution montages are shown in Appendix A, and the full size montages will be provided electronically.

Point Count Analysis

The point count program is an automated SEM analysis in the backscattered electron imaging mode. Points in a 5 by 5 point grid were examined per field at a magnification of 50x. The number of fields examined are shown in Table 12. Examination includes the collection of an EDS spectrum at each grid point where the peak areas for selected elements are presented in terms of percent of the total EDS peak areas of the selected elements. Ancillary data such as brightness (video), number of x-ray counts and location coordinates are also acquired for each point. These data will be reported electronically. Microimages at individual points were not collected, but field images were and will be provided electronically.

The elemental composition data were summarized by creating a set of rules to define compositional types. The summary data are shown in Table 13. The rules and the size distribution by particle type are shown in Appendix B. The particle by particle data will be

provided electronically. The rules are somewhat arbitrary and, if desired, the samples can be resummarized applying new rules. Pores are defined as low brightness, low total counts and low carbon content. Manual analysis showed the calcium-rich (calcite) particles often associated with silicon so a "clean" and a "dirty" calcite were defined. Dolomite, apatite and silicon-rich (quartz) were also defined. A variety of undifferentiated alumino-silicates were also defined. A miscellaneous class was "defined" as everything else and turned out to be mostly calcium and silicon.

Table 12. – List of file location, magnification, fields analyzed

Sample	DataFiles	Mag.	Fields
Top	000365_A	50	168
West	901467_A	50	402
North	901476_A	50	225

Table 13. Percent particle classes by sample and total number of points

		Number %	
Classes	Top	West	North
Calcite	84.12	78.65	68.91
Calcite+Qtz	5.27	9.9	20.05
Dolomite	4.48	4.36	5.3
Quartz	0.19	0.57	0.69
Apatite	0.1	0.03	0.11
AlSi	0.02	0.04	ND
Misc.	0.64	1.66	1.33
Pore	5.18	4.79	3.59
N. Counts	4193	10000	5620

High-Z CCSEM analysis

The high-Z CCSEM analysis is set to characterize particles that are larger than 0.2 um and are brighter than the matrix in the backscattered electron image where brightness is proportional to the average atomic number (Z). Each field was examined at a magnification of 1000x. The North and West samples were too long to maintain constant working distance in the SEM.

These samples were analyzed in four adjacent segments (A to D) that measured approximately 0.3 mm by 20 mm each. The area analyzed for the top sample was approximately 3 x 3 mm. In addition to the data described in the point count CCSEM analysis, physical measures were also acquired for each particle. A microimage (32x32 pixel resolution) and the complete 1024 channel EDS spectrum were saved for each particle. After automated analysis, the particles were classified, and representative examples of the most common classes were relocated and analyzed manually. Table 14 identifies the 9 subsamples and lists the number of particles that were relocated.

Table 14. List of Hi-ZCCSEM analyses, the area analyzed and the number of particles that were relocated for manual SEM analysis

Sample	Section	DataFiles	Area Analyzed (mm2)	Reloc Img
Top	-	901502_A	6.229	31
North	A	901497_A	5.160	30
	B	901497_B	5.434	29
	C	901498_C	5.480	40
	D	901498_D	5.478	19
West	A	901501_A	5.480	38
	B	901501_B	5.480	36
	C	901501_C	5.480	37
	D	901501_D	5.134	29

Because the high atomic number particles are quite small, the EDS spectra commonly include the matrix material rich in calcium and, to a lesser amount, silicon. Therefore, calcium and silicon were not included in the list of elements to be identified in the high-Z analyses. However, the saved EDS spectra would reveal peaks for those elements when present, and the manual relocation assesses if those elements are background or indeed associated with the high Z particle. Figure 109A shows a calcium peak that was not identified in the CCSEM analysis, and the P-rich particles are interpreted as apatite. Many of the iron-rich particles were associated with silicon, where silicon was not in the immediate matrix.

The rules and CCSEM summaries (size distribution by particle class for each subsample) are reported in Appendix B. CCSEM image/spectra and MSEM review data will be provided electronically. As opposed to the point count CCSEM where the composition was relatively simple, the high-Z composition is quite variable, and there are EDS peak location overlaps in some of the observed elements. When recognized before the analysis, these issues may be

accounted for within the rules. This complexity can be illustrated with two examples. Phosphorus has a small peak on the low energy side of its major peak that often gets called by CCSEM as tungsten (Figure 109A). The P-rich rule was written to add the area attributed to tungsten to that of phosphorus when phosphorus is present at high levels. The peaks for vanadium and cerium overlap and often both elements are attributed to the same peak (Figure 109B). Because these elements are not commonly found together, the entire peak is attributed to the element in greater abundance.

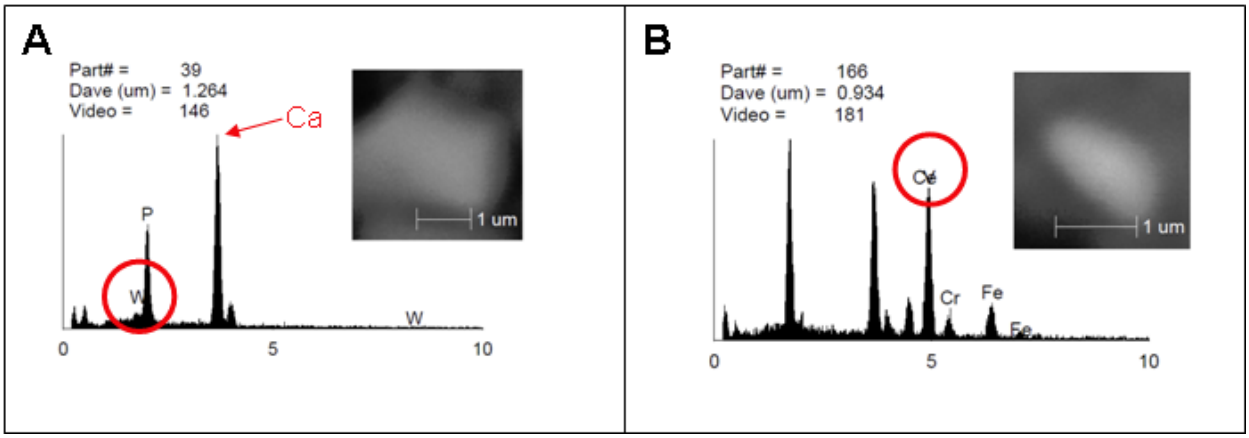

Figure 109. Misidentification of W in the presence of P. Also note that calcium was not in the list of elements and was not identified in the CCSEM analysis. Figure 2B illustrates the misidentification of Ce in the presence of V.

As mentioned above, four continuous analyses were performed for the North and West samples. The data are summarized in Table 15 for particle count data by section, and in Table 16 for summary by sample in both counts and percent. The size and elemental composition data are presented in Appendix B. The particle by particle data will be delivered electronically.

It was expected that the sections in various orientations would have similar results. Table 15 and Table 16 show reasonable correlations among the identified components, with the exception of Classes 2, 3 and 4. Class 4 was a "catch-all" class to group otherwise unclassified particles that are rich in the metals vanadium, chromium, iron and nickel. The particles in this class were generally rich in vanadium with titanium of Class 2. When the particles in Class 2 and Class 4 are added, they all total about 14%.

The difference in the tungsten abundances in the samples is more difficult to explain. It does not seem reasonable that the North sample can have 17% tungsten and the West and Top samples have less than 1%. Sample contamination could be considered, but new grinding/polishing paper was used for each sample making contamination unlikely. The major peak for tungsten overlaps that of silicon. However, tungsten has secondary peaks by which it can be positively identified. Slight variations in operating conditions may have resulted in the misidentification of tungsten as silicon.

The issues resulting from the particles being smaller than the beam interaction volume can be resolved by obtaining a small sample of material and dissolving the calcite leaving an insoluble residue that can be deposited onto a filter medium for particle by particle analysis.

Table 15. Number of particles in each compositional class for each 20 mm section of the north and West samples and the Top sample

		No. of Particles by Class NORTH Sections				No. of Particles by Class WEST Sections				Top
	Class	Sect A	Sect B	Sect C	Sect D	Sect A	Sect B	Sect C	Sect D	
1	Fe-rich	83	180	82	32	234	148	147	75	156
2	TiV-rich	19	30	11	9	63	46	46	24	61
3	W-rich	73	56	66	34	0	2	1	9	2
4	Metal-bearing	22	63	28	13	24	7	10	3	9
5	P-rich	7	29	3	11	22	18	30	45	60
6	FeNi-rich	11	28	18	3	35	24	21	13	35
7	Zr-rich	24	41	17	10	16	16	14	9	24
8	FeCr-rich	3	14	2	4	23	21	9	10	10
9	Other	6	25	13	3	15	7	10	4	16
10	FeTi-rich	2	1	0	1	26	23	20	9	19
11	FeTiV-rich	2	2	0	1	26	20	19	10	20
12	FeV-rich	7	18	7	7	10	8	12	2	6
13	FeZr-bearing	8	7	4	4	5	6	5	4	4
14	BaS-rich	5	21	2	1	8	3	1	0	2
15	S-bearing	6	20	5	3	1	1	3	0	1
16	V-rich	3	16	7	3	3	3	2	0	1
17	FeNi-bearing	4	7	2	3	9	5	6	1	4
18	CuZn-rich	3	3	2	3	10	4	4	0	23
19	ZnS-rich	4	3	3	1	4	2	2	5	11
20	FeS-rich	0	4	3	1	7	1	2	5	3
21	FeZr-rich	2	4	5	0	4	5	3	0	4
22	FeTiZr-rich	1	0	0	0	6	4	6	2	3
23	SrS-rich	1	8	1	0	1	0	2	5	1
24	Fe-bearing	2	5	2	1	3	3	2	0	1
25	FeVNi-rich	1	4	3	2	2	1	0	0	3
26	Ni-rich	1	2	0	0	2	1	2	3	4
27	Zn-rich	6	2	0	2	1	0	0	0	2
28	CuZn-beraing	4	0	2	2	0	2	0	1	3
29	Cu-rich	1	2	1	2	3	0	0	0	1
30	FeCrNi-rich	2	1	0	1	2	1	0	2	1
31	LaCe-rich	0	0	0	0	2	2	3	0	0
32	Ti-rich	0	0	0	0	1	4	0	1	6
33	Sr-rich	0	3	0	0	1	0	0	0	1
34	FeVP-rich	0	1	0	0	1	1	0	0	0
35	FeZrNi-rich	0	1	0	0	1	0	0	0	0
36	TiSr-rich	0	0	0	0	0	1	0	0	0
37	TiZr-rich	0	0	0	0	1	0	0	0	0
38	FeTiNi-rich	0	0	0	0	0	1	0	0	1
39	Cr-rich	0	0	0	0	0	0	0	0	1
40	CrNi-rich	0	0	0	0	0	0	0	0	0
41	FeSr-rich	0	0	0	0	0	0	0	0	0
42	FeZrV-rich	0	0	0	0	0	0	0	0	0
	Totals	313	601	289	157	572	391	382	242	499

Table 16. Number and number percent by compositional class for the three samples and the grand totals

		Totals by Subsample						Grand Totals	
	Class	North (No)	West (No)	Top (No)	North (%)	West (%)	Top (%)	Total (No)	Total (%)
1	Fe-rich	377	604	156	27.72	38.06	31.26	1137	32.99
2	TiV-rich	69	179	61	5.07	11.28	12.22	309	8.97
3	W-rich	229	12	2	16.84	0.76	0.40	243	7.05
4	Metal-bearing	126	44	9	9.26	2.77	1.80	179	5.19
5	P-rich	50	115	60	3.68	7.25	12.02	225	6.53
6	FeNi-rich	60	93	35	4.41	5.86	7.01	188	5.46
7	Zr-rich	92	55	24	6.76	3.47	4.81	171	4.96
8	FeCr-rich	23	63	10	1.69	3.97	2.00	96	2.79
9	Other	47	36	16	3.46	2.27	3.21	99	2.87
10	FeTi-rich	4	78	19	0.29	4.91	3.81	101	2.93
11	FeTiV-rich	5	75	20	0.37	4.73	4.01	100	2.90
12	FeV-rich	39	32	6	2.87	2.02	1.20	77	2.23
13	FeZr-bearing	23	20	4	1.69	1.26	0.80	47	1.36
14	BaS-rich	29	12	2	2.13	0.76	0.40	43	1.25
15	S-bearing	34	5	1	2.50	0.32	0.20	40	1.16
16	V-rich	29	8	1	2.13	0.50	0.20	38	1.10
17	FeNi-bearing	16	21	4	1.18	1.32	0.80	41	1.19
18	CuZn-rich	11	18	23	0.81	1.13	4.61	52	1.51
19	ZnS-rich	11	13	11	0.81	0.82	2.20	35	1.02
20	FeS-rich	8	15	3	0.59	0.95	0.60	26	0.75
21	FeZr-rich	11	12	4	0.81	0.76	0.80	27	0.78
22	FeTiZr-rich	1	18	3	0.07	1.13	0.60	22	0.64
23	SrS-rich	10	8	1	0.74	0.50	0.20	19	0.55
24	Fe-bearing	10	8	1	0.74	0.50	0.20	19	0.55
25	FeVNi-rich	10	3	3	0.74	0.19	0.60	16	0.46
26	Ni-rich	3	8	4	0.22	0.50	0.80	15	0.44
27	Zn-rich	10	1	2	0.74	0.06	0.40	13	0.38
28	CuZn-beraing	8	3	3	0.59	0.19	0.60	14	0.41
29	Cu-rich	6	3	1	0.44	0.19	0.20	10	0.29
30	FeCrNi-rich	4	5	1	0.29	0.32	0.20	10	0.29
31	LaCe-rich	0	7	0	0.00	0.44	0.00	7	0.20
32	Ti-rich	0	6	6	0.00	0.38	1.20	12	0.35
33	Sr-rich	3	1	1	0.22	0.06	0.20	5	0.15
34	FeVP-rich	1	2	0	0.07	0.13	0.00	3	0.09
35	FeZrNi-rich	1	1	0	0.07	0.06	0.00	2	0.06
36	TiSr-rich	0	1	0	0.00	0.06	0.00	1	0.03
37	TiZr-rich	0	1	0	0.00	0.06	0.00	1	0.03
38	FeTiNi-rich	0	1	1	0.00	0.06	0.20	2	0.06
39	Cr-rich	0	0	1	0.00	0.00	0.20	1	0.03
40	CrNi-rich	0	0	0	0.00	0.00	0.00	0	0.00
41	FeSr-rich	0	0	0	0.00	0.00	0.00	0	0.00
42	FeZrV-rich	0	0	0	0.00	0.00	0.00	0	0.00
	Totals	1360	1587	499	100.00	100.00	100.00	3446	100.00

These results are submitted pursuant to RJ Lee Group's current terms and conditions of sale, including the company's standard warranty and limitation of liability provisions. No responsibility or liability is assumed for the manner in which the results are used or interpreted. Unless notified to return the samples covered in this report, RJ Lee Group will store them for a period of thirty (30) days before discarding.

Should you have any questions regarding this information, please do not hesitate to contact me.

Sincerely,

Stephen Kennedy

Senior Scientist

Generalized list of Electronic Data, 4 MB Flash Drives

Drive 1

Optical Montage data

Drive 2

01 Sample Photographs

PowerPoint presentation of uncut and cut core sample 02 SEM Montage

CCSEM Files (especially HDZ and PXZ)

Large, Medium and Small TIF montages

Large montage in ECW format

All individual images

03 Point Count (Top, North and West)

CCSEM files (especially HDZ and PXZ)

Particle by Particle data (XL) (Subset of data in PXZ file)

CCSEM summary distribution file (ZSS)

Field images

04 High-Z (Top, North and West by Section)

Summary – HiZ.xls (Subset of data in PXZ files for all 9 sections) CCSEM Files (especially HDZ and PXZ)

CCSEM summary distribution file (ZSS)

MSEM review images (individual images and PDF file)

CCSEM image with chemistry (PDF)

CCSEM microimages (in MAG0 folder)

Reduced pixel resolution Optical and SEM montages

Figure 110 A1. Optical montage of the top of the Top sample. North is up. (Color is not true.)

Figure 111 A2. Optical montage of the top of the North sample. Up is up. (Color is near true.)

Figure 112 A3. Optical montage of the West sample. Up is up. (Color is near true.)

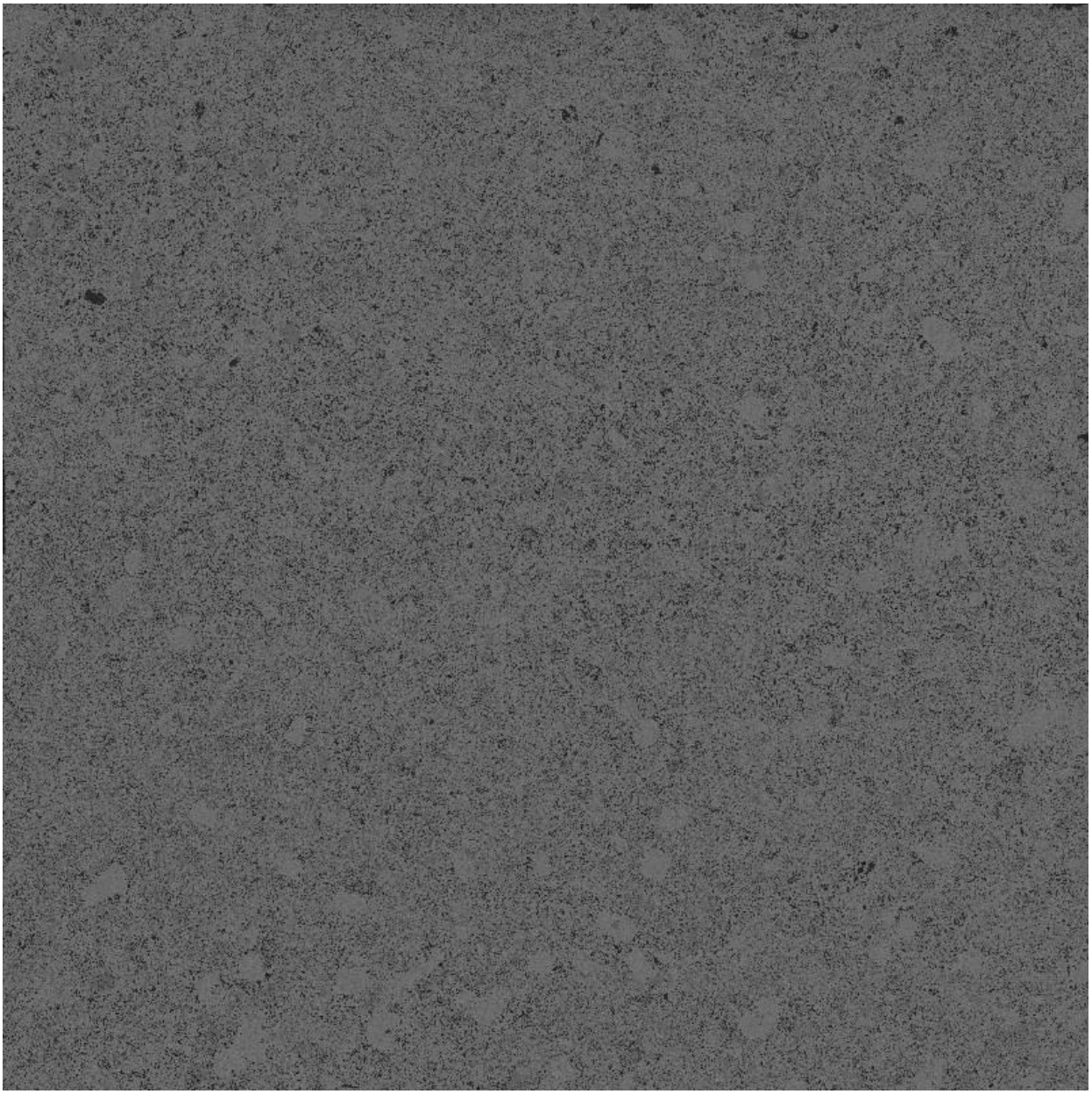

Figure 113 A4. SEM montage in the BE imaging mode of the Top sample. Up is North.

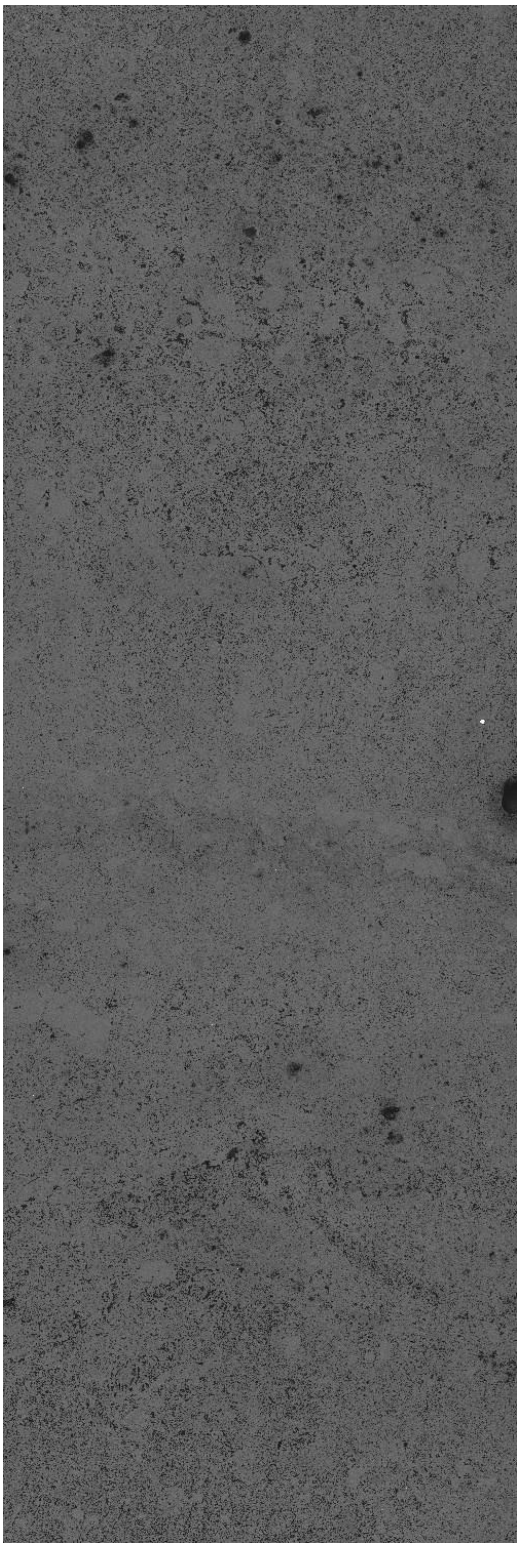

Figure 114 A5. SEM montage in the BE imaging mode of the North sample. Up is up.

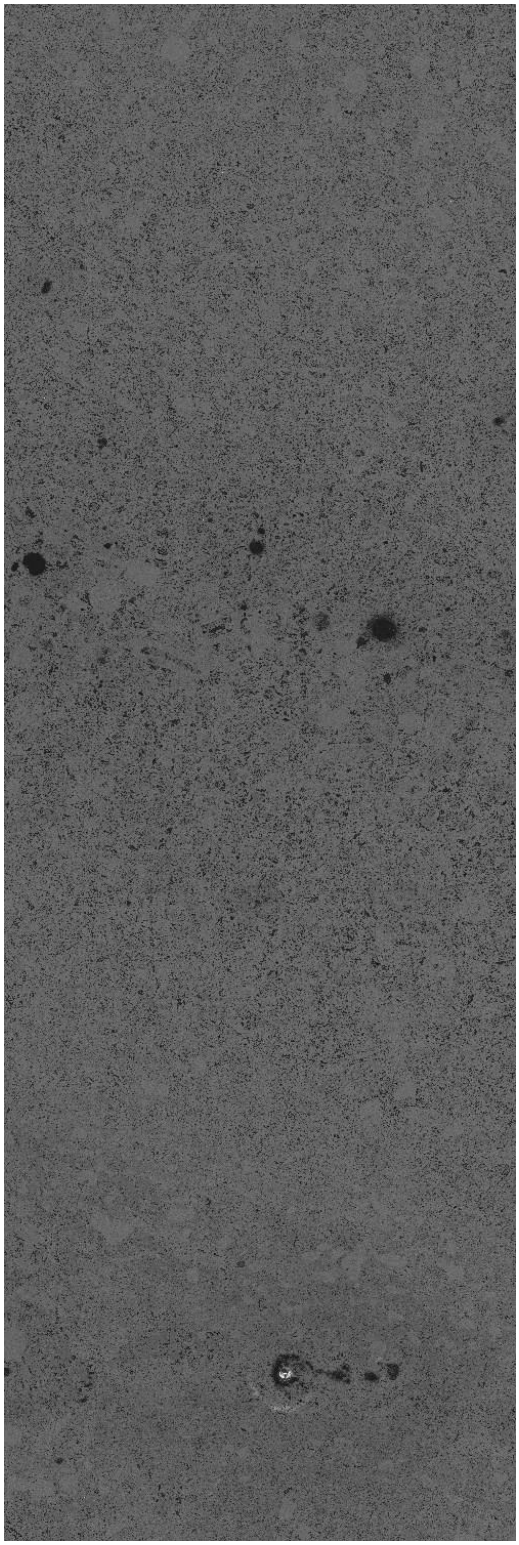

Figure 115 A5. SEM montage in the BE imaging mode of the West sample. Up is up.

B

CCSEM Point Count and CCSEM High-Z Analysis Results

CCSEM Point Count Rules

Pore	Video<40 and Counts<1000
Pore	C>=50
Apatite	Ca>=40 and P>=8 and Ca+P+C>=85
AlSi	Al>=10 and Si>=10 and Al+Si+K>=50
Quartz	Si>=60
Dolomite	Mg>=10 and Ca>=40 and C+Ca+Mg>=85 and Mg>Si
Calcite	Ca>=50 and C+Ca>=85 and Mg<10 and Si<10
Calcite+Qtz	Ca>=50 and Ca+C>=65 and Si>=10
Misc.	True

CCSEM Point Count Results - TOP

Client_Name	Harbert
Client_Number	TOP
Project_Number	TEH1007704
Sample_Number	10077491
Analysis_Date	11/22/09
DataFiles	000365_A\10077491.*

Table 17. "Top" mineral classes.

Classes	#	Number %
Calcite	3527	84.12
Calcite+Qtz	221	5.27
Pore	217	5.18
Dolomite	188	4.48
Misc.	27	0.64
Quartz	8	0.19
Apatite	4	0.10
AlSi	1	0.02
Totals	4193	100.00

Table 18. "Top" Average Composition.

Classes	#	C	Na	Mg	Al	Si	P	S	K	Ca	Ti	Fe	Zn	Zr	La
Calcite	3527	12	0	0	0	1	0	0	0	87	0	0	0	0	0
Calcite+Qtz	221	10	0	0	0	16	0	0	0	74	0	0	0	0	0
Pore	217	71	0	0	0	2	0	0	0	27	0	0	0	0	0
Dolomite	188	13	0	22	0	1	0	0	0	65	0	0	0	0	0
Misc.	27	20	0	1	0	32	0	0	0	46	0	0	0	0	0
Quartz	8	6	0	0	0	73	0	0	0	22	0	0	0	0	0
Apatite	4	20	0	0	0	2	12	0	0	65	0	0	0	0	0
AlSi	1	10	0	0	29	40	0	0	16	5	0	0	0	0	0
Totals	4193	15	0	1	0	2	0	0	0	82	0	0	0	0	0

CCSEM Point Count Results - West

Client_Name	Harbert
Client_Number	West
Project_Number	TEH1007704
Sample_Number	10077491
Analysis_Date	12/3/09
DataFiles	901467_A\10077491.*

Table 19. "West" mineral classes.

Classes	#	Number %
Calcite	7865	78.65
Calcite+Qtz	990	9.90
Pore	479	4.79
Dolomite	436	4.36
Misc.	166	1.66
Quartz	57	0.57
AlSi	4	0.04
Apatite	3	0.03
Totals	10000	100.00

Table 20. "West" Average Composition.

Classes	#	C	Na	Mg	Al	Si	P	S	K	Ca	Ti	Fe	Zn	Zr	La
Calcite	7865	4	0	0	0	1	0	0	0	95	0	0	0	0	0
Calcite+Qtz	990	3	0	0	0	17	0	0	0	80	0	0	0	0	0
Pore	479	51	0	0	1	9	0	0	0	38	0	0	0	0	0
Dolomite	436	3	0	22	0	1	0	0	0	74	0	0	0	0	0
Misc.	166	12	0	1	1	38	0	0	0	48	0	0	0	0	0
Quartz	57	9	0	0	0	77	0	0	0	14	0	0	0	0	0
AlSi	4	15	0	0	12	62	0	0	0	12	0	0	0	0	0
Apatite	3	3	0	0	0	5	24	0	0	68	0	0	0	0	0
Totals	10000	6	0	1	0	4	0	0	0	89	0	0	0	0	0

CCSEM Point Count Results - North

Client_Name	Harbert
Client_Number	North
Project_Number	TEH1007704
Sample_Number	10077491
Analysis_Date	12/17/09
DataFiles	901476_A\10077491.*

Table 21. "North" mineral classes.

Classes	#	Number %
Calcite	3873	68.91
Calcite+Qtz	1127	20.05
Dolomite	298	5.30
Pore	202	3.59
Misc.	75	1.33
Quartz	39	0.69
Apatite	6	0.11
Totals	5620	100.00

Table 22. "North" Average Composition.

Classes	#	C	Na	Mg	Al	Si	P	S	K	Ca	Ti	Fe	Zn	Zr	La
Calcite	3873	2	0	0	0	3	0	0	0	95	0	0	0	0	0
Calcite+Qtz	1127	1	0	0	0	16	0	0	0	83	0	0	0	0	0
Dolomite	298	1	0	24	0	3	0	0	0	73	0	0	0	0	0
Pore	202	54	0	1	2	9	1	2	1	26	1	0	0	2	1
Misc.	75	13	0	3	0	30	1	1	1	50	0	0	0	1	0
Quartz	39	11	0	0	0	79	0	0	0	11	0	0	0	0	0
Apatite	6	5	0	0	0	4	13	0	0	78	0	0	0	0	0
Totals	5620	4	0	1	0	6	0	0	0	88	0	0	0	0	0

High-Z CCSEM Rules

01	P-rich	P>=85
02	P-rich	P>=50 and P+W>=85
03	Fe-rich	Fe>=80
04	Ti-rich	Ti>=85
05	V-rich	V>=85
06	V-rich	V>Ce and V+Ce>=85
07	Cr-rich	Cr>=85
08	Ni-rich	Ni>=85
09	Cu-rich	Cu>=85
10	Zn-rich	Zn>=85
11	Zr-rich	Zr>=85
12	W-rich	W>=85
13	Sr-rich	Sr>=85
14	CuZn-rich	Cu>=50 and Zn>=18 and Cu+Zn>=80
15	FeS-rich	Fe>=20 and S>=20 and Fe+S>=85
16	ZnS-rich	Zn>=25 and S>=22 and Zn+S>=85
17	BaS-rich	Ba>=40 and S>=40 and Ba+S>=85
18	FeNi-rich	Fe>=45 and Ni>=6 and Fe+Ni>=85
19	FeTi-rich	Fe>=30 and Ti>=25 and Fe+Ti>=80
20	FeV-rich	Fe>=40 and V>=10 and Fe+V>=85
21	FeV-rich	V>Ce and Fe>=40 and V+Ce>=10 and Fe+V+Ce>=85
22	FeZr-rich	Fe>=30 and Zr>=10 and Fe+Zr>=85
23	CrNi-rich	Cr>=15 and Ni>=60 and Cr+Ni>=85
24	LaCe-rich	La+Ce>=40
25	FeCr-rich	Fe>=55 and Cr>=10 and Fe+Cr>=85
26	FeSr-rich	Fe>=35 and Sr>=8 and Fe+Sr>=80
27	FeVP-rich	Fe>=35 and V>=10 and P>=30 and Fe+V+P>=80
28	TiSr-rich	Ti>=25 and Sr>=55 and Ti+Sr>=85
29	TiZr-rich	Ti>=15 and Zr>=40 and Ti+Zr>=80
30	TiV-rich	Ti+Ba>=15 and V>=9 and Ti+Ba+V>=85
31	SrS-rich	Sr>=30 and S>=10 and Sr+S>=85
32	FeTiV-rich	Fe>=15 and Ti>=5 and V>=10 and Fe+Ti+V+Ni>=85
33	FeVNi-rich	Fe>=20 and V>=6 and Ni>=6 and Fe+V+Ni>=85
34	FeTiNi-rich	Fe>=15 and Ti>=8 and Ni>=8 and Fe+Ti+V>=85
35	FeTiZr-rich	Fe>=15 and Ti>=6 and Zr>=15 and Fe+Ti+Zr>=85
36	FeZrNi-rich	Fe>=30 and Zr>=30 and Ni>=8 and Fe+Zr+Ni>=85
37	FeZrV-rich	Fe>=30 and Zr>=15 and V>=10 and Fe+Zr+V>=85
38	FeCrNi-rich	Fe>=50 and Cr>=10 and Ni>=5 and Fe+Cr+Ni>=85
39	FeZr-bearing	Fe>=20 and Zr>=10 and Fe+Zr>=50
40	FeNi-bearing	Fe>=10 and Ni>=10 and Fe+Ni>=50
41	CuZn-beraing	Cu>=10 and Zn>=10 and Cu+Zn>=50
42	Fe-bearing	Fe>=50
43	S-bearing	S>=25
44	Metal-bearing	V+Cr+Fe+Ni>=50
45	Other True	

High-Z CCSEM Results - Top

Client_Name
Harbert
Client_Number
Top
Project_Number TEH1007704
Sample_Number 9077491T
DataFiles 901502_A\9077491T.*

Mag	Fields	Particles
1000	788.1279	499

Table 23. "Top" CCSEM particle elemental distribution

Classes	#	Number %
Fe-rich	156	31.26
TiV-rich	61	12.22
P-rich	60	12.02
FeNi-rich	35	7.01
Zr-rich	24	4.81
CuZn-rich	23	4.61
FeTiV-rich	20	4.01
FeTi-rich	19	3.81
Other	16	3.21
ZnS-rich	11	2.20
FeCr-rich	10	2.00
Metal-bearing	9	1.80
FeV-rich	6	1.20
Ti-rich	6	1.20
Ni-rich	4	0.80
FeZr-rich	4	0.80
FeNi-bearing	4	0.80
FeZr-bearing	4	0.80
FeTiZr-rich	3	0.60
FeS-rich	3	0.60
CuZn-beraing	3	0.60
FeVNi-rich	3	0.60
W-rich	2	0.40
Zn-rich	2	0.40
BaS-rich	2	0.40
V-rich	1	0.20
Cr-rich	1	0.20
FeTiNi-rich	1	0.20
Fe-bearing	1	0.20
SrS-rich	1	0.20
FeCrNi-rich	1	0.20
Sr-rich	1	0.20
Cu-rich	1	0.20
S-bearing	1	0.20
Totals	499	100.00

High-Z CCSEM Results - Top

Table 24. High-Z CCSEM "Top" Size Distribution by Average Diameter (microns)

Classes	Number %	Mean	StdDev	0.2 - 0.5	0.5 - 1.0	1.0 - 2.0	2.0 - 4.0	4.0 - 8.0	>>>
Fe-rich	31.3	0.5	0.4	62.2	28.2	8.3	1.3	0.0	0.0
TiV-rich	12.2	0.5	0.2	60.7	31.1	8.2	0.0	0.0	0.0
P-rich	12.0	0.7	0.3	31.7	55.0	13.3	0.0	0.0	0.0
FeNi-rich	7.0	0.4	0.2	77.1	20.0	2.9	0.0	0.0	0.0
Zr-rich	4.8	0.4	0.2	70.8	29.2	0.0	0.0	0.0	0.0
CuZn-rich	4.6	0.7	0.4	47.8	34.8	17.4	0.0	0.0	0.0
FeTiV-rich	4.0	0.5	0.3	55.0	40.0	5.0	0.0	0.0	0.0
FeTi-rich	3.8	0.5	0.3	73.7	15.8	10.5	0.0	0.0	0.0
Other	3.2	0.4	0.2	81.3	18.8	0.0	0.0	0.0	0.0
ZnS-rich	2.2	0.7	0.6	54.5	18.2	18.2	9.1	0.0	0.0
FeCr-rich	2.0	0.3	0.1	90.0	10.0	0.0	0.0	0.0	0.0
Metal-bearing	1.8	0.4	0.2	55.6	44.4	0.0	0.0	0.0	0.0
FeV-rich	1.2	0.5	0.2	66.7	33.3	0.0	0.0	0.0	0.0
Ti-rich	1.2	0.7	0.7	66.7	16.7	0.0	16.7	0.0	0.0
Ni-rich	0.8	0.4	0.1	100.0	0.0	0.0	0.0	0.0	0.0
FeZr-rich	0.8	0.4	0.2	75.0	25.0	0.0	0.0	0.0	0.0
FeNi-bearing	0.8	0.3	0.1	100.0	0.0	0.0	0.0	0.0	0.0
FeZr-bearing	0.8	0.7	0.2	25.0	75.0	0.0	0.0	0.0	0.0
FeTiZr-rich	0.6	0.4	0.1	66.7	33.3	0.0	0.0	0.0	0.0
FeS-rich	0.6	0.4	0.0	100.0	0.0	0.0	0.0	0.0	0.0
CuZn-beraing	0.6	0.4	0.1	66.7	33.3	0.0	0.0	0.0	0.0
FeVNi-rich	0.6	0.6	0.4	66.7	0.0	33.3	0.0	0.0	0.0
W-rich	0.4	0.3	0.1	100.0	0.0	0.0	0.0	0.0	0.0
Zn-rich	0.4	0.3	0.1	100.0	0.0	0.0	0.0	0.0	0.0
BaS-rich	0.4	0.4	0.0	100.0	0.0	0.0	0.0	0.0	0.0
V-rich	0.2	0.6	0.0	0.0	100.0	0.0	0.0	0.0	0.0
Cr-rich	0.2	1.1	0.0	0.0	0.0	100.0	0.0	0.0	0.0
FeTiNi-rich	0.2	0.8	0.0	0.0	100.0	0.0	0.0	0.0	0.0
Fe-bearing	0.2	0.4	0.0	100.0	0.0	0.0	0.0	0.0	0.0
SrS-rich	0.2	0.4	0.0	100.0	0.0	0.0	0.0	0.0	0.0
FeCrNi-rich	0.2	0.4	0.0	100.0	0.0	0.0	0.0	0.0	0.0
Sr-rich	0.2	0.5	0.0	100.0	0.0	0.0	0.0	0.0	0.0
Cu-rich	0.2	0.4	0.0	100.0	0.0	0.0	0.0	0.0	0.0
S-bearing	0.2	0.6	0.0	0.0	100.0	0.0	0.0	0.0	0.0
Totals	100.0	0.5	0.3	61.3	30.3	7.6	0.8	0.0	0.0

Table 25. High-Z CCSEM "Top" Average Composition

Classes	#	Si	P	S	Ti	V	Cr	Fe	Ni	Cu	Zn	Sr	Zr	Ba	La	Ce	W
Fe-rich	156	0	0	0	0	1	0	95	4	0	0	0	0	0	0	0	0
TiV-rich	61	0	0	0	45	50	3	1	0	0	0	0	0	0	0	0	1
P-rich	60	0	90	1	0	0	0	0	0	0	0	0	0	0	0	0	10
FeNi-rich	35	0	0	0	0	2	1	70	26	0	0	0	0	0	0	1	0
Zr-rich	24	0	0	0	0	0	0	0	0	0	0	0	99	0	0	0	1
CuZn-rich	23	0	0	0	0	0	0	0	1	67	30	0	0	0	0	0	2
FeTiV-rich	20	0	0	0	24	25	2	41	6	0	0	0	2	0	0	0	0
FeTi-rich	19	0	1	0	45	7	0	44	2	0	0	0	1	0	0	0	0
Other	16	0	5	1	23	7	0	8	2	1	0	0	27	2	1	1	21
ZnS-rich	11	0	0	63	0	0	0	0	0	0	37	0	0	0	0	0	0
FeCr-rich	10	0	0	1	0	1	22	68	8	0	0	0	0	0	0	0	0
Metal-bearing	9	0	1	0	22	48	4	10	11	0	0	0	1	0	0	4	0

FeV-rich	6	0	1	1	3	23	1	66	5	0	0	0	0	0	0	0	0
Ti-rich	6	0	3	0	89	9	0	0	0	0	0	0	0	0	0	0	0
Ni-rich	4	0	0	0	0	0	0	3	97	0	0	0	0	0	0	0	0
FeZr-rich	4	0	0	0	0	0	0	61	6	0	0	0	33	0	0	0	0
FeNi-bearing	4	0	0	0	0	0	2	35	63	0	0	0	0	0	0	0	0
FeZr-bearing	4	0	0	0	25	6	0	43	9	0	0	0	17	0	0	0	0
FeTiZr-rich	3	0	0	0	30	7	0	43	2	0	0	0	17	0	0	0	0
FeS-rich	3	0	0	73	0	0	0	27	0	0	0	0	0	0	0	0	0
CuZn-beraing	3	0	2	2	0	0	0	0	2	70	18	0	0	0	0	0	6
FeVNi-rich	3	0	2	0	1	13	0	70	11	0	0	0	0	0	2	0	0
W-rich	2	0	0	7	0	0	0	0	6	0	0	0	0	0	0	0	88
Zn-rich	2	0	0	0	0	0	0	0	0	0	100	0	0	0	0	0	0
BaS-rich	2	0	0	42	0	0	0	2	0	0	0	0	0	50	0	0	6
V-rich	1	0	0	0	0	91	5	0	0	0	0	0	0	0	0	4	0
Cr-rich	1	0	0	0	0	0	86	14	0	0	0	0	0	0	0	0	0
FeTiNi-rich	1	0	0	0	14	5	0	72	9	0	0	0	0	0	0	0	0
Fe-bearing	1	0	0	0	0	0	19	54	7	0	0	0	0	0	0	0	20
SrS-rich	1	0	0	39	0	0	0	0	0	0	0	61	0	0	0	0	0
FeCrNi-rich	1	0	0	5	0	0	19	65	11	0	0	0	0	0	0	0	0
Sr-rich	1	0	0	0	0	0	0	0	0	0	0	96	0	0	4	0	0
Cu-rich	1	0	0	0	0	0	0	0	0	100	0	0	0	0	0	0	0
S-bearing	1	0	0	59	0	0	0	16	0	13	12	0	0	0	0	0	0
Totals	499	0	11	2	11	10	1	43	5	4	3	0	6	0	0	0	3

High-Z CCSEM Results – North Section A

Client_Name	Harbert
Client_Number	North A (0 – 20 mm)
Project_Number	TEH1007708
Sample_Number	10077491N
DataFiles	901497_A\10077491.*

Mag	Fields	Particles
1000	652.8583	313

Table 26. "North A" (0 – 20 mm) CCSEM particle elemental distribution

Classes	#	Number %
Fe-rich	83	26.52
W-rich	73	23.32
Zr-rich	24	7.67
Metal-bearing	22	7.03
TiV-rich	19	6.07
FeNi-rich	11	3.51
FeZr-bearing	8	2.56
P-rich	7	2.24
FeV-rich	7	2.24
Zn-rich	6	1.92
S-bearing	6	1.92
Other	6	1.92
BaS-rich	5	1.60
ZnS-rich	4	1.28
FeNi-bearing	4	1.28
CuZn-beraing	4	1.28
V-rich	3	0.96
FeCr-rich	3	0.96
CuZn-rich	3	0.96
FeCrNi-rich	2	0.64
Fe-bearing	2	0.64
FeTi-rich	2	0.64
FeTiV-rich	2	0.64
FeZr-rich	2	0.64

FeVNi-rich	1	0.32
SrS-rich	1	0.32
Ni-rich	1	0.32
Cu-rich	1	0.32
FeTiZr-rich	1	0.32
Totals	313	100.00

Table 27. High-Z CCSEM "North A" (0 – 20 mm) Size Distribution by Average Diameter (microns)

Classes	Number	%	Mean	StdDev	0.2 – 0.5	0.5 – 1.0	1.0 – 2.0	2.0 – 4.0	4.0 – 8.0	>>>
Fe-rich	26.5	0.5	0.4	60.2	34.9	3.6	1.2	0.0	0.0	
W-rich	23.3	0.4	0.2	68.5	28.8	2.7	0.0	0.0	0.0	
Zr-rich	7.7	0.5	0.3	70.8	25.0	4.2	0.0	0.0	0.0	
Metal-bearing	7.0	0.5	0.2	59.1	36.4	4.5	0.0	0.0	0.0	
TiV-rich	6.1	0.4	0.2	84.2	15.8	0.0	0.0	0.0	0.0	
FeNi-rich	3.5	0.5	0.2	72.7	27.3	0.0	0.0	0.0	0.0	
FeZr-bearing	2.6	0.5	0.2	50.0	50.0	0.0	0.0	0.0	0.0	
P-rich	2.2	0.8	0.3	14.3	57.1	28.6	0.0	0.0	0.0	
FeV-rich	2.2	0.5	0.2	71.4	28.6	0.0	0.0	0.0	0.0	
Zn-rich	1.9	1.0	0.5	33.3	16.7	50.0	0.0	0.0	0.0	
S-bearing	1.9	0.4	0.2	66.7	33.3	0.0	0.0	0.0	0.0	
Other	1.9	0.3	0.1	83.3	16.7	0.0	0.0	0.0	0.0	
BaS-rich	1.6	0.4	0.1	80.0	20.0	0.0	0.0	0.0	0.0	
ZnS-rich	1.3	0.7	0.3	50.0	25.0	25.0	0.0	0.0	0.0	
FeNi-bearing	1.3	0.4	0.1	100.0	0.0	0.0	0.0	0.0	0.0	
CuZn-beraing	1.3	0.9	1.0	50.0	25.0	0.0	25.0	0.0	0.0	
V-rich	1.0	0.6	0.3	66.7	0.0	33.3	0.0	0.0	0.0	
FeCr-rich	1.0	0.3	0.1	100.0	0.0	0.0	0.0	0.0	0.0	
CuZn-rich	1.0	0.7	0.5	66.7	0.0	33.3	0.0	0.0	0.0	
FeCrNi-rich	0.6	0.3	0.1	100.0	0.0	0.0	0.0	0.0	0.0	
Fe-bearing	0.6	0.7	0.1	0.0	100.0	0.0	0.0	0.0	0.0	
FeTi-rich	0.6	0.4	0.2	50.0	50.0	0.0	0.0	0.0	0.0	
FeTiV-rich	0.6	0.3	0.0	100.0	0.0	0.0	0.0	0.0	0.0	
FeZr-rich	0.6	0.5	0.2	50.0	50.0	0.0	0.0	0.0	0.0	
FeVNi-rich	0.3	0.3	0.0	100.0	0.0	0.0	0.0	0.0	0.0	
SrS-rich	0.3	0.4	0.0	100.0	0.0	0.0	0.0	0.0	0.0	
Ni-rich	0.3	0.4	0.0	100.0	0.0	0.0	0.0	0.0	0.0	
Cu-rich	0.3	0.3	0.0	100.0	0.0	0.0	0.0	0.0	0.0	
FeTiZr-rich	0.3	0.5	0.0	0.0	100.0	0.0	0.0	0.0	0.0	
Totals	100.0	0.5	0.3	65.2	29.4	4.8	0.6	0.0	0.0	

Table 28. High-Z CCSEM "North A" (0 – 20 mm) Average Composition

Classes	#	Si	P	S	Ti	V	Cr	Fe	Ni	Cu	Zn	Sr	Zr	Ba	La	Ce	W
Fe-rich	83	0	0	1	0	1	0	92	5	0	0	0	0	0	0	0	0
W-rich	73	0	0	0	0	0	0	0	0	0	0	0	0	0	0	0	100
Zr-rich	24	0	0	0	0	0	0	0	0	0	0	0	97	0	0	3	0
Metal-bearing	22	0	3	0	5	30	4	29	7	0	0	0	2	14	0	6	0
TiV-rich	19	0	0	0	8	51	7	0	0	0	0	0	0	34	0	0	0
FeNi-rich	11	0	0	0	0	0	1	71	26	0	0	0	0	0	0	1	0
FeZr-bearing	8	0	0	0	4	8	0	44	10	0	0	0	23	11	0	0	0
P-rich	7	0	86	0	0	0	0	0	0	0	0	0	0	0	0	0	14
FeV-rich	7	0	0	0	0	21	3	65	3	0	0	0	0	5	0	2	0
Zn-rich	6	0	0	2	0	1	1	1	0	2	92	0	0	0	2	0	0
S-bearing	6	0	1	69	0	0	0	0	0	1	4	0	0	21	0	1	2
Other	6	0	0	2	0	6	1	6	4	29	1	0	26	8	1	0	16
BaS-rich	5	0	0	46	0	0	0	0	0	0	0	0	0	52	0	0	2
ZnS-rich	4	0	0	73	0	0	0	0	0	0	27	0	0	0	0	0	0

FeNi-bearing	4	0	0	3	0	0	1	32	59	0	0	0	0	2	2	0	0
CuZn-beraing	4	0	0	0	0	0	0	0	7	71	16	0	0	0	0	0	7
V-rich	3	0	0	0	0	67	7	0	0	0	0	0	0	0	0	27	0
FeCr-rich	3	0	0	2	0	0	28	62	4	0	0	0	0	0	0	3	0
CuZn-rich	3	0	0	1	0	0	0	0	6	72	21	0	0	0	0	0	0
FeCrNi-rich	2	0	0	5	0	0	23	59	11	0	0	0	0	0	0	3	0
Fe-bearing	2	0	0	0	0	3	0	75	4	0	0	0	3	16	0	0	0
FeTi-rich	2	0	0	0	41	14	0	43	3	0	0	0	0	0	0	0	0
FeTiV-rich	2	0	4	0	31	12	3	39	6	0	0	0	4	0	0	0	0
FeZr-rich	2	0	0	0	0	0	0	63	6	0	0	0	29	3	0	0	0
FeVNi-rich	1	0	0	0	0	20	0	65	7	0	0	0	0	8	0	0	0
SrS-rich	1	0	0	34	0	0	0	0	0	0	0	66	0	0	0	0	0
Ni-rich	1	0	0	0	0	0	0	0	100	0	0	0	0	0	0	0	0
Cu-rich	1	0	0	0	0	0	0	0	0	100	0	0	0	0	0	0	0
FeTiZr-rich	1	0	0	0	31	13	0	38	0	0	0	0	18	0	0	0	0
Totals	313	0	2	4	1	7	1	35	5	3	3	0	9	5	0	1	24

Client_Name	Harbert
Client_Number	North B (20 – 40 mm)
Project_Number	TEH1007708
Sample_Number	10077491N
DataFiles	901497_B\10077491.*

Mag	Fields	Particles
1000	687.5094	601

Table 29. "North B" (20 – 40 mm) CCSEM particle elemental distribution

Classes	#	Number %
Fe-rich	180	29.95
Metal-bearing	63	10.48
W-rich	56	9.32
Zr-rich	41	6.82
TiV-rich	30	4.99
P-rich	29	4.83
FeNi-rich	28	4.66
Other	25	4.16
BaS-rich	21	3.49
S-bearing	20	3.33
FeV-rich	18	3.00
V-rich	16	2.66
FeCr-rich	14	2.33
SrS-rich	8	1.33
FeNi-bearing	7	1.16
FeZr-bearing	7	1.16
Fe-bearing	5	0.83
FeVNi-rich	4	0.67
FeS-rich	4	0.67
FeZr-rich	4	0.67
ZnS-rich	3	0.50
Sr-rich	3	0.50
CuZn-rich	3	0.50
FeTiV-rich	2	0.33
Cu-rich	2	0.33
Zn-rich	2	0.33
Ni-rich	2	0.33
FeTi-rich	1	0.17
FeCrNi-rich	1	0.17
FeVP-rich	1	0.17
FeZrNi-rich	1	0.17
Totals	601	100.00

Table 30. High-Z CCSEM "North B" (20 – 40 mm) Size Distribution by Average Diameter (microns)

Classes	Number	%	Mean	StdDev	0.2 - 0.5	0.5 - 1.0	1.0 - 2.0	2.0 - 4.0	4.0 - 8.0	>>>
Fe-rich	30.0	0.5	0.2	66.7	31.1	2.2	0.0	0.0	0.0	
Metal-bearing	10.5	0.4	0.3	71.4	20.6	7.9	0.0	0.0	0.0	
W-rich	9.3	0.6	0.4	51.8	37.5	8.9	1.8	0.0	0.0	
Zr-rich	6.8	0.4	0.2	75.6	24.4	0.0	0.0	0.0	0.0	
TiV-rich	5.0	0.5	0.2	66.7	30.0	3.3	0.0	0.0	0.0	
P-rich	4.8	0.6	0.3	31.0	55.2	13.8	0.0	0.0	0.0	
FeNi-rich	4.7	0.4	0.2	67.9	32.1	0.0	0.0	0.0	0.0	
Other	4.2	0.5	0.2	76.0	20.0	4.0	0.0	0.0	0.0	
BaS-rich	3.5	0.6	0.4	47.6	33.3	19.0	0.0	0.0	0.0	
S-bearing	3.3	0.6	0.3	40.0	50.0	10.0	0.0	0.0	0.0	
FeV-rich	3.0	0.5	0.2	61.1	38.9	0.0	0.0	0.0	0.0	
V-rich	2.7	0.5	0.2	43.8	56.3	0.0	0.0	0.0	0.0	
FeCr-rich	2.3	0.4	0.2	92.9	7.1	0.0	0.0	0.0	0.0	
SrS-rich	1.3	0.5	0.2	75.0	25.0	0.0	0.0	0.0	0.0	
FeNi-bearing	1.2	0.4	0.1	85.7	14.3	0.0	0.0	0.0	0.0	
FeZr-bearing	1.2	0.7	0.3	42.9	42.9	14.3	0.0	0.0	0.0	
Fe-bearing	0.8	0.4	0.1	100.0	0.0	0.0	0.0	0.0	0.0	
FeVNi-rich	0.7	0.6	0.1	0.0	100.0	0.0	0.0	0.0	0.0	
FeS-rich	0.7	0.2	0.1	100.0	0.0	0.0	0.0	0.0	0.0	
FeZr-rich	0.7	0.4	0.2	75.0	25.0	0.0	0.0	0.0	0.0	
ZnS-rich	0.5	1.2	1.2	66.7	0.0	0.0	33.3	0.0	0.0	
Sr-rich	0.5	0.7	0.1	0.0	100.0	0.0	0.0	0.0	0.0	
CuZn-rich	0.5	0.5	0.2	33.3	66.7	0.0	0.0	0.0	0.0	
FeTiV-rich	0.3	0.5	0.1	50.0	50.0	0.0	0.0	0.0	0.0	
Cu-rich	0.3	0.6	0.0	0.0	100.0	0.0	0.0	0.0	0.0	
Zn-rich	0.3	0.8	0.5	50.0	0.0	50.0	0.0	0.0	0.0	
Ni-rich	0.3	0.4	0.2	50.0	50.0	0.0	0.0	0.0	0.0	
FeTi-rich	0.2	0.6	0.0	0.0	100.0	0.0	0.0	0.0	0.0	
FeCrNi-rich	0.2	0.3	0.0	100.0	0.0	0.0	0.0	0.0	0.0	
FeVP-rich	0.2	0.3	0.0	100.0	0.0	0.0	0.0	0.0	0.0	
FeZrNi-rich	0.2	0.5	0.0	100.0	0.0	0.0	0.0	0.0	0.0	
Totals	100.0	0.5	0.3	62.7	32.3	4.7	0.3	0.0	0.0	

Table 31. High-Z CCSEM "North B" (20 – 40 mm) Average Composition

Classes	#	Si	P	S	Ti	V	Cr	Fe	Ni	Cu	Zn	Sr	Zr	Ba	La	Ce	W
Fe-rich	180	0	0	1	0	1	0	93	3	0	0	0	0	0	0	0	0
Metal-bearing	63	0	1	0	1	30	4	26	7	0	0	0	1	23	0	6	0
W-rich	56	0	0	0	0	0	0	0	0	0	0	0	0	0	0	0	100
Zr-rich	41	0	0	0	0	0	0	0	0	0	0	0	98	0	0	2	0
TiV-rich	30	0	0	0	1	49	7	0	0	0	0	0	0	42	0	0	0
P-rich	29	0	83	1	0	0	0	0	0	0	0	0	0	0	0	0	16
FeNi-rich	28	0	0	2	1	2	0	69	25	0	0	0	0	0	0	1	0
Other	25	0	4	3	0	5	1	22	2	6	2	0	13	30	0	1	11
BaS-rich	21	0	1	43	0	0	0	0	0	0	0	0	0	56	0	0	0
S-bearing	20	0	2	37	0	0	0	0	0	0	1	3	0	55	0	0	3
FeV-rich	18	0	0	0	0	25	3	62	3	0	0	0	0	0	0	6	0
V-rich	16	0	0	0	0	65	11	0	0	0	0	0	0	0	0	25	0
FeCr-rich	14	0	0	2	0	0	25	66	6	0	0	0	0	0	0	0	0
SrS-rich	8	0	0	32	0	0	0	0	0	0	0	66	0	0	1	1	0
FeNi-bearing	7	0	1	0	0	6	1	36	50	0	0	0	0	6	0	1	0
FeZr-bearing	7	0	0	0	0	11	0	37	4	0	0	0	24	24	0	0	0
Fe-bearing	5	0	5	3	0	9	7	63	3	0	0	0	0	9	0	1	0
FeVNi-rich	4	0	0	2	3	14	1	61	13	0	0	0	0	6	0	0	0
FeS-rich	4	0	0	70	0	0	1	29	0	0	0	0	0	0	0	0	0
FeZr-rich	4	0	0	0	0	0	0	48	7	0	0	0	43	2	0	0	0
ZnS-rich	3	0	3	65	0	0	0	0	0	2	31	0	0	0	0	0	0
Sr-rich	3	0	0	0	0	0	0	0	0	0	2	98	0	0	0	0	0
CuZn-rich	3	0	3	0	0	0	0	0	0	66	31	0	0	0	0	0	0

FeTiV-rich	2	0	0	4	20	24	3	50	0	0	0	0	0	0	0	0	0
Cu-rich	2	0	0	0	0	0	3	0	0	95	3	0	0	0	0	0	0
Zn-rich	2	0	0	0	0	0	5	0	0	5	91	0	0	0	0	0	0
Ni-rich	2	0	0	4	0	0	0	0	97	0	0	0	0	0	0	0	0
FeTi-rich	1	0	0	0	40	10	0	42	0	0	0	0	9	0	0	0	0
FeCrNi-rich	1	0	0	0	0	0	22	60	12	0	0	0	0	0	0	6	0
FeVP-rich	1	0	34	0	0	13	9	39	0	0	0	0	0	0	0	5	0
FeZrNi-rich	1	0	0	0	0	0	0	37	23	0	0	0	36	4	0	0	0
Totals	601	0	5	4	0	9	2	41	4	1	1	1	8	10	0	2	11

Client_Name	Harbert
Client_Number	North C (40 – 60 mm)
Project_Number	TEH1007708
Sample_Number	10077491N
DataFiles	901498_C\10077491.*

Mag	Fields	Particles
1000	693.3582	289

Table 32. "North C" (40 – 60 mm) CCSEM particle elemental distribution

Classes	**#**	**Number %**
Fe-rich	82	28.37
W-rich	66	22.84
Metal-bearing	28	9.69
FeNi-rich	18	6.23
Zr-rich	17	5.88
Other	13	4.50
TiV-rich	11	3.81
FeV-rich	7	2.42
V-rich	7	2.42
FeZr-rich	5	1.73
S-bearing	5	1.73
FeZr-bearing	4	1.38
P-rich	3	1.04
FeS-rich	3	1.04
ZnS-rich	3	1.04
FeVNi-rich	3	1.04
FeCr-rich	2	0.69
BaS-rich	2	0.69
Fe-bearing	2	0.69
CuZn-beraing	2	0.69
FeNi-bearing	2	0.69
CuZn-rich	2	0.69
Cu-rich	1	0.35
SrS-rich	1	0.35
Totals	289	100.00

Table 33. High-Z CCSEM "North C" (40 – 60 mm) Size Distribution by Average Diameter (microns)

Classes	Number	%	Mean	StdDev	0.2 - 0.5	0.5 - 1.0	1.0 - 2.0	2.0 - 4.0	4.0 - 8.0	>>>
Fe-rich	28.4		0.5	0.2	68.3	30.5	1.2	0.0	0.0	0.0
W-rich	22.8		0.6	0.3	43.9	43.9	12.1	0.0	0.0	0.0
Metal-bearing	9.7		0.4	0.1	75.0	25.0	0.0	0.0	0.0	0.0
FeNi-rich	6.2		0.6	0.4	50.0	38.9	11.1	0.0	0.0	0.0
Zr-rich	5.9		0.5	0.2	52.9	47.1	0.0	0.0	0.0	0.0
Other	4.5		0.4	0.1	69.2	30.8	0.0	0.0	0.0	0.0
TiV-rich	3.8		0.5	0.2	54.5	45.5	0.0	0.0	0.0	0.0
FeV-rich	2.4		0.7	0.3	28.6	42.9	28.6	0.0	0.0	0.0
V-rich	2.4		0.4	0.2	57.1	42.9	0.0	0.0	0.0	0.0
FeZr-rich	1.7		0.5	0.2	40.0	60.0	0.0	0.0	0.0	0.0
S-bearing	1.7		1.0	0.8	40.0	20.0	20.0	20.0	0.0	0.0
FeZr-bearing	1.4		0.5	0.2	50.0	50.0	0.0	0.0	0.0	0.0
P-rich	1.0		0.6	0.1	33.3	66.7	0.0	0.0	0.0	0.0
FeS-rich	1.0		0.6	0.2	33.3	66.7	0.0	0.0	0.0	0.0
ZnS-rich	1.0		0.8	0.6	66.7	0.0	33.3	0.0	0.0	0.0
FeVNi-rich	1.0		0.4	0.2	33.3	66.7	0.0	0.0	0.0	0.0
FeCr-rich	0.7		0.5	0.0	0.0	100.0	0.0	0.0	0.0	0.0
BaS-rich	0.7		0.5	0.3	50.0	50.0	0.0	0.0	0.0	0.0
Fe-bearing	0.7		0.7	0.0	0.0	100.0	0.0	0.0	0.0	0.0
CuZn-beraing	0.7		0.6	0.2	50.0	50.0	0.0	0.0	0.0	0.0
FeNi-bearing	0.7		0.4	0.2	50.0	50.0	0.0	0.0	0.0	0.0
CuZn-rich	0.7		0.5	0.1	50.0	50.0	0.0	0.0	0.0	0.0
Cu-rich	0.3		0.4	0.0	100.0	0.0	0.0	0.0	0.0	0.0
SrS-rich	0.3		0.4	0.0	100.0	0.0	0.0	0.0	0.0	0.0
Totals	100.0		0.5	0.3	56.1	38.4	5.2	0.3	0.0	0.0

Table 34. High-Z CCSEM "North C" (40 – 60 mm) Average Composition

Classes	#	Si	P	S	Ti	V	Cr	Fe	Ni	Cu	Zn	Sr	Zr	Ba	La	Ce	W
Fe-rich	82	0	0	0	0	1	0	93	5	0	0	0	0	0	0	0	0
W-rich	66	0	0	0	0	0	0	0	0	0	0	0	0	0	0	0	100
Metal-bearing	28	0	1	1	1	30	5	31	5	0	0	0	1	22	0	5	0
FeNi-rich	18	0	1	2	0	3	0	73	21	0	0	0	0	0	0	0	0
Zr-rich	17	0	0	0	0	0	0	0	0	0	0	0	97	0	0	2	0
Other	13	0	1	0	0	12	1	23	7	12	1	0	9	34	0	0	0
TiV-rich	11	0	0	0	6	49	6	0	0	0	0	0	1	38	0	0	0
FeV-rich	7	0	0	0	0	18	3	69	4	0	0	0	1	2	0	4	0
V-rich	7	0	0	0	0	64	8	1	0	0	0	0	0	0	0	26	0
FeZr-rich	5	0	0	0	0	0	0	61	6	0	0	0	32	0	0	0	0
S-bearing	5	0	5	59	0	1	9	4	0	1	8	0	0	12	0	0	1
FeZr-bearing	4	0	0	0	0	8	0	33	7	0	0	0	39	14	0	0	0
P-rich	3	0	82	3	0	0	0	0	0	0	0	0	0	0	0	0	15
FeS-rich	3	0	3	74	0	0	0	24	0	0	0	0	0	0	0	0	0
ZnS-rich	3	0	0	74	0	0	0	0	0	0	26	0	0	0	0	0	0
FeVNi-rich	3	0	0	0	0	10	3	58	20	0	0	0	0	7	0	2	0
FeCr-rich	2	0	0	0	0	2	27	65	7	0	0	0	0	0	0	0	0
BaS-rich	2	0	0	45	0	0	0	0	0	0	0	0	0	56	0	0	0
Fe-bearing	2	0	0	0	0	22	3	58	3	0	0	0	0	16	0	0	0
CuZn-beraing	2	0	0	5	0	0	0	0	12	70	15	0	0	0	0	0	0
FeNi-bearing	2	0	0	3	0	0	0	48	42	0	0	0	0	8	0	0	0
CuZn-rich	2	0	0	0	0	0	0	0	2	80	18	0	0	0	0	0	0
Cu-rich	1	0	0	0	0	0	0	0	0	100	0	0	0	0	0	0	0
SrS-rich	1	0	0	30	0	0	0	0	0	0	0	70	0	0	0	0	0
Totals	289	0	1	3	0	8	1	40	4	2	1	0	7	6	0	1	23

Client_Name Harbert
Client_Number North D (60 – 80 mm)
Project_Number TEH1007708
Sample_Number 10077491N

DataFiles 901498_D\10077491.*

Mag	Fields	Particles
1000	693.1438	157

Table 35. "North D" (60 – 80 mm) CCSEM particle elemental distribution

Classes	#	Number %
W-rich	34	21.66
Fe-rich	32	20.38
Metal-bearing	13	8.28
P-rich	11	7.01
Zr-rich	10	6.37
TiV-rich	9	5.73
FeV-rich	7	4.46
FeZr-bearing	4	2.55
FeCr-rich	4	2.55
FeNi-bearing	3	1.91
V-rich	3	1.91
Other	3	1.91
CuZn-rich	3	1.91
FeNi-rich	3	1.91
S-bearing	3	1.91
Zn-rich	2	1.27
Cu-rich	2	1.27
CuZn-beraing	2	1.27
FeVNi-rich	2	1.27
FeTi-rich	1	0.64
FeCrNi-rich	1	0.64
FeS-rich	1	0.64
BaS-rich	1	0.64
Fe-bearing	1	0.64
ZnS-rich	1	0.64
FeTiV-rich	1	0.64
Totals	157	100.00

Table 36. High-Z CCSEM "North D" (60 – 80 mm) Size Distribution by Average Diameter (microns)

Classes	Number	%	Mean	StdDev	0.2 - 0.5	0.5 - 1.0	1.0 - 2.0	2.0 - 4.0	4.0 - 8.0	>>>
W-rich	21.7	0.8	0.4	17.6	70.6	8.8	2.9	0.0	0.0
Fe-rich	20.4	0.7	0.4	40.6	50.0	6.3	3.1	0.0	0.0
Metal-bearing	8.3	0.6	0.4	46.2	46.2	7.7	0.0	0.0	0.0
P-rich	7.0	0.6	0.2	27.3	63.6	9.1	0.0	0.0	0.0
Zr-rich	6.4	0.5	0.3	50.0	40.0	10.0	0.0	0.0	0.0
TiV-rich	5.7	0.5	0.2	55.6	44.4	0.0	0.0	0.0	0.0
FeV-rich	4.5	0.7	0.2	14.3	71.4	14.3	0.0	0.0	0.0
FeZr-bearing	2.5	0.6	0.3	25.0	50.0	25.0	0.0	0.0	0.0
FeCr-rich	2.5	1.1	0.9	0.0	75.0	0.0	25.0	0.0	0.0
FeNi-bearing	1.9	0.7	0.2	33.3	66.7	0.0	0.0	0.0	0.0
V-rich	1.9	0.4	0.1	66.7	33.3	0.0	0.0	0.0	0.0
Other	1.9	0.5	0.2	33.3	66.7	0.0	0.0	0.0	0.0
CuZn-rich	1.9	0.8	0.1	0.0	100.0	0.0	0.0	0.0	0.0
FeNi-rich	1.9	1.1	0.3	0.0	33.3	66.7	0.0	0.0	0.0
S-bearing	1.9	1.2	0.4	0.0	33.3	66.7	0.0	0.0	0.0
Zn-rich	1.3	1.8	0.9	0.0	50.0	0.0	50.0	0.0	0.0
Cu-rich	1.3	0.8	0.5	50.0	0.0	50.0	0.0	0.0	0.0
CuZn-beraing	1.3	0.3	0.0	100.0	0.0	0.0	0.0	0.0	0.0
FeVNi-rich	1.3	0.5	0.1	50.0	50.0	0.0	0.0	0.0	0.0
FeTi-rich	0.6	0.5	0.0	100.0	0.0	0.0	0.0	0.0	0.0
FeCrNi-rich	0.6	0.4	0.0	100.0	0.0	0.0	0.0	0.0	0.0
FeS-rich	0.6	0.3	0.0	100.0	0.0	0.0	0.0	0.0	0.0
BaS-rich	0.6	0.3	0.0	100.0	0.0	0.0	0.0	0.0	0.0
Fe-bearing	0.6	0.4	0.0	100.0	0.0	0.0	0.0	0.0	0.0
ZnS-rich	0.6	0.5	0.0	0.0	100.0	0.0	0.0	0.0	0.0
FeTiV-rich	0.6	1.1	0.0	0.0	0.0	100.0	0.0	0.0	0.0
Totals	100.0	0.7	0.4	33.8	53.5	10.2	2.5	0.0	0.0

Table 37. High-Z CCSEM "North D" (60 – 80 mm) Average Composition

Classes	#	Si	P	S	Ti	V	Cr	Fe	Ni	Cu	Zn	Sr	Zr	Ba	La	Ce	W
W-rich	34	0	0	0	0	0	0	0	0	0	0	0	0	0	0	0	100
Fe-rich	32	0	0	1	0	2	0	93	3	0	1	0	0	0	0	0	0
Metal-bearing	13	0	2	0	0	26	8	28	10	0	0	0	1	20	0	4	0
P-rich	11	0	85	0	0	0	0	0	0	0	0	0	0	0	0	0	15
Zr-rich	10	0	0	0	0	0	0	0	0	0	0	0	98	1	0	1	0
TiV-rich	9	0	0	0	4	45	6	0	0	0	0	0	1	44	0	0	0
FeV-rich	7	0	0	0	1	20	3	64	4	0	0	0	0	0	0	7	0
FeZr-bearing	4	0	0	0	0	4	0	34	5	0	0	0	26	31	0	0	0
FeCr-rich	4	0	0	0	0	0	27	68	4	0	0	0	0	0	0	1	0
FeNi-bearing	3	0	7	2	0	0	0	34	57	0	0	0	0	0	0	0	0
V-rich	3	0	0	0	0	64	6	3	0	0	0	0	0	0	0	26	0
Other	3	0	19	2	0	7	2	12	2	0	26	0	5	22	0	0	3
CuZn-rich	3	0	0	0	0	0	0	0	1	71	26	0	0	0	0	2	0
FeNi-rich	3	0	2	0	0	5	0	76	16	0	0	0	0	0	0	2	0
S-bearing	3	0	0	56	0	0	6	2	0	8	28	0	0	0	0	0	0
Zn-rich	2	0	0	0	0	0	0	0	0	4	96	0	0	0	0	0	0
Cu-rich	2	0	0	0	0	0	0	0	0	93	8	0	0	0	0	0	0
CuZn-beraing	2	0	0	0	0	0	0	0	10	76	13	0	0	0	0	0	0
FeVNi-rich	2	0	0	0	8	7	3	76	8	0	0	0	0	0	0	0	0
FeTi-rich	1	0	0	0	50	10	0	40	0	0	0	0	0	0	0	0	0
FeCrNi-rich	1	0	0	9	0	0	19	63	9	0	0	0	0	0	0	0	0
FeS-rich	1	0	0	79	0	0	0	21	0	0	0	0	0	0	0	0	0
BaS-rich	1	0	0	44	0	0	0	0	0	0	0	0	0	56	0	0	0
Fe-bearing	1	0	33	0	0	0	0	58	9	0	0	0	0	0	0	0	0
ZnS-rich	1	0	0	67	0	0	0	0	0	8	25	0	0	0	0	0	0
FeTiV-rich	1	0	0	0	34	31	4	22	9	0	0	0	0	0	0	0	0
Totals	157	0	7	3	1	8	2	32	4	4	3	0	7	6	0	1	23

```
Client_Name     Harbert
Client_Number   West A (0 - 20 mm)
Project_Number  TEH1007708
Sample_Number   9077491W
DataFiles       901501_A\9077491W.*

Mag       Fields    Particles
1000      693.3582  572
```

Table 38. "West A" (0 - 20 mm) CCSEM particle elemental distribution

Classes	#	Number %
Fe-rich	234	40.91
TiV-rich	63	11.01
FeNi-rich	35	6.12
FeTi-rich	26	4.55
FeTiV-rich	26	4.55
Metal-bearing	24	4.20
FeCr-rich	23	4.02
P-rich	22	3.85
Zr-rich	16	2.80
Other	15	2.62
FeV-rich	10	1.75
CuZn-rich	10	1.75
FeNi-bearing	9	1.57
BaS-rich	8	1.40
FeS-rich	7	1.22
FeTiZr-rich	6	1.05
FeZr-bearing	5	0.87
ZnS-rich	4	0.70
FeZr-rich	4	0.70
V-rich	3	0.52
Cu-rich	3	0.52
Fe-bearing	3	0.52

LaCe-rich	2	0.35
FeVNi-rich	2	0.35
Ni-rich	2	0.35
FeCrNi-rich	2	0.35
TiZr-rich	1	0.17
FeZrNi-rich	1	0.17
FeVP-rich	1	0.17
Sr-rich	1	0.17
Zn-rich	1	0.17
SrS-rich	1	0.17
S-bearing	1	0.17
Ti-rich	1	0.17
Totals	572	100.00

Table 39. High-Z CCSEM "West A" (0 – 20 mm) Size Distribution by Average Diameter (microns)

				0.2 -	0.5 -	1.0 -	2.0 -	4.0 -	
Classes	**Number %**	**Mean**	**StdDev**	**0.5**	**1.0**	**2.0**	**4.0**	**8.0**	**>>>**
Fe-rich	40.9	0.5	0.3	59.4	33.8	6.8	0.0	0.0	0.0
TiV-rich	11.0	0.5	0.3	57.1	36.5	6.3	0.0	0.0	0.0
FeNi-rich	6.1	0.4	0.2	71.4	28.6	0.0	0.0	0.0	0.0
FeTi-rich	4.5	0.4	0.2	69.2	30.8	0.0	0.0	0.0	0.0
FeTiV-rich	4.5	0.6	0.3	57.7	30.8	11.5	0.0	0.0	0.0
Metal-bearing	4.2	0.5	0.2	70.8	29.2	0.0	0.0	0.0	0.0
FeCr-rich	4.0	0.3	0.2	82.6	17.4	0.0	0.0	0.0	0.0
P-rich	3.8	0.5	0.2	54.5	40.9	4.5	0.0	0.0	0.0
Zr-rich	2.8	0.5	0.2	62.5	37.5	0.0	0.0	0.0	0.0
Other	2.6	0.7	0.4	46.7	33.3	20.0	0.0	0.0	0.0
FeV-rich	1.7	0.5	0.1	60.0	40.0	0.0	0.0	0.0	0.0
CuZn-rich	1.7	0.6	0.2	30.0	70.0	0.0	0.0	0.0	0.0
FeNi-bearing	1.6	0.5	0.3	77.8	11.1	11.1	0.0	0.0	0.0
BaS-rich	1.4	0.4	0.2	75.0	25.0	0.0	0.0	0.0	0.0
FeS-rich	1.2	0.5	0.2	85.7	0.0	14.3	0.0	0.0	0.0
FeTiZr-rich	1.0	0.6	0.2	50.0	33.3	16.7	0.0	0.0	0.0
FeZr-bearing	0.9	0.6	0.1	40.0	60.0	0.0	0.0	0.0	0.0
ZnS-rich	0.7	0.4	0.2	50.0	50.0	0.0	0.0	0.0	0.0
FeZr-rich	0.7	0.3	0.1	100.0	0.0	0.0	0.0	0.0	0.0
V-rich	0.5	0.5	0.3	66.7	33.3	0.0	0.0	0.0	0.0
Cu-rich	0.5	0.8	0.5	33.3	33.3	33.3	0.0	0.0	0.0
Fe-bearing	0.5	0.6	0.1	33.3	66.7	0.0	0.0	0.0	0.0
LaCe-rich	0.3	0.4	0.2	50.0	50.0	0.0	0.0	0.0	0.0
FeVNi-rich	0.3	0.5	0.0	50.0	50.0	0.0	0.0	0.0	0.0
Ni-rich	0.3	0.6	0.2	50.0	50.0	0.0	0.0	0.0	0.0
FeCrNi-rich	0.3	0.3	0.1	100.0	0.0	0.0	0.0	0.0	0.0
TiZr-rich	0.2	0.3	0.0	100.0	0.0	0.0	0.0	0.0	0.0
FeZrNi-rich	0.2	0.3	0.0	100.0	0.0	0.0	0.0	0.0	0.0
FeVP-rich	0.2	0.5	0.0	0.0	100.0	0.0	0.0	0.0	0.0
Sr-rich	0.2	0.6	0.0	0.0	100.0	0.0	0.0	0.0	0.0
Zn-rich	0.2	0.2	0.0	100.0	0.0	0.0	0.0	0.0	0.0
SrS-rich	0.2	0.3	0.0	100.0	0.0	0.0	0.0	0.0	0.0
S-bearing	0.2	0.3	0.0	100.0	0.0	0.0	0.0	0.0	0.0
Ti-rich	0.2	1.2	0.0	0.0	0.0	100.0	0.0	0.0	0.0
Totals	100.0	0.5	0.3	61.4	33.0	5.6	0.0	0.0	0.0

Table 40. High-Z CCSEM "West A" (0 – 20 mm) Average Composition

Classes	#	Si	P	S	Ti	V	Cr	Fe	Ni	Cu	Zn	Sr	Zr	Ba	La	Ce	W
Fe-rich	234	0	0	1	0	1	0	94	4	0	0	0	0	0	0	0	0
TiV-rich	63	0	0	0	39	55	3	2	0	0	0	0	0	0	0	0	0
FeNi-rich	35	0	0	1	0	1	0	70	26	0	0	0	0	0	0	1	0
FeTi-rich	26	0	0	0	44	8	0	44	2	0	0	0	2	0	0	0	0
FeTiV-rich	26	0	1	0	27	31	1	36	2	0	0	0	1	0	0	0	0
Metal-bearing	24	0	1	1	17	41	9	15	8	0	0	0	2	0	0	6	0
FeCr-rich	23	0	0	0	0	0	22	69	8	0	0	0	0	0	0	0	0
P-rich	22	0	92	0	0	0	0	0	0	0	0	0	0	0	0	0	8
Zr-rich	16	0	0	0	0	0	0	0	0	0	0	0	97	0	0	0	2
Other	15	0	5	2	8	6	0	5	3	7	2	0	35	6	0	0	21
FeV-rich	10	0	0	0	3	22	2	68	3	0	0	0	0	1	0	0	0
CuZn-rich	10	0	0	1	0	0	0	0	2	65	31	0	0	0	0	0	1
FeNi-bearing	9	0	1	3	7	1	0	37	49	0	0	0	0	0	1	0	0
BaS-rich	8	0	0	47	0	0	0	0	0	0	1	0	0	52	0	0	0
FeS-rich	7	0	0	72	0	0	0	28	0	0	0	0	0	0	0	0	0
FeTiZr-rich	6	0	0	0	27	4	0	38	6	0	0	0	25	0	0	0	0
FeZr-bearing	5	0	0	0	0	0	1	63	17	0	1	0	16	2	0	0	0
ZnS-rich	4	0	0	68	0	0	0	0	0	0	33	0	0	0	0	0	0
FeZr-rich	4	0	0	0	2	0	0	64	7	0	0	0	27	1	0	0	0
V-rich	3	0	0	0	0	88	8	2	0	0	0	0	0	3	0	0	0
Cu-rich	3	0	0	0	0	0	0	0	0	100	0	0	0	0	0	0	0
Fe-bearing	3	0	0	2	3	3	24	60	2	0	0	0	0	0	0	0	5
LaCe-rich	2	0	0	0	0	4	0	0	25	0	0	0	0	0	50	22	0
FeVNi-rich	2	0	0	0	0	34	2	40	13	0	0	0	0	6	0	4	0
Ni-rich	2	0	0	0	0	0	0	5	96	0	0	0	0	0	0	0	0
FeCrNi-rich	2	0	0	6	0	0	22	61	12	0	0	0	0	0	0	0	0
TiZr-rich	1	0	0	0	21	0	0	0	0	0	0	0	79	0	0	0	0
FeZrNi-rich	1	0	0	0	0	6	0	45	13	0	0	0	30	6	0	0	0
FeVP-rich	1	0	31	0	0	17	4	47	0	0	0	0	0	0	0	0	0
Sr-rich	1	0	0	0	0	0	0	0	0	0	0	100	0	0	0	0	0
Zn-rich	1	0	0	0	0	0	0	0	0	6	94	0	0	0	0	0	0
SrS-rich	1	0	0	33	0	0	0	0	0	0	0	67	0	0	0	0	0
S-bearing	1	0	0	39	0	0	0	0	0	0	0	0	0	41	0	0	20
Ti-rich	1	0	0	0	85	15	0	0	0	0	0	0	0	0	0	0	0
Totals	572	0	4	3	9	11	2	54	6	2	1	0	5	1	0	0	1

```
Client_Name     Harbert
Client_Number   West B (20 - 40 mm)
Project_Number  TEH1007708
Sample_Number   9077491W
DataFiles       901501_B\9077491W.*

Mag       Fields    Particles
1000      693.3582  391
```

Table 41. "West B" (20 – 40 mm) CCSEM particle elemental distribution

Classes	#	Number %
Fe-rich	148	37.85
TiV-rich	46	11.76
FeNi-rich	24	6.14
FeTi-rich	23	5.88
FeCr-rich	21	5.37
FeTiV-rich	20	5.12
P-rich	18	4.60
Zr-rich	16	4.09
FeV-rich	8	2.05
Metal-bearing	7	1.79
Other	7	1.79
FeZr-bearing	6	1.53
FeNi-bearing	5	1.28
FeZr-rich	5	1.28
CuZn-rich	4	1.02

FeTiZr-rich	4	1.02
Ti-rich	4	1.02
Fe-bearing	3	0.77
V-rich	3	0.77
BaS-rich	3	0.77
CuZn-beraing	2	0.51
LaCe-rich	2	0.51
ZnS-rich	2	0.51
W-rich	2	0.51
Ni-rich	1	0.26
FeS-rich	1	0.26
FeVNi-rich	1	0.26
FeTiNi-rich	1	0.26
FeVP-rich	1	0.26
TiSr-rich	1	0.26
S-bearing	1	0.26
FeCrNi-rich	1	0.26
Totals	391	100.00

Table 42. High-Z CCSEM "West B" (40 – 60 mm) Size Distribution by Average Diameter (microns)

					0.2 - 0.5	0.5 - 1.0	1.0 - 2.0	2.0 - 4.0	4.0 - 8.0	
Classes	**Number**	**%**	**Mean**	**StdDev**	**0.5**	**1.0**	**2.0**	**4.0**	**8.0**	**>>>**
Fe-rich	37.9	0.6	0.4	52.7	35.8	10.8	0.7	0.0	0.0	
TiV-rich	11.8	0.5	0.2	43.5	52.2	4.3	0.0	0.0	0.0	
FeNi-rich	6.1	0.5	0.3	62.5	33.3	4.2	0.0	0.0	0.0	
FeTi-rich	5.9	0.4	0.2	65.2	30.4	4.3	0.0	0.0	0.0	
FeCr-rich	5.4	0.6	0.3	47.6	42.9	9.5	0.0	0.0	0.0	
FeTiV-rich	5.1	0.5	0.2	70.0	25.0	5.0	0.0	0.0	0.0	
P-rich	4.6	0.6	0.2	38.9	61.1	0.0	0.0	0.0	0.0	
Zr-rich	4.1	0.5	0.2	62.5	37.5	0.0	0.0	0.0	0.0	
FeV-rich	2.0	0.5	0.2	62.5	37.5	0.0	0.0	0.0	0.0	
Metal-bearing	1.8	0.5	0.1	57.1	42.9	0.0	0.0	0.0	0.0	
Other	1.8	0.7	0.5	57.1	14.3	28.6	0.0	0.0	0.0	
FeZr-bearing	1.5	0.6	0.2	33.3	66.7	0.0	0.0	0.0	0.0	
FeNi-bearing	1.3	0.7	0.3	40.0	40.0	20.0	0.0	0.0	0.0	
FeZr-rich	1.3	0.6	0.3	40.0	40.0	20.0	0.0	0.0	0.0	
CuZn-rich	1.0	0.5	0.1	50.0	50.0	0.0	0.0	0.0	0.0	
FeTiZr-rich	1.0	0.7	0.4	75.0	0.0	25.0	0.0	0.0	0.0	
Ti-rich	1.0	0.5	0.2	50.0	50.0	0.0	0.0	0.0	0.0	
Fe-bearing	0.8	0.3	0.0	100.0	0.0	0.0	0.0	0.0	0.0	
V-rich	0.8	0.5	0.2	33.3	66.7	0.0	0.0	0.0	0.0	
BaS-rich	0.8	1.0	0.7	33.3	33.3	0.0	33.3	0.0	0.0	
CuZn-beraing	0.5	0.5	0.1	50.0	50.0	0.0	0.0	0.0	0.0	
LaCe-rich	0.5	0.3	0.0	100.0	0.0	0.0	0.0	0.0	0.0	
ZnS-rich	0.5	0.8	0.1	0.0	100.0	0.0	0.0	0.0	0.0	
W-rich	0.5	0.3	0.0	100.0	0.0	0.0	0.0	0.0	0.0	
Ni-rich	0.3	0.6	0.0	0.0	100.0	0.0	0.0	0.0	0.0	
FeS-rich	0.3	0.4	0.0	100.0	0.0	0.0	0.0	0.0	0.0	
FeVNi-rich	0.3	0.9	0.0	0.0	100.0	0.0	0.0	0.0	0.0	
FeTiNi-rich	0.3	0.8	0.0	0.0	100.0	0.0	0.0	0.0	0.0	
FeVP-rich	0.3	0.2	0.0	100.0	0.0	0.0	0.0	0.0	0.0	
TiSr-rich	0.3	0.4	0.0	100.0	0.0	0.0	0.0	0.0	0.0	
S-bearing	0.3	0.5	0.0	0.0	100.0	0.0	0.0	0.0	0.0	
FeCrNi-rich	0.3	0.3	0.0	100.0	0.0	0.0	0.0	0.0	0.0	
Totals	100.0	0.5	0.3	53.5	38.9	7.2	0.5	0.0	0.0	

Table 43. High-Z CCSEM "West B" (0 – 20 mm) Average Composition

Classes	#	Si	P	S	Ti	V	Cr	Fe	Ni	Cu	Zn	Sr	Zr	Ba	La	Ce	W
Fe-rich	148	0	0	0	0	1	0	93	4	0	0	0	0	0	0	0	0
TiV-rich	46	0	0	0	51	45	1	0	0	0	0	0	0	0	0	0	1
FeNi-rich	24	0	0	1	1	1	0	69	27	0	0	0	1	0	0	1	0
FeTi-rich	23	0	1	0	42	8	0	46	3	0	0	0	1	0	0	0	0
FeCr-rich	21	0	0	0	0	0	22	68	9	0	0	0	0	0	0	0	0
FeTiV-rich	20	0	0	1	25	31	1	37	4	0	0	0	1	0	0	0	0
P-rich	18	0	95	0	0	0	0	0	0	0	0	0	0	0	0	0	5
Zr-rich	16	0	0	0	1	0	0	0	0	0	0	0	98	0	0	1	1
FeV-rich	8	0	0	0	4	22	2	70	2	0	0	0	0	0	0	1	0
Metal-bearing	7	0	3	1	8	21	10	15	28	0	0	0	1	0	6	6	1
Other	7	0	0	1	15	3	0	9	5	30	1	0	17	0	1	2	15
FeZr-bearing	6	0	0	0	7	3	1	53	18	0	0	0	18	0	0	0	0
FeNi-bearing	5	0	0	0	8	2	0	34	52	2	1	0	0	0	1	0	0
FeZr-rich	5	0	0	0	2	0	0	66	4	0	0	0	28	0	0	0	0
CuZn-rich	4	0	0	0	0	0	0	1	5	68	26	0	0	0	0	0	0
FeTiZr-rich	4	0	0	0	30	4	0	34	4	0	0	0	28	0	0	0	0
Ti-rich	4	0	0	0	91	9	0	0	0	0	0	0	0	0	0	0	0
Fe-bearing	3	0	0	1	0	0	7	65	1	0	0	0	0	0	0	0	25
V-rich	3	0	0	0	7	83	2	0	0	0	0	0	0	0	0	7	0
BaS-rich	3	0	0	46	0	0	0	0	0	0	0	0	0	50	0	0	4
CuZn-beraing	2	0	0	0	0	0	0	0	11	62	15	0	0	0	0	0	13
LaCe-rich	2	0	0	5	0	0	0	0	0	0	0	0	0	0	50	33	13
ZnS-rich	2	0	0	69	0	0	0	0	0	0	32	0	0	0	0	0	0
W-rich	2	0	4	0	0	0	0	0	0	0	0	0	0	8	0	0	89
Ni-rich	1	0	0	4	0	0	0	0	96	0	0	0	0	0	0	0	0
FeS-rich	1	0	0	52	0	0	0	48	0	0	0	0	0	0	0	0	0
FeVNi-rich	1	0	0	0	0	56	5	26	6	0	0	0	0	0	0	7	0
FeTiNi-rich	1	0	0	0	17	6	0	67	10	0	0	0	0	0	0	0	0
FeVP-rich	1	0	30	0	0	19	0	37	0	0	0	0	0	0	0	0	14
TiSr-rich	1	0	0	0	35	0	0	0	0	0	0	65	0	0	0	0	0
S-bearing	1	0	0	52	0	0	8	0	40	0	0	0	0	0	0	0	0
FeCrNi-rich	1	0	8	0	0	0	19	65	8	0	0	0	0	0	0	0	0
Totals	391	0	5	1	12	10	2	53	6	2	1	0	6	0	1	1	2

```
Client_Name     Harbert
Client_Number   West C (40 – 60 mm)
Project_Number  TEH1007708
Sample_Number   9077491W
DataFiles       901501_C\9077491W.*

Mag       Fields    Particles
1000      693.3582  382
```

Table 44. "West C" (40 – 60 mm) CCSEM particle elemental distribution

Classes	#	Number %
Fe-rich	147	38.48
TiV-rich	46	12.04
P-rich	30	7.85
FeNi-rich	21	5.50
FeTi-rich	20	5.24
FeTiV-rich	19	4.97
Zr-rich	14	3.66
FeV-rich	12	3.14
Other	10	2.62
Metal-bearing	10	2.62
FeCr-rich	9	2.36
FeTiZr-rich	6	1.57
FeNi-bearing	6	1.57
FeZr-bearing	5	1.31
CuZn-rich	4	1.05
S-bearing	3	0.79

LaCe-rich	3	0.79
FeZr-rich	3	0.79
Fe-bearing	2	0.52
SrS-rich	2	0.52
FeS-rich	2	0.52
ZnS-rich	2	0.52
Ni-rich	2	0.52
V-rich	2	0.52
W-rich	1	0.26
BaS-rich	1	0.26
Totals	382	100.00

Table 45. High-Z CCSEM "West C" (40 – 60 mm) Size Distribution by Average Diameter (microns)

				0.2 -	0.5 -	1.0 -	2.0 -	4.0 -	
Classes	**Number %**	**Mean**	**StdDev**	**0.5**	**1.0**	**2.0**	**4.0**	**8.0**	**>>>**
Fe-rich	38.5	0.6	0.4	40.8	47.6	10.9	0.7	0.0	0.0
TiV-rich	12.0	0.5	0.2	45.7	52.2	2.2	0.0	0.0	0.0
P-rich	7.9	0.6	0.3	53.3	33.3	13.3	0.0	0.0	0.0
FeNi-rich	5.5	0.6	0.2	47.6	42.9	9.5	0.0	0.0	0.0
FeTi-rich	5.2	0.5	0.3	55.0	30.0	15.0	0.0	0.0	0.0
FeTiV-rich	5.0	0.7	0.4	47.4	36.8	15.8	0.0	0.0	0.0
Zr-rich	3.7	0.5	0.2	57.1	42.9	0.0	0.0	0.0	0.0
FeV-rich	3.1	0.6	0.3	41.7	41.7	16.7	0.0	0.0	0.0
Other	2.6	0.7	0.4	50.0	30.0	20.0	0.0	0.0	0.0
Metal-bearing	2.6	0.6	0.2	50.0	40.0	10.0	0.0	0.0	0.0
FeCr-rich	2.4	0.6	0.2	44.4	55.6	0.0	0.0	0.0	0.0
FeTiZr-rich	1.6	0.7	0.3	33.3	33.3	33.3	0.0	0.0	0.0
FeNi-bearing	1.6	0.5	0.2	33.3	66.7	0.0	0.0	0.0	0.0
FeZr-bearing	1.3	0.8	0.3	20.0	60.0	20.0	0.0	0.0	0.0
CuZn-rich	1.0	0.7	0.3	25.0	75.0	0.0	0.0	0.0	0.0
S-bearing	0.8	0.5	0.1	33.3	66.7	0.0	0.0	0.0	0.0
LaCe-rich	0.8	0.8	0.4	33.3	33.3	33.3	0.0	0.0	0.0
FeZr-rich	0.8	0.4	0.2	66.7	33.3	0.0	0.0	0.0	0.0
Fe-bearing	0.5	0.8	0.5	50.0	0.0	50.0	0.0	0.0	0.0
SrS-rich	0.5	0.7	0.1	0.0	100.0	0.0	0.0	0.0	0.0
FeS-rich	0.5	0.5	0.2	50.0	50.0	0.0	0.0	0.0	0.0
ZnS-rich	0.5	0.7	0.3	50.0	0.0	50.0	0.0	0.0	0.0
Ni-rich	0.5	0.8	0.4	50.0	0.0	50.0	0.0	0.0	0.0
V-rich	0.5	0.8	0.4	50.0	0.0	50.0	0.0	0.0	0.0
W-rich	0.3	0.7	0.0	0.0	100.0	0.0	0.0	0.0	0.0
BaS-rich	0.3	2.1	0.0	0.0	0.0	0.0	100.0	0.0	0.0
Totals	100.0	0.6	0.3	44.2	44.2	11.0	0.5	0.0	0.0

Table 46. High-Z CCSEM "West C" (40 – 60 mm) Average Composition

Classes	**#**	**Si**	**P**	**S**	**Ti**	**V**	**Cr**	**Fe**	**Ni**	**Cu**	**Zn**	**Sr**	**Zr**	**Ba**	**La**	**Ce**	**W**
Fe-rich	147	0	0	0	0	1	0	93	5	0	0	0	0	0	0	0	0
TiV-rich	46	0	0	0	43	53	2	1	0	0	0	0	0	0	0	1	1
P-rich	30	0	90	1	0	0	0	0	0	0	0	0	0	0	0	0	9
FeNi-rich	21	0	0	1	0	1	0	69	26	0	0	0	0	0	0	1	0
FeTi-rich	20	0	0	0	43	6	0	45	5	0	0	0	0	0	0	0	0
FeTiV-rich	19	0	0	0	23	26	1	43	5	0	0	0	2	0	0	0	0
Zr-rich	14	0	0	0	0	2	0	0	0	0	0	0	97	0	0	0	1
FeV-rich	12	0	1	0	4	25	0	64	4	0	0	0	0	1	0	1	0
Other	10	0	22	0	20	3	0	8	2	1	0	0	22	7	0	3	11
Metal-bearing	10	0	6	0	12	43	13	17	1	0	0	0	0	0	0	4	4
FeCr-rich	9	0	0	0	0	0	25	66	8	0	0	0	0	0	0	0	0
FeTiZr-rich	6	0	0	0	33	7	0	36	6	0	0	0	19	0	0	0	0
FeNi-bearing	6	0	2	0	0	0	3	31	65	0	0	0	0	0	0	0	0
FeZr-bearing	5	0	0	1	11	9	0	44	12	0	0	0	20	3	0	0	0

CuZn-rich	4	0	0	2	0	0	0	0	0	68	31	0	0	0	0	0	0
S-bearing	3	0	0	72	0	0	0	0	0	4	0	0	0	16	0	3	5
LaCe-rich	3	0	0	0	0	0	0	0	0	0	0	0	0	0	15	67	19
FeZr-rich	3	0	0	0	0	0	0	63	9	0	0	0	28	0	0	0	0
Fe-bearing	2	0	0	2	5	7	0	77	3	0	0	0	0	0	0	0	8
SrS-rich	2	0	0	36	0	0	0	0	0	0	0	64	0	0	0	0	0
FeS-rich	2	0	0	70	0	0	0	30	0	0	0	0	0	0	0	0	0
ZnS-rich	2	0	0	65	0	0	0	0	0	0	28	0	0	0	0	0	7
Ni-rich	2	0	0	0	0	0	0	6	95	0	0	0	0	0	0	0	0
V-rich	2	0	0	0	4	89	4	4	0	0	0	0	0	0	0	0	0
W-rich	1	0	0	0	0	0	0	0	0	0	0	0	0	0	0	0	100
BaS-rich	1	0	0	46	0	0	0	0	0	0	0	0	0	54	0	0	0
Totals	382	0	8	2	10	11	1	51	6	1	0	0	5	1	0	1	2

Client_Name Harbert
Client_Number West D (60 – 80 mm)
Project_Number TEH1007708
Sample_Number 9077491W
DataFiles 901501_D\9077491W.*

Mag	Fields	Particles
1000	649.6183	239

Table 47. "West D" (60 – 80 mm) CCSEM particle elemental distribution

Classes	#	Number %
Fe-rich	75	30.99
P-rich	45	18.60
TiV-rich	24	9.92
FeNi-rich	13	5.37
FeTiV-rich	10	4.13
FeCr-rich	10	4.13
Zr-rich	9	3.72
FeTi-rich	9	3.72
W-rich	9	3.72
SrS-rich	5	2.07
FeS-rich	5	2.07
ZnS-rich	5	2.07
FeZr-bearing	4	1.65
Other	4	1.65
Ni-rich	3	1.24
Metal-bearing	3	1.24
FeCrNi-rich	2	0.83
FeV-rich	2	0.83
FeTiZr-rich	2	0.83
Ti-rich	1	0.41
FeNi-bearing	1	0.41
CuZn-beraing	1	0.41
Totals	242	100.00

Table 48. High-Z CCSEM West D (60 – 80 mm) Size Distribution by Average Diameter (microns)

				0.2 -	0.5 -	1.0 -	2.0 -	4.0 -	
Classes	**Number %**	**Mean**	**StdDev**	**0.5**	**1.0**	**2.0**	**4.0**	**8.0**	**>>>**
Fe-rich	31.0	0.6	0.3	54.7	37.3	6.7	1.3	0.0	0.0
P-rich	18.6	0.6	0.3	46.7	37.8	15.6	0.0	0.0	0.0
TiV-rich	9.9	0.5	0.2	66.7	25.0	8.3	0.0	0.0	0.0
FeNi-rich	5.4	0.5	0.2	46.2	53.8	0.0	0.0	0.0	0.0
FeTiV-rich	4.1	0.6	0.3	40.0	50.0	10.0	0.0	0.0	0.0
FeCr-rich	4.1	0.6	0.4	60.0	30.0	10.0	0.0	0.0	0.0
Zr-rich	3.7	0.5	0.3	55.6	33.3	11.1	0.0	0.0	0.0

FeTi-rich	3.7	0.4	0.1	77.8	22.2	0.0	0.0	0.0	0.0
W-rich	3.7	0.8	0.3	33.3	44.4	22.2	0.0	0.0	0.0
SrS-rich	2.1	0.5	0.2	60.0	40.0	0.0	0.0	0.0	0.0
FeS-rich	2.1	1.1	1.5	80.0	0.0	0.0	20.0	0.0	0.0
ZnS-rich	2.1	0.6	0.4	60.0	20.0	20.0	0.0	0.0	0.0
FeZr-bearing	1.7	0.5	0.2	50.0	50.0	0.0	0.0	0.0	0.0
Other	1.7	1.0	0.5	25.0	25.0	50.0	0.0	0.0	0.0
Ni-rich	1.2	0.7	0.5	33.3	33.3	33.3	0.0	0.0	0.0
Metal-bearing	1.2	0.3	0.2	66.7	33.3	0.0	0.0	0.0	0.0
FeCrNi-rich	0.8	0.4	0.1	50.0	50.0	0.0	0.0	0.0	0.0
FeV-rich	0.8	0.5	0.1	50.0	50.0	0.0	0.0	0.0	0.0
FeTiZr-rich	0.8	0.6	0.1	0.0	100.0	0.0	0.0	0.0	0.0
Ti-rich	0.4	0.6	0.0	0.0	100.0	0.0	0.0	0.0	0.0
FeNi-bearing	0.4	0.6	0.0	0.0	100.0	0.0	0.0	0.0	0.0
CuZn-beraing	0.4	0.3	0.0	100.0	0.0	0.0	0.0	0.0	0.0
Totals	100.0	0.6	0.4	52.9	36.8	9.5	0.8	0.0	0.0

Table 49. High-Z CCSEM West D (60 – 80 mm) Average Composition

Classes	#	Si	P	S	Ti	V	Cr	Fe	Ni	Cu	Zn	Sr	Zr	Ba	La	Ce	W
Fe-rich	75	0	0	0	0	1	0	94	4	0	0	0	0	0	0	0	0
P-rich	45	0	93	1	0	0	0	0	0	0	0	0	0	0	0	0	6
TiV-rich	24	0	0	0	45	50	2	0	0	0	0	0	0	0	0	1	2
FeNi-rich	13	0	0	1	1	2	0	70	27	0	0	0	0	0	0	0	0
FeTiV-rich	10	0	1	1	24	24	0	41	6	0	0	0	4	0	0	0	0
FeCr-rich	10	0	0	0	0	0	22	68	8	0	0	0	0	0	0	0	1
Zr-rich	9	0	0	0	0	0	0	1	0	0	0	0	98	0	0	0	1
FeTi-rich	9	0	0	0	42	3	0	51	3	0	0	0	1	0	0	0	0
W-rich	9	0	0	1	0	0	0	0	1	0	0	0	0	0	0	1	97
SrS-rich	5	0	0	33	0	0	0	0	0	0	0	67	0	0	0	0	0
FeS-rich	5	0	0	73	0	0	0	27	0	0	0	0	0	0	0	0	0
ZnS-rich	5	0	1	65	0	0	0	0	0	0	32	0	0	0	0	0	2
FeZr-bearing	4	0	0	0	12	7	0	40	12	2	0	0	25	3	0	0	0
Other	4	0	0	6	0	2	0	1	0	0	0	0	41	1	0	0	49
Ni-rich	3	0	0	0	0	0	0	7	93	0	0	0	0	0	0	0	0
Metal-bearing	3	0	0	0	9	50	4	0	24	0	0	0	0	0	0	13	0
FeCrNi-rich	2	0	0	8	0	0	23	60	9	0	0	0	0	0	0	0	0
FeV-rich	2	0	0	0	5	29	0	61	6	0	0	0	0	0	0	0	0
FeTiZr-rich	2	0	0	0	33	5	0	32	7	0	0	0	23	0	0	0	0
Ti-rich	1	0	0	0	88	12	0	0	0	0	0	0	0	0	0	0	0
FeNi-bearing	1	0	0	0	23	0	0	58	19	0	0	0	0	0	0	0	0
CuZn-beraing	1	0	0	0	0	0	0	0	5	39	16	0	0	0	0	0	40
Totals	242	0	17	4	8	7	1	42	5	0	1	1	5	0	0	0	6

BIBLIOGRAPHY

Abramoff, M. D., P. J. Magelhaes and S. J. Ram (2004). " Image Processing with ImageJ." Biophotonics International **11**(7): 36-42.

Aki, K. and P. G. Richards (1980). Quantitative seismology, Freeman San Francisco.

Alemu, B. L., E. Aker, M. Soldal, Ø. Johnsen and P. Aagaard (2013). "Effect of sub-core scale heterogeneities on acoustic and electrical properties of a reservoir rock: a CO2 flooding experiment of brine saturated sandstone in a computed tomography scanner." Geophysical Prospecting **61**(1): 235-250.

Baechle, G. T., A. Colpaert, G. P. Eberli and R. J. Weger (2008). "Effects of Microporosity on Sonic Velocity in Carbonate Rocks." The Leading Edge(August 2008).

Batzle, M. and Z. Wang (1992). "Seismic properties of pore fluids." Geophysics **57**(11): 1396-1408.

Bergenback, R. E. and R. T. Terriere (1953). " Petrography and petrology of Scurry reef, Scurry County, Texas." American Association of Petroleum Geologists Bulletin **37**(5): 1014-1029.

Biot, M. A. (1955). "Theory of elasticity and consolidation for a porous anisotropic solid." Journal of Applied Physics **26**(2): 182-185.

Birch, F. (1961). "The velocity of compressional waves in rocks to 10 kilobars: 2." Journal of Geophysical Research **66**(7): 2199-2224.

Bolte, S. and F. P. Cordelieres (2006). "A guided tour into subcellular colocalization analysis in light microscopy." Journal of Microscopy **224**(3): 213-232.

Brajanovski, M., B. Gurevich and M. Schoenberg (2005). "A model for P-wave attenuation and dispersion in a porous medium permeated by aligned fractures." Geophysical Journal International **163**(1): 372-384.

Brajanovski, M., T. M. Müller and B. Gurevich (2006). "Characteristic frequencies of seismic attenuation due to wave-induced fluid flow in fractured porous media." Geophysical Journal International **166**(2): 574-578.

Brnak, J., B. Petrich and M. R. Konopczynski (2006). "Application of smartwell technology to the CO2 EOR project: A case study." Society of Petroleum Engineers Journal **100117**.

Burnside, R. J. (1959). "Geology of part of Horseshoe Atoll in Borden and Howard

Counties, Texas." Geological Survey Professional Paper **315-B**.

Carcione, J. M. and U. Tinivella (2001). "The seismic response to overpressure: a modelling study based on laboratory, well and seismic data." Geophysical Prospecting **49**(5): 523-539.

Castagna, J. P., H. W. Swan and D. J. Foster (1998). "Framework for AVO gradient and intercept interpretation." Geophysics **63**(3): 948-956.

Chilingarian, G. V., S. J. Mazzullo and H. H. Rieke (1992). Carbonate reservoir characterization: a geologic-engineering analysis, Elsevier.

Darcy, H. (1856). Les fontaines publiques de la ville de Dijon, V. Dalmont.

Delaney, D. (2013). Ultrasonic Seismic Wave Attenuation, Petrophysical Models and Work Flows for Better Subsurface Imaging, Energy Exploration, and Tracking of Sequestrated Carbon Dioxide. Master of Science Master's Thesis, University of Pittsburgh.

Dougherty, B. and K.-H. Kunzelmann (2006). Computing Local Thickness of 3D Structures with ImageJ. Microscopy & Microanalysis 2007 Meeting, Ft. Lauderdale, Florida.

Dvorkin, J., G. Mavko and A. Nur (1995). "Squirt Flow in Fully Saturated Rocks." Geophysics **60**(1): 97-107.

Eberhart-Phillips, D., D.-H. Han and M. D. Zoback (1989). "Empirical relationships among seismic velocity, effective pressure, porosity, and clay content in sandstone." Geophysics **54**(1): 82-89.

Emery, D., K. Myers, G. Bertram, C. Griffiths, N. Milton, T. Reynolds, M. Richards and S. Sturrock (1996). Sequence Stratigraphy. Cambridge, MA, Marston Book Services Ltd.

Freund, D. (1992). "Ultrasonic compressional and shear velocities in dry clastic rocks as a function of porosity, clay content, and confining pressure." Geophysical Journal International **108**(1): 125-135.

Galloway, D., D. Jones and S. Ingebritsen (1999). "Land subsidence in the United States: US Geological Survey Circular 1182."

Galloway, W. E. (1983). "Depositional Architecture and Reservoir Characterization of Late Paleozoic Submarine Slope and Basin Depositional Systems - Midland and Delaware Basins, Texas." Aapg Bulletin-American Association of Petroleum Geologists **67**(3): 466-466.

Gassmann, F. (1951). "Elasticity of porous media." Vierteljahrschrift der Naturforschenden gesellschaft in Zurich **96**: 1-21.

Han, D.-h. (1987). Effects of porosity and clay content on acoustic properties of sandstones and unconsolidated sediments, Stanford Univ., CA (USA).

Han, D.-H. (2011). "FLAG Fluid Calculator." from http://www.rpl.uh.edu/.

Han, W. S. (2008). EVALUATION OF CO2 TRAPPING MECHANISMS AT THE NORTHERN PLATFORM: SITE OF 35 YEARS OF CO2 INJECTION. Doctorate of Philosophy, The New Mexico Institute of Mining and Technology.

Harris, J. M. and R. T. Langan (2001). "Crosswell Seismic Profiling: Principle to Applications." Search and Discovery Article **40030**: 2001.

Hashin, Z. and S. Shtrikman (1961). "Note on Effective Constants of Composite Materials." Journal of the Franklin Institute-Engineering and Applied Mathematics **271**(5): 423-&.

Hersch, J. B. (1987). "Exploration methods-lower Tuscaloosa trend, southwest Mississippi." AAPG (Am. Assoc. Pet. Geol.) Bull.;(United States) **71**(CONF-8710198-).

Hill, R. (1952). "The Elastic Behaviour of a Crystalline Aggregate." Proceedings of the Physical Society. Section A **65**(5): 349.

Hilterman, F. (1983). "Seismic lithology." SEG Continuing Education Course, SEG, Tulsa.

Hovorka, S. D., T. A. Meckel and R. H. Treviño (2013). "Monitoring a large-volume injection at Cranfield, Mississippi—Project design and recommendations." International Journal of Greenhouse Gas Control **18**(0): 345-360.

Hovorka, S. D., T. A. Meckel, R. H. Trevino, J. Lu, J.-P. Nicot, J.-W. Choi, D. Freeman, P. Cook, T. M. Daley, J. B. Ajo-Franklin, B. M. Freifeild, C. Doughty, C. R. Carrigan, D. L. Brecque, Y. K. Kharaka, J. J. Thordsen, T. J. Phelps, C. Yang, K. D. Romanak, T. Zhang, R. M. Holt, J. S. Lindler and R. J. Butsch (2011). "Monitoring a large volume CO_2 injection: Year two results from SECARB project at Denbury's Cranfield, Mississippi, USA." Energy Procedia **4**(0): 3478-3485.

Huitt, J. (1956). "Fluid flow in simulated fractures." AIChE Journal **2**(2): 259-264.

Izgec, O., B. Demiral, H. Bertin and S. Akin (2008). "CO2 injection into saline carbonate aquifer formations I: laboratory investigation." Transport in Porous Media **72**(1): 1-24.

Johnston, D. H., M. N. Toksoz and A. Timur (1979). "Attenuation of seismic waves in dry and saturated rocks: II. Mechanisms." Geophysics **44**(4): 691-711.

Jones, S. M. (1995). "Velocities and quality factors of sedimentary rocks at low and high effective pressures." Geophysical Journal International **123**(3): 774-780.

Kane, A. V. (1979). "Performance review of large-scale CO2-Wag enhanced recovery project, unit-Kelly-Snyder field." Society of Petroleum Engineers(7091).

Kaselow, A. and S. A. Shapiro (2004). "Stress sensitivity of elastic moduli and electrical resistivity in porous rocks." Journal of Geophysics and Engineering **1**(1): 1-11.

Kearey, P., M. Brooks and I. Hill (2002). An introduction to geophysical exploration. Malden, MA, Blackwell Science.

Khaksar, A., C. Griffiths and C. McCann (1999). "Compressional-and shear-wave velocities as a function of confining stress in dry sandstones." Geophysical Prospecting **47**(4): 487-508.

Khinast, J., G. F. Krammer, C. Brunner and G. Staudinger (1996). "Decomposition of limestone: The influence of CO2 and particle size on the reaction rate." Chemical Engineering Science **51**(4): 623-634.

Kirstetter, O. and C. MacBeth (2001). Compliance-based interpretation of dry frame pressure sensitivity in shallow marine sandstone. Expanded Abstracts.

Langston, M. V., S. F. Hoadley and D. N. Young (1988). Definitive CO_2 flooding response in the Unit. SPE Enhanced Oil Recovery Symposium.

Langston, M. V., S. F. Hoadley and D. N. Young (1988). "Definitive CO_2 flooding response in the Unit." Society of Petroleum Engineers(17321).

Larkin, R. J. (2006). "Well Construction: CO2 enhanced Oil Recovery Flood, Unit."

Lasaga, A. C. (1984). "Chemical-Kinetics of Water-Rock Interactions." Journal of Geophysical Research **89**(Nb6): 4009-4025.

Lasaga, A. C., R. J. Kirkpatrick, R. A. Berner and D. E. Anderson (1981). Reviews in Mineralogy. Chelsea, Michigan 48118, BookCrafters, Inc.

Lu, J. M., Y. K. Kharaka, J. J. Thordsen, J. Horita, A. Karamalidis, C. Griffith, J. A. Hakala, G. Ambats, D. R. Cole, T. J. Phelps, M. A. Manning, P. J. Cook and S. D. Hovorka (2012). "CO_2-rock-brine interactions in Lower Tuscaloosa Formation at Cranfield CO_2 sequestration site, Mississippi, USA." Chemical Geology **291**: 269-277.

Madonna, C., B. S. G. Almqvist and E. H. Saenger (2012). "Digital rock physics: numerical prediction of pressure-dependent ultrasonic velocities using micro-CT imaging." Geophysical Journal International **189**(3): 1475-1482.

Margrave, G. and E. Krebes (2001). Zoeppritz Explorer. University of Calgary, Consortium for Research in Elastic Wave Exploration Seismology.

Mavko, G., T. Mukerji and J. Dvorkin (1998). The Rock Physics Handbook: Tools for Seismic Analysis in Porous Media. Cambridge, United Kingdom, Cambridge University Press.

Mavko, G., T. Mukerji and J. Dvorkin (2003). Introduction to Rock Physics (Class), Cambridge University Press.

McKenna, J., B. Gurevich, M. Urosevic and B. Evans (2003). "New technologies to beat the odds-Rock physics--Application to geological storage of CO2." APPEA Journal-Australian Petroleum Production and Exploration Association **43**(1): 567-576.

Myers, D. A., P. T. Stafford and R. J. Burnside (1956). "Geology of the late Paleozoic Horseshoe Atoll in west Texas." Bureau of Economic Geology **5607**.

NER (2006). Autolab 1500 Operations Manual. G. S. C. F. Laboratory, New England Research, Inc.

NER (2013). AUTOLAB 1500 Fact Sheet. N. E. Research.

NETL (2012). Carbon Utilization and Storage Atlas, National Energy Technology Laboratory, Department of Energy.

O'Dowd, W. (2008). Factsheet for Southwest Regional Partnership on Carbon Sequestration Field Validation Test.

Parsons, R. (1966). "Permeability of idealized fractured rock." Old SPE Journal **6**(2): 126-136.

Prasad, M. and M. H. Manghnani (1997). "Effects of pore and differential pressure on compressional wave velocity and quality factor in Berea and Michigan sandstones." Geophysics **62**(4): 1163-1176.

Pride, S. R., J. G. Berryman and J. M. Harris (2004). "Seismic attenuation due to wave-induced flow." Journal of Geophysical Research: Solid Earth (1978–2012) **109**(B1).

Purcell, C. (2012). Velocity Measurements in Reservoir Rock Samples From a Limestone Unit Using Various Pore Fluids, and Integration with Well Logs and Seismic Data. Doctor of Philosophy, University of Pittsburgh.

Raines, M. A. (2005). "Kelly-Snyder (Cisco-Canyon) Fields/ Unit. West Texas Geological Society: Oil and gas fields in west Texas." West Texas Geological Society, Midland, Texas. **8**(05-114): 69-78.

Reid, A. M. and S. A. T. Reid (1991). "The Cogdell field study, Kent and Scurry counties, Texas: A post-mortem. In M. Candelaria, eds., The Permian basin plays: tomorrow's technology today." West Texas Geological Society Publication 91-89: 39-66.

Roden, R. (2008). "Examples of Gas Pay on AVO Crossplots."

Ross, C. P. and D. L. Kinman (1995). "Nonbright-Spot AVO: Two Examples." Geophysics **60**(5): 1398-1408.

Rutherford, S. R. and R. H. Williams (1989). "Amplitude-versus-offset variations in gas sands." Geophysics **54**(6): 680-688.

Sanpaz (2009). Components of the Cauchy stress tensor in Cartesian coordinates. Inkscape. Components_stress_tensor_cartesian.svg.png, Wikipedia.

Schatzinger, R. A. (1988). "Changes in facies and depositional environments along and across the trend of Horseshoe Atoll, Scurry and Kent Counties, Texas. In, B.K., Cunningham, eds., Permian and Pennsylvanian Stratigraphy Midland basin, west Texas: Studies to aid hydrocarbon exploration. Permian Basin." Society for Economic Paleontologists and Mineralogists Publication **88**(28): 79-95.

Schoenberg, M. and J. Douma (1988). "Elastic Wave-Propagation in Media with Parallel Fractures and Aligned Cracks." Geophysical Prospecting **36**(6): 571-590.

Shapiro, S. A. (2003). "Elastic piezosensitivity of porous and fractured rocks." Geophysics **68**(2): 482-486.

Shapiro, S. A. K., Axel (2005). "Porosity and elastic anisotropy of rocks under tectonic stress and pore-pressure changes." Geophysics **70**(5).

Sheriff, R. E. and L. P. Geldart (1995). Exploration seismology. Cambridge ; New York, Cambridge University Press.

Shuey, R. (1985). "A simplification of the Zoeppritz equations." Geophysics **50**(4): 609-614.

SPE (1999). CO_2 flooding. Richardson, Tex., Society of Petroleum Engineers.

Stutzman, P. E. (1999). "Specimen Preparation for Scanning Electron Microscopy." the Twenty-First International Conference on Cement Microscopy.

Thomsen, L. (1972). "Elasticity of polycrystals and rocks." Journal of Geophysical Research **77**(2): 315-327.

Thomsen, L. (1986). "Weak elastic anisotropy." Geophysics **51**(10): 1954-1966.

Thomsen, L. (1995). "Elastic anisotropy due to aligned cracks in porous rock." Geophysical Prospecting **43**(6): 805-829.

Timoshenko, S. P. and J. Goodier (2011). "Theory of elasticity." International Journal of Bulk Solids Storage in Silos **1**(4): 567-567.

Toews, K. L., R. M. Shroll, C. M. Wai and N. G. Smart (1995). "pH-Defining Equilibrium between Water and Supercritical CO2. Influence on SFE of Organics and Metal Chelates." Analytical Chemistry **67**(22): 4040-4043.

Toksöz, M., D. Johnston and A. Timur (1979). "Attenuation of seismic waves in dry and saturated rocks: I. Laboratory measurements." Geophysics **44**(4): 681-690.

Van Eldik, R. and D. A. Palmer (1982). "Effects of pressure on the kinetics of the dehydration of carbonic acid and the hydrolysis of CO2 in aqueous solution." Journal of Solution Chemistry **11**(5): 339-346.

Vest, E. L. J. (1970). "Oil Fields of Pennsylvanian-Permian Horseshoe Atoll, West Texas." AAPG Special Volumes **M 14: Geology of Giant Petroleum Fields**: 185-203.

Waite, L. E. (1993). "Upper Pennsylvanian Seismic Sequences and Facies of the Eastern and Southern Horseshoe Atoll, Midland Basin, West Texas."

Wikipedia_Commons. "http://upload.wikimedia.org/wikipedia/commons/4/44/NMO_Correction.png."

Winkler, K. W. (1985). "Dispersion analysis of velocity and attenuation in Berea sandstone." Journal of Geophysical Research **90**(B8): 6793-6800.

Womack, R. (1950). "Brookhaven oil field, Lincoln County, Mississippi." AAPG Bulletin **34**(7): 1517-1529.

Zhang, R., R. Ghosh, M. K. Sen and S. Srinivasan (2012). "Time-lapse surface seismic inversion with thin bed resolution for monitoring CO_2 sequestration: A case study from Cranfield, Mississippi." International Journal of Greenhouse Gas Control.

Zimmerman, R. W., W. H. Somerton and M. S. King (1986). "Compressibility of porous rocks." Journal of Geophysical Research: Solid Earth **91**(B12): 12765-12777.

Zoeppritz, K. (1919). "On the reflection and penetration of seismic waves through unstable layers." Goettinger Nachr **1**: 66-84.